Diesel Oxidation NO$_x$ Adsorption Catalysts

Sara Viéitez-Calo

Thesis submitted in accordance with the requirements

for the degree of Doctor of Philosophy

Prof Stan E. Golunski

Prof Stuart H. Taylor

School of Chemistry

Cardiff University   **2015**

To everyone who has supported me during the course of this thesis

"Countries can attain a certain level of emission reductions on their own, but they can do much more if they collaborate with each other, in particular with certain specific sectors."

Christiana Figueres

UN Climate Chief

2015

ACKNOWLEDGMENTS

AGRADECIMIENTOS

ABSTRACT

Worldwide usage of diesel engines has been rising rapidly and, accordingly, more stringent emission standards are introduced to lower the concentrations of diesel exhaust pollutants.

NO_x abatement is crucial, especially in diesel engines where controlling NO_x is extremely difficult as oxygen is always in excess. The title and objective of this thesis arises from a novel approach, the diesel oxidation NO_x adsorption catalyst (DONAC), where NO_x is to be stored by a diesel oxidation catalyst (DOC).

Supported platinum catalysts are the most used technology for diesel oxidation catalysts. Hence, the investigation of the oxidation properties of supported platinum catalysts and particularly, how these properties are affected by the support material, is of great importance. This work addresses not only the effect of the support, platinum loading, preparation method, calcination conditions and platinum precursor, but also the effect of the titania phase composition (anatase or anatase-rutile). A series of supported platinum catalysts including Pt/TiO_2, Pt/SiO_2, Pt/Al_2O_3, Pt/TiO_2-SiO_2 and $Pt/SiO_2-Al_2O_3$ were prepared by non-aqueous impregnation and chemical vapour impregnation. In order to determine the effect of the support on the structural and electronic properties of the supported platinum catalysts detailed characterisation including XRD, BET, CO chemisorption, NH_3-TPD, H_2-TPR, TGA, DRIFTS, Raman, XPS, SEM, TEM and EDX was performed. Two relevant oxidation reactions, total oxidation of propane and oxidation of nitric oxide to nitrogen dioxide, were studied.

It is found that the activity of supported platinum catalysts is greatly affected by the support material, in general, their performance is enhanced by addition of SiO_2 to the TiO_2 support. The activity of the platinum catalysts depends strongly on oxidation state, with platinum in

metallic state being most active. However, it is not only the platinum oxidation state but a combination of several factors including metal dispersion, surface area, morphology and phase composition of the support that explains the variations in catalytic activity. Morphology and phase composition play an active role in the redox properties of the support and its interaction with supported metal particles. The high propane oxidation activity of Pt supported on anatase TiO_2 is attributed to highly reactive oxygen species within the support.

DeNO$_x$ technologies based on the concept of NO$_x$ storage have proven to be effective, however further studies are needed to succeed in finding an optimum NO$_x$ storage system. A series of metal (Cu, Fe and Pt) -exchanged zeolites with different compositions ($SiO_2/Al_2O_3 = 5.1 - 50$) and frameworks (Y, ZSM-5 and BETA) were prepared by two different exchange methods (WIE and CVI). The DOE method was applied to investigate the way in which preparation experimental variables affect the NO$_x$ storage capacity of Cu^{II}/ZSM-5 (30). Evaluation of NO$_x$ storage capacity, in the presence and absence of O$_2$, of metal-exchanged zeolites was carried out. In order to correlate the physicochemical properties of the metal-exchanged zeolites with their NO$_x$ storage performance, characterisation including XRD, BET, NH$_3$-TPD, H$_2$-TPR, DRIFTS, UV-Vis DRS, XPS, TEM and EDX was performed.

It is found that the NO$_x$ adsorption/desorption capacity and the stability of those adsorption species formed, is greatly affected by the nature of the exchanged metal and the structure and acidity of the zeolite support. Due to the intrinsic adsorption capacity of the parent zeolite, H$^+$-ZSM-5 (23), Cu^{II}/ZSM-5 (23) catalysts prepared by WIE and CVI exhibit high NO$_x$ storage capacities. The initial redox state, Cu^{2+}/Cu^+ and Fe^{2+}/Fe^{3+} ratio, and bonding strength of the metal ions to the framework affect the reducibility of metal species and consequently the storage capacity.

The preparation method is found to be crucial in controlling metal loading, nature and distribution of active species and crystallites size. The statistical approach allowed for a significant enhancement in the storage capacity of Cu^{II}/ZSM-5 (30) and, in particular, the amount of NO_x desorbed at high temperature. Temperature is found to have the greatest effect on the NO_x storage capacity. In addition, its influence is dependent on the copper precursor concentration.

Among the zeolite based catalysts studied, potential candidates for application under real working conditions, those that exhibit greater NO_x desorption at high temperatures (T > 200 °C) were found.

GLOSSARY

Å	Angstrom (10^{-10} meters)
AQ IMP	Aqueous impregnation
a.u.	Arbitrary units
BET	Brunauer, Emmet and Teller
BETA	Zeolite BEA
cm	Centimetre
cm^{-1}	Reciprocal Centimetre
^{o}C	Degrees Celsius
CVI	Catalyst prepared by Chemical Vapour Impregnation
DRIFTS	Diffuse Reflectance Infrared Fourier Transform Spectroscopy
DOC	Diesel oxidation catalyst
DOE	Statistical design of experiments
DPF	Diesel particulate filter
EDX	X-ray energy dispersive spectroscopy
eV	Electron Volts
FID	Flame ionisation detector
FTIR	Fourier transform infrared spectroscopy
g	Gram
GC	Gas Chromatography
GHSV	Gas hourly space velocity
h	Hours
HC	Hydrocarbons
ICP-MS	Inductively Coupled Plasma Mass Spectroscopy
WIE	Catalyst prepared by Wet Ion Exchange
IMP	Catalyst prepared by Impregnation
IWI	Catalyst prepared Incipient wetness impregnation
M	Molar
mg	Milligram (10^{-3} g)
mol	Moles
min	Minutes
MSI	Metal-support interaction
nm	Nanometre (10^{-9} m)
NSR	NO_x storage reduction catalyst
PM	Particulate matter
SCR	Selective catalytic reduction
SMSI	Strong metal support interaction

SEM	Scanning electron microscopy
SiO_2/Al_2O_3	Molar ratio of SiO_2 to Al_2O_3 in a zeolite
TCD	Thermal conductivity detector
TEM	Transmission electron microscopy
TGA	Thermogravimetric analysis
TPR	Temperature programmed reduction
TOF	Turnover frequency
TWC	Three-way catalyst
NH_3-TPD	Temperature programmed ammonia desorption
UV-Vis	Ultraviolet- Visible spectroscopy
VOC	Volatile organic compounds
wt. %	Weight percent
XPS	X-ray photoelectron spectroscopy
XRD	X-ray diffraction
Y	Zeolite FAU
ZSM-5	Zeolite ZSM-5
μmol	Micromoles (10^{-6} moles)

TABLE OF CONTENTS

Introduction

1

1.1 Introduction

Since legislation was established to control emissions from vehicles, heterogeneous catalysts have been used to reduce the concentration of the pollutants emitted.

The term catalysis was first introduced by Berzelius in 1836. A catalyst increases the rate of a chemical reaction without itself being consumed or changed in the process. Catalysis affects the kinetics of a reaction, not its thermodynamics.
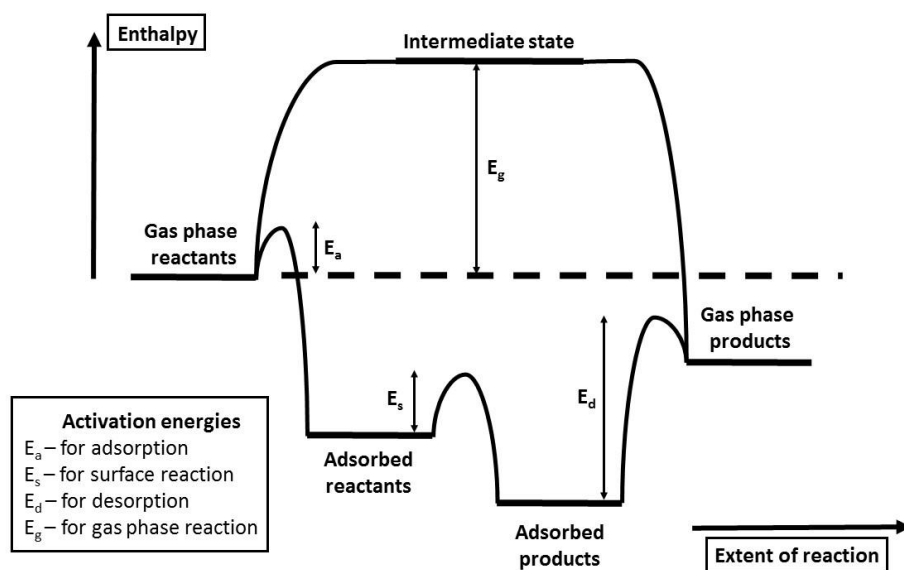
Figure 1.1. The simplified energy level diagram associated with a catalytic reaction. Reproduced from reference [1].

Catalysts do not and cannot change the thermodynamic equilibrium of a reaction. The overall change in free energy for the catalytic reaction equals that of the uncatalysed

reaction. Hence, the catalyst does not affect the equilibrium constant of the overall reaction. The catalyst provides an alternative reaction pathway that is, often, more complicated and includes several catalytic intermediates. However, the highest activation barrier in the catalysed pathway is still lower than that of the uncatalysed reaction. Hence, a catalyst offers an energetically favourable alternative to the uncatalysed reaction, thus enabling processes to be carried out under industrially feasible operating conditions.

Catalyst activity, selectivity and durability are the three most important characteristics of a catalyst. Activity refers to the extent to which the reaction is promoted by the presence of the catalyst. Selectivity determines which reactions are favoured in the presence of the catalyst, of the many reactions that could possibly occur. Durability is indispensable for commercial catalysts and refers to the absence of deactivation following use or aging of the catalyst.

Catalysts can be classified into three categories: homogeneous catalysts, heterogeneous catalysts and biocatalysts. In homogeneous catalysis, the catalyst is in the same phase as the reactants and products. In heterogeneous catalysis, the catalyst and the reactants are in different phases. Often, the catalyst is a solid and the reactants are gases or liquids. One important advantage of heterogeneous catalysis is that the catalyst is easy to separate and recover. In biocatalytic processes, natural catalysts are used. In most cases, the biocatalyst is an enzyme; a complex protein that catalyses reactions in living cells. The structure of enzymes offers a very shape-specific active site and therefore enzymes are highly specific catalysts.

A catalysed reaction comprises of five different steps: i) transport of the reactant(s) from the reaction medium (gas / liquid phase) to the catalyst surface, ii) chemisorption at the active centre, iii) reaction takes place to form the chemisorbed product(s), iv) desorption

of the product(s) and v) transport of the product(s) from the catalyst surface to the reaction medium.
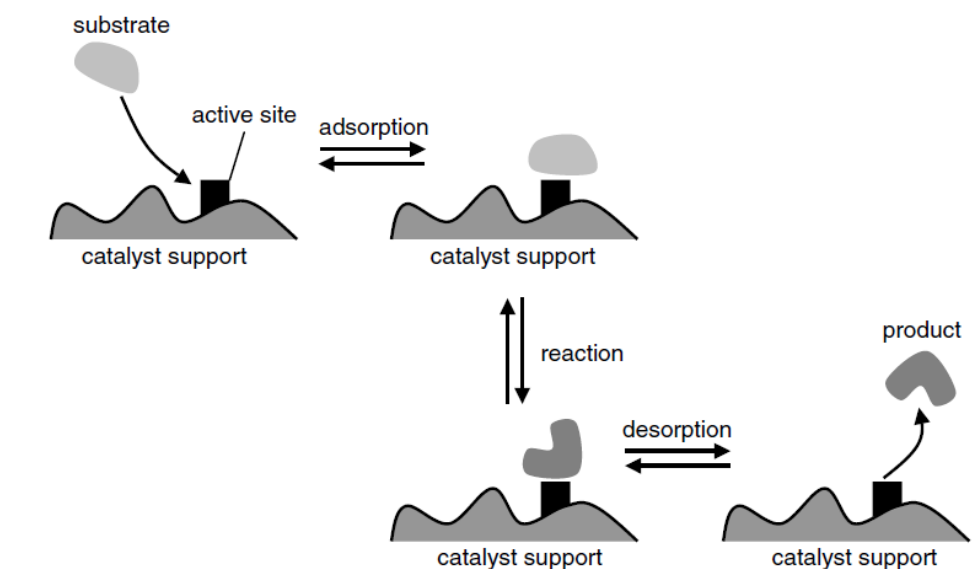
Figure 1.2. Schematic of reaction on a catalyst surface that follows the Langmuir-Hinshelwood model. Taken from reference [2].

Adsorption is the first reactive step in the cycle of heterogeneous catalysis. The reaction mechanisms describe the adsorption and desorption of reactant(s) molecules at a catalytically active surface. For the reaction A + B → C, the Langmuir-Hinshelwood mechanism assumes that both reactants, A and B, are adsorbed on the catalyst surface before the reaction takes place. The so- called Eley-Rideal mechanism, describes the situation where only A is adsorbed on the catalyst surface and B from the reaction medium reacts with adsorbed molecules of A to form the product C. In the third mechanism, the Mars-Van-Krevelen mechanism, the surface itself participates actively in the reaction; one of the reactant forms a thin surface layer of metal-reactant on the catalytic surface and the other reactant reacts directly from the reaction medium with the chemically bonded atoms from the reactant surface. The Langmuir-Hinshelwood mechanism is the most common

situation in heterogeneous catalysis, partly because many reactants are activated by the adsorption on the catalyst surface.

The creation of a surface requires energy because bonds have to be broken. Thus, the total energy of the system increases, meaning that the surface free energy is always positive. The surface free energy is related to the cohesive energy of the solid and to the number of bonds between an atom and its nearest neighbours that have to be broken to create the surface. Because the surface is a region of high energy, thermodynamics dictates a tendency to minimise this energy. Minimization of the surface free energy is the driving force behind surface relaxation, surface reconstruction, sintering and adsorption.
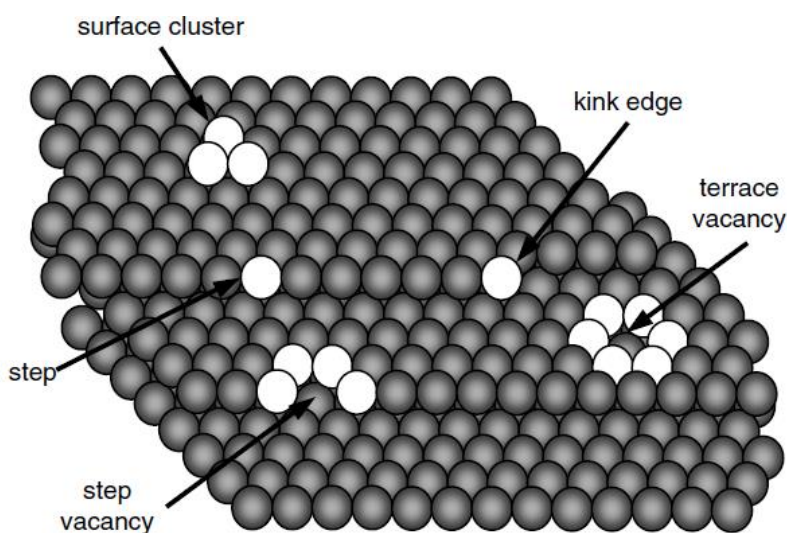
Figure 1.3. Schematic representation of a solid catalyst crystal surface. Taken from reference [2].

The catalyst is, mostly, an inactive surface with a few very active sites. Catalytic surfaces are not uniform. As shown in Figure 1.3, metal crystal surfaces possess vacancies, terraces, steps and kinks. The surface free energy is related to the number of unsaturated bonds in the surface atom. Generally, low coordination surface atoms have the highest surface free energy, the highest reactivity and the strongest binding for the adsorbate (high heat of

adsorption). Hence, some catalytic reactions show dependence on the nature of the structure involved.

The interaction between catalysts and substrates, intermediates and products is of great importance and dictates catalyst performance. The catalyst/substrate interactions must be optimal, not too weak and not too strong. The active site follows Sabatier's principle, is often not the energetically preferred site for adsorption, but that site which optimises the adsorption of reactants on the surface and desorption of products after reaction. Bulk parameters, such as particle size, shape and mechanical strength of the catalyst as well as, mass and heat transfer are crucial. Mass transport limitations decrease the rate of the reactant(s) adsorption and product(s) desorption. In addition, uneven heat transfer can lead to hotspots, sintering and runaway reactions. Ideally, the active sites should all be identical and isolated. However, industrial heterogeneous catalysts are often amorphous, multicomponent and multiphase solids that contain many types of active sites.

As already mentioned, the catalytic cycle consists of several elementary reactions or steps. The experimental reaction rate is not the average or the cumulative rate of these steps but the rate of the slowest step(s) in the cycle, also called the rate-determining step(s). The reaction rate depends on the heat of adsorption and follows a volcano plot. At the start of the reaction the heat of adsorption increases and as more reactants bind to the catalyst, the reaction rate also increases. When the heat of adsorption is too strong, desorption of the substrates (or products) is not feasible and the reaction rate starts to decrease.

A catalyst is not consumed during the reaction. While the catalyst may undergo changes during the catalytic cycle, it returns to its original form at the end of the cycle. Because the active site is regenerated, each site can participate in many consecutives cycles. As a result, only a small catalyst: substrate ratio is required and this ratio reflects the catalyst's

efficiency, which is measured as turnover number (TON) or turnover frequency (TOF). In real applications, the catalytic system can lose or gain activity due to sensitivity to changes in acidity/basicity, temperature, pressure or phase composition. Moreover, with increasing conversion, products and by-products might bind to the catalyst and change the preferred reaction pathway. Processes including deactivation, sintering, inhibition and poisoning can cause a drop in catalytic performance.

1.2 Diesel exhaust emissions

In theory, the combustion reaction that takes place in engines (petrol or diesel) should completely oxidise the hydrocarbons (HC) present in the fuel to CO_2 and H_2O. Hence, the exhaust would be formed of N_2 and air. Unfortunately, this is not what happens under real working conditions. Fuel combustion involves many different reactions due to its complex composition. Not all the HC are oxidised and consequently, the exhaust emissions present a variety of compounds including partially combusted oxygenates and CO.

Popularity of diesel-powered cars has increased considerably since the early 1980s. The superior fuel economy and lower car tax in several countries makes diesel cars an attractive alternative to conventional petrol vehicles. Nowadays, around 50 % of all new European cars have a diesel engine. Operation at low exhaust temperatures and high O_2 concentrations is characteristic of diesel engines. However, not only the operation mode is different in a diesel engine, exhaust emissions control and aftertreatment needs differ significantly from those applied in petrol powered vehicles.

Exhaust emissions vary with the equivalence ratio λ. The engine must operate in a very small window of fuel-air ratio because the chemical reactions that reduce NO_x and oxidize

HC and CO are mixture dependent and mutually exclusive. As illustrated in Figure 1.4, while in a fuel rich environment, at $\lambda < 1$, the activity for reduction of NO_x is high, in a lean environment, at $\lambda > 1$, the reverse occurs and the oxidation of CO an HC is feasible.
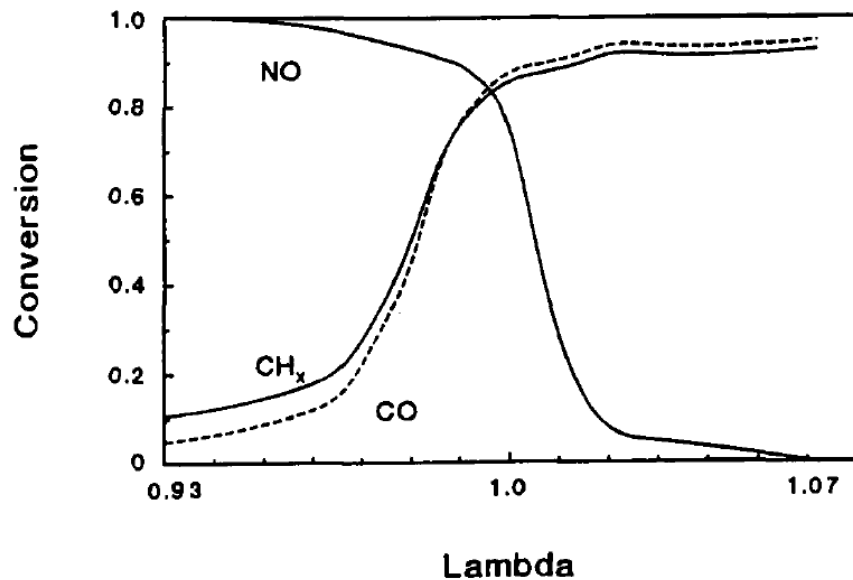
Figure 1.4. The concentration of CO, NO and CH_x emitted by a gasoline engine as a function of λ, the fuel-air ratio. Taken from reference [3].

1.2.1   Composition

Diesel exhaust emissions present a truly complex composition. A large variety of compounds in different concentrations form the exhaust; including oxygen (O_2), nitrogen (N_2), water (H_2O), carbon dioxide (CO_2), carbon monoxide (CO), hydrocarbons (HC), nitrogen oxides (NO_x), sulphur oxides (SO_x) and particulate matter (PM). Among these, special attention has been paid to those present in higher concentration, which are related to air quality problems and exhibit adverse effects on the environment or human health.

Hydrocarbons (HC) and volatile organic compounds (VOC)

Diesel engine emissions are composed of a variety of organic compounds, ranging from C_2 to C_{12+}[4][5]. These compounds are attributed to unburnt HC, HC partial oxidation during combustion and pyrolysis and evaporation from the fuel tank.

The term VOC refers to volatile hydrocarbons, typically those with a boiling point below 100 °C.

Some of these compounds contribute to ozone depletion. Under atmospheric conditions, in the presence of sunlight, HCs react with NO_x to produce ozone-containing photochemical smog. Breathing problems and asthma are a direct consequence. Low levels of other secondary pollutants such as peroxyacetylnitrate (PAN), which are lachrymators, are also formed through reaction of HCs with NO_x.

$$HC \; + \; NO_x \; + \; h\nu \; \rightarrow \; O_3 \; + \; \text{other products}$$ Equation 1.1
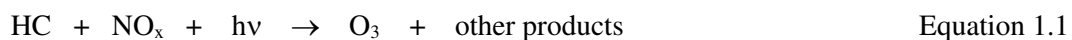
Adverse effects on health are also attributed to the carcinogenic character of various of these HC [6].

In extremely fuel-rich regions of the flame, HC polymerization is favoured over oxidation. As a result, polycyclic aromatic hydrocarbons (PAH) are formed. Limiting the emissions of these compounds is of great importance due to their carcinogenic and mutagenic character.

Carbon dioxide (CO_2)

CO_2 is the major product of the total oxidation of HCs. It is a nontoxic gas but represents one of the most important greenhouse gases and contributes towards acidification of oceans.

Restrictions on CO_2 emissions is then associated with finding alternatives to fossil- fuelled cars, for example electric or hydrogen cars.

Carbon monoxide (CO)

CO is the product of incomplete combustion. It is an intermediate in the oxidation of HCs to CO_2 and H_2O. Only when the temperature and the concentration of oxygen is sufficiently high will CO be oxidised to CO_2. Hence, poor mixing and insufficient oxygen concentrations lead to an increase in the CO levels emitted.

$$4 C_nH_m + (2n + m) O_2 \rightarrow 2m H_2O + 4n CO$$ Equation 1.2
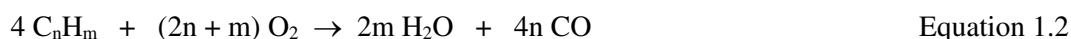
CO is an extremely toxic gas, which reduces the ability of blood to carry oxygen, causes headaches, respiratory problems and at high concentrations or long exposure, death.

Nitrogen oxides (NO_x)

Nitrogen oxides (NO_x) are a mixture containing mostly nitrogen monoxide, also called nitric oxide, (NO) and between 5 and 10 % of nitrogen dioxide (NO_2).

Nitric oxide (NO) is the principal nitrogen- containing by-product of combustion. NO is formed by three mechanisms: thermal, prompt and fuel NO_x formation [7].

At high combustion temperatures, N_2 and O_2 react to establish an equilibrium with NO. The formation of NO by oxidation of atmospheric nitrogen can be expressed in terms of the overall reaction:

$$N_2 + O_2 \leftrightarrow 2 NO$$ Equation 1.3
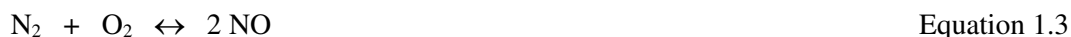
The reaction is highly endothermic [ΔH^0 (298 K) = 90.4 kJ·mol^{-1}]. As a result, the equilibrium concentration of NO is high at high temperatures, typical of stoichiometric

combustion, and decreases rapidly away from that point. The direct reaction of N_2 with O_2 is too slow to account for significant NO formation. In 1947, Zeldovich *et al.* postulated a simple chain mechanism for thermal NO formation, where oxygen atoms produced in flames by dissociation of O_2 or by radical attack on O_2, react with nitrogen molecules to form NO.

$$N_2 + O \leftrightarrow NO + N \hspace{4cm} \text{Equation 1.4}$$

$$N + O_2 \leftrightarrow NO + O \hspace{4cm} \text{Equation 1.5}$$

Due to the high activation energy, the formation of NO by this mechanism is extremely temperature sensitive and proceeds at a slower rate than the oxidation of the fuel constituents. The production of atomic oxygen required for the first reaction represented in Equation 1.4, is also highly temperature sensitive

NO can be formed from N_2 in air through a mechanism distinct from the thermal mechanism. Prompt NO is produced under low temperature, fuel-rich conditions and at short residence times. This mechanism was first postulated by Fenimore *et al.* in 1971. The NO formed is the result of the attack of a hydrocarbon free radical on N_2.

$$HC + N_2 \rightarrow HCN + N \hspace{4cm} \text{Equation 1.6}$$

Under certain fuel-rich conditions, the concentration of such hydrocarbon radicals is high enough that reactions with N_2 are important and this leads to significant NO formation. These reactions have relatively low activation energies and proceed at a rate comparable to that of the oxidation of the fuel.

Fuels contain organically bound nitrogen that is readily oxidised to NO during combustion. The contribution of fuel-nitrogen to NO_x formation is most clearly shown when the

production of NO from N_2 is not feasible.

Although NO is thermodynamically unstable at room temperature, the concentration of NO is maintained when the gas rapidly expands during cool down. Consequently, significant amounts of NO_x (up to 3500 ppm of NO with traces of NO_2) are present in the exhaust effluent of diesel vehicles.

$$2\,NO\ +\ O_2\ \rightarrow\ 2\,NO_2 \qquad\qquad\qquad \text{Equation 1.7}$$

During combustion, only NO is formed. However, as the NO cools, it can be oxidised to NO_2 as shown in Equation 1.7. The oxidation of NO to NO_2 is a third-order reaction, with the rate depending on the square of the NO concentration as in Equation 1.8.

$$\frac{dNO_2}{dt} = k\left(P_{O_2}\right)\left(P_{NO}\right)^2 \qquad\qquad\qquad \text{Equation 1.8}$$

NO_x represent serious environmental hazards. Compounds resulting from the oxidation of NO_x by ozone (O_3), $OH^.$ or $^.HNO_2$ radicals contribute to photochemical smog and acid rain.

$$2\,NO\ +\ O_3\ \rightarrow\ N_2O_5\ +\ O_2 \qquad\qquad\qquad \text{Equation 1.9}$$

$$N_2O_5\ +\ H_2O\ \rightarrow\ \ 2\,HNO_3 \qquad\qquad\qquad \text{Equation 1.10}$$

O_3 is also formed via photochemical dissociation of NO_2 followed by reaction of the atomic oxygen with O_2 (Equation 1.11). However, because of the low concentration of NO_2 in exhaust effluent, the contribution of this reaction to the total amount of O_3 present and ozone depletion is minimal.

$$NO_2\ +\ h\nu\ \rightarrow\ NO\ +\ O \qquad\qquad\qquad \text{Equation 1.11}$$

$$O\ +\ O_2\ +\ M\ \rightarrow\ O_3\ +\ M \qquad\qquad\qquad \text{Equation 1.12}$$

Sulphur oxides (SO$_x$)

Sulphur is present naturally in petrol and diesel fuel. Sulphur dioxide (SO$_2$) is formed during combustion. Other sulphur compounds, such as hydrogen sulfide (H$_2$S), are also commonly encountered. SO$_2$ reacts to form acids, which are associated with acid rain and engine corrosion. Sulphur compounds can also contribute to formation of O$_3$ and particulate matter. Additionally, due to its catalyst- poisoning effects, sulphur needs to be removed from the fuel during the refining process.

Particulate matter (PM)

During combustion under fuel- rich conditions, reactive intermediates lead to formation of carbon that is not completely oxidised during lean conditions. As a result, surface material composed of agglomerated carbon particles is formed.

Emission of these particles directly concerns human health. Respiratory problems and cardiovascular diseases can be caused by inhalation of these particles, as small particles are able to pass deep into the lungs and even into the bloodstream.

1.2.2   Legislation

The consciousness of the adverse effects to environmental and human health caused by emissions from combustion sources has grown significantly worldwide. Several air pollutants are now continuously monitored and their emissions have been regulated in many countries, including carbon oxides (CO$_x$), nitrogen oxides (NO$_x$), particulate matter (PM), sulphur oxides (SO$_x$) and volatile organic compounds (VOC).

Although the first European standard was introduced in 1970, fitting of catalytic converters on vehicles was not mandatory until 1993.

Table 1.1. EURO emissions standards limits expressed in g/km [8]

Limits g/km	Euro 1 (1992)		Euro 2 (1996)		Euro 3 (2000)		Euro 4 (2005)		Euro 5 (2009)		Euro 6 (2014)	
	Petrol	Diesel	Petrol	Diesel	Petrol	Diesel	Petrol	Diesel	Petrol	Diesel	Petrol	Diesel
CO	2.72	2.72	2.2	1	2.3	0.64	1	0.5	1	0.5	1	0.5
HC	-	-	-	-	0.20	-	0.10	-	0.10	-	0.10	-
HC + NO_x	0.97	0.97	0.5	0.7	-	0.56	-	0.30	-	0.23	-	0.17
NO_x	-	-	-	-	0.15	0.5	0.08	0.25	0.06	0.18	0.06	0.08
PM	0.14	0.14	x	0.08	x	0.05	x	0.025	0.005	0.005	0.005	0.005

Euro Standards define the acceptable exhaust emissions limits of new vehicles sold in EU member states. Hence, every new car must pass all of those safety and environmental tests dictated by the legislation.

The Euro 1 standard was established in 1992 and imposes fitting of catalytic converters to reduce emissions (mainly CO). As presented in Table 1.1, emission limits have been progressively tightened since.

The latest standard, Euro 6, applies to all new prototype vehicles and manufactured cars from September 2014. This imposes a further, significant reduction in NO_x emissions from diesel engines (55 % reduction compared to Euro 5). The second stage of the Euro 6 introduces real driving emissions (RDE) tests. From September 2017, cars will be tested to ensure that they meet strict limits in a variety of on-road conditions.
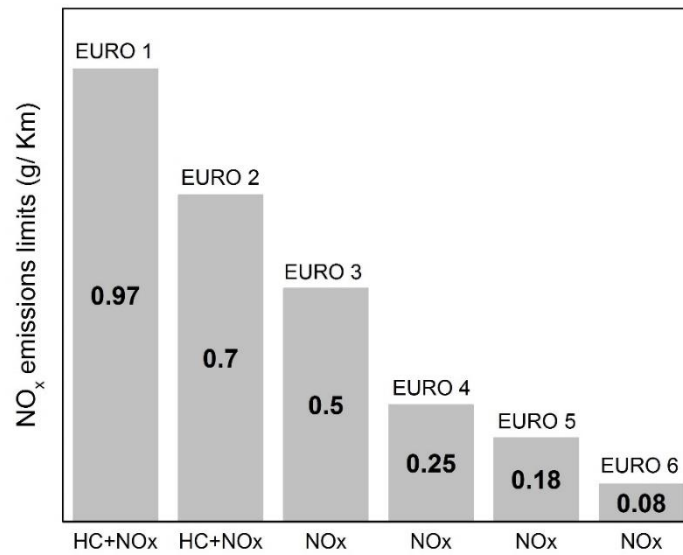
Figure 1.5. EURO emissions standards NO_x limits for diesel vehicles expressed in g/km

Horizon 2020 [9] is the eight framework programme (FP8) implemented by the European Commission in the 2014-2020 period to support and foster research in the European research area (ERA). The FP8 also defines the European environmental research and innovation policy [10], which addresses global challenges for sustainable development and environmental protection. The programme targets the establishment of future low emission vehicles with limits lower than Euro 6 and further improvement in fuel efficiency. The implementation of mandatory 2020 CO_2 emission targets for new passenger cars and light-commercial vehicles in the European Union is among the emission standards imposed and by 2021, all new cars must meet a 95 g CO_2/km emission limit.

1.2.3 Aftertreatment

To meet increasingly stringent regulations, combustion strategies, aftertreatment components and fuel compositions have been under continuous investigation.

The process involved in the scale up of aftertreatment technologies, used to lower the emission levels of pollutants, from laboratory to commercial applications is complex. The main challenge is the optimisation of aftertreatment catalytic systems, reducing cost and complexity without sacrificing performance or stability [11] [12].

Until now, research has focused primarily on investigating the applicability of three noble metals, Pt, Pd and Rh to exhaust aftertreatment technologies. These metals are promising candidates because they show sufficient activity, excellent thermal stability, inertness with respect to reactions with the support material and resistance to sulphur poisoning. Other noble metals such as Ru, Ir or Os have not been studied in the same detail because they form volatile oxides. Due to the high cost and limited availability of noble metals, many studies have tried to find an alternative catalyst using base metal oxides including oxides of Ni, Fe Cu, Co, Mn or Cr. However, supported base metal oxides lack the intrinsic reactivity, durability and poisoning resistance required for automotive applications.

$$CO \; + \; \tfrac{1}{2} \, O_2 \; \rightarrow \; CO_2 \qquad\qquad \text{Equation 1.13}$$

$$CO \; + \; NO \; \rightarrow \; \tfrac{1}{2} \, N_2 \; + \; CO_2 \qquad\qquad \text{Equation 1.14}$$

$$C_xH_y \; + \; n \, O_2 \; \rightarrow \; x \, CO_2 \; + \; y/2 \, H_2O \qquad\qquad \text{Equation 1.15}$$

$$C_xH_y \; + \; m \, NO \; \rightarrow \; m/2 \, N_2 \; + \; y/2 \, H_2O \; + \; x \, CO_2 \qquad\qquad \text{Equation 1.16}$$
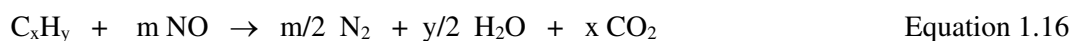
The first catalytic system for converting HC, CO and NO_x employed, was a dual-bed converter. Three way catalysts (TWC) were introduced to respond to stricter NO_x standards and resolve the limitations of dual-bed converters. The term TWC refers to a catalyst that

simultaneously catalyses the three types of reactions represented in the equations above (1.13-1.16): CO oxidation, HC oxidation and NO_x reduction.

Although significantly improved, TWC are still the primary catalytic exhaust aftertreatment in use today. Since their introduction, the cost and performance of TWC have been greatly enhanced.

During the development of TWC formulations, cerium compounds were incorporated. CeO_2 exhibits interesting redox and storage properties [13] [14] [15] [16] [17] [18] [19] [20]. CeO_2 is used as an O_2 trap: O_2 is adsorbed under lean conditions (excess of O_2) and released under rich conditions (excess of fuel). Hence, the composition of the exhaust is buffered around the stoichiometric point, which enhances the conversion of HC, CO and especially NO_x. The reactions involved in oxygen storage are shown in Equations 1.17 and 1.18:

$$2\,CeO_2 \;+\; CO \;\rightarrow\; Ce_2O_3 \;+\; CO_2 \qquad\qquad\qquad \text{Equation 1.17}$$

$$Ce_2O_3 \;+\; \tfrac{1}{2}\,O_2 \;\rightarrow\; 2\,CeO_2 \qquad\qquad\qquad\qquad \text{Equation 1.18}$$

In traditional stoichiometric gasoline engines, the combustion mixture always contains sufficient oxygen to just combine with the fuel. In contrast, oxygen is always in excess in diesel engines. While an oxidising atmosphere should be advantageous for the oxidation of HCs and CO, it makes controlling NO_x emissions extremely difficult. Consequently, those TWC which exhibit high performance in gasoline engines are not as efficient in diesel engines. Although nitric oxide is thermodynamically unstable ($\Delta H_f = +90$ kJ/mol), under lean conditions it is not possible to achieve its catalytic dissociation to O_2 and N_2. Hence, NO_x can only be converted to N_2 by reaction with a reductant.

In order to address the challenges posed by the use of diesel engines, new aftertreatment components are required. Typically a diesel catalytic converter comprises of an oxidation catalyst, a particulate filter and a module for NO_x abatement such as NSR or SCR [12] [21].

Diesel oxidation catalyst (DOC)

One of the most effective and economically viable methods to reduce HC and CO emissions is total catalytic oxidation to carbon dioxide and water.

In 1989, Volkswagen launched the Umweltdiesel Golf fitted with a monolithic Pt oxidation catalyst. This was the first commercial application of DOC and was present in all Euro 3 and later vehicles. Since then, Pt based catalysts are the most frequently used aftertreatment technology for oxidation of HC and CO. Efforts were focused upon optimising catalytic systems with highly dispersed platinum and stability to thermal sintering. In addition, Pd was found to possess higher resistance to sulphur poisoning.

Frequently, two or more metals, typically Pt/Pd and Pt/Rh, are used in combination in DOCs. Bimetallic catalyst systems show significant improvement in activity, thermal stability and resistance against sintering.

While the excess of oxygen contributes positively to the oxidation reaction, the fuel efficient nature of diesel engines is associated with a lower temperature of operation compared to gasoline engines. When the engine starts, the temperature is low (120-150 °C in urban conditions) but a large percentage of total HC emissions are produced during the cold start period. Hence, it is important to improve the low-temperature oxidation activity of these catalysts. An alternative to this is the use of storage components, such as zeolites, to adsorb HC at low temperatures and desorbed them at high temperatures, by which point the Pt based catalyst is sufficiently active to oxidise these compounds.

Although oxidation catalysts were introduced first to control HC and CO emissions, their application is also extended to control NO_x.

Lean NO_x trapping or NO_x storage reduction (NSR)

While NO_x emissions can be limited by decreasing the flame temperature/burn duration, retarding the ignition/ injection time and through exhaust gas recirculation, the use of catalysts is necessary for its abatement whilst maintaining the engine power output.

NSR catalysts comprise of: i) a storage component, typically alkali or alkaline earth metals oxides (BaO) ii) precious metals that catalyse the oxidation/reduction reactions (Pt) and iii) support metal oxides (Al_2O_3). $Pt/BaO/Al_2O_3$ is the most typical NSR catalyst [22].

NSR systems are based on a mixed lean/rich operation mode, working under cyclic operations with periodic changes. The following steps describe the NSR reaction mechanism:

Under lean conditions:

i) NO is oxidised to NO_2 over Pt

$$2\,NO \;+\; O_2 \;\rightarrow\; 2\,NO_2 \hspace{3cm} \text{Equation 1.19}$$

ii) NO_x (NO and NO_2) is adsorbed on the storage component (BaO) in the form of nitrite or nitrate species

$$NO_2 \;+\; BaCO_3 \;\rightarrow\; BaNO_3 \;+\; CO_2 \hspace{2cm} \text{Equation 1.20}$$
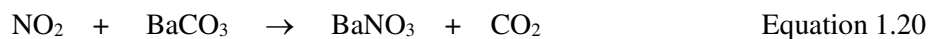
Switch to rich conditions:

iii) Evolution of reducing agents, such as H_2, CO or hydrocarbons from the rich exhaust mixture

iv) NO_x is desorbed from the storage component (BaO)

$$2\ BaNO_3\ \ \rightarrow\ \ 2\ BaO\ +\ 2\ NO\ \ +\ O_2 \qquad\qquad \text{Equation 1.21}$$

$$BaO\ +\ CO_2\ \ \rightarrow\ \ BaCO_3 \qquad\qquad\qquad \text{Equation 1.22}$$
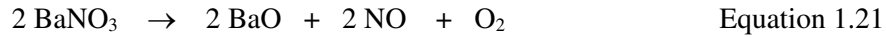
v)   Pt catalyses the reduction of NO_x to N_2

The NO oxidation step is crucial in the overall NSR mechanism. The storage component is more effective where NO_x is adsorbed as NO_2, since NO is more weakly adsorbed than NO_2. Hence the rate of oxidation of NO to NO_2 determines the performance of a NO_x storage catalyst and the temperature at which the NO_x, adsorbed in the form of nitrites or nitrates, is destabilised and desorbed.

The following mechanism was proposed by Bhatia *et al*. [23] to describe the mechanism involved in the oxidation of NO based on reversible adsorption of NO, O_2 and NO_2:

$$NO +\ Pt\ \ \leftrightarrow\ \ NO\text{-Pt} \qquad\qquad\qquad \text{Equation 1.23}$$

$$O_2\ \ +\ \ 2\ Pt\ \ \leftrightarrow\ 2\ O\text{-Pt} \qquad\qquad\qquad \text{Equation 1.24}$$

$$NO\text{-Pt}\ \ +\ \ O\text{-Pt}\ \ \leftrightarrow\ \ NO_2\text{-Pt}\ \ +\ \ Pt \qquad\qquad \text{Equation 1.25}$$

$$NO_2\text{-Pt}\ \ \leftrightarrow\ \ NO_2\ \ +\ \ Pt \qquad\qquad\qquad \text{Equation 1.26}$$
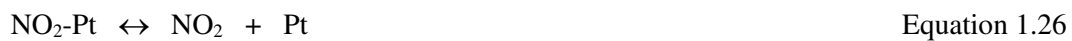
O_2 adsorption was found to be the rate-determining step.

Frequently, NO_x storage catalysts have two supported layers. The first layer consists of Pt and a storage component, such as BaO. Another precious metal, often Rh, is incorporated into the top layer. While Pt catalyses the oxidation of NO, Rh catalyses the reduction of NO_x to N_2 under rich conditions. Hence, the NO_x desorbed from the storage component has to pass through the Rh layer.

One of the main problems with NSR catalysts is that deactivation occurs in the presence of sulphur compounds. When SO_2 is present in the exhaust, Pt catalyses the oxidation reaction, forming SO_3. Subsequently, SO_3 reacts with the basic element of the storage component to form MSO_4. As sulphates are thermodynamically more stable than nitrates, MSO_4 accumulates over the surface of the storage component, decreasing its NO_x storage capacity. In order to decompose the sulphates formed and recover the storage capacity, the catalyst must be exposed to higher temperatures than those used to desorb NO_x.

Selective catalytic reduction (SCR)

During selective catalytic reduction (SCR) the reduction is selective to NO_x. Thus, reduction of NO_x (Equation 1.27) successfully competes with the reduction of O_2 (Equation 1.28), even when O_2 is in a large excess. HC- and Urea-SCR are the main technologies used.

$$HC \ + \ NO_x \ \rightarrow \ N_2 \ + \ H_2O \ + \ CO_2 \quad\quad\quad\quad\quad\quad\quad \text{Equation 1.27}$$

$$HC \ + \ O_2 \ \rightarrow \ H_2O \ + \ CO_2 \quad\quad\quad\quad\quad\quad\quad\quad\quad \text{Equation 1.28}$$

At high temperatures HC oxidation is favoured, resulting in a decrease in NO_x reduction. This is because the enthalpy associated with HC oxidation is greater than that of NO_x reduction. As a consequence, NO_x reduction can only occur in a restricted temperature range. Conversion in this narrow window can be improved by increasing the concentration of HC in the gas mixture, however this has a higher cost.

HC-SCR catalysts explored include those containing Pt [24], Cu, Ir and also Ag [25][26][27][28]. Catalyst formulations containing zeolites can provide enhanced NO_x reduction activity due to their ability to maintain a high concentration of hydrocarbons within the catalyst [29][30][31][32][33][34][35][36][37][38][39][40][41].

NH_3 is used as a reductant for experimental convenience. Indeed, urea may readily decompose into NH_3 in the Urea-SCR catalytic system [42]. NH_3-SCR is very selective to reduction of NO_x [43]. However, this technology presents several disadvantages associated with the use of NH_3 as reductant as NH_3 is expensive, difficult to transport and is itself a pollutant.

Pt based catalysts present high performance at relatively low temperatures but V based catalysts are more commonly used at temperatures typical of heavy-duty diesel engines [44] [45]. Metal-exchanged zeolites, especially those containing Fe, Co, Cu and Ce, represent a group of promising SCR catalysts due to their significant performance [46] [47] [48] [49].

It should be considered that at high temperatures, NO can also be formed through oxidation of NH_3. Hence total NO_x conversion is decreased considerably. V based catalysts exhibit good selectivity for NO_x reduction, with only small amounts of N_2O formed.

Diesel particulate filter (DPF)

The function of the DPF is to efficiently filter mass PM emissions. Diesel PM filtration generally involves the processes of diffusion and interception, coupled with thermophoresis and electrophoresis.

The most successful and frequently used DPF are porous ceramic wall-flow filters made of cordierite, silicon carbide or aluminium titanate. In these systems, the exhaust gas passes through whilst PM is trapped in the filter.

As the PM accumulates in the filter the backpressure increases, which results in a decrease in engine performance. Hence, in order to maintain optimal filter performance, the PM collected on the filter must be regularly removed. Regeneration of the filter occurs through a passive or active regeneration, in which the PM collected on the filter is oxidised via

reactions with O_2, NO_2 or HC. While the temperature of the engine is not high enough to oxidise the PM, NO is oxidised to NO_2 over the Pt oxidising catalyst. Subsequently, the NO_2 oxidises PM to produce NO, CO_2 and H_2O.

$$5\,NO_2 \;+\; 2\,CH \;\;\rightarrow\;\; 5\,NO \;+\; 2\,CO_2 \;+\; H_2O \qquad\qquad \text{Equation 1.29}$$
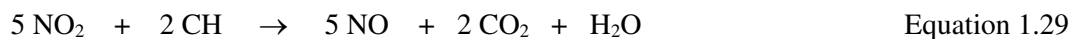
1.3 Catalysts for emissions abatement

With vehicle emission regulations becoming more stringent, highly active, low cost catalysts are required. Hence, development of active catalysts that are chemically and thermally stable and resistant to sintering and poisoning is addressed in many studies [50].

1.3.1 Supported metal catalysts

Supported metal catalysts consist of small metal particles dispersed over a support. Supported metal catalysts, where the metal is a precious metal such as Pt, Pd or Rh, are among the most important components of catalytic exhaust removal technologies.

When designing new catalysts, the active phase, typically metal particles, is as important as the support. The active phase is the catalytically active site where the principal or rate-determining step of the reaction occurs. Among the different roles of a support, the most relevant are: dispersing the active phase of the catalyst, increasing metal surface area and improving the catalytic performance through interactions with the metal through a metal support interaction (MSI).The MSI plays a crucial role in catalysis as it not only affects the catalytic activity and selectivity but also the thermal stability of the catalyst [51]. Hence, MSI studies provide very valuable information.

MSI is a synergistic relationship. While the support improves the dispersion of metal particles and suppresses sintering, the metal particle can also enhance the redox properties and oxygen storage capacity of the support. The extent of the metal support interaction depends on various factors including the metal loading, the nature of the support and the preparation method.

Metal support interactions have been one of the main challenges since the early exhaust aftertreatment catalysts and persist today. How to most effectively support the active phase, and enhance the MSI is therefore a key consideration.

1.3.1.1 Strong metal support interactions (SMSI)

The term strong metal support interaction (SMSI) was first introduced by Tauster *et al.* in 1978 [52] to explain the significant decrease in the chemisorption capacity of group VIII noble metals supported on TiO_2 after reduction at high temperatures, above500 °C. The study showed that while reduction at 200 °C gives rise to well dispersed metal particles with the capacity to adsorb H_2 and CO, reduction at higher temperatures suppresses the adsorption almost completely. Characterisation studies confirmed that the metal dispersion was not decreased by metal agglomeration at higher reduction temperatures. Hence, the effect was explained as a chemical interaction between the noble metal and the support via metal bonding or formation of intermetallic compounds.

Ten months later. Horsley *et al.* [53] developed a molecular orbital model to study the SMSI of Pt supported on TiO_2. The study suggested that suppression of H_2 chemisorption was caused by insertion of Pt atoms into surface oxygen ion vacancies in the support through a chemical bonding.

In 1981, Tauster *et al.* published an investigation of the metal-support interaction between group VIII metals and different transition metal oxides and its influence on Fischer-Tropsch synthesis [54]. In this study, the unusual chemisorption properties of catalysts that exhibit SMSI were associated with superior activity and selectivity. The metal-support interaction was explained based on electron transfer from cations present within the support, such as Ti^{3+} or Nb^{4+}, to the metal particle.

Since SMSIs were found to directly affect catalytic activity, multiple studies focus on understanding these interactions in further detail. SMSI were explained in terms of electronic and geometric effects. The first is based on charge transfer between the metal and the support. While Ti^{4+} ions in TiO_2 have a d^0 configuration, reduced TiO_2 present Ti^{3+} ions which present a d^1 configuration. The electron gained is transferred from the support to the metal particle, resulting in a strong metal support interaction. Encapsulation of the particle by the support is evidence of a geometric effect. Several studies provided evidence of both theories: reporting changes in the chemical nature of surface metal atoms and formation of a thin layer of reduced oxide covering the metal particle, which results in suppression of H_2 chemisorption performance [55] [56]. However, the degree to which the metal-support interaction involves electron transfer or involves changes in electronic properties induced by metal particle size and shape caused by heat treatments is not completely clear.

Since then, the controversial nature of SMSI has been investigated [57] [58] [59] [60] [61] [62] [63] [64] [65] [66]. In 1999, the effects of the support on the morphology and electronic properties of supported metal particles were reviewed [67]. The effect of the support on the activity of supported metal catalysts was found to be caused by i) charge of the metal particle, ii) changes in metal particle shape and crystallographic structure and iii) presence of active sites at the metal-support interface.

Although several studies have reported cases in which catalytic activity is enhanced by a SMSI [68] [19], occasionally, SMSI is also found to have a detrimental effect on the catalytic activity [69]. Liotta *et al.* found that the C_3H_6-SCR activity of supported platinum catalysts decreased when pretreated in H_2 at high temperatures (T > 800 °C). In this case, structural and electronic modifications were induced by SMSI and catalysts reduced at higher temperatures exhibited a decrease in the exposed metal surface area.

Evidence of SMSI between Pt and TiO_2 under oxidising atmospheres has also been reported [70]. In this case, XPS and Ar^+ sputtering analysis suggested that Pt^0 can thermally diffuse into TiO_2 and be oxidised to Pt^{2+} to substitute for lattice Ti^{4+} or form interstitial ions.

The SMSI extent has been found to be dependent on the phase composition [71] and crystal size of the support [72]. Hence, Pd/TiO_2 catalysts exposed to H_2 exhibit SMSI for anatase TiO_2 but not for rutile TiO_2. In addition, stronger metal support interactions were associated with smaller TiO_2 crystal sizes.

More recently, in 2013, Tingting *et al.* [51] published a review of the interactions between precious metals and supports in catalysts with application in automotive exhaust aftertreatent. The review covers literature which focuses on understanding and optimising SMSI between precious metals and Al_2O_3 or Ce_2O_3 based supports to avoid the deactivation caused by sintering.
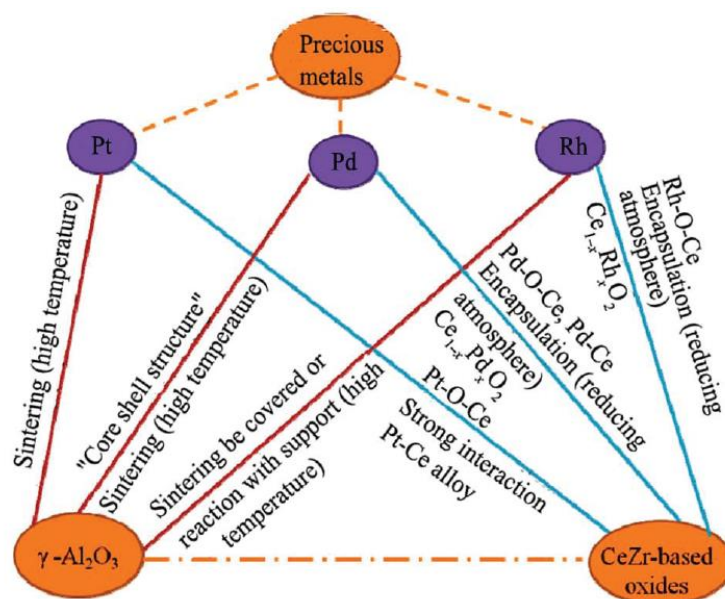
Figure 1.6. Representation of metal-support interactions in automotive exhaust catalysts. Taken

from reference [51]

Several authors found evidence of inhibition of sintering through a SMSI [73] [74]. Recent

studies showed stabilisation of small Ag and Pt particles supported Ceria through strong

metal-support bonding. Precious metals can also improve the oxygen storage capacity of

the support [75] [76] [77] [78]. Various investigations have reported examples where Pt, Pd and Rh

supported particles enhance the reduction of surface oxygen in CeO_2 and CeO_2-ZrO_2

supports.

1.3.2 Zeolite based catalysts

The term zeolite derives from Greek and means "stone that boils". In 1756, Baron von Cronstedt gave this name to minerals, found in rocks of volcanic origin, which released water and appeared to boil when heated rapidly.

Zeolites are microporous crystalline aluminosilicates with the following formula:

$M_{x/n}[(AlO_2)_x(SiO_2)_y]\cdot zH_2O$ where
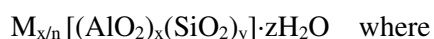
M is an exchangeable cation with valency n and y may vary from 2 to ∞.

Zeolites exhibit high surface areas, typically of the order of $300 - 700 \ m^2/g$, with more than 98 % of the total surface area corresponding to highly accessible internal surfaces.

Structurally, zeolites are composed of TO_4 tetrahedra (T = Si or Al) connected through their oxygen atoms which form a three-dimensional network containing channels and cavities of molecular dimensions. Hence, the basic building unit of zeolites is the tetrahedron in which each oxygen atom is coordinated to two T atoms.
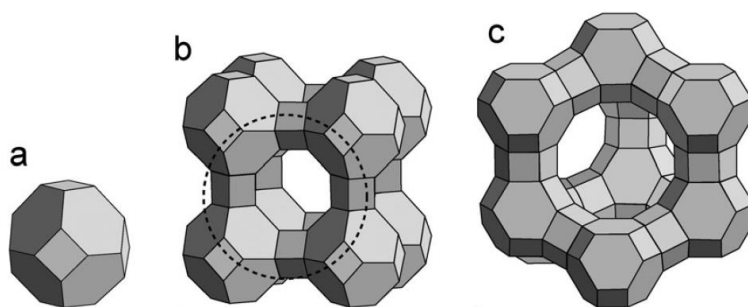
Figure 1.7. Zeolite structures including: a) sodalite cage b) zeolite A and c) zeolite Y.

Taken from reference [79].

The secondary building unit (SBU) of zeolites are non-chiral and can contain up to 16 T atoms. A unit cell always contains the same number of SBUs, however, different

combinations of SBUs within the zeolite framework are, rarely, encountered. The building

block of zeolites is the zeolite cage; large polyhedral building blocks which are stacked to

form the structure. The extended structure of the zeolite can be tailored such that the

cavities and channels are of specific sizes. The sodalite cage, illustrated in Figure 1.6 a), is

the structural element of faujasite. The sodalite cage has the structure of a truncated

cuboctahedra and is made up of 4-rings and 6-rings.

When Si^{4+} is isomorphously replaced by Al^{3+}, a negative charge is generated in the lattice.

A cation compensates this negative charge and, in the case of charge compensating protons,

generates Brønsted acid sites. The maximum number of protonic sites is proportional to the

number of framework Al atoms. From a structural point of view, the Brønsted acid site in

a zeolite is represented by a resonance hybrid of structures I and II. Structure I is a fully

bridged oxygen with a weakly bonded proton and structure II is a silanol group with a weak

Lewis acid interaction of the hydroxyl oxygen with an Al [80].
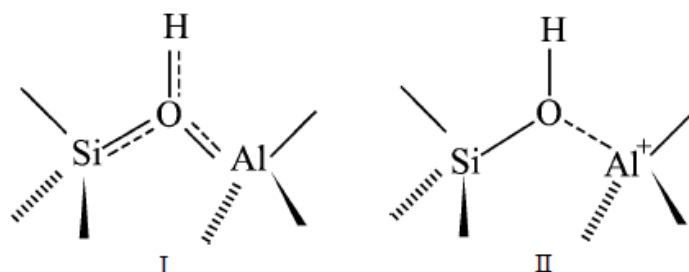
Figure 1.8 Resonance hybrid of structures in a zeolite. Taken from reference [80]

These positively charged cations, required to balance the structure's charge, are

exchangeable by ion exchange methods. Hence, the number and density of protons can be

adjusted through post synthesis treatments, including dealumination and ion exchange. The

level of exchange varies with the Si/Al ratio. An increase in the Si/Al ratio (decrease in

aluminium content), is associated with a decrease in the concentration of acid sites as well as an increase in the acid strength and proton activity coefficients.

The acid strength of the Brønsted acid sites can also be controlled through isomorphous substitution of Si^{4+} for a trivalent cation other than Al^{3+}, Substitution can be achieved by either synthesis or postsynthesis methods. To evenly distribute the metal species within the channel, channel dimensions must be large enough for the hydrated/hydrolysed metal ions to freely diffuse through them. Tetrahedral structures are stable for cations with $0.414 > \rho < 0.225$ ($\rho = r_M/r_O$, where r_M and r_O are the ratios of the cation and the oxygen ion respectively). Other requirements for a true substitution imply some flexibility of the heteroelements to accept the tetrahedral coordination and an oxidation state compatible with the overall framework charge.

The thermal and chemical stability of zeolites depends on their composition. Whereas zeolites with low silica content exhibit a decomposition temperature of 700 °C, are unstable in acid solutions, hydrophilic and tend to have structures with 4, 6 and 8 member rings; high-silica zeolites are more thermally stable (up to 1300 °C), stable in acid solutions, hydrophobic and tend to form 5 member rings [81].

As with the hydrophilicity, the polarity of a given zeolite can be controlled by changing the framework Si/Al ratio and number of silanol groups. Hence zeolites can be prepared with a wide range of surface polarities which makes them selective adsorbents for polar or non-polar molecules.

Zeolites have a natural or synthetic origin. At least 50 natural and 200 synthetic zeolite structure types have been recognised [82]. These differ in the size, shape and connectivity of their channels, usually being from 8 to 30 rings.

Framework Type Data

framework viewed along [111] (upper right: projection down [110])

12-ring viewed along <111>

|(Ca,MgNa$_2$)$_{29}$ (H$_2$O)$_{240}$| [Al$_{58}$Si$_{134}$O$_{384}$]-FAU
cubic, Fd **3**m , a = 24.74Å

Framework Type Data

framework viewed along [010]

10-ring viewed along [100]

10-ring viewed along [010]

|Na$_n$ (H$_2$O)$_{16}$| [Al$_n$Si$_{96}$-nO$_{192}$]-MFI, n < 27
orthorhombic, Pnma, a = 20.07Å, b = 19.92Å, c = 13.42Å

Framework Type Data

framework viewed along [010]

12-ring viewed along <100>

12-ring viewed along [001]

|Na$_7$| [Al$_7$Si$_{57}$O$_{128}$]-*BEA
tetragonal, **P**4122, **a** = 12.661Å, **c** = 26.406Å

Figure 1.9 Framework and channel view for a FAU, MFI and BEA structural type zeolite [83]

Zeolite structures are designated by a 3 letter code according to the Commission of the International Zeolite Association (IZA). Most zeolites can be classified in three groups [84]:

i)   Small pore zeolites with eight membered-ring pore apertures and channel diameters of 0.30-0.45 nm

ii)   Medium pore zeolites with ten membered-ring apertures and channel diameters of 0.45-0.60 nm

iii)   Large pore zeolites with 12 membered-ring apertures and channel diameters of 0.6-0.8 nm

Due to their structure and well defined, regular pore distribution, zeolites offer shape selectivity control as molecular sieves. This property is used in applications to discriminate reactants and products based on size and shape.

The tuneable textural properties and acidity characteristic of zeolites means that they play a crucial role in adsorption, catalysis and ion-exchange applications. Zeolites are one of the most important groups of industrial heterogeneous catalysts with applications in a large variety of reactions, from acid to base and redox catalysts. Zeolites are widely used in oil refining and petrochemistry but also in environmental catalysis and the synthesis of chemicals [85].

XRD, SEM, MAS NMR and IR spectroscopy are the techniques most frequently used for characterisation of zeolites [81]. XRD allows determination of the zeolite structure and purity. The size and morphology of zeolite crystallites can be analysed by SEM. NMR provides information regarding the framework Si/Al ratio and coordination environment.

Framework properties, including Si/Al ratios and the nature of acid sites are obtained using IR spectroscopy

1.4 References

1.   Bowker, M., *The Basis and Applications of Heterogeneous Catalysis*. Oxford University Press Inc.: 1998.
2.   Rothenberg, G., *Catalysis. Concepts and Green Applications*. Wiley-VCH: 2008.
3.   Moulijn, J. A.; Leeuwen, P. W. N. M. v.; Santen, R. A. v., *CATALYSIS. An Integrated Approach to Homogeneous, Heterogeneous and Industrial Catalysis.* Elsevier: 1993.
4.   Payri, F.; Bermúdez, V. R.; Tormos, B.; Linares, W. G., Hydrocarbon emissions speciation in diesel and biodiesel exhausts. *Atmospheric Environment* **2009,** *43* (6), 1273-1279.
5.   Gerald Liu, Z.; Berg, D. R.; Vasys, V. N.; Dettmann, M. E.; Zielinska, B.; Schauer, J. J., Analysis of C1, C2, and C10 through C33 particle-phase and semi-volatile organic compound emissions from heavy-duty diesel engines. *Atmospheric Environment* **2010,** *44* (8), 1108-1115.
6.   Brookes, P.; Duncan, M. E., Carcinogenic Hydrocarbons and Human Cells in Culture. *Nature* **1971,** *234* (5323), 40-43.
7.   Flagan, R. C.; Seinfeld, J. H., *Fundamentals of air pollution engineering*. Prentice-Hall: 1988.
8.   AUTOMOBILE   ASSOCIATION   DEVELOPMENTS   LIMITED   (GB) https://www.theaa.com/motoring_advice/fuels-and-environment/euro-emissions-standards.html.
9.   HORIZON 2020. https://:ec.europa.eu/programmes/horizon2020.
10.   The European environmental research and innovation policy. https://:ec.europa.eu/research/environment/index.cfm?pg=policy.
11.   Gandhi, H. S.; Graham, G. W.; McCabe, R. W., Automotive exhaust catalysts. *Journal of Catalysis* **2003,** *216*, 433-442.
12.   Twigg, M. V., Catalytic control of emissions from cars. *Catalysis Today* **2011,** *163* (1), 33-41.
13.   Cordatos, H.; Ford, D.; Gorte, R. J., Simulated Annealing Study of the Structure and Reducibility in Ceria Clusters. *The Journal of Physical Chemistry* **1996,** *100* (46), 18128-18132.
14.   Yao, H. C.; Yao, Y. F. Y., Ceria in automotive exhaust catalysts. *Journal of Catalysis* **1984,** *86* (2), 254-265.
15.   Laachir, A.; Perrichon, V.; Badri, A.; Lamotte, J.; Catherine, E.; Lavalley, J. C.; El Fallah, J.; Hilaire, L.; Le Normand, F.; Quemere, E.; Sauvion, G. N.; Touret, O., Reduction of CeO2 by hydrogen. Magnetic susceptibility and Fourier-transform infrared, ultraviolet and X-ray photoelectron spectroscopy measurements. *Journal of the Chemical Society, Faraday Transactions* **1991,** *87* (10), 1601-1609.
16.   Bernal, S.; Calvino, J. J.; Cifredo, G. A.; Gatica, J. M.; Omil, J. A. P.; Pintado, J. M., Hydrogen chemisorption on ceria: influence of the oxide surface area and degree of reduction. *Journal of the Chemical Society, Faraday Transactions* **1993,** *89* (18), 3499-3505.
17.   Nunan, J. G.; Robota, H. J.; Cohn, M. J.; Bradley, S. A., Physicochemical properties of Ce-containing three-way catalysts and the effect of Ce on catalyst activity. *Journal of Catalysis* **1992,** *133* (2), 309-324.
18.   Oh, S. H.; Eickel, C. C., Effects of cerium addition on CO oxidation kinetics over alumina-supported rhodium catalysts. *Journal of Catalysis* **1988,** *112* (2), 543-555.
19.   Promoting Platinum metals by Ceria Platinum *Met. ReV.* **1988,** *32*, 73.

20.   Kašpar, J.; Fornasiero, P.; Graziani, M., Use of CeO2-based oxides in the three-way catalysis. *Catalysis Today* **1999,** *50* (2), 285-298.

21.   Twigg, M. V., Progress and future challenges in controlling automotive exhaust gas emissions. *Applied Catalysis B: Environmental* **2007,** *70* (1–4), 2-15.

22.   Liu, G.; Gao, P.-X., A review of NOx storage/reduction catalysts: mechanism, materials and degradation studies. *Catalysis Science & Technology* **2011,** *1* (4), 552-568.

23.   Bhatia, D.; McCabe, R. W.; Harold, M. P.; Balakotaiah, V., Experimental and kinetic study of NO oxidation on model Pt catalysts. *Journal of Catalysis* **2009,** *266* (1), 106-119.

24.   Liu, X.; Jiang, Z.; Chen, M.; Shi, J.; Zhang, Z.; Shangguan, W., Low-Temperature Performance of Pt/TiO2 for Selective Catalytic Reduction of Low Concentration NO by C3H6. *Industrial & Engineering Chemistry Research* **2011,** *50* (13), 7866-7873.

25.   Yu, Y.; He, H.; Zhang, X.; Deng, H., A common feature of H2-assisted HC-SCR over Ag/Al2O3. *Catalysis Science & Technology* **2014,** *4* (5), 1239-1245.

26.   Schuricht, F.; Reschetilowski, W., Simultaneous selective catalytic reduction (SCR) of NOx and N2O over Ag/ZSM-5 – Catalytic studies and mechanistic implications. *Microporous and Mesoporous Materials* **2012,** *164* (0), 135-144.

27.   Yoon, D. Y.; Park, J.-H.; Kang, H.-C.; Kim, P. S.; Nam, I.-S.; Yeo, G. K.; Kil, J. K.; Cha, M.-S., DeNOx performance of Ag/Al2O3 catalyst by n-dodecane: Effect of calcination temperature. *Applied Catalysis B-Environmental* **2011,** *101* (3-4), 275-282.

28.   Hussain, M.; Russo, N.; Saracco, G., NOx Abatement by HC-Assisted SCR over Combustion Synthesized-Supported Ag Catalysts. *Industrial & Engineering Chemistry Research* **2011,** *51* (22), 7467-7474.

29.   Li, Y.; Hall, W. K., Stoichiometric catalytic decomposition of nitric oxide over copper-exchanged zeolite (CuZSM-5) catalysts. *The Journal of Physical Chemistry* **1990,** *94* (16), 6145-6148.

30.   Bennett, C. J.; Bennett, P. S.; Golunski, S. E.; Hayes, J. W.; Walker, A. P., Selective reduction of nitrogen oxides under oxidising exhaust-gas conditions. *Applied Catalysis A: General* **1992,** *86* (2), L1-L6.

31.   Li, L.; Guan, N., HC-SCR reaction pathways on ion exchanged ZSM-5 catalysts. *Microporous and Mesoporous Materials* **2009,** *117* (1–2), 450-457.

32.   Li, L.; Zhang, F.; Guan, N.; Richter, M.; Fricke, R., Selective catalytic reduction of NO by propane in excess oxygen over IrCu-ZSM-5 catalyst. *Catalysis Communications* **2007,** *8* (3), 583-588.

33.   Adelman, B. J.; Beutel, T.; Lei, G. D.; Sachtler, W. M. H., Mechanistic Cause of Hydrocarbon Specificity over Cu/ZSM-5 and Co/ZSM-5 Catalysts in the Selective Catalytic Reduction of NOx. *Journal of Catalysis* **1996,** *158* (1), 327-335.

34.   Feng, X.; Keith Hall, W., FeZSM-5: A Durable SCR Catalyst for NOxRemoval from Combustion Streams. *Journal of Catalysis* **1997,** *166* (2), 368-376.

35.   Chen, H.-Y.; Voskoboinikov, T.; Sachtler, W. M. H., Reduction of NOxover Fe/ZSM-5 Catalysts: Adsorption Complexes and Their Reactivity toward Hydrocarbons. *Journal of Catalysis* **1998,** *180* (2), 171-183.

36.   Schwidder, M.; Kumar, M. S.; Klementiev, K.; Pohl, M. M.; Bruckner, A.; Grunert, W., Selective reduction of NO with Fe-ZSM-5 catalysts of low Fe content - I. Relations between active site structure and catalytic performance. *Journal of Catalysis* **2005,** *231* (2), 314-330.

37.   Guzmán-Vargas, A.; Delahay, G.; Coq, B.; Lima, E.; Bosch, P.; Jumas, J.-C., Influence of the preparation method on the properties of Fe-ZSM-5 for the selective catalytic reduction of NO by n-decane. *Catalysis Today* **2005,** *107–108* (0), 94-99.

38.   Cortes, J. M. G.; Gomez, M. J. I.; de Lecea, C. S. M., The selective reduction of NOx with propene on Pt-beta catalyst: A transient study. *Applied Catalysis B-Environmental* **2007,** *74* (3-4), 313-323.

39.   Xin, M.; Hwang, I. C.; Kim, D. H.; Cho, S. I.; Woo, S. I., The effect of the preparation conditions of Pt/ZSM-5 upon its activity and selectivity for the reduction of nitric oxide. *Applied Catalysis B: Environmental* **1999,** *21* (3), 183-190.

40.   Takami, A.; Takemoto, T.; Iwakuni, H.; Yamada, K.; Shigetsu, M.; Komatsu, K., Zeolite-supported precious metal catalysts for NOx reduction in lean burn engine exhaust. *Catalysis Today* **1997,** *35* (1-2), 75-81.

41.   Guo, J.; Konno, M.; Chikahisa, T.; Murayama, T.; Iwamoto, M., NOx reduction characteristics of Pt-ZSM-5 catalyst with diesel engine exhaust. *JSAE Review* **1995,** *16* (1), 21-25.

42.   Koebel, M.; Strutz, E. O., Thermal and Hydrolytic Decomposition of Urea for Automotive Selective Catalytic Reduction Systems: Thermochemical and Practical Aspects. *Industrial & Engineering Chemistry Research* **2003,** *42* (10), 2093-2100.

43.   Koebel, M.; Elsener, M.; Kleemann, M., Urea-SCR: a promising technique to reduce NOx emissions from automotive diesel engines. *Catalysis Today* **2000,** *59* (3–4), 335-345.

44.   Zhao, X.; Huang, L.; Li, H.; Hu, H.; Han, J.; Shi, L.; Zhang, D., Highly dispersed V2O5/TiO2 modified with transition metals (Cu, Fe, Mn, Co) as efficient catalysts for the selective reduction of NO with NH3. *Chinese Journal of Catalysis* **2015,** *36* (11), 1886-1899.

45.   Zhang, Y.; Zhu, X.; Shen, K.; Xu, H.; Sun, K.; Zhou, C., Influence of ceria modification on the properties of TiO2–ZrO2 supported V2O5 catalysts for selective catalytic reduction of NO by NH3. *Journal of Colloid and Interface Science* **2012,** *376* (1), 233-238.

46.   Deka, U.; Lezcano-Gonzalez, I.; Warrender, S. J.; Lorena Picone, A.; Wright, P. A.; Weckhuysen, B. M.; Beale, A. M., Changing active sites in Cu–CHA catalysts: deNOx selectivity as a function of the preparation method. *Microporous and Mesoporous Materials* **2013,** *166* (0), 144-152.

47.   Brüggemann, T. C.; Keil, F. J., Theoretical Investigation of the Mechanism of the Selective Catalytic Reduction of Nitrogen Oxide with Ammonia on Fe-Form Zeolites. *The Journal of Physical Chemistry C* **2011,** *115* (48), 23854-23870.

48.   Iwasaki, M.; Yamazaki, K.; Banno, K.; Shinjoh, H., Characterization of Fe/ZSM-5 DeNOx catalysts prepared by different methods: Relationships between active Fe sites and NH3-SCR performance. *J. Catal.* **2008,** *260* (2), 205-216.

49.   Chen, H. Y.; Sun, Q.; Wen, B.; Yeom, Y. H.; Weitz, E.; Sachtler, W. M. H., Reduction over zeolite-based catalysts of nitrogen oxides in emissions containing excess oxygen - Unraveling the reaction mechanism. *Catalysis Today* **2004,** *96* (1-2), 1-10.

50.   McCarty, J. G.; Gusman, M.; Lowe, D. M.; Hildenbrand, D. L.; Lau, K. N., Stability of supported metal and supported metal oxide combustion catalysts. *Catalysis Today* **1999,** *47* (1–4), 5-17.

51.   Zheng, T.; He, J.; Zhao, Y.; Xia, W.; He, J., Precious metal-support interaction in automotive exhaust catalysts. *Journal of Rare Earths* **2014,** *32* (2), 97-107.

52.   Tauster, S. J.; Fung, S. C.; Garten, R. L., Strong metal-support interactions. Group 8 noble metals supported on titanium dioxide. *Journal of the American Chemical Society* **1978,** *100* (1), 170-175.

53.   Horsley, J. A., A molecular orbital study of strong metal-support interaction between platinum and titanium dioxide. *Journal of the American Chemical Society* **1979,** *101* (11), 2870-2874.

54.   Tauster, S. J.; Fung, S. C.; Baker, R. T. K.; Horsley, J. A., Strong Interactions in Supported-Metal Catalysts. *Science (New York, N.Y.)* **1981,** *211* (4487), 1121-1125.

55.   Encapsulation and Electronic Effects in a Thin-Film Model of a Rhodium-Titania Strong Metal-Support Interaction Catalyst.

56.   Vannice, M. A.; Hasselbring, L. C.; Sen, B., Metal-support effects on hydrogen and carbon monoxide heats of adsorption on titania-supported platinum. *The Journal of Physical Chemistry* **1985,** *89* (14), 2972-2973.

57.   Lewera, A.; Timperman, L.; Roguska, A.; Alonso-Vante, N., Metal–Support Interactions between Nanosized Pt and Metal Oxides (WO3 and TiO2) Studied Using X-ray Photoelectron Spectroscopy. *The Journal of Physical Chemistry C* **2011,** *115* (41), 20153-20159.

58.   Caballero, A.; Holgado, J. P.; Gonzalez-delaCruz, V. M.; Habas, S. E.; Herranz, T.; Salmeron, M., In situ spectroscopic detection of SMSI effect in a Ni/CeO2 system: hydrogen-induced burial and dig out of metallic nickel. *Chemical Communications* **2010,** *46* (7), 1097-1099.

59.   Lin, W.; Herzing, A. A.; Kiely, C. J.; Wachs, I. E., Probing Metal–Support Interactions under Oxidizing and Reducing Conditions: In Situ Raman and Infrared Spectroscopic and Scanning Transmission Electron Microscopic–X-ray Energy-Dispersive Spectroscopic Investigation of Supported Platinum Catalysts. *The Journal of Physical Chemistry C* **2008,** *112* (15), 5942-5951.

60.   Jiang, Z.; Zhang, W.; Jin, L.; Yang, X.; Xu, F.; Zhu, J.; Huang, W., Direct XPS Evidence for Charge Transfer from a Reduced Rutile TiO2(110) Surface to Au Clusters. *The Journal of Physical Chemistry C* **2007,** *111* (33), 12434-12439.

61.   Goodman, D. W., "Catalytically active Au on Titania:" yet another example of a strong metal support interaction (SMSI)? *Catalysis Letters* **2005,** *99* (1-2), 1-4.

62.   Bowker, M.; Stone, P.; Morrall, P.; Smith, R.; Bennett, R.; Perkins, N.; Kvon, R.; Pang, C.; Fourre, E.; Hall, M., Model catalyst studies of the strong metal–support interaction: Surface structure identified by STM on Pd nanoparticles on TiO2(110). *Journal of Catalysis* **2005,** *234* (1), 172-181.

63.   Ramaker, D. E.; de Graaf, J.; van Veen, J. A. R.; Koningsberger, D. C., Nature of the Metal–Support Interaction in Supported Pt Catalysts: Shift in Pt Valence Orbital Energy and Charge Rearrangement. *Journal of Catalysis* **2001,** *203* (1), 7-17.

64.   de Resende, N. S.; Eon, J.-G.; Schmal, M., Pt–TiO2–γ Al2O3Catalyst: I. Dispersion of Platinum on Alumina-Grafted Titanium Oxide. *Journal of Catalysis* **1999,** *183* (1), 6-13.

65.   Schierbaum, K. D.; Fischer, S.; Torquemada, M. C.; de Segovia, J. L.; Román, E.; Martín-Gago, J. A., The interaction of Pt with TiO2(110) surfaces: a comparative XPS, UPS, ISS, and ESD study. *Surface Science* **1996,** *345* (3), 261-273.

66.   Pesty, F.; Steinrück, H.-P.; Madey, T. E., Thermal stability of Pt films on TiO2(110): evidence for encapsulation. *Surface Science* **1995,** *339* (1–2), 83-95.

67.   Stakheev, A. Y.; Kustov, L. M., Effects of the support on the morphology and electronic properties of supported metal clusters: modern concepts and progress in 1990s. *Applied Catalysis A: General* **1999,** *188* (1–2), 3-35.

68.   van de Loosdrecht, J.; van der Kraan, A. M.; van Dillen, A. J.; Geus, J. W., Metal-Support Interaction: Titania-Supported and Silica-Supported Nickel Catalysts. *Journal of Catalysis* **1997,** *170* (2), 217-226.

69.   Ivanova, A. S.; Slavinskaya, E. M.; Gulyaev, R. V.; Zaikovskii, V. I.; Stonkus, O. A.; Danilova, I. G.; Plyasova, L. M.; Polukhina, I. A.; Boronin, A. I., Metal–support interactions in Pt/Al2O3 and Pd/Al2O3 catalysts for CO oxidation. *Applied Catalysis B: Environmental* **2010,** *97* (1–2), 57-71.

70.   Zhang, M.; Jin, Z.; Zhang, Z.; Dang, H., Study of strong interaction between Pt and TiO2 under oxidizing atmosphere. *Applied Surface Science* **2005,** *250* (1–4), 29-34.

71.   Li, Y.; Xu, B.; Fan, Y.; Feng, N.; Qiu, A.; He, J. M. J.; Yang, H.; Chen, Y., The effect of titania polymorph on the strong metal-support interaction of Pd/TiO2 catalysts and their application in the liquid phase selective hydrogenation of long chain alkadienes. *Journal of Molecular Catalysis A: Chemical* **2004,** *216* (1), 107-114.

72.   Bonne, M.; Samoila, P.; Ekou, T.; Especel, C.; Epron, F.; Marécot, P.; Royer, S.; Duprez, D., Control of titania nanodomain size as a route to modulate SMSI effect in Pt/TiO2 catalysts. *Catalysis Communications* **2010,** *12* (2), 86-91.

73.   Farmer, J. A.; Campbell, C. T., Ceria Maintains Smaller Metal Catalyst Particles by Strong Metal-Support Bonding. *Science (New York, N.Y.)* **2010,** *329* (5994), 933-936.

74.   Shinjoh, H.; Hatanaka, M.; Nagai, Y.; Tanabe, T.; Takahashi, N.; Yoshida, T.; Miyake, Y., Suppression of Noble Metal Sintering Based on the Support Anchoring Effect and its Application in Automotive Three-Way Catalysis. *Topics in Catalysis* **2009,** *52* (13-20), 1967-1971.

75.   Fornasiero, P.; Kašpar, J.; Sergo, V.; Graziani, M., Redox Behavior of High-Surface-Area Rh-, Pt-, and Pd-Loaded Ce0.5Zr0.5O2Mixed Oxide. *Journal of Catalysis* **1999,** *182* (1), 56-69.

76.   Liotta, L. F.; Longo, A.; Pantaleo, G.; Di Carlo, G.; Martorana, A.; Cimino, S.; Russo, G.; Deganello, G., Alumina supported Pt(1%)/Ce0.6Zr0.4O2 monolith: Remarkable stabilization of ceria–zirconia solution towards CeAlO3 formation operated by Pt under redox conditions. *Applied Catalysis B: Environmental* **2009,** *90* (3–4), 470-477.

77.   He, H.; Dai, H. X.; Ng, L. H.; Wong, K. W.; Au, C. T., Pd-, Pt-, and Rh-Loaded Ce0.6Zr0.35Y0.05O2 Three-Way Catalysts: An Investigation on Performance and Redox Properties. *Journal of Catalysis* **2002,** *206* (1), 1-13.

78.   Promoting Platinum Metals by Ceria METAL-SUPPORT INTERACTIONS IN AUTOCATALYSTS. *Platinum Met. Rev.* **1988,** *32* (2), 73.

79.   Bougeard, D.; Smirnov, K. S., Modelling studies of water in crystalline nanoporous aluminosilicates. *Physical Chemistry Chemical Physics* **2007,** *9* (2), 226-245.

80.   Corma, A., State of the art and future challenges of zeolites as catalysts. *Journal of Catalysis* **2003,** *216* (1–2), 298-312.

81.   Auerbach, S. M.; Currado, K. A.; Dutta, P. K., *HANDBOOK OF ZEOLITES SCIENCE AND TECHNOLOGY*. Marcel Dekker Inc: New York, 2003.

82.   INTERNATIONAL ZEOLITE DATABASE   http://www.iza-structure.org/databases/.

83.   Baerlocher, C.; McCuske, L. B.; Olson, D. H., *ATLAS OF ZEOLITE FRAMEWORK TYPES 6th edition*. Elsevier: 2007.

84.   Guisnet, M.; Gilson, J. P., *Zeolites for Cleaner Technologies*. Imperial College Press: London, 2002.

85.   Cejka, J.; Centi, G.; Perez-Pariente, J.; Roth, W. J., Zeolite-based materials for novel catalytic applications: Opportunities, perspectives and open problems. *Catalysis Today* **2012,** *179* (1), 2-15.

Scope and objectives   *2*

Nitrogen oxides (NO_x) are major polluters of the atmosphere, with a direct harmful effect upon the environment and human health. NO_x are a major source of acid rain, photochemical smog and ozone depletion. NO_x contributes to the acidification and eutrophication of soil and water, leading to changes in species diversity. Accordingly, more stringent emission standards have been introduced to lower the concentrations of these pollutants.

NO_x abatement is crucial, especially in diesel engines where controlling NO_x is extremely difficult as oxygen is always in excess. The title and objective of this thesis addresses a novel approach; the diesel oxidation NO_x adsorption catalyst (DONAC), where NO_x is to be stored by the diesel oxidation catalyst (DOC).

DONAC provides an alternative to current approaches for NO_x abatement and requires an adsorption catalyst which stores NO_x at low temperatures (T < 250 °C) and releases it at higher temperatures, when NO_x is reduced in the SCR system.

Enhancing the performance of oxidation catalysts is important in order to improve NO_x storage capacities, as the oxidation of NO to NO_2 is an essential first step in the storage mechanism. Hence, Chapter 4 is dedicated to investigating the oxidation properties of supported platinum catalysts and particularly, how these properties are affected by the support material. The total oxidation of propane and oxidation of NO to NO_2 under lean conditions are the two reactions studied. In order to determine the effect of the support on

the structural and electronic properties of Pt catalysts and correlate these with oxidation performance, full characterisation is performed.

The overall aim is to find an optimal zeolite-based system for NO_x storage. The zeolite composition and structure are likely to affect the storage capacity of the zeolite-based system. The Si/Al ratio influences the number of adsorption sites but also the affinity for H2O, surface acidity and the stability of the zeolite, factors that have an impact on the storage capacity. The internal channels, their geometry and the extent to which they are interconnected determines which gas-phase components reach the active sites. Hence, the zeolite channels need to be large enough to allow diffusion of NO and NO_2, but small enough to exclude hydrocarbon molecules that block the adsorption sites. The inclusion of metals on the parent zeolite not only increases the number of adsorption sites but can also change the reactivity of the zeolite-based catalyst and promote its deactivation through dealumination.

The purpose is, then, to study the adsorption, storage and release of NO_x by metal-exchanged zeolites under synthetic diesel exhaust gas, as a function of the temperature. A range of zeolites with different compositions and structures were used in order to correlate the NO_x storage capacity with the physical and chemical characteristic of the parent zeolites. In addition, the effect of modifying the parent zeolites through post synthesis treatments, heat treatments and ion-exchange, was also examined.

Chapter 5 covers the initial screening of metal-exchanged zeolites for NO_x storage under different conditions and a study of the effect of the Si/Al ratio, internal channels and inclusion of base and precious metals.

The catalyst preparation method has a significant effect on the NO_x storage capacity of metal exchanged zeolites. Chapter 6 adopts the statistical design of experiments (DOE)

method to enhance the adsorption/desorption properties of the Cu^{II}/ZSM-5 (30) catalyst system. In this chapter, experimental design is used to generate a set of data to evaluate the influence which the experimental variables used for catalyst preparation has upon NO_x storage performance. Furthermore, in order to correlate the physicochemical properties of the metal exchanged zeolites with their NO_x storage performance, characterisation studies are performed.

3

Experimental

3.1 Materials

Unless specified, reagents were used as received.

- Propane (5000 ± 5 % ppm C_3H_8 /He, *BOC gases*)

- Nitric oxide (1000 ± 10 % ppm NO /He, *BOC gases*)

- Nitric oxide (5000 ± 1 % ppm NO /N_2, *BOC gases*)

- Oxygen (99.999% *BOC gases*)

- Helium (99.999% *BOC gases*)

- Nitrogen (99.999% *BOC gases*)

- Iron (III) Acetylacetonate, $Fe(C_5H_9O2)_3$ (98%, *Sigma Aldrich)*

- Copper (II) Acetylacetonate, $Cu(acac)_2$ (98%, *Sigma Aldrich*)

- Platinum (II) Acetylacetonate, $Pt(acac)_2$ (48 wt. % Pt, *Alfa Aesar*)

- Iron (III) Chloride Hexahydrate, $FeCl_3 \cdot 6H_2O$ (98 %, *Sigma Aldrich*)

- Iron (II) Sulfate Heptahydrate, $F(SO_4) \cdot 7H_2O$ (99 %, *Sigma Aldrich*)

- Copper (II) Acetate, $Cu(CH_3COO)_2$ (98%, *Sigma Aldrich*)

- Platinum (IV) nitrate, $Pt(NO_3)_4$ (15 wt. % Pt, *Alfa Aesar*)

- Chloroplatinic acid hydrate, $H_2Cl_6Pt \cdot xH_2O$ (99%, *Sigma Aldrich*)

- Zeolite Y (H^+ form, SiO_2:Al_2O_3 = 5.1,30, *Alfa Aesar*)

- ZSM-5 (NH_4^+ form, SiO_2:Al_2O_3 = 23,30,50, *Alfa Aesar*)

- Zeolite BETA (NH_4^+ form, SiO_2:Al_2O_3 = 38, *Alfa Aesar*)

- Titanium Dioxide, TiO_2 (P25, *Degussa*)

- Titanium Dioxide, TiO_2 (Anatase, 99.7%, *Sigma Aldrich*)

- Titanium Dioxide, TiO_2 (Rutile, 99.8 %, *Alfa Aesar*)

- Silicon Dioxide, SiO_2, (Aerocat, *Degussa*)

- Aluminium oxide, γ-Al_2O_3 (Anhydrous, *Merck*)

- TiO_2 (A-R), (Anatase (80%), Rutile (20 %), *Commercial support*)

- TiO_2-SiO_2 (A-R) 5 % mol Si, (Anatase (80%), Rutile (20 %), *Commercial support*)

- TiO_2-SiO_2(A-R)16 % mol Si, (Anatase (80%), Rutile (20 %), *Commercial support*)

- TiO_2 (A) (Anatase, *Commercial support*)

- TiO_2-SiO_2 (A-R) 10 % mol Si, (Anatase, *Commercial support*)

- Al_2O_3-SiO_2 10 % mol Si, (*Commercial support*)

- Toluene (Laboratory reagent grade, 99 %, *Fisher*)

- Ammonium hydroxide 35 %, $NH_4(OH)$ (Analytical reagent grade, *Fisher*)

3.2 Catalyst Preparation

3.2.1 Supported platinum catalysts

A series of metal oxides (TiO_2, SiO_2 and Al_2O_3) and mixed metal oxides (TiO_2-SiO_2 and Al_2O_3-SiO_2) included in the materials list, were used as supports.

Supported platinum catalysts were prepared by the different impregnation techniques described below. In all cases, the impregnation procedure was followed by a drying step at 110 °C for 16 h and a heat treatment at 400 °C (10 °C/min, 5 h) under different atmospheres (static air, flowing air, flowing helium and flowing 5 % H_2/Ar).

The calcination temperature used when preparing supported platinum catalysts influences both the dispersion and oxidation state of Pt [1]. It is known that increasing the calcination temperature above 400 °C results in an increase in the concentration of metallic platinum [2]. In addition, when using TiO_2 supports, phase transformation occurs at high temperature. The anatase-rutile transformation results in a decrease in BET surface area, which is known to have a detrimental effect on the performance of the supported metal catalysts.
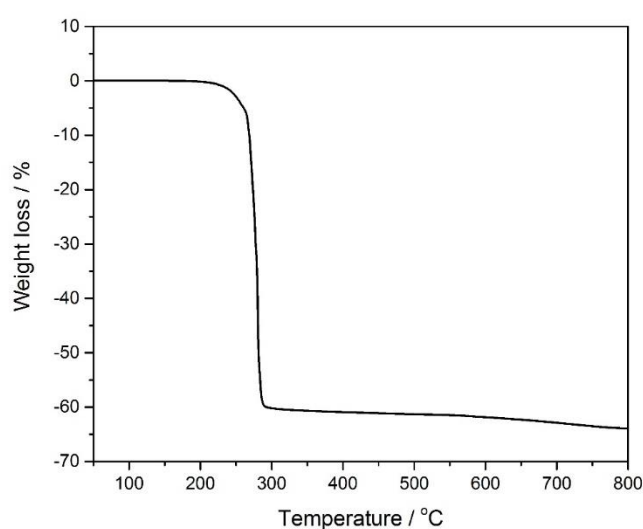
Figure 3.1. TG curve of the platinum (II) acetylacetonate precursor in air

Thermogravimetric analysis of the platinum (II) acetylacetonate precursor, presented in

Figure 3.1, shows that decomposition occurs in the 200 - 300 °C window.
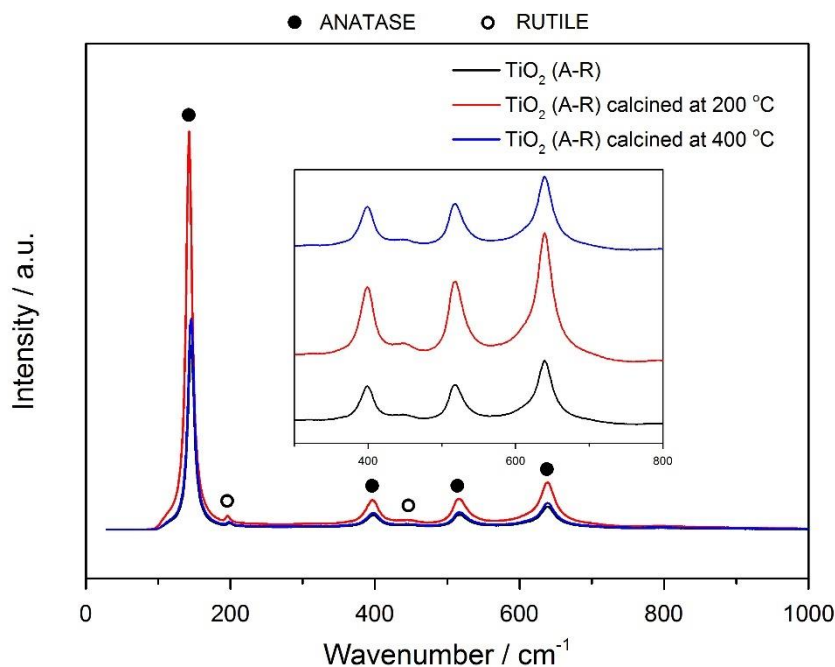
Figure 3.2. Raman spectra of the TiO_2 (A-R) support

calcined in static air for 5 h at 200 and 400 °C

Raman spectra of fresh and calcined TiO_2 (A-R) support are shown in Fig. 3.2. Two

different calcination temperatures, 200 °C and 400 °C, were used to investigate whether a

phase transformation of TiO_2 from anatase to rutile occurs at these temperatures. The

analysis revealed that TiO_2 (A-R) presents a biphasic anatase - rutile structure and that the

calcination temperatures studied do not change the phase structure, confirming that the

anatase to rutile transformation has an onset temperature of over 600 °C at ambient pressure,

as has been reported before by Hanaor *et al.*[3].

Hence, the calcination temperature was set to 400 °C, allowing complete decomposition of

the platinum precursor.

3.2.1.1 Non-aqueous impregnation (IMP)

Catalysts of 0.5 wt. %, 1 wt. % and 1.5 wt. % Pt were prepared by impregnating the as-received support ($\approx$ 2 g) with a solution of Pt(acac)$_2$ in toluene (0.0403 g in 100 mL). The suspensions were stirred for 24 h at room temperature (*ca.* 25 °C). Toluene was removed by a rotatory evaporator.

3.2.1.2 Chemical vapour impregnation (CVI)

Catalysts of 1 wt. % Pt were prepared by CVI. The as-received support ($\approx$ 2 g) was added to the desired mass of Pt(acac)$_2$ (0.0403 g). Following physical mixing of the metal precursor and support, the dry mixture was transferred to a Schlenk flask and heated to sublimation- deposition temperature (145 ^{o}C) under continuous vacuum (*ca.* 10^{-3} mbar) for 1 hour. The sample was then allowed to cool to ambient temperature. This process is illustrated in Figure 3.3.
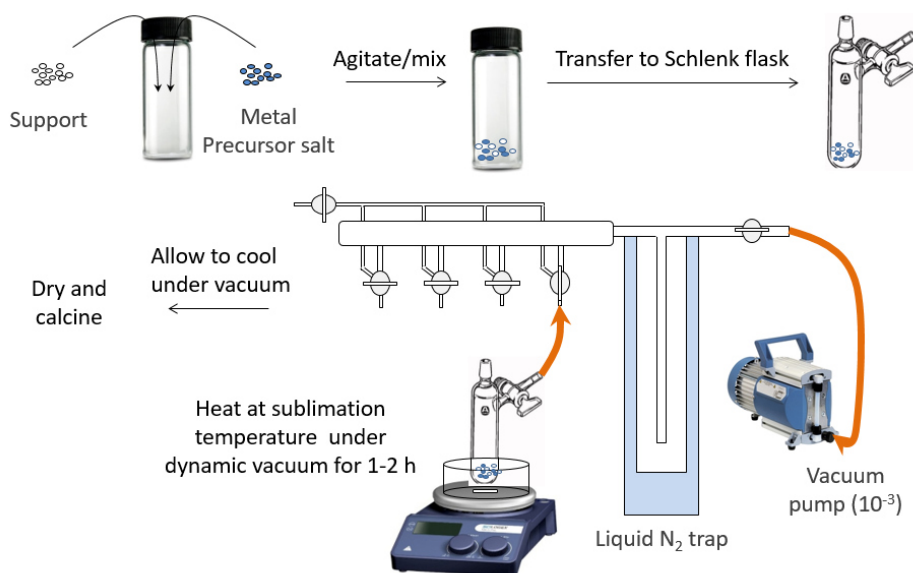
Figure 3.3. Schematic representation of the CVI preparation method

3.2.1.3 Aqueous impregnation (AQ IMP)

Catalysts of 1 wt. % Pt were prepared by impregnating the as-received support ($\approx$ 2 g) with a solution of $Pt(NO_3)_4$ in deionized H_2O (0.1241 g in 100 mL). The suspensions were stirred for 24 h at room temperature (*ca.* 25 °C). Water was removed by a rotatory evaporator.

3.2.1.4 Incipient Wetness impregnation (IWI)

Catalysts of 1 wt. % Pt were prepared by IWI. Prior to impregnation, the pore volume of the support was determined by adding the solvent dropwise until no loose material was observed. The desired mass of $Pt(NO_3)_4$ (0.1241 g) was dissolved in an amount of deionized H_2O corresponding to the pore volume of the support ($\approx$ 2 mL). The Pt precursor solution was added dropwise to the support during mixing until a paste was formed.

To ensure homogeneous impregnation of the Pt precursor onto the support, a modified IWI method was used. In this case, the desired mass of $Pt(NO_3)_4$ (0.1241 g) was dissolved in a limited volume of deionized H_2O ($\approx$ 4 mL).

3.2.2 Metal exchanged zeolites

A series of zeolites with different framework type (Y, ZSM-5 and BETA) and acidity (SiO_2/Al_2O_3 = 5.1 - 50), included in the materials list, were used as supports. Commercial zeolites were purchased from Alfa Aesar. Prior to exchange, those in the ammonium form were activated via conversion to their acid form. The NH_4^+ was transformed to the H^+ form by calcination for 5 h at 550 °C (20 °C/min) in flowing air.

Metal exchanged zeolites were prepared by the different exchange techniques described below. In all cases, the exchange procedure was followed by a drying step at 110 °C for 16 hours and calcination for 3 hours at 550 °C (20 °C/min) in static air.

3.2.2.1 Wet ion exchange (WIE)

Various metal containing zeolite catalysts were prepared by wet ion exchange using an aqueous solution of copper (II) acetate, iron (III) chloride, iron (II) sulphate and chloroplatinic acid.

The stepwise procedure was as follows; a 50 mM aqueous solution of the metal precursor (1.853 g of $Cu(CH_3COO)_2$ in 200 mL of deionised H_2O, for Cu^{II} containing zeolites; and 2.758 g of $FeCl_3 \cdot 6H_2O$ in 200 mL of deionised H_2O, for Fe^{III} containing zeolites) was placed in contact with the zeolite support in the H^+ form ($\approx$ 2 g) at 25 °C under vigorous stirring during either 24 or 48 h. Pt^{IV} containing zeolites were prepared by WIE with an aqueous solution of 0.5 mM H_2PtCl_6 following the same procedure. Fe^{II} containing zeolites were also prepared in a similar way, under a N_2 atmosphere.

The solid phase was then separated from the aqueous metal solution by vacuum filtration. The solid was washed thoroughly with deionized H_2O.

3.2.2.2 Chemical vapour impregnation (CVI)

1 wt. % Cu, Fe and Pt monometallic exchanged zeolites were prepared by CVI. Prior to exchange, a known mass of the zeolite in the H^+ form (typically 3.5 g) was heat treated at 150 °C for 2 h under continuous vacuum. Subsequently, the dried zeolite support ($\approx$ 2 g) was added to the desired mass of metal acetylacetonate (0.0824 g of $Cu(acac)_2$, 0.1265 g of $Fe(acac)_3$ and 0.0403 g of $Pt(acac)_2$. Following physical mixing of the metal precursor and zeolite, the dry mixture was transferred to a Schlenk flask and heated to sublimation-

deposition temperature (150 ^{o}C) under continuous vacuum (*ca.* 10^{-3} mbar) for 2 hours. The sample was then allowed to cool to ambient temperature.

Bi- and tri- metallic exchanged zeolites were prepared by CVI following the same procedure. In this case, the dried zeolite support ($\approx$ 2 g) was added to the desired mass of each metal acetylacetonate and physically mixed.

3.2.2.3 Statistical design of experiments (DOE)

The most significant parameters that affect the WIE and CVI methods were screened based on a fractional factorial design.

Cu^{II}/ZSM-5 (30) catalysts were prepared by the same WIE procedure described, using copper (II) acetate as the precursor. The aqueous copper solution concentration, washing volume, solution temperature, time and pH were adjusted based on the DOE matrix described in Table 6.2 in Chapter 6. Experiments at high temperature (90 °C) were performed under reflux conditions. The initial pH of the aqueous copper solution was monitored with a pH meter and adjusted to the desired value by dropwise addition of NH$_4$(OH) 35%.

Cu^{II}/ZSM-5 (30) catalysts were also prepared by the same CVI procedure described, using copper (II) acetylacetonate as precursor. The copper loading, impregnation temperature and time were adjusted based on the DOE matrix described in Table 6.7 in Chapter 6.

3.3 Catalyst Testing

3.3.1 Propane oxidation

3.3.1.1 Reactor schematic

Catalytic testing for the total oxidation of propane under flow conditions was carried out in the custom built reactor shown in Figure 3.4.

1.	Oxygen cylinder	9.	Thermocouple
2.	Propane / He cylinder	10.	Tube furnace
3.	7 micron filter	11.	Reactor tube
4.	Non return valves	12.	Catalyst bed
5.	Mass flow controllers	13.	Gas chromatograph
6.	Electronic flow controller box	14.	Multiposition valves
7.	Furnace temperature controller	15.	GC columns
8.	Temperature controller	16.	Computer
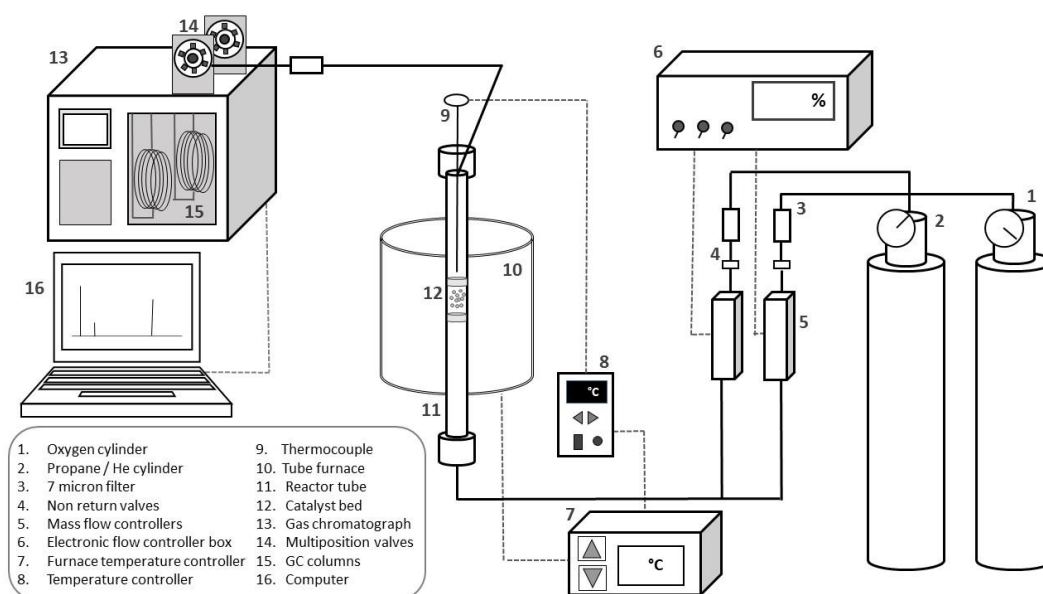
Figure 3.4. Schematic representation of the propane oxidation reactor

The catalytic total oxidation of propane was carried out in a stainless steel reactor tube (0.5 cm *i.d.*) heated using a tubular Carbolite furnace at atmospheric pressure. For each experiment, the catalyst was packed to a constant volume to give a gas hourly space velocity (GHSV) of 50,000 h^{-1}. A typical catalyst bed consisted of *ca*. 30 mg of powdered catalyst (0.06 mL) sandwiched between two quartz wool layers. The reactor feed contained 5000 ppm propane in synthetic air (20 % O_2, He as balance gas) with a total flow rate of 50 mL/min. The volumetric ratio used for the catalytic combustion of propane was C_3H_8:O_2=1:50. The gas flow was adjusted by mass flow controllers. Temperature heating

tapes were used to keep the reactor lines heated and ensure that the feed stayed in the gas phase. The reactants and products were analysed by an online Varian 3800 gas chromatograph with a thermal conductivity (TCD) and flame ionisation detector (FID). Two chromatographic columns were employed: Hayesep Q (to separate CO_2 and hydrocarbons) and MolSieve 13X (to separate CO and O_2). The experiments were performed in a temperature programmed way between 100 °C and 500 °C at intervals of 50 °C, and the reaction temperature was measured by a thermocouple placed within the catalyst bed. Analyses were made at each temperature until a steady-state was attained, three analyses were taken and data averaged.

3.3.1.2 Sample delivery and temperature program

Analytes were separated and analysed using a Varian 3800 GC with FID and TCD detectors. The reaction gas was injected into the GC using a six-port valve (V1) heated to 210 °C, and He was used as the carried gas.

Table 3.1. Valve sequence program

Time min	V1 (Sample injection)		V2 (Bypass)	
	Fill (-)	Inject (+)	Series (+)	Bypass (-)
Initial		+	+	
0.01	-		+	
1.32	-			_

Hydrocarbons and CO_2 were separated in the HayeSep Q column (80-100 mesh, 1.8 m). CO and O_2 were separated in the MolSieve 13 X column (80-100 mesh, 2 m). Because CO_2 binds irreversibly to the MolSieve column causing deactivation, a second six-port valve (V2) is necessary to bypass this column after CO and O_2 are eluted (1.32 min after the

analysis starts). The valve sequence parameters for the sample delivery program used are described in Table 3.1.

An effective separation and elution of the analytes was achieved with the column oven temperature program described in Table 3.2.

Table 3.2. Temperature program for column oven

Step	Temperature °C	Rate °C/min	Hold min	Total min
Initial	50	-	0.0	0
1	68	2.0	3.50	12.50
2	220	70.0	2.50	17.17

Analytes were identified by comparing their retention times with those of commercial standards. O_2, CO_2 and CO were detected in the TCD channel and C_3H_8 in the FID channel. The TCD is a universal detector generally used for detection of inorganic compounds. The current signal is generated based on the difference in thermal conductivity between the sample gas and the reference carrier gas. The FID is the industry standard detector used for analysis of HC concentrations. The current signal is generated based on the detection of ions formed during combustion of HC in a hydrogen flame. The response is proportional to the concentration of HCs.

The overall chromatogram obtained from both channels presents three peaks at ca. 0.9 min (O_2), 1.6 min (CO_2) and 14.1 min (C_3H_8). Other selective oxidation products, such as C_3H_6, were not detected, indicating that propane is completely oxidised by the catalyst to form CO_2 and H_2O.

3.3.1.3 Data analysis & quantification

Quantitative analysis was performed by quantifying reactants consumed and products formed.

Propane conversion (%) was determined from propane consumption with the difference between the propane inlet and outlet concentration using the following equation:

$$\left(\frac{C_3H_{8_{IN}} - C_3H_{8_{OUT}}}{C_3H_{8_{IN}}}\right) \cdot 100$$

$C_3H_{8\ IN}$ was calculated with the peak area counts prior to light off, when conversion is zero and the outlet propane concentration is equal to the inlet propane concentration. $C_3H_{8\ OUT}$ corresponds to the average peak area counts obtained at each temperature.

The GC was calibrated for CO_2 analysis by injecting known amounts of CO_2. The response factor (RF = peak area / analyte concentration) was obtained from the calibration plot that correlates the analyte concentration with the peak area.

Conversion (%) was also calculated from products formed, with the average peak area counts obtained for propane and CO_2 at each temperature:

$$\left(\frac{Products_{OUT}}{C_3H_{8_{OUT}} + Products_{OUT}}\right) \cdot 100 = \left(\frac{\frac{CO_2}{3}}{C_3H_8 + \frac{CO_2}{3}}\right) \cdot 100$$

While for conversions below 10 %, conversion was obtained with conversion from products, for conversions greater or equal to 10 %, conversion was determined from the consumption of propane.

Blank experiments conducted in an empty reactor tube showed negligible activity over the temperature range used in this study. Quantification of the error associated with the testing

methodology was obtained by measuring the standard deviation for propane conversion when the same catalyst was tested three times. Results give an error of ± 4 % conversion. Carbon balances were in the range 100 ± 10%.

3.3.2 NO$_x$ storage

3.3.2.1 Reactor schematic

The NO$_x$ adsorption/desorption experiments were carried out under atmospheric pressure in the fixed-bed flow reactor shown in Figure 3.4.

1.	Helium cylinder	9.	Thermocouple
2.	NO / He cylinder	10.	Tube furnace
3.	Oxygen cylinder	11.	Reactor tube
4.	7 micron filter	12.	Catalyst bed
5.	Mass flow controllers	13.	IR spectrometer
6.	Electronic flow controller box	14.	Computer
7.	Furnace temperature controller		
8.	Temperature controller		
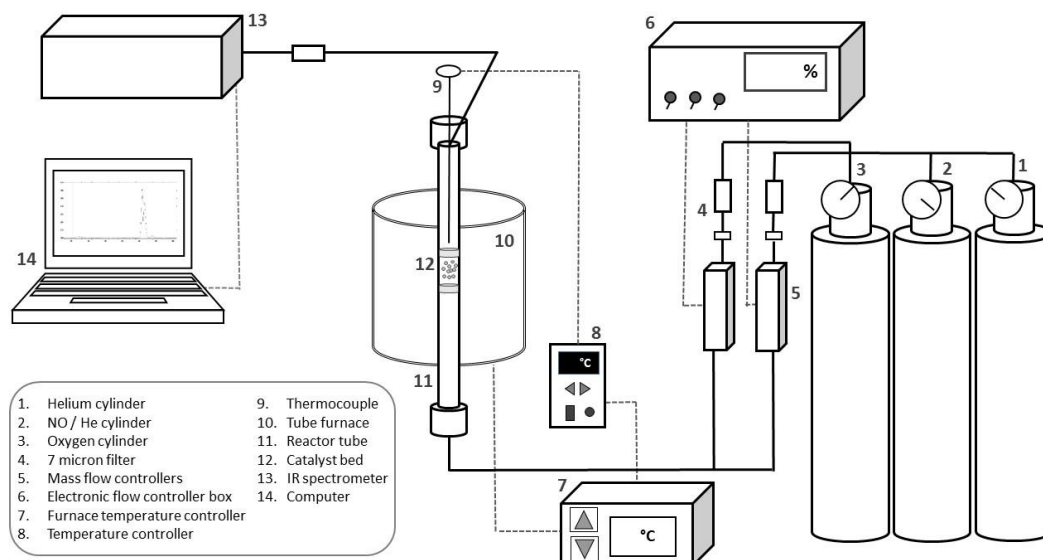
Figure 3.4. Schematic representation of the NO$_x$ reactor

The catalyst (*ca.* 300 mg, 0.4 mL), or hereafter also called adsorbent, in the form of pellets (20-40 mesh size) was sandwiched between two quartz wool layers in a stainless steel tube (1 cm *i.d.*). The reactor tube was fitted in a tubular furnace that controlled the temperature of the catalyst bed. The temperature in the catalyst bed was monitored with a thermocouple. Temperature heating tapes were used to keep the reactor lines heated and ensure that the feed stayed in the gas phase, therefore avoiding condensation. The gas mixture, which

varied during the experiment, was fed from cylinders using mass flow controllers. The total gas flow was 200 mL/min which corresponded to a gas hourly space velocity (GHSV) of 35,000h^{-1}. The effluent composition was analysed continuously by a FT-IR spectrometer (Gasmet DX-4000) equipped with a 0.4 L heated cell, to ensure the sample stays in gaseous phase. Concentration results in ppm were measured using the Calcmet^{TM} software with internal calibration. Prior to NO adsorption, the sample was pretreated at 500 °C in a flow of He and then cooled to 30 °C. Subsequently, the He flow was switched to a model flue gas for NO$_x$ adsorption at 30 °C. For experiments in the absence of O$_2$, the model flue gas contained 1000 ppm NO balanced in He. For experiments in the presence of O$_2$, the model flue gas contained 1000 ppm NO in 7.5 % O$_2$, balanced in He. The volumetric ratio used for NO$_x$ adsorption in the presence of O$_2$ was NO:O$_2$=1:75. The adsorbent was first by-passed to control the inlet NO$_x$ concentration. After saturation of the catalyst, identified by the NO concentration regaining the inlet value, the adsorbent was again bypassed to allow flushing of the lines with He. Temperature programme desorption (TPD) was then conducted with a flow of 100 % He. After a purging period at constant temperature to remove the reversibly adsorbed NO$_x$ species, the adsorbent was heated at 10 °C/min up to 500 °C.

NO$_x$ storage experiments under real working conditions were performed in the same reactor using a more complicated gas mixture. The gas mixture, which varied during the experiment, was fed from cylinders using mass flow controllers. Water vapour was added into the feed with a controlled evaporator mixer. The total gas flow was 200 mL/min which corresponded to a gas hourly space velocity (GHSV) of 30,000 h^{-1}. Prior to storage, the sample was heated up to 500 °C (10 °C/min) and then cooled to 80 °C in a gas mixture containing 10 v. % O$_2$, 5 v. % H$_2$O and 5 v. % CO$_2$ balanced in N$_2$. Subsequently, the sample was exposed to a model flue gas during storage at 80 °C and TPD up to 500 °C

(10 °C/min). The model flue gas contained 10 v. % O_2, 5 v. % H_2O, 5 v. % CO_2, 200 ppm NO, 200 ppm CO and 500 ppm C_3H_8 balanced in N_2.

3.3.2.2 Data analysis & quantification

Quantitative analysis of NO_x during the adsorption-desorption processes was carried out by continuously monitoring the effluent gas composition using a FTIR spectrometer.

Identification of IR active species is possible because each molecule possesses a unique IR absorption spectrum. The IR spectrum is the result of vibrational excitation caused by the interaction of a molecule with infrared radiation. All different vibrations, rotations and their combinations result in absorption bands of specific wavelengths in the IR region.

Quantification of the IR spectra is possible using the Beer-Lambert law, which establishes a direct relationship between the infrared radiation absorbance presented by an analyte and its concentration:

$$\log\left(\frac{I_0}{I}\right) = \log(A) = \log\left(\frac{1}{T}\right) = \varepsilon \cdot L \cdot C$$

Where: I_0 = intensity of the incident IR radiation (before sample IR absorption), I = intensity of the transmitting IR radiation (after sample IR absorption), A = absorbance, T = transmittance, ε = absorptivity, L = optical path length and C = sample concentration

Quantitative analysis of multiple components is possible because the infrared radiation absorption at each wavelength is directly proportional to the concentration of absorbing molecules.

The Calcmet^{TM} software calculates the concentration of each molecule by comparing the sample IR spectrum with reference IR spectra. This is feasible because the software possesses a reference library with the IR spectrum of each single gas molecule at specific

concentrations. Hence, to obtain reliable results, the analysis library must have the IR spectra of all those molecules present in the sample in the concentration range studied.

Prior to sample analysis, the spectrometer cell was flushed until signal stabilisation and a background was acquired using flowing He, which does not absorb infrared radiation. Sample analysis was then carried out in a continuous measurement mode at specific time intervals. Short time intervals of 2 seconds are required because adsorption/desorption processes occur rapidly. IR spectra were acquired and measured automatically at those time intervals specified. Quantification of the spectra gives the evolution of the concentration (expressed as ppm or v. %) of each molecule present in the sample with time. The error associated with quantification of the spectra using the library reference spectra was found to be 2.6 %. This value was determined by measuring the standard deviation of the NO_x concentration obtained from the FITR spectrum acquired for 12 different gas samples with same the NO_x concentration.

The representation of the overall concentration profile was obtained by plotting the results in Origin® 9.1 analysis and graphing software. Total areas for adsorption and desorption peaks were calculated using the integration tool. NO_x adsorption/desorption capacities, expressed in $mg_{NOx}/g_{catalyst}$, were calculated by integration of the NO adsorption/desorption curves and correlation with the response factor. The response factor was obtained by correlating integrated areas with known amounts of NO. It should be noted that the results obtained are an estimation of time on-line analysis. The spectrometer cell volume is 0.4 L, therefore using a 200 mL/min gas flow it takes approximately 2 minutes to fill the cell with the reaction gas. Hence, when using time intervals below 2 minutes, quantification of NO_x concentrations is likely underestimated due to dilution by residual feed gas in the cell.

NO conversion (%) was determined from NO consumption with the difference between the NO inlet and outlet concentrations using the following equation:

$$\left(\frac{NO_{IN} - NO_{OUT}}{NO_{IN}}\right) \cdot 100$$

NO_{IN} is equal to the inlet NO concentration when conversion is zero. Thus, NO_{IN} corresponds to the concentration of NO before storage, when the catalyst bed is bypassed. NO_{OUT} corresponds to the steady state concentration obtained at the end of the storage period. Nitrogen balances were in the range 100 ± 8 %.

3.3.3 Oxidation of NO to NO_2

NO oxidation experiments were performed in the same reactor shown in Figure 3.4. For each experiment, the catalyst was packed to a constant volume to give a gas hourly space velocity (GHSV) of 50,000 h^{-1}. The bed contained *ca.* 30 mg of powdered catalyst (0.24 mL) sandwiched between two quartz wool layers. The reactor feed contained 1000 ppm NO in 7.5 % O_2, He as balance gas with a total flow rate of 200 mL/min. The volumetric ratio used for the catalytic combustion of propane was $NO:O_2=1:75$. The gas flow was adjusted by mass flow controllers. Temperature heating tapes were used to keep the reactor lines heated and ensure that the feed stayed in the gas phase. The experiments were performed in a temperature programmed way between 100 °C and 500 °C at intervals of 50 °C. The reaction temperature was measured by a thermocouple placed within the catalyst bed. Analyses were made at each temperature until a steady-state in activity was attained. The effluent gas composition was analysed continuously by a FT-IR spectrometer (Gasmet DX-4000) equipped with a 0.4 L heated cell, to ensure the sample stayed in the gas phase. Concentration results in ppm were determined using the Calcmet™ software with internal calibration.

3.3.3.1 Data analysis

NO conversion (%) was determined from NO consumption with the difference between the NO inlet and outlet concentrations using the following equation:

$$\left(\frac{NO_{\text{IN}} - \text{NO}_{\text{OUT}}}{\text{NO}_{\text{IN}}}\right) \cdot 100$$

NO_{IN} is equal to the inlet NO concentration when conversion is zero. Thus, NO_{IN} corresponds to the concentration of NO at 25 °C when the catalyst bed is bypassed. NO_{OUT} corresponds to the steady state concentration obtained at each temperature. Nitrogen balances were in the range 100 ± 8 %.

3.4 Catalyst characterisation

Characterisation of the catalysts prepared and tested over the course of this thesis was performed using a series of analytical techniques. The background theory and experimental procedure followed for each characterisation technique is here explained.

3.4.1 X-Ray Powder Diffraction (XRD)

XRD is a powerful and frequently used characterisation technique for crystal structure analysis of solid materials. It is a bulk technique, used for identification and quantification of crystalline phases and estimation of crystallite sizes.

X-rays are electromagnetic radiation with wavelengths in the region of 10^{-10} m (1 Å). X-Rays are generated in a vacuum tube when high energy electrons, released by the cathode (a tungsten filament), collide with the atoms and nuclei of the anode or metal target (typically copper). When electrons have enough energy, the metal target's inner orbital electrons are dislodged and electrons from higher energy levels fill the vacancies. As a result, X-rays of specific wavelength are emitted. Generated X-rays are filtered, collimated and concentrated to produce monochromatic radiation, which is directed towards the sample.

Crystalline materials are formed by repetition of ordered arrangements of atoms. X-ray wavelengths are about the same order as molecular bond lengths (1 Å). Hence, XRD techniques require long-range order. Interaction of the indecent X-Rays with the sample results in a constructive interference when Bragg's law is complied. Hence, X-ray diffraction is dictated by the Bragg equation [4]:

$$n\lambda = 2\,d\,\sin\theta \quad \text{where:}$$

n is the order of reflection, an integer number (n = 1,2,3 …)

λ is the incident X-ray wavelength

d is the distance between two lattice planes

θ is the angle of incidence

The diffracted X-Rays are detected, processed and counted with a movable detector that scans the radiation intensity as a function of the angle 2θ.

Each crystalline material possesses a unique characteristic X-Ray pattern used as a "fingerprint". Thus, identification of crystalline phases present in a sample is possible through comparison with a database of XRD patterns. Structure determination is achieved by conversion of the diffraction peaks to d-spacings.

It is possible to calculate the crystallite size of a given phase using the diffraction peak's width via the Debye-Scherrer equation [5]:

$$\beta_k = \frac{k\,\lambda}{d_{hkl}\,\cos\theta} \quad \text{where:}$$

β_k is the peak with ($\beta_k = \beta_{obs} - \beta_{std}$)

β_{obs} is the overall peak with

β_{std} is the instrument line broadening component

k is the Scherrer constant, a shape factor

λ is the incident X-ray wavelength

d_{hkl} is the crystalline size

θ is the peak position

The main limitation of this technique is that samples require sufficient long range order to observe clear diffraction peaks and that its application is restricted to compounds with

particle sizes of greater than 4 nm. The rotation of the ground/ powdered sample maximises the chance that particles are orientated such that a certain crystal plane is at the θ right angle defined by the Bragg's law, contributing to the diffraction pattern.

Powder X-ray diffraction patterns were obtained on a PANanalytical X'Pert Pro diffractometer using Cu Kα ray source operating at 40 kV and 40 mA. The signal was recorded for 2θ comprised between 10^0 and 80^0 with a step of 0.02^0. The XRD patterns were analysed following the JCPDS database.

3.4.2 X-Ray Photoelectron Spectroscopy (XPS)

XPS is a frequently used characterisation technique for qualitative and quantitative analysis of the elements present on a sample's surface and determination of the metal oxidation state of surface species.

This technique is based upon the photoelectric effect. The sample atoms are irradiated with monochromatic X-ray radiation. If the energy of the incident photon (hυ) is equal to or greater than the binding energy (E_b) of a core or valance electron, this electron is ejected with kinetic energy (E_k) given by the following equation [6]:

$$E_k = h\upsilon - E_b - \varphi \quad \text{where:}$$

E_k is the ejected electron's kinetic energy

h is the Plank's constant

υ is the frequency of the incident radiation

E_b is the binding energy of the electron with respect to the Fermi level of the sample

φ is the work function of the spectrometer

XPS spectra are typically a representation of the intensity of the photoelectrons generated against the binding energy. Analysis of the composition of the sample is based on the fact that each atom possesses a set of characteristic binding energies. XPS spectra also contain information about the chemical environments of the different elements because the energy levels of the core electrons are dependent on the oxidation state of the atom. Generally, an increase in oxidation state is associated with an increase in binding energy [6]. Hence, a metal in its oxide form will give a XPS peak shifted towards higher binding energies with respect to that peak corresponding to the metallic form.

The main limitation of this technique is that it is surface sensitive, as XPS has a probing depth of between 1.5 and 6 nm, depending on the photoelectron's kinetic energy.

X-ray photoelectron spectroscopy (XPS) analysis of the samples was carried out on a Kratos Axis Ultra DKD photoelectron spectrometer equipped with a monochromatic Al source (1486.6 eV). All spectra were obtained with a pass energy of 40 eV for high resolution scans and 160 eV for survey spectra over an analysis area of 700 x 300 µm. All binding energies were normalized with respect to the C (1s) peak of surface adventitious carbon (284.7 eV). Qualitative and quantitative interpretation of the data was carried out using CasaXPS software.

3.4.3 Brunauer Emmett Teller (BET) surface area analysis

Nitrogen adsorption at 77 K is the most frequently used technique for pore analysis and surface area determination. Physisorption of nitrogen is a phenomenon similar to liquefaction or condensation. At low temperature, N_2 forms a monolayer that is only dependant on the N_2 molecule size ($0.16 \ nm^2$). After the sample surface has been cleaned

under vacuum, it is dosed with the adsorbate gas (typically N_2) at different pressures. The adsorption isotherm is a representation of the volume of adsorbed nitrogen against the relative pressure.

The isotherm shape depends on the pore structure of the sample [7]. Four different types of adsorption isotherm are represented in Figure 3.5. The BET isotherm is based on either the type II or III isotherm. The type I shows a monolayer (Langmuir isotherm). The type II isotherm shows how the adsorbate covers the surface gradually until a monolayer is formed and that as the pressure increases further, multilayer growth occurs. Type IV shows first a monolayer, followed by filling the mesopores. The black dot in isotherms I, II and IV indicates the formation of monolayer (point B).
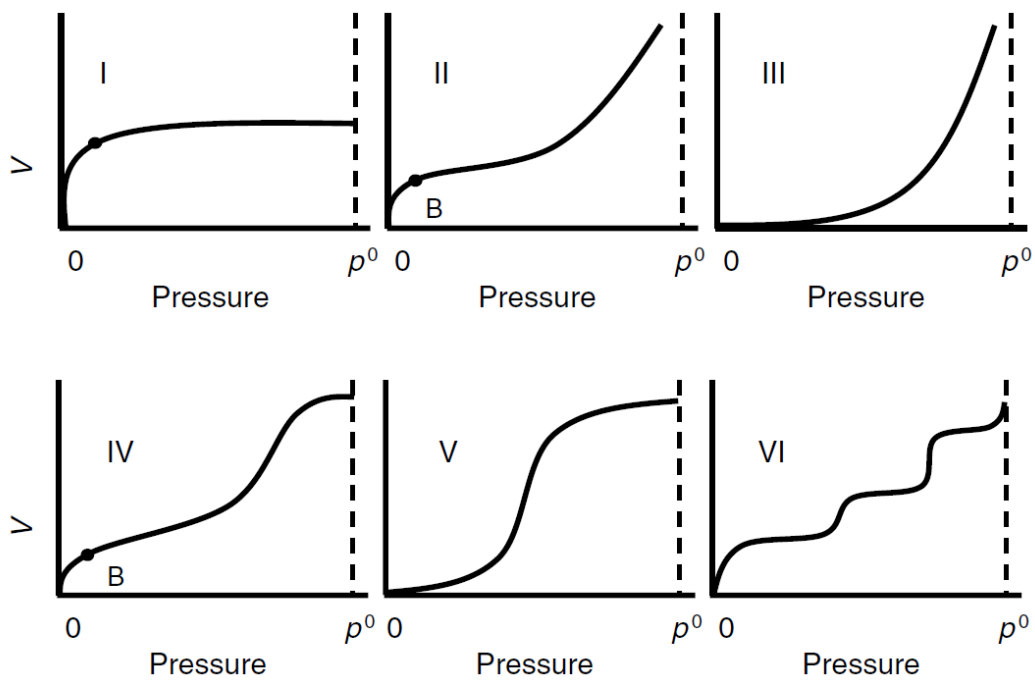

Figure 3.5. Nitrogen adsorption isotherm types. Taken from Reference [8].

Brunauer Emmet and Teller developed the BET method for determination of surface area considering multilayer adsorption, which was not addressed by the Langmuir isotherm. The BET linearised equation is [9]:

$$\frac{P}{V(P_0 - P)} = \frac{1}{V_m \cdot C} + \frac{(C-1)}{V_m \cdot C} \cdot \frac{P}{P_0} \qquad \text{where:}$$

P is the equilibrium pressure

P_o is the saturation pressure

V is the volume adsorbed

V_m is the volume required to cover the surface in a monolayer

C is a constant

A plot of $\frac{P}{V(P_0 - P)}$ versus $\frac{P}{P_0}$ gives a straight line, with intercept equal to $\frac{1}{V_m \, C}$ and gradient equal to $\frac{(C-1)}{V_m \cdot C}$.

The surface area of a sample is then calculated with the following equation:

$$S = \frac{V_m}{22414} \cdot (N_A \cdot S \cdot 10^{-8}) \qquad \text{where:}$$

V_m is the volume required to cover the surface in a monolayer

N_A is the Avagadro's number (6.022×10^{23})

S is the cross section area of N_2 (0.162 nm^2)

The BET surface areas of mesoporous materials (metal oxides) were measured on a Micromeritics Gemini 2360 analyser, coupled with a Micromeritics FlowPrep 060. Before N_2 adsorption at 77 K, the samples were cleaned with N_2 at 120 °C for 45 minutes. Analysis was performed through a five-point BET method using adsorption data in the standard pressure range 0.05-0.35 P/P_0.

Analysis of the surface area and pore volume of microporous materials (zeolites) was performed on an Autosorb-1 Quantachrome instrument. Before N_2 adsorption at 77 K, the samples were cleaned with N_2 at 200 °C for 12 hours under vacuum. Analysis was performed through an 80-point BET method using adsorption data in the linear region of

the isotherm, corresponding to a standard pressure range 0.0003-0.05 P/P_0. A Monte Carlo based model was used in determining pore volumes.

3.4.4 Temperature programmed reduction (TPR)

TPR is a characterisation technique used to obtain qualitative and quantitative analysis of the reducible species present in a sample.

The sample is exposed to a reducing atmosphere (typically H_2 balanced in an inert gas) whilst it is heated according to a programmed linear temperature ramp. If reducible species are present in the sample, then reduction will take place at a determined temperature through consumption of H_2. As a result, a reduction peak is obtained. Occasionally, negative peaks are observed due to release of H_2 stored in the sample. Generally, the consumption of H_2 is monitored using a TCD. TPR curves are the representation of the TCD signal versus temperature. It is a powerful technique when studying interactions between the metal and support as the reduction profile of a metal oxide is affected by the support via a MSI [6].

Temperature programmed reduction (TPR) was carried out using a TPDRO 1100 series analyser. Samples ($\approx$ 20 mg of reducible material) were pre-treated at 110 °C (20 °C/min) for 1 hour in a flow of Argon (20 mL/min). Subsequently, H_2-TPR was conducted by heating the sample to 800 °C (10 °C/min), with a 5 minutes hold at the T_{max}, in a flow of 10% H_2/Argon. Hydrogen uptake was monitored using a TCD.
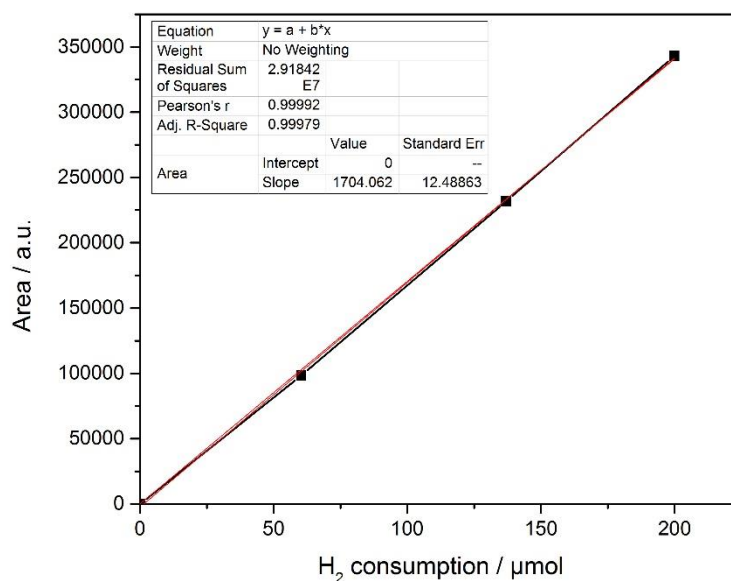
Figure 3.6. H_2-TPR calibration curve

A calibration curve was obtained by quantification of the amount of H_2 consumed during reduction of known masses of CuO. CuO is reduced to Cu metallic at 350 °C in a single step:

$$CuO \ + \ H_2 \ \rightarrow \ Cu^0 \ + \ H_2O \hspace{3cm} \text{Equation 3.1}$$

The amount of H_2 consumed is directly proportional to the amount of CuO, with a stoichiometry of 1:1. The area under the H_2-TPR curve was integrated using Origin®9.1.

Figure 3.6 shows the linear regression plot and equation that correlates the area under the TPR curve with the amount of H_2 consumed during reduction.

3.4.5 NH$_3$-Temperature programmed desorption (NH$_3$-TPD)

TPD techniques are based on the desorption of a probe molecule, previously adsorbed on the sample surface, when it is heated accordingly to a programmed linear temperature ramp. Generally, the adsorption/desorption are monitored using a TCD. TPD curves are the representation of the TCD signal versus temperature. Qualitative and quantitative analysis of the data provides information regarding the adsorption energy, interaction between adsorbates and the extent of adsorbate coverage.

NH$_3$-TPD is a useful technique used to determine the acidity of a sample [10]. The probe molecule, NH$_3$, is adsorbed onto the surface based on its interaction with acidic surface species. The desorption of NH$_3$ at different temperatures, during the TPD, is dictated by the strength of the bond between adsorbate and substrate. Thus, the NH$_3$-TPD curve represents the distribution of weak and strong acid sites (low and high temperature desorption respectively). The acid density and adsorption capacity of a sample can be calculated via quantification of the amount of NH$_3$ desorbed.

NH$_3$-TPD was carried out using a CHEMBET TPR/TPD chemisorption Analyser, Quantachrome Instruments fitted with a TCD. The samples were first pre-treated 130 °C (15 °C /min) for 1 hour in a flow of He (30 mL/min). Subsequently, NH$_3$ adsorption was carried out by exposing the sample to pure NH$_3$ until surface saturation (*ca.* 15 minutes). The adsorption temperature was set to 30 °C, unless another adsorption temperature is specified. Weakly adsorbed NH$_3$ was removed by flushing with He at 100 °C for 1 hour. TPD to 900 °C (15 °C/min) was then conducted in a flow of He (30 mL/min) to desorb chemisorbed ammonia. NH$_3$ desorption was monitored using a TCD, current 180 mV, attenuation 1.

A calibration curve was obtained by injecting known volumes (and therefore known mol) of pure NH_3 directly into the TCD sampling loop. By integrating the corresponding area under the TCD curve a calibration factor for NH_3 was determined.

Equation	y = a + b*x	
Weight	No Weighting	
Residual Sum of Squares	13181.84 926	
Pearson's r	0.99874	
Adj. R-Square	0.99734	
		Value	Standard E
Peak area	Intercept	0	--
	Slope	108.242	1.31675
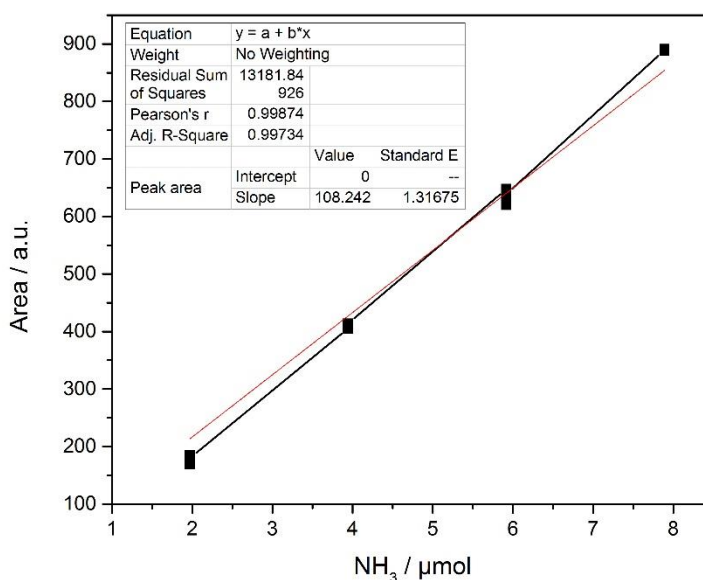
Figure 3.7 NH_3-TPD calibration curve

Figure 3.7 shows the linear regression plot and equation that correlates the area under the TPD curve with the amount of NH_3 injected. Quantification of the acid site density of the samples was calculated with the area under the curve obtained by integration in Origin®9.1.

3.4.6 CO Chemisorption

Characterisation techniques based on chemisorption are commonly used in catalysis to determine physicochemical properties of the samples.

Chemisorption is characterised by an interaction between the adsorbate and the sample surface through a chemical bond formation. When the interaction is relatively weak, only

physisorption occurs. Chemisorption is usually associated with an activation energy (E_a = 60 - 100 kJ/mol) and takes place at temperatures above the critical temperature of the adsorbate. Chemisorption involves formation of a monolayer of the adsorbate on the surface through a chemical bond with localised active sites. However, further physical adsorption on top of the chemisorbed layer forming a multilayer and diffusion of the chemisorbed species into the bulk of the material should also be taken into consideration. Assuming formation of a monolayer, the number of active sites can be determined by quantifying the amount of adsorbate chemisorbed (chemisorbed gas). For quantification purposes, the stoichiometry of the chemisorption, which indicates the number of metal atoms that are bonded to one molecule of adsorbate, is essential to obtain accurate results.

CO and H_2 chemisorption techniques are often used in catalysis to determine the surface area, particle size and dispersion of exposed active sites (exposed active metal atoms on the surface of the support).

The active surface area (ASA) represents the surface area of active sites present in the sample surface given as m^2/g:

$$ASA = \frac{N_m \cdot S \cdot A_m}{166} \qquad \text{where:}$$

N_m is the number of gas molecules adsorbed

S is the adsorption stoichiometry

A_m is the cross sectional area of the active surface metal atom

For a specific metal particle shape, the average crystallite size is calculated as:

$$\text{Average crystallite size} = \frac{100 \cdot N \cdot f}{ASA \cdot \rho} \qquad \text{where:}$$

N is the mass of the active metal

f is the shape correlation factor (6 for spherical particles)

ASA is the active surface area

ρ is the active metal density

The metal dispersion represents the amount of active metal atoms exposed and available to catalyse the surface reaction, given as percentage of the total metal loading:

$$D = \frac{N_m \cdot S \cdot M}{100 \cdot x} \qquad \text{where:}$$

D is the metal dispersion

N_m is the number of gas molecules adsorbed

S is the adsorption stoichiometry

M is the molecular weight of the active metal

x is the total metal loading of the sample (expresses as wt. %)

CO chemisorption was performed using a Quantachrome ChemBET TPR/TPD chemisorption analyser. Prior to chemisorption of CO at 30 °C, samples were treated under pure H_2 (30 mL/min) at 200 °C for 2 hours. The platinum dispersion was calculated from the total CO uptake, based on the assumption of a 1:1 stoichiometry of CO adsorbed: surface platinum atoms.

3.4.7 Thermogravimetric analysis (TGA)

Thermogravimetric analysis determines the weight loss of a material as a function of temperature in a controlled atmosphere. This technique is used to identify the temperature at which chemical changes occur including redox reactions, decompositions, phase

transformations and desorption of adsorbed species. TGA curves are the representation of the weight loss, given as a percentage of the initial sample weight, versus temperature.

TGA analysis was conducted using a TGA/DSC Setaram instrument. Approximately 20 mg of the sample was placed in an Al crucible. After stabilisation, TGA was conducted in air (40 mL/min) by heating the sample from 30 °C to 800 °C (10 °C/min).

3.4.8 Diffuse Reflectance Infrared Fourier Transform Spectroscopy (DRIFTS)

Infrared (IR) spectroscopy is a characterisation technique which is used for chemical analysis and determination of molecular structure.

It is a vibrational spectroscopy technique. The sample is irradiated with infrared radiation, which exhibits wavenumbers in the region of $400 - 5000$ cm^{-1}. Molecular vibrations occur in the IR region. Hence, IR-active molecules absorb IR radiation at energies which correspond to the frequency of a mode of vibration, the molecule will then vibrate undergoing transition to a higher energy vibrational state [11]. The dipole moment of the molecular bond has to change during vibration in order to be IR active. Some vibrations are infrared inactive such as the stretching vibrations of completely symmetrical double and triple bonds. The frequency at which a bond vibrates is dependent upon the bond strength and mass of atoms bonded, and is therefore characteristic of a particular bond. Specific functional groups in chemical compounds have characteristic absorption frequencies. Hence, IR spectroscopy provides qualitative and quantitative information about the different functional groups present in a sample.

An IR spectrum represents the transmission of the IR radiation through the sample at each wavelength. For each wavelength, the transmittance is calculated by dividing the intensity

of IR radiation that has passed through the sample by the intensity of the incident IR radiation. Usually, results are shown as an absorption spectrum, which graphically represents the amount of IR absorbed by the sample at each specific wavelength.

Incident radiation

Sample
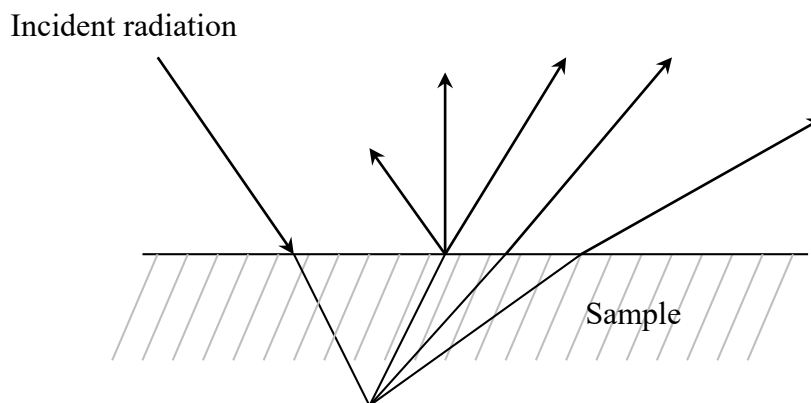
Figure 3.8 An illustration of diffuse reflectance

Fourier Transform Infrared (FTIR) is a non-dispersive IR spectroscopy. This method overcomes the limitation of dispersive instruments; the scanning process is sped up by measuring all of the IR frequencies simultaneously. A parallel, polychromatic radiation is directed from the IR source to an interferometer. The interferometer produces a unique type of signal with all of infrared frequencies. A spectrum with all of the individual frequencies is obtained from the digitised interferogram by performing a Fourier Transform. This is applied by a computer, utilising a Fast Fourier Transform (FFT) algorithm.

Diffuse reflection Fourier Transform Infrared (DRIFT) spectroscopy measures the IR radiation reflected as a combination of internal and external reflections [12]. It is used to maximise the interaction between IR radiation and the sample, which is crucial to obtain IR spectra of solids [6].

In situ DRIFTS studies are generally used to understand chemisorption on supported metal catalysts and to identify adsorbed species and intermediates, which are crucial in

elucidating the mechanisms involved in catalytic reactions. DRIFTS is also used to investigate Brønsted acidity of catalysts such as zeolites, associated with changes in the near IR region (4000 – 3000 cm^{-1}) [10].

When applying chemisorption techniques, some considerations should be addressed, including the determination of physisorption or chemisorption, the nature of the chemical bond and the formation of multilayers of the adsorbate. Spectroscopic studies such as FTIR are used to identify the bonding geometry of adsorbate molecules with the active metal. The adsorbate molecule adopts a range of bonding geometries with coordination to one (linear), two (bridging) or three metal atoms (bridging three fold).

DRIFT spectra were collected on a Bruker Tensor 27 spectrometer fitted with a liquid N_2-cooled Mercury Cadmium Telluride (MCT) detector. Samples were housed within a Praying Mantis high temperature diffuse reflection environmental reaction chamber (HVC-DRP-4) *in situ* cell fitted with zinc selenide windows. Background scans were taken using finely ground KBr. Prior to analysis, samples were ground to a fine powder in an Agate pestle and mortar. For *in situ* heat treatments a Harrick ATC heater was used in heating the sample cell according to a predefined heating program which was controlled via Watlow EZ-Zone software. The gas flow was adjusted by mass flow controllers. Scans were collected across the range 4000 cm^{-1} to 600 cm^{-1}, 4 cm^{-1} frequency, 64 scans.

CO-DRIFTS studies were performed as follows. Prior to CO exposure, the sample was reduced in 10% H_2/N_2 (30 mL/min) at 300°C (10 $^{\circ}$C/min) for 2 hours and subsequently cooled to 30 $^{\circ}$C in N_2. The sample was then exposed to a flow of 100 % CO (30 mL/min) at 30 $^{\circ}$C. Successive experiments were carried out to collect information about CO adsorption on the catalyst surface. Scans were taken at 1 minute intervals across the range 4000 cm^{-1} to 500 cm^{-1}, 4 cm^{-1} frequency, 64 scans.

The oxidation of NO to NO_2 was studied using DRIFTS as follows. For experiments using NO, CaF_2 windows were used on the *in situ* cell. The sample was exposed to 5000 ppm NO/N_2 (27 mL/min) and O_2 (3 mL/min). The sample cell was heated from 100 °C to 500 °C at intervals of 50 °C. Successive experiments were carried out to collect time resolved information about the NO oxidation. At each temperature, 15 scans were taken at 1 minute intervals across the range 4000 cm^{-1} to 500 cm^{-1}, 4 cm^{-1} frequency, 64 scans.

3.4.9 Diffuse Reflectance UV-Vis Spectroscopy (UV-Vis DRS)

UV-Vis spectroscopy is a characterisation technique used for qualitative and quantitative analysis of chromophores present in a sample.

Ultraviolet-Visible radiation exhibits wavelengths in the region of 200 – 900 nm. The promotion of valence electrons to higher energy levels occurs in the UV-Vis region. Valence electrons are generally found in single (σ), double or triple (π) and non-bonding orbitals. When a sample is irradiated with UV-Vis radiation, photons of a specific energy are absorbed and employed in exciting valence electrons to higher energy states. The electronic transition usually involves the promotion of an electron from a HOMO to a LUMO orbital. The energy needed to promote electrons between orbitals depends on the bonding system and atoms involved. Hence, the wavelength at which an absorption band is observed provides information as to ionic charge, local environments and electronic bonding, all of which effects the transition energy [13].

The electronic transitions are determined by selection rules. The spin selection rule ($\Delta S = 0$) states that changes in spin multiplicity are forbidden. The Laporte selection rule states that a change in the symmetry of the complex is needed for a transition to occur.

Mathematical treatments of the energy levels of orbital systems suggest that while some electronic transitions are statistically probable, other transitions have a probability of zero and are said to be "forbidden" but they frequently occur giving weak absorption bands. Some particularly useful forbidden transitions are d $\rightarrow$ d absorptions in transition metals.

UV Vis spectra were collected using a Varian 4000 UV-Vis spectrophotometer. Prior to analysis, samples were ground to a fine powder in an Agate pestle and mortar. Background scans were taken using a high purity PTFE disc. Scans were collected across the wavelength range 200-800 nm, at a scan rate of 150 nm min^{-1}, with a UV – visible changeover wavelength of 350 nm.

3.4.10 Raman Spectroscopy

Raman spectroscopy is a powerful and frequently used characterisation technique used for chemical analysis and determination of molecular structure.

It is a vibrational spectroscopy based on the Raman scattering phenomena produced by interaction of a sample with incident electromagnetic radiation. Raman scattering is associated with absorption of radiation energy which corresponds to vibrational and rotational modes of molecular bonds. Selection rules dictate which molecules are Raman active and thus, which rotations and vibrations are permitted. In order to be Raman active, a molecule must possess changeable polarizability and lack centres of symmetry.

When the kinetic energy of the scattered photon is equal to the energy of the incident radiation, elastic scattering occurs and is termed Rayleigh. If the kinetic energy of the scattered photon is different to the energy of the incident radiation, elastic scattering occurs

and it is termed anti-Stokes or Stokes depending on whether the scattered photon gains or loses kinetic energy respectively.
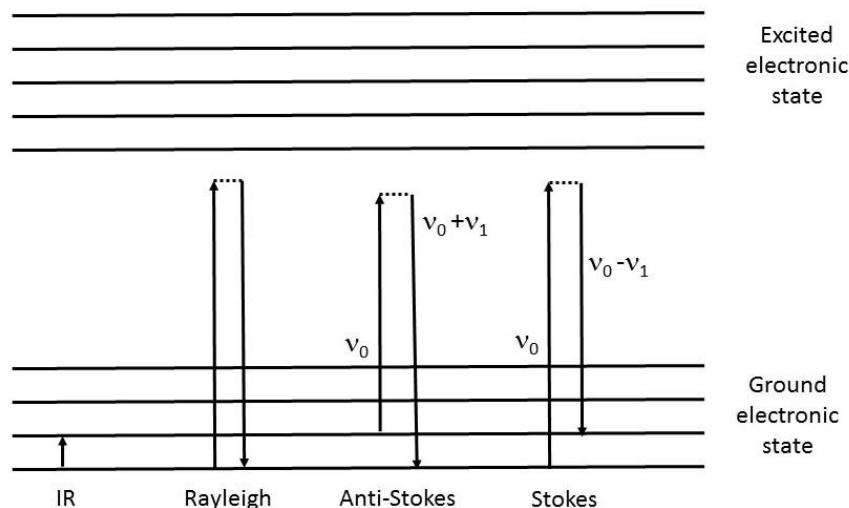
Figure 3.9 Representation of excitation and relaxation of the molecular energy states during Raman scattering

The Raman spectrum represents the intensity of the scattered radiation at each wavelength. It is formed of a primary band corresponding to Rayleigh and two symmetric secondary bands corresponding to Raman Stokes and Anti-Stokes. Each material exhibits a characteristic set of bands located at specific wavelengths that provide information about the chemical bonds and molecular structure.

To maximise the scattering, high intensity monochromatic radiation is required. Hence, lasers are the most common source of incident radiation.

Raman spectra were obtained using a Renishaw inVia Raman microscope equipped with a Stellar-REN 3B argon ion laser ($\lambda = 514$ nm) operated at a power of 20 mW.

3.4.11 Scanning Electron Microscopy (SEM)

Electron microscopy is a powerful characterisation technique frequently used to determine the topology, morphology and composition of a sample. It is generally used to determine the size and shape of supported metal particles.

It is based on the interaction of an electron beam with the sample. Electrons have characteristic wavelengths in the range of atomic radius (< 1 Å) and thus, it is possible to obtain images with atomic detail.

Primary electron beam

X-rays

Photons

Backscattered electrons

Secondary electrons

Auger electrons

Diffracted electrons

Loss electrons

Transmitted electrons
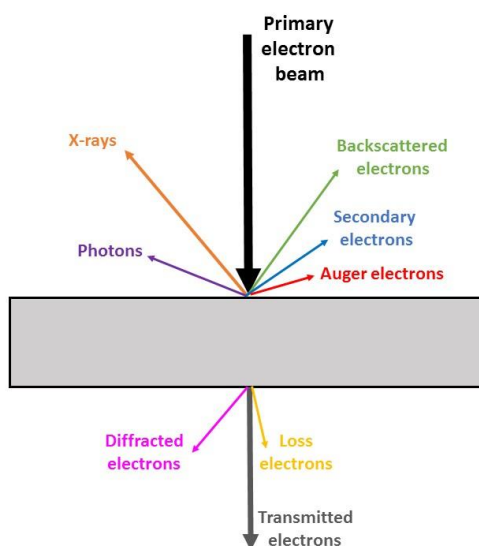
Figure 3.10 Representation of the interaction between the primary electron beam and the sample in an electron microscope

When the primary electron beam, with energy between 100 and 400 eV, hits the sample several processes can occur [6]. These interactions are illustrated in Figure 3.10.

- The electrons can pass through the sample without losing energy or losing energy as result of consecutive inelastic collisions.

- Emission of secondary electrons occurs via electron excitation by collisions with the electron beam. Most of the secondary electrons emitted correspond to

conduction band electrons, which have their last energy loss process in the surface region.

- If orientations are favourable, electrons are diffracted by particles present in the sample. Detection of diffracted electrons is used to obtain dark-field images and crystallographic information.

- Electrons can be scattered by collisions with atoms present in the sample. Backscattering is associated with elastic scattering, which involves changes in the trajectory of the incident electrons without significant change in their kinetic energy. Backscattering is dependent on the atomic number (Z), as heavier atoms have a higher probability of producing an elastic collision because of their greater cross-sectional area. Hence, detection of backscattered electrons provides information about the distribution of different elements in a sample.

- Auger electrons and X-Rays are emitted as a result of relaxation of ionised core atoms.

- Electrons can excite characteristic vibrations in the sample.

- Interaction of the sample with the electrons can produce the emission of photons in the UV to IR range. This emission is usually associated with recombination of electron-hole pairs in the sample.

Electron microscopes usually operate under high vacuum to prevent electron scattering. The electron beam is generated from a field emission gun (FEG) formed of a very fine single crystal of tungsten. A series of fine apertures and lenses focus the beam to a fine point and direct it onto the sample, producing different types of emissions.

Scanning electron microscopy (SEM) is based on the detection of either secondary and backscattered electrons as a function of the position of the beam. The 3D images obtained

represent the topology, morphology and composition of the sample in the area irradiated. SEM has a probing depth of between 3 and 10 nm.

Scanning electron microscopy images were obtained using a Carl Zeiss EVO 40 operated at 25 kV. All samples were mounted on carbon Leit adhesive discs. Images were collected using backscattered and secondary electron detectors. For EDX (X-ray energy dispersive spectroscopy) analysis, high probe currents (up to 25 nA) were required to allow sufficient generation of X-rays. The data was collected using an Oxford EDX analyser coupled to the EVO 40 SEM.

3.4.12 Transmission Electron Microscopy (TEM)

Transmission electron microscopy (TEM) is based on the detection of transmitted and diffracted electrons. Bright field images represent a 2D projection of the transmitted electrons, which depends on the mass distribution; the density and thickness of the sample. Dark field images represent the diffracted electrons, which have a slightly different angle than that of the transmitted beam. Contrast in the images is caused by attenuation of the electron beam, dependent on the density and thickness of the sample, and also by diffraction and interference [6]. TEM instruments operate in a similar way to an optical microscope, with electromagnetic lenses and an electron beam instead of optical lenses and light. Typically, a TEM instrument has superior magnification and resolution to a SEM instrument.

TEM is widely used in catalysis to determinate the dispersion, particle size and morphology of supported particles and to investigate metal support interactions [14].

Scanning Transmission Electron Microscopy (STEM) combines both TEM and SEM operation modes. It is possible to select specific regions of the sample that are irradiated

with the primary electron beam and obtain either bright or dark field images. Dark field images are obtained based on the electrons that are diffracted by the metal particles and thus, images of supported metal particles with improved contrast are obtained.

High resolution TEM (HRTEM) analyses were conducted on a JEOL-2100 JEM electron microscope at an accelerating voltage of 300 kV. The catalysts for TEM observation were dispersed in ethanol and dropped onto a copper mesh with a carbon micro-grid. STEM-EDX imaging experiments were performed on the same instrument.

3.4.13 X-Ray Energy Dispersive Spectroscopy (EDX)

Usually, SEM and TEM instruments are coupled with EDX analysis, which provides information as to the elemental composition of a sample.

Upon interaction of the electron beam with the sample, if the incident electron has enough energy it will eject a bound electron from an orbital of the atom. The core electron vacancy generated, is filled with an electron from a higher energy level and a X-ray photon with energy equal to the energy gain is emitted. The emitted X-rays are detected with an energy-dispersive X-ray detector that is located in a fixed position with respect to the sample. The detector consists of a liquid nitrogen cooled semiconductor crystal (typically $Si(Li)$). The X-ray is converted into a photoelectron with kinetic energy equal to $E_k = E_{X\text{-ray}} - E_b$, where E_b is the binding energy of the photoelectron emitted. This photoelectron utilises its kinetic energy in creating electron-hole pairs (3.8 eV per pair). The current detected is proportional to the number of electron-hole pairs formed [6].

The EDX spectrum represents the intensity of the signal detected as a function of the wavelength of the X-rays generated. Each atomic element has a characteristic wavelength

or set of wavelengths attributed to the energy difference between core electrons and higher energy electrons. Hence, EDX allows qualitative and quantitative analysis of the different elements present in the sample.

The area of the discrete regions analysed is limited by the microscope's resolution.

3.5 References

1.   Rossin, J. A., Effects of pretreatment conditions on the activity of a Pt/Al2O3 catalyst for the oxidation of Di(n-propyl)sulfide. *Journal of Molecular Catalysis* **1990,** *58* (3), 363-372.

2.   Aramendía, M. A.; Colmenares, J. C.; Marinas, A.; Marinas, J. M.; Moreno, J. M.; Navío, J. A.; Urbano, F. J., Effect of the redox treatment of Pt/TiO2 system on its photocatalytic behaviour in the gas phase selective photooxidation of propan-2-ol. *Catalysis Today* **2007,** *128* (3–4), 235-244.

3.   Hanaor, D. H.; Sorrell, C., Review of the anatase to rutile phase transformation. *J Mater Sci* **2011,** *46* (4), 855-874.

4.   Jauncey, G. E. M., The Scattering of X-Rays and Bragg's Law. *Proceedings of the National Academy of Sciences of the United States of America* **1924,** *10* (2), 57-60.

5.   Patterson, A. L., The Scherrer Formula for X-Ray Particle Size Determination. *Physical Review* **1939,** *56* (10), 978-982.

6.   Niemantsverdriet, J. W., Spectroscopy in Catalysis: An Introduction, Third Edition. In *Spectroscopy in Catalysis*, Wiley-VCH Verlag GmbH & Co. KGaA: 2007; pp I-XVIII.

7.   Leofanti, G.; Padovan, M.; Tozzola, G.; Venturelli, B., Surface area and pore texture of catalysts. *Catalysis Today* **1998,** *41* (1–3), 207-219.

8.   Rothenberg, G., *Catalysis. Concepts and Green Applications*. Wiley-VCH: 2008.

9.   Lowell, S.; Shields, J. E.; Thomas, M. A.; Thommes, M., *Characterization of Porous Solids and Powders: Surface Area, Pore Size and Density*. Springer Netherlands: 2004.

10.   Farneth, W. E.; Gorte, R. J., Methods for Characterizing Zeolite Acidity. *Chemical Reviews* **1995,** *95* (3), 615-635.

11.   Williams, D. H. F., Ian *Spectroscopic methods in organic chemistry* 4th edition ed.; McGraw-Hill: London and New York 1995 p329.

12.   Mark, B. M., Fundamentals and Applications of Diffuse Reflectance Infrared Fourier Transform (DRIFT) Spectroscopy. In *Structure-Property Relations in Polymers*, American Chemical Society: 1993; Vol. 236, pp 351-375.

13.   Schoonheydt, R. A., UV-VIS-NIR spectroscopy and microscopy of heterogeneous catalysts. *Chemical Society Reviews* **2010,** *39* (12), 5051-5066.

14.   Yang, J. C.; Small, M. W.; Grieshaber, R. V.; Nuzzo, R. G., Recent developments and applications of electron microscopy to heterogeneous catalysis. *Chemical Society Reviews* **2012,** *41* (24), 8179-8194.

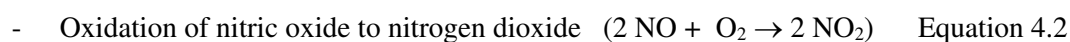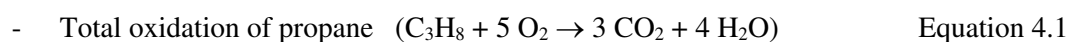# *Oxidation properties of supported platinum catalysts*

4

4.1 Introduction

Diesel oxidation catalysts (DOC) are used in exhaust aftertreatment to cut pollutants emitted from diesel engines. DOCs generally consist of a monolith honeycomb matrix coated with the active phase, contained in a stainless steel canister. As its name indicates, an oxidation catalyst will promote the oxidation of compounds of a reducing character. The DOC is designed to oxidise carbon monoxide, gas phase hydrocarbons and the soluble organic fraction (SOF) of diesel particulate matter to CO_2 and H_2O. Generally, the DOC is combined with a diesel particulate filter and either a NO_x storage catalyst (NSC) or a selective catalytic reduction (SCR) catalyst and is positioned upstream of the other units. The title and objective of this thesis arises from a novel approach, the diesel oxidation NO_x adsorption catalyst (DONAC), where NO_x is to be stored by the DOC.

Platinum-based diesel oxidation catalysts are the most used technology and much of the DOCs development has focussed on decreasing the light-off temperature in order to improve the oxidation activity, principally during cold starts.

The aim of this chapter is to investigate the oxidation properties of supported platinum catalysts and particularly, how these properties are affected by the support material. Two oxidation reactions were studied:

- Total oxidation of propane   ($C_3H_8 + 5\,O_2 \rightarrow 3\,CO_2 + 4\,H_2O$)   Equation 4.1

- Oxidation of nitric oxide to nitrogen dioxide   ($2\,NO + O_2 \rightarrow 2\,NO_2$)   Equation 4.2

4.2 Total oxidation of propane

4.2.1 The effect of the support

Propane is not the most representative hydrocarbon (HC) of the diesel engines exhaust composition. Despite this, total oxidation of propane was investigated because short chain alkanes are recognised as some of the most difficult VOCs to oxidise [1] and thus, it is expected that a catalyst which promotes the oxidation of propane at low temperatures will also perform well under real conditions.

The catalytic activity of supported metal catalysts is governed by a complex mix of different factors including dispersion, morphology, reducibility, electronic structure and mechanical and chemical properties. The properties of supported catalysts are known to be affected by the support in many catalytic reactions and consequently, the interaction between the active phase and the support becomes crucial in understanding the catalytic behaviour and in catalyst design.

Although Al_2O_3 has been extensively used as a support, it is of great interest to investigate other metal oxides as potential supports for HC oxidation catalysts [2][3][4][5][6][7]. Specifically, mixed metal oxide supports show exclusive and interesting effects on catalyst performance [8][9][10][11][12][13][14][15].

Many studies have investigated platinum catalysts for the total oxidation of VOCs [16][17][18][19]. Nevertheless, a degree of uncertainty persists in determining whether the reaction is structure sensitive and in the true nature of the active site.

The aim of this study is to rationalise the effect of a series of mixed TiO_2 and Al_2O_3 based supports on propane combustion in an oxidising atmosphere over platinum catalysts.

4.2.1.1 Metal oxide supports

In this section, commercial metal oxide supports - TiO_2 P25, SiO_2 and γ-Al_2O_3 - were used to prepare supported platinum catalysts by non-aqueous impregnation for total oxidation of propane under an oxidizing atmosphere.

Alumina (Al_2O_3) is extensively used as a support for commercial diesel oxidation catalysts [20]. This is due to a favourable combination of its properties including: surface area, pore volume, pore size distribution, Lewis acidity, thermal and mechanical stability, interaction with Pt group metals and low manufacturing cost. However, its high reactivity with SO_x results in performance degradation by sulphur poisoning [21] [22] [23] [24].

Titania (TiO_2) is a reducible support that exhibits a strong metal-support interaction (SMSI) with Pt group metals and is broadly used in heterogeneous catalysis due to its tuneable surface area and pore distribution. Additional desirable physical properties include: Lewis acidity, redox properties, thermal stability and mechanical strength [25]. TiO_2 also presents high corrosion resistance and sulphur tolerance, leading to superior catalytic activity and durability in an oxidising atmosphere [26] [27] [28].

Silica (SiO_2) is an irreducible support with high surface area. Compared with alumina, possesses lower thermal stability. It is assumed to be relatively inert and presents high resistance to sulphur poisoning, however supported platinum particles suffer from sintering due to weak metal-support interactions [29].

Among the different roles of supports, the most relevant are: dispersing the active phase of the catalyst, increasing metal surface area and improving the catalytic performance through interactions between the metal and support. The morphology, surface area, pore volume and pore size distribution of the support material plays an important role in enhancing

catalyst stability and performance. The BET surface area and density of the supports used in this section are listed in Table 4.1. SiO_2 exhibits the highest surface area at 222 m^2/g, which is 1.7 and 4.1 times greater than those of Al_2O_3 and TiO_2 respectively. Of the three supports, TiO_2 P25 is the least dense (0.16 g/mL).

Table 4.1. Surface area measured by N_2 physisorption and density of the commercial supports and supported platinum catalysts

Catalyst support	Surface area $_{BET}$ (m^2/g)	Density (g/mL)
TiO_2 P25	54	0.16
2 wt. % Pt/TiO_2 P25	51	0.49
SiO_2	222	0.25
2 wt. % Pt/SiO_2	181	0.15
γ-Al_2O_3	130	1.18
2 wt. % Pt/Al_2O_3	118	0.75

The catalytic activities of supported platinum catalysts (2 wt. % Pt) for the total oxidation of propane were evaluated and the results are shown in Figure 4.1. 2% wt. % Pt/SiO_2 is the least active, requiring a relatively high temperature before any activity is observed (350 $^{\circ}C$) and failing to achieve 100 % propane conversion, even at 500 $^{\circ}C$. TiO_2 P25 and γ-Al_2O_3 based catalysts exhibit similar behaviour, with 100 % propane conversion to CO_2 at 450 $^{\circ}C$ and T_{50} values of 350 $^{\circ}C$ ($\pm$ 4 $^{\circ}C$).

$\blacksquare$ 2 wt. % Pt/TiO_2 P25 $\blacktriangle$ 2 wt. % Pt/Al_2O_3 $\bullet$ 2 wt. % Pt/SiO_2
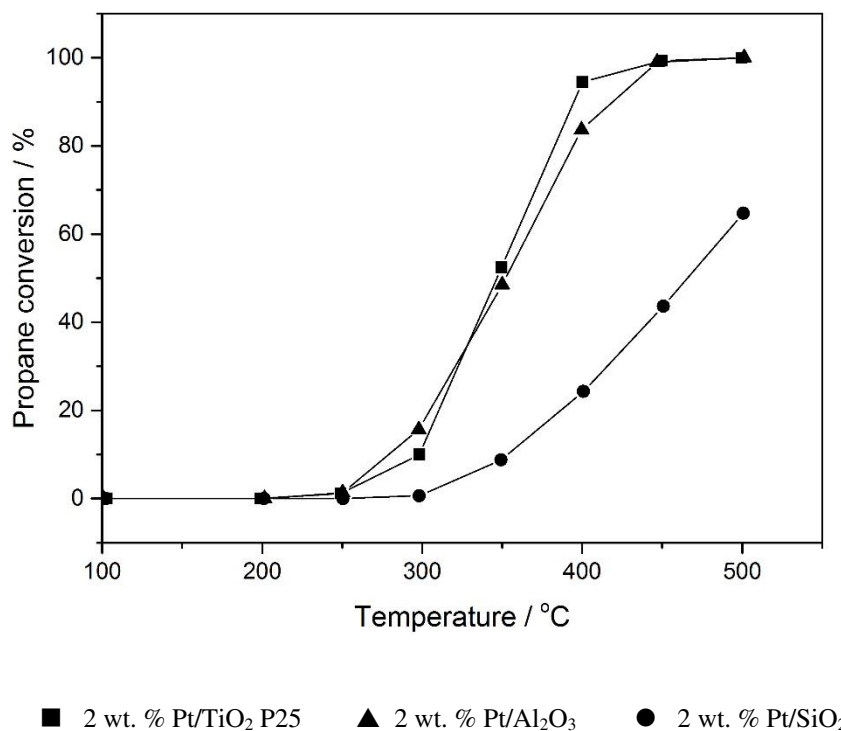
Figure 4.1. Total oxidation of propane over supported platinum catalysts

Reaction conditions: Flow reactor, GHSV = 50,000 h^{-1}, C_3H_8:O_2 = 1:50

Catalysts prepared by non-aqueous impregnation and calcined at 400 $^{\circ}$C in static air

These trends differ from those obtained in previous studies. Yazawa *et al.* [30] reported that 5 wt. % platinum supported on SiO_2 is more active for propane oxidation ($T_{50} \approx 307$ $^{\circ}$C) than that supported on Al_2O_3 ($T_{50} \approx 397$ $^{\circ}$C). In addition, Avila *et al.* [16] reported that 0.5 wt. % platinum supported on TiO_2 is more active ($T_{50} \approx 327$ $^{\circ}$C) than that supported on Al_2O_3 ($T_{50} \approx 395$ $^{\circ}$C). This could be ascribed to differing testing conditions as Yazawa *et al.* and Avila *et al.* used O_2/C_3H_8 ratios of 2.5 and 12.4 respectively. Additionally, the catalysts used in the work of Yazawa *et al.* were reduced in a N_2/H_2 atmosphere at 550 $^{\circ}$C before catalytic testing. The oxygen concentration was therefore much lower than that used in the present work (O_2/C_3H_8 = 50). This is significant, as it has been reported that

the catalytic activity of platinum supported upon metal oxides varies with the reaction mixture composition [11] [31]. Indeed, work carried out by Men *et al*. demonstrated that propane conversion on supported platinum catalysts is suppressed in an excess of oxygen, with chemisorbed O_2 acting as an inhibitor for the reaction at full coverage [1]. The O_2/C_3H_8 ratio used in the work presented in this thesis is equal to 50, which is much higher that the stoichiometric ratio of 5. In this way oxygen is in excess, which is representative of the real working conditions in a diesel engine.

The temperatures for 10 % (T_{10}) and 50 % (T_{50}) propane conversion over supported platinum catalysts containing 1 and 2 wt. % Pt are reported in Figure 4.2.
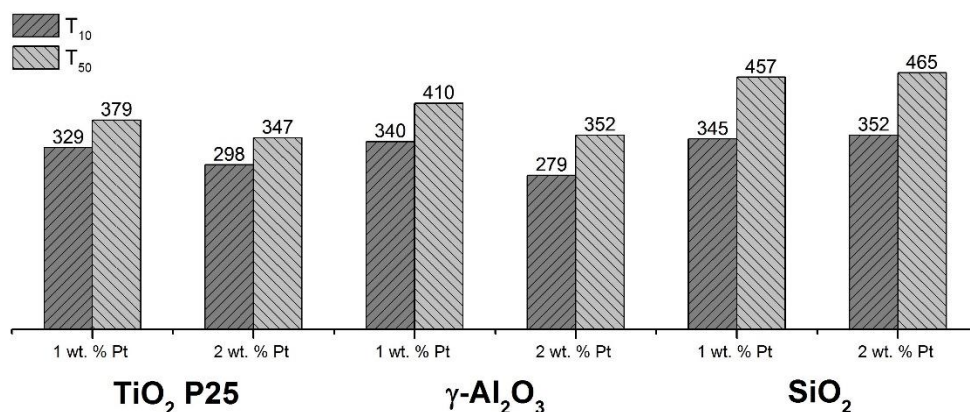

Figure 4.2. Temperature in degrees Celsius for 10 % propane conversion (T_{10}) and 50 % propane conversion (T_{50}) over supported platinum catalysts

Based on a lower T_{50} value, the most active catalyst at 1 wt. % Pt is Pt/TiO_2, with the overall order of activity found to be thus:

$$Pt/TiO_2 \; > \; Pt/Al_2O_3 \; > \; Pt/SiO_2$$

For catalysts containing 2 wt. % Pt, both Pt/TiO_2 and Pt/Al_2O_3 present comparable T_{50} values of 347 ^oC and 352 ^oC respectively. These are *ca.* 115 ^oC lower than the T_{50} observed for Pt/SiO_2 (465 ^oC), obeying the following order of catalytic activity:

$$Pt/TiO_2 \approx Pt/Al_2O_3 > Pt/SiO_2$$

Given that propane oxidation is a highly exothermic reaction and that mass transfer limitations are negligible at low temperatures, it is probably more telling to compare the T_{10} values, which obey a similar sequence.

Increasing support surface area does not necessarily correlate with increasing catalyst activity. For the Pt catalysts represented in Figures 4.1 and 4.2, Pt/TiO_2 P25 shows superior catalytic performance to Pt/SiO_2 catalysts, despite SiO_2 having a higher surface area.

Compared to the bare supports, surface areas decreased after impregnation of platinum, as shown in Table 4.1. Depositing 2 wt. % Pt onto TiO_2 P25, SiO_2 and γ-Al_2O_3 results in a decrease in the BET surface area of 6 %, 19 % and 9 % respectively.

In order to determine the platinum particle size and dispersion on these supports, detailed electron microscopy studies were performed. Figure 4.3 shows representative micrographs obtained from Scanning Electron Microscopy (SEM) using a Backscattered detector (BSD). In these images, the platinum particles display bright contrast.

Relatively well dispersed platinum particles with spherical-oblong morphology and a mean diameter of 200 nm (0.2 μm) are observed on the TiO_2 P25 support. Figure 4.3 b) shows spherical platinum particles of 50-100 nm supported on the SiO_2 support; and also larger clusters of platinum (2 and 4.5 μm) indicating sintering. Platinum is poorly dispersed on the surface of γ-Al_2O_3, with isolated spherical platinum particles (mean diameter of 60 nm) found in certain regions.
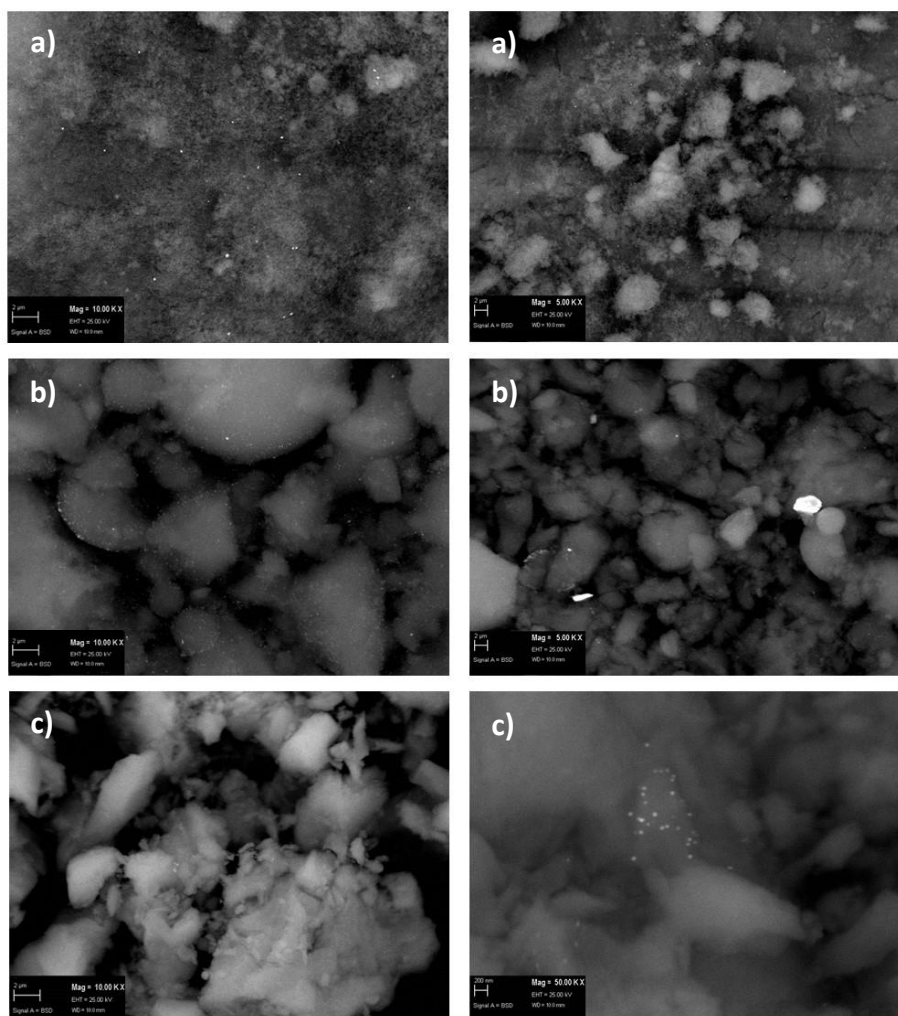
Figure 4.3. Selected scanning electron microscopy (SEM) images (BSD detector) of

a) 1 wt. % Pt/TiO$_2$ P25 b) 1 wt. % Pt/SiO$_2$ and c) 1 wt. % Pt/Al$_2$O$_3$

The surface state of the supported platinum catalysts and oxidation state of the platinum

was investigated by X-ray photoelectron spectroscopy (XPS). Figure 4.4 shows the Pt 4f

region in the XPS spectra of the calcined catalysts. After correcting the C 1s value to

284.7 eV, each spectrum can be fitted with pairs of Gaussian-Lorentzian curves of equal

half-widths, an intensity ratio of ¾ and a separation of 3.3 eV. For 1 wt. % Pt/TiO$_2$ and

1 wt. % Pt/SiO$_2$ (Figures 4.4 a and b), spectra are fitted with a pair of signals at 72.3 eV (Pt 4f$_{7/2}$) and 75.6 eV (Pt 4f$_{5/2}$), attributed to platinum (II) oxide (PtO). On the Pt/Al$_2$O$_3$ catalyst (Figure 4.4 c), analysis of the XPS spectra is difficult due to the intense Al 2p signal which overlaps with the Pt 4f region. However, spectral deconvolution in (c) reveals the presence of two possible platinum environments; the signal of Pt 4f$_{7/2}$ at 71.6 eV is assigned to metallic platinum and that at 74.3 eV to platinum (IV) oxide (PtO$_2$).
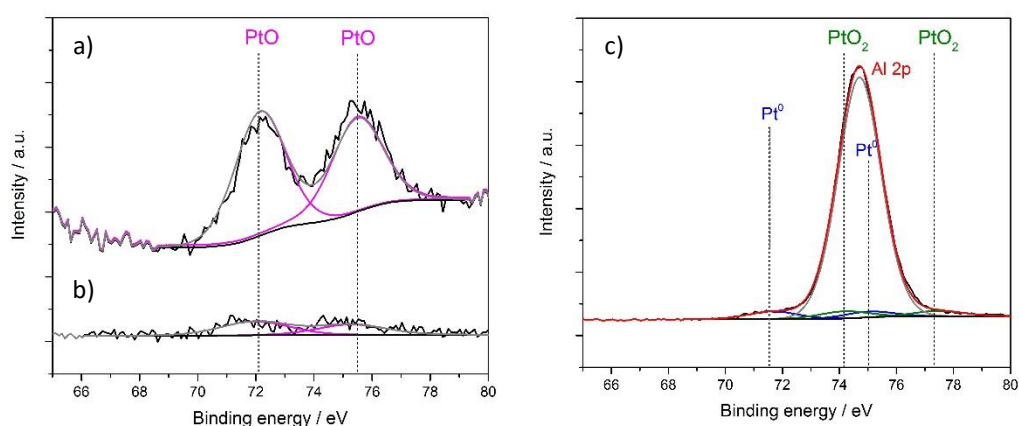
Figure 4.4. XPS spectra in the Pt 4f binding energy region of

a) 1 wt. % Pt/TiO$_2$ P25 b) 1 wt. % Pt/SiO$_2$ and c) 1 wt. % Pt/Al$_2$O$_3$

Quantitative analysis of the supported platinum catalysts obtained from the Pt 4f region of XPS spectra is presented in Table 4.2. A higher concentration of surface platinum species is observed for Pt/TiO$_2$ P25 ($\approx$ 11 wt %) and Pt/Al$_2$O$_3$ ($\approx$ 6 wt %) than with Pt/SiO$_2$ ($\approx$ 3 wt. %). This could be attributed to heterogeneous dispersion of the platinum on SiO$_2$. Note that in all cases the surface content of platinum exceeds total theoretical loading (1 wt % Pt), indicating a platinum concentration gradient between the surface and bulk of the catalyst.

Table 4.2. Quantitative analysis of the supported platinum catalysts obtained from the XPS spectra

Catalyst	Pt At. %	Pt Wt. %	Pt^0 Conc. %	Pt^{2+} Conc. %	Pt^{4+} Conc. %
1 wt. % Pt/TiO_2 P25	10.6	11.1	0	100	0
1 wt. % Pt/SiO_2	2.3	3.1	0	100	0
1 wt. % Pt/Al_2O_3	4.8	6.3	53	0	47

Whilst platinum oxide (PtO) is exclusively observed on the Pt/TiO_2 and Pt/SiO_2 catalysts, platinum was found to exist as both (+4) oxide (with $\approx$ 47 % PtO_2) and metallic state (with $\approx$ 53 % Pt^0) on the Pt/Al_2O_3 catalyst. However, as mentioned before, the spectral deconvolution and quantification for Pt/Al_2O_3 should be considered carefully as the Al 2p signal overlaps with the Pt 4f region and could lead to false interpretation.

Based on the results presented, it is possible that the inferior catalytic activity observed in Figures 4.1 and 4.2 for Pt/SiO_2 catalysts is due to the sintering of PtO particles and the lower concentration of platinum species at the catalyst' surface. These results are in agreement with previous studies which showed that the catalytic activity of DOCs is affected by platinum sintering [32] [33].

4.2.1.2 Mixed metal oxide supports

It has been shown in the previous section that, at equal loading, platinum supported on TiO_2 presents comparable catalytic activity for propane oxidation to an Al_2O_3 supported catalyst. As mentioned previously, TiO_2 shows high tolerance to sulphur poisoning [26]. As this is an important requirement of DOCs, novel TiO_2 - based mixed oxide supports were investigated.

To improve catalytic activity whilst also increasing mechanical strength, thermal stability, surface area and modulating surface acidity, titania and alumina can be modified through addition of other metal oxides. Using a combination of different metal oxides results in a novel category of supports with superior performance, through combining the characteristics intrinsic to each constituent metal oxide and interactions between oxide phases.

Three groups of commercially available mixed-oxide supports were used: (i) anatase + 20 % rutile TiO_2 – (SiO_2), (ii) anatase- only TiO_2 – (SiO_2) and (iii) γ Al_2O_3-SiO_2 mixed oxide supports. Limited information about the physicochemical properties of these commercial supports was provided by the supplier, therefore full characterisation was performed.

A summary of the physicochemical properties of the six different supports used in this section are shown in Table 4.3. Anatase-rutile TiO_2 based supports are found to be denser than anatase- only TiO_2 based supports, which are denser than the Al_2O_3-SiO_2 support.

Table 4.3. Physicochemical properties of the supports

Support	Surface area [a] (m²/g)	Density (g/mL)	Particle size [b] D (0.50) μm	Acidity [c] μmol NH₃/g
Anatase + 20 % Rutile TiO₂ based supports				
TiO₂ (A-R)	52	0.76	30.07	1666
TiO₂-SiO₂ (5 mol % Si, A-R)	84	0.68	30.88	1330
TiO₂-SiO₂ (16 mol % Si, A-R)	72	0.60	47.51	613
Anatase TiO₂ based supports				
TiO₂ (A)	80	0.58	1.62	934
TiO₂-SiO₂ (10 mol % Si, A)	107	0.51	1.41	1142
γ-Al₂O₃ based supports				
Al₂O₃-SiO₂ (10 mol % Si)	197	0.4	X	1813

[a] Surface area measured by N_2 physisorption, density

[b] Particle size distribution determined by light scattering analysis

[c] Acidity measured by NH_3-TPD

The BET surface area of the anatase-rutile titania support (TiO₂ A-R) is ≈ 50 m²/g. Comparable with that of TiO₂ P25, this increases by up to 38 % with increasing SiO₂ content (72 m² / g). The supports with anatase as the only crystalline phase (TiO₂ A) present higher surface area. Additionally, the Al₂O₃-SiO₂ support exhibits the highest surface area of 197 m²/g, which is 2.7 and 1.8 times larger than TiO₂-SiO₂ (16 mol % Si, A-R) and TiO₂-SiO₂ (10 mol % Si, A) respectively.

The acidity of the supports was probed using temperature-programmed desorption of NH₃ preadsorbed at 100 °C. The NH₃-TPD curves are shown in Figure 4.5. Generally, the profile presents a broad desorption corresponding to several overlapping desorption events between 200 and 800 °C. This is comparable with those obtained in recent publications [15]

[16] [34]. The peaks represent different acid sites strengths, with desorption occurring in two regions: low temperature region (T < 400 °C) being attributed to desorption of NH_3 from weak acid sites and high temperature region (T > 400 °C) being assigned to desorption of NH_3 from strong Brønsted and Lewis acid sites. Weak acid sites are generally associated with terminal hydroxyl (-OH) groups and presence of Si-O-Ti in the support [35].
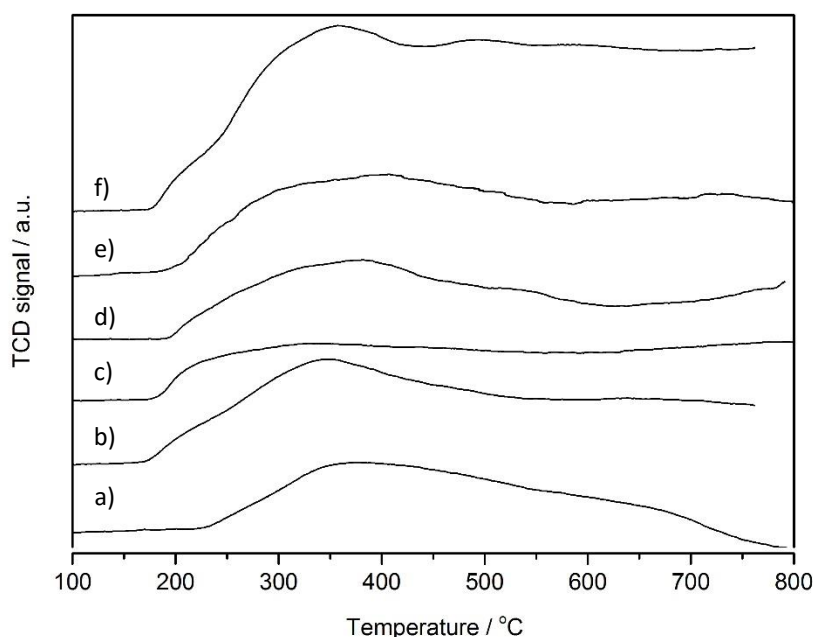
Figure 4.5. NH_3-TPD profiles of the supports:

a) TiO_2 (A-R), b) TiO_2-SiO_2 (5 mol % Si, A-R), c) TiO_2-SiO_2 (16 mol % Si, A-R),

d) TiO_2 (A), e) TiO_2-SiO_2 (10 mol % Si, A) and f) Al_2O_3-SiO_2 (10 mol % Al)

All supports present comparable acidic sites strength with a broad desorption peak centred near 350 °C assigned to weak acid sites on the surface, and several shoulder peaks at higher temperatures (at ≈ 500 and 625 °C). The total number of acid sites per g of support was quantified from the total amount of NH_3 desorbed from the surface using the response factor calculated using the NH_3 calibration presented in Chapter 3, Figure 3.8. The results

reported in Table 4.3 are given as total acid site density (μmol NH_3/g support). The total acid site density of TiO_2 (A) is about 44 % lower than that of TiO_2 (A-R). Furthermore, while the acid site density of the anatase-rutile titania (TiO_2 A-R) based mixed oxide supports decreases with increasing SiO_2 content (Table 4.3), acidity increases upon addition of SiO_2 to the anatase- only titania support (TiO_2 A) (Table 4.3). Of the supports analysed, Al_2O_3-SiO_2 is the most acidic. The acidity trends obtained for the TiO_2 A-R supports are inconsistent with those obtained in previous studies [9 34 36 37 38], which showed that the Brønsted acidity of TiO_2-based supports increases with increasing SiO_2 content. Contrarily, other investigations demonstrated that in mixed TiO_2-SiO_2 oxides, both the density and strength of acid sites decreases with increasing SiO_2 content. These studies showed that the molecularly dispersed titanium cations on the silica surface act as redox sites rather than acid sites for methanol oxidation, increasing the oxidising potential [39 40 41].

The source of the acidity of TiO_2-SiO_2 mixed oxides is debated. Tanabe *et al.* proposed that new Brønsted acid sites could be created by a charge imbalance at Ti-O-Si interfaces in the SiO_2 [42]. Work by Notari *et al.* [43] showed that high purity TiO_2-SiO_2 mixed oxides do not contain Brønsted acid sites. These results were opposite to studies by Bonelli *et al.*[44] and Junling *et al.* [45], who demonstrated the presence of Brønsted acid sites on TiO_2-SiO_2 with high titania loadings and also found that isolates Ti^{4+} cations on TiO_2-SiO_2 have strong Lewis acidity. Differences in synthesis conditions and thermal treatments could be responsible for the variation in the reported acidity of TiO_2-SiO_2 mixed oxides.

Further studies using Hammett indicators and IR spectra of adsorbed pyridine would be beneficial in understanding in more detail the nature of acid sites (Lewis and Brønsted) on the surface of these supports. In addition, to complete the study of the acidic and basic

properties of the supports and catalysts, CO_2-TPD experiments to measure the surface

basicity should be performed.
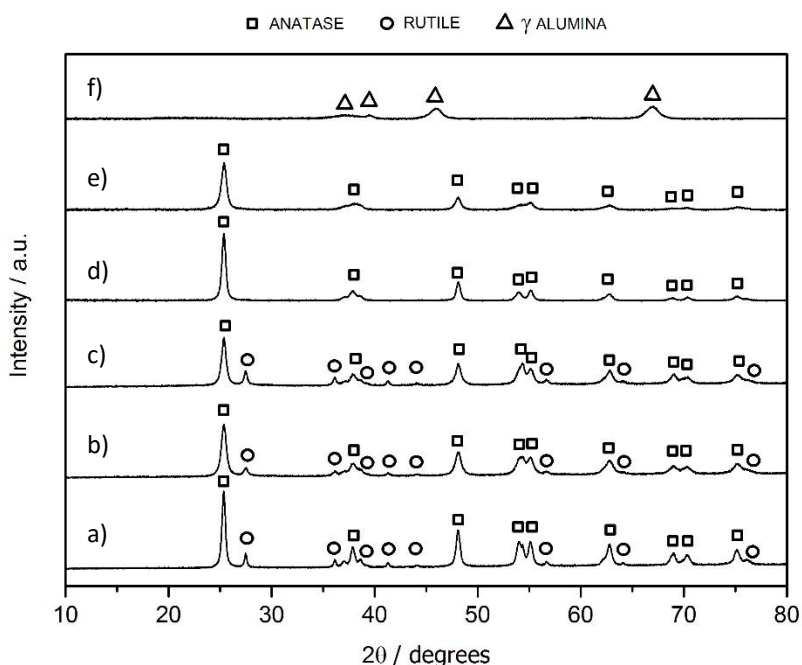
Figure 4.6. Powder X-Ray diffraction patterns of the supports:

a) TiO_2 (A-R), b) TiO_2-SiO_2 (5 mol % Si, A-R), c) TiO_2-SiO_2 (16 mol % Si, A-R),

d) TiO_2 (A), e) TiO_2-SiO_2 (10 mol % Si, A) and f) Al_2O_3-SiO_2 (10 mol % Al)

The X-Ray Diffraction (XRD) patterns of the supports are shown in Figure 4.6. As expected,

anatase and rutile crystalline phases are present in the TiO_2 (A-R) based supports and only

anatase is found in the TiO_2 (A) based supports. The main anatase (101) peak appears at

2θ of 25°, and that corresponding to rutile (110) appears at 27.4°. No SiO_2 diffraction peaks

are observed, which indicates that the silica exists in an amorphous phase. In pure SiO_2, the

amorphous structure has a characteristic wide peak at 2θ of around 23°. The relative

proportions of the crystalline titania phases in the biphase supports, calculated following

the JCPDS database, are approximately 80 % anatase and 20 % rutile, concordant with the

phase composition of the widely used TiO_2 P25 [46]. In the case of the Al_2O_3-SiO_2 support, the XRD pattern exhibits the characteristic peaks of γ-Al_2O_3, which is formed from well-ordered boehmite with diffraction peaks at 2θ of 37°, 39°, 45° and 66°.

The different titania phase composition (anatase- only and biphase anatase-rutile structure) of the supports was confirmed by Raman Spectroscopy, Figure 4.7. The characteristic peaks of the anatase phase are observed at 400, 520 and 650 cm^{-1}, the peak at 450 and the shoulder at 610 cm^{-1} are attributed to the rutile phase.
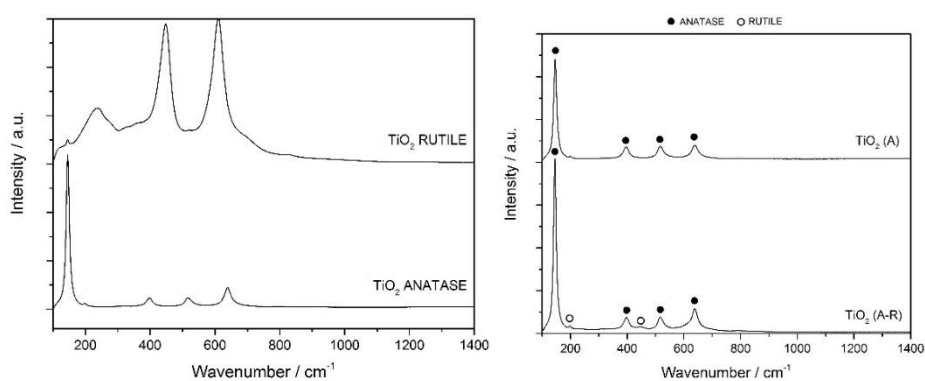
Figure 4.7. Raman spectra of the supports

Figure 4.8 shows representative scanning electron microscopy (SEM) images of the as-received supports. Significant variation in morphology is observed: anatase-rutile TiO_2 and Al_2O_3-SiO_2 supports are mainly formed by interconnected spheres, whilst anatase- only TiO_2 supports present a more compact aspect with large aggregates forming a "cloud-like" shape.

Particle size distribution of the supports measured by light scattering are shown in Table 4.3. These confirm the difference in metal oxide particle size between anatase-rutile and anatase- only supports, with D (0.5) = 40 μm for TiO_2 (A-R) and D (0.5) = 1.5 μm for TiO_2 (A).
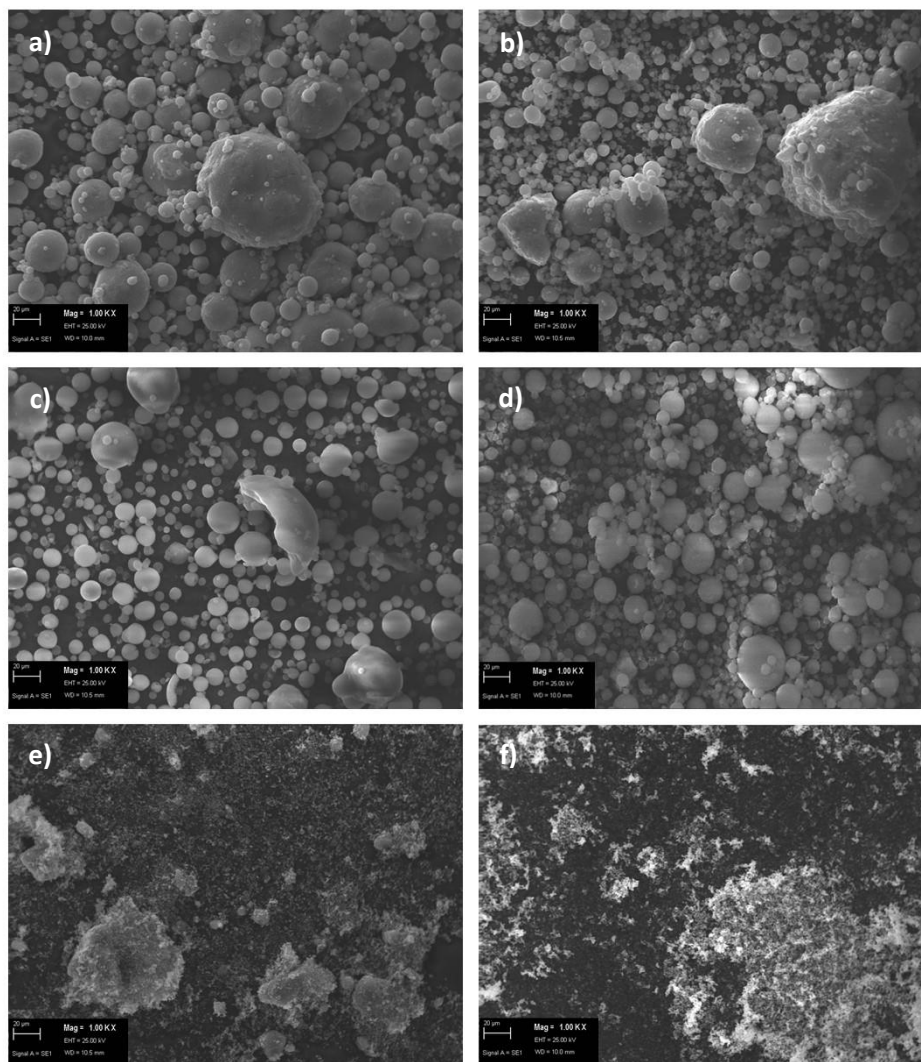
Figure 4.8. Selected scanning electron microscopy (SEM) images (SE1 detector) of the supports

a) TiO_2 (A-R), b) TiO_2-SiO_2 (5 mol % Si, A-R), c) TiO_2-SiO_2 (16 mol % Si, A-R),

d) Al_2O_3-SiO_2 (10 mol % Al), e) TiO_2 (A) and f) TiO_2-SiO_2 (10 mol % Si, A)

Figure 4.9 shows the XPS spectra in the O 1s region of the as-received supports. The

spectrum of anatase-rutile, TiO_2 (A-R), contains one peak appearing at 529.9 eV, which is

typical for TiO_2 molecules. Spectra of TiO_2-SiO_2 supports show two peaks; one appearing

at ≈ 530 eV, typical of TiO_2, and another peak at ≈ 532 eV, typical of SiO_2 [47]. The relative

heights indicate that, as expected, the SiO_2 peak intensity increases with the SiO_2 content

of the support. Notice that the spectrum for the anatase- only TiO_2 (A) support indicates the presence of a shoulder centred at ≈ 532 eV, this peak can be assigned to SiO_2 but also to the surface adsorbed hydroxyl group (Ti-OH) [48] [49].
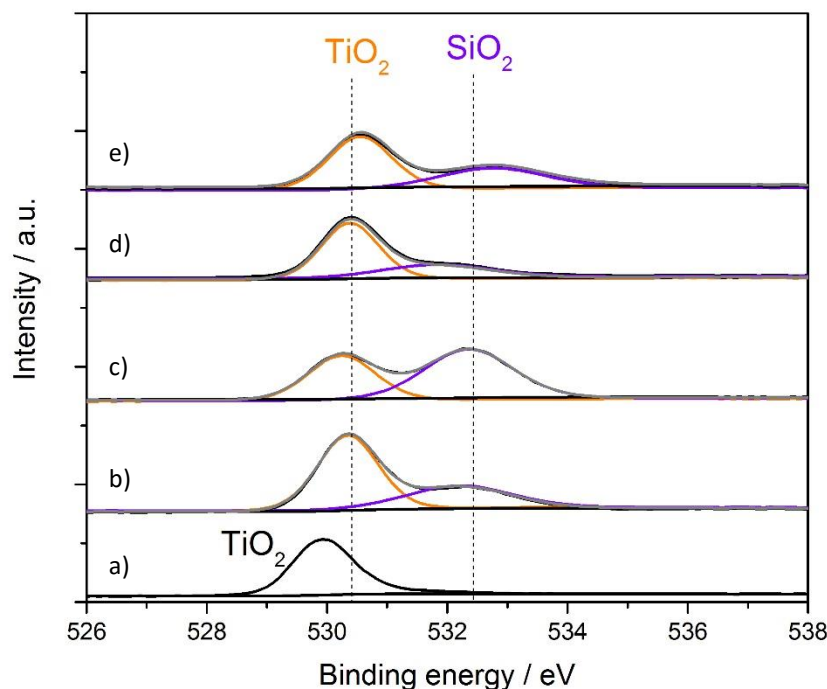
Figure 4.9. XPS spectra in the O 1S binding energy region of the fresh supports:

a) TiO_2 (A-R), b) TiO_2-SiO_2 (5 mol % Si, A-R), c) TiO_2-SiO_2 (16 mol % Si, A-R),

d) TiO_2 (A), e) TiO_2-SiO_2 (10 mol % Si, A)

Figure 4.10 shows the XPS spectra in the O 1s and Si 2p region of the titania supports: TiO_2 P25, TiO_2 (A-R) and TiO_2 (A). Whilst only one oxygen environment, associated with the TiO_2, is found for the anatase-rutile support, two different oxygen environments are present for the anatase- only titania and commercial TiO_2 P25 supports. These results suggest the presence of a small amount of SiO_2 in TiO_2 P25 and TiO_2 (A) and correlate with the XPS spectra in the Si 2p binding energy region.
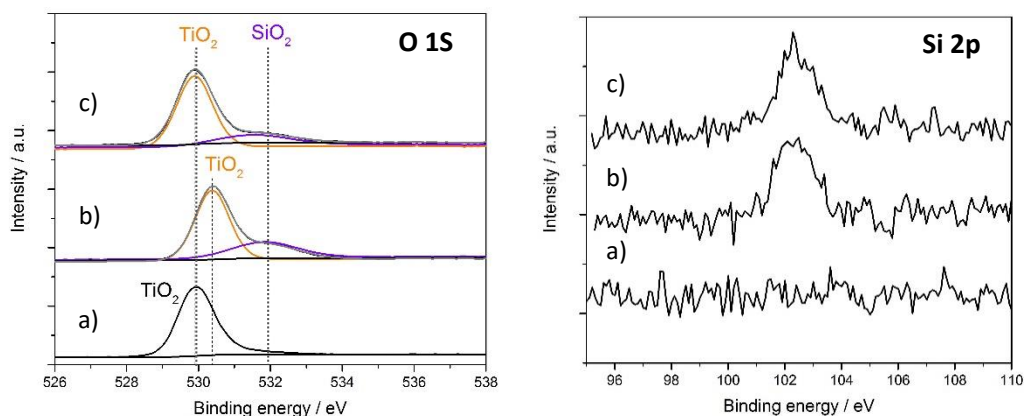
Figure 4.10. XPS spectra in the O 1S and Si 2p binding energy region of the titania supports:

a) TiO_2 (A-R)   b) TiO_2 (A)   c) TiO_2 P25

Quantitative analysis of the supports obtained from the XPS spectra is presented in Table 4.4. The surface silicon composition correlates with the theoretical loading provided by the support supplier. Note that in the case of the TiO_2 (A) support, the surface silicon represents approximately 2.5 wt. % of the total composition. This is similar to that of the TiO_2 P25, which presents 2 wt % silicon.

Table 4.4. Quantitative analysis of the supported platinum catalysts obtained from the XPS spectra

Catalyst	Ti		Al		Si		O	
	At %	Wt. %	At %	Wt. %	At %	Wt. %	At %	Wt. %
TiO_2 (A-R)	32.01	58.49	0	0	0	0	67.99	41.51
TiO_2-SiO_2 (5 % mol Si, A-R)	24.30	47.41	0	0	6.57	7.52	69.13	45.07
TiO_2-SiO_2 (16 % mol Si, A-R)	14.41	30.80	0	0	14.89	18.68	70.70	50.52
TiO_2 (A)	28.58	53.90	0	0	2.29	2.53	69.13	43.57
TiO_2-SiO_2 (10 % mol Si, A)	19.93	47.33	0	0	10.27	12.22	69.80	47.33
Al_2O_3-SiO_2 (10 mol % Si)	0	0	0.72	7.20	18.92	27.14	80.36	65.66

Signals in the W 4d region are observed for the anatase- only TiO_2-SiO_2 (10 % mol Si, A) support, Appendix A. This result is exclusive to this support. TEM imaging coupled with EDX confirms the presence of tungsten in this support, with quantitative analysis showing that tungsten accounts 7 wt. % of the support composition.
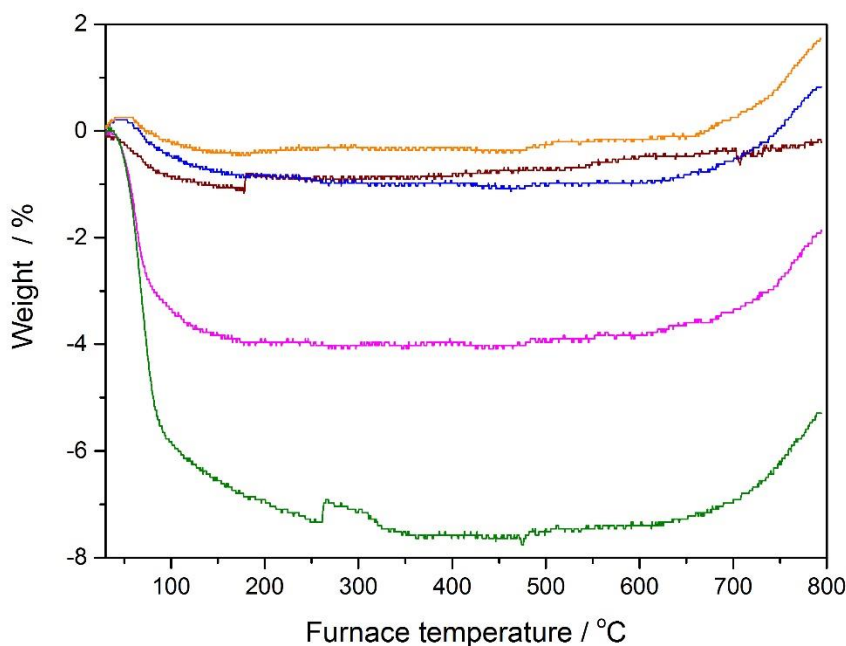
(---) TiO_2 (A-R)   **(---)** TiO_2-SiO_2 (5 % mol Si, A-R)   **(---)** TiO_2-SiO_2 (16 % mol Si, A-R)

(---) TiO_2 (A-R)   **(---)** TiO_2-SiO_2 (5 % mol Si, A-R)

Figure 4.11. TG curves of the supports

Thermogravimetric (TG) analyses of the supports are presented in Figure 4.11. TG curves show a weight loss below 100 °C, corresponding to a broad endothermic peak assigned to desorption of surface water. The weight loss is lower than 1 % for the anatase-rutile based supports, whilst TiO_2 (A) and TiO_2-SiO_2 (10 % mol Si, A) show a weight loss of 4 % and 6 % respectively. This indicates that anatase-based supports may be more hydrophilic. A discrete increase in weight of ≈ 2 % at temperatures above 650 °C is observed for all the

supports, very likely due to solid-state transformations of anatase to rutile. *In situ* XRD analysis should be performed to support these observations.

The effect of these mixed metal oxide supports on propane oxidation over platinum catalysts under oxidising atmosphere was studied.

Many studies [12 50 51] have confirmed that metal oxide supports present negligible intrinsic activity for propane oxidation and that, although the metal-support interaction plays a crucial role in the performance, the active phase is the noble metal. Therefore, catalytic tests were performed using the supported platinum catalysts but not the blank supports.

■ 1 wt. % Pt/TiO_2 (A-R)   ▼ 1 wt. % Pt/TiO_2-SiO_2 (5 % mol Si, A-R)

▲ 1 wt. % Pt/TiO_2-SiO_2 (16 % mol Si, A-R)

Figure 4.12. Total oxidation of propane over supported platinum catalysts

Reaction conditions: Flow reactor, GHSV = 50,000 h^{-1}, C_3H_8:O_2 = 1:50

Catalysts prepared by non-aqueous impregnation and calcined at 400 ºC in static air

Figure 4.12 shows the platinum catalysts to be active for the total oxidation of propane to CO_2 and H_2O. Propane conversion as a function of reaction temperature varied with the nature of the support material. For the 1 wt. % platinum catalysts supported on anatase-rutile TiO_2 based supports, the propane oxidation activity increases in the sequence: Pt/TiO_2 (A-R) < Pt/TiO_2 -SiO_2 (5 mol % Si, A-R) < Pt/TiO_2 -SiO_2 (16 mol % Si, A-R). Therefore, the catalytic activity is found to be promoted by the SiO_2 content of the support. The Pt/TiO_2 (A-R) system (T_{50} = 357 °C) presents comparable catalytic activity to platinum supported on commercial TiO_2 P25 (T_{50} = 379 °C),

It has been shown that catalytic activity is enhanced through using a combination of titania and silica as the support for platinum catalysts. This enhancement of activity is not the result of the additive effect of Pt/TiO_2 and Pt/SiO_2, since the activity of Pt/SiO_2 catalysts for propane oxidation is very low, indeed they are almost inactive at 350 °C. This suggests that there is a synergistic effect between TiO_2 and SiO_2 for the catalytic oxidation of propane over supported platinum catalysts.

In order to understand the interaction of TiO_2 with SiO_2 in further detail, a new support was prepared by physical mixing of the TiO_2 (A-R) and the TiO_2 (A-R)-SiO_2 support resulting in a MIX support with *ca*. 12 mol % of Si. Total oxidation of propane results for the platinum catalyst prepared using this MIX support (grey curve) and using the chemically prepared TiO_2-SiO_2 supports are presented in Figure 4.13. Although platinum supported on the TiO_2+TiO_2-SiO_2 MIX support presents favourable performance to that supported on pure TiO_2 (A-R), the catalyst prepared using the chemically mixed TiO_2-SiO_2 support is still more active than either. This suggests that the enhancement in activity is the result of a synergistic effect and interaction between TiO_2 and SiO_2 which forms during the chemical preparation of the mixed metal oxides supports.

■   1 wt. % Pt/TiO_2 (A-R)   ▲   1 wt. % Pt/TiO_2-SiO_2 (16 % mol Si, A-R)

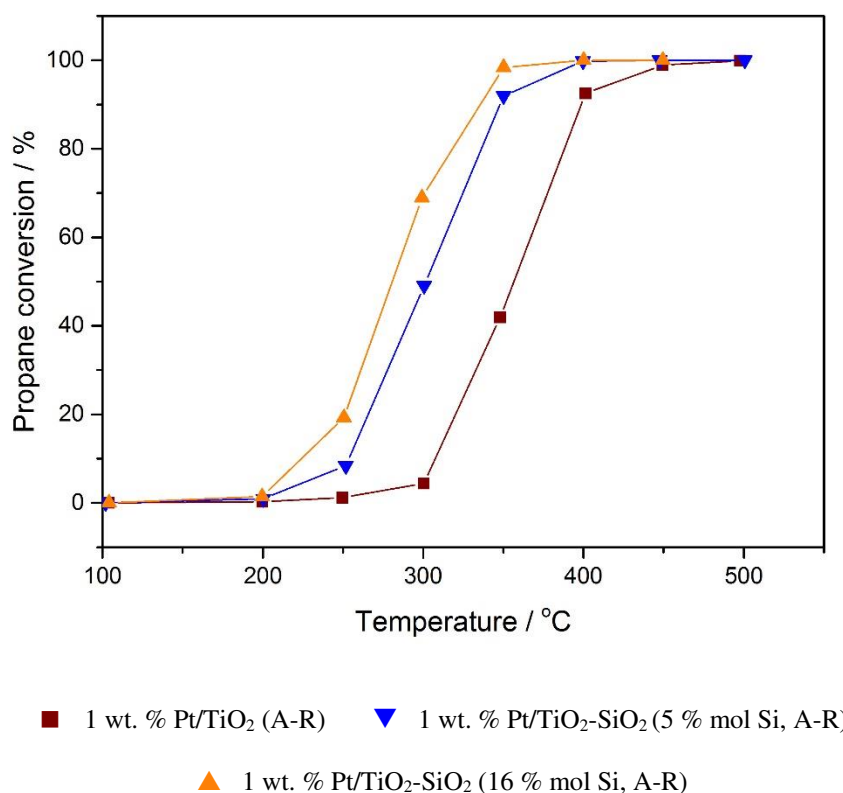◄   1 wt. % Pt/TiO_2 + TiO_2-SiO_2 (12 % mol Si, A-R) MIX

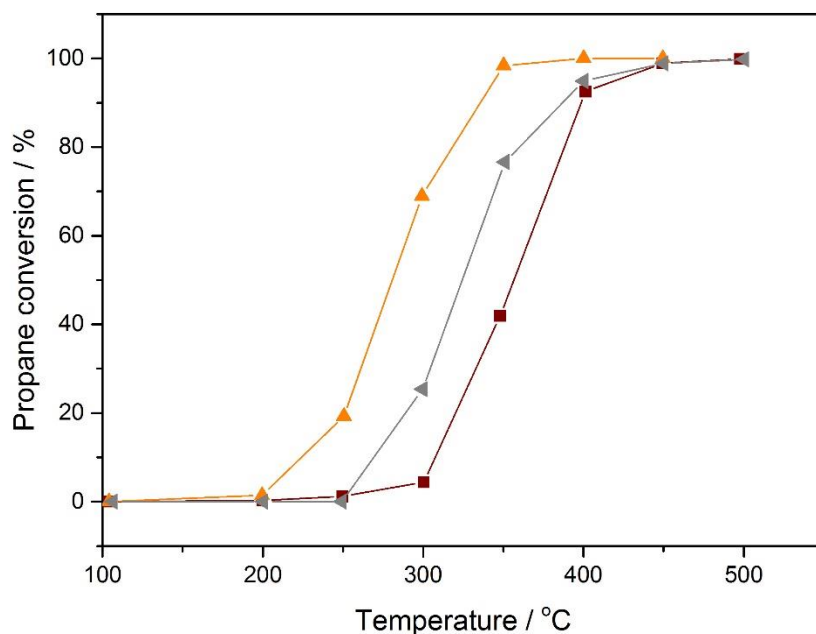**Figure 4.13** Total oxidation of propane over supported platinum catalysts

Reaction conditions: Flow reactor, GHSV = 50,000 h^{-1}, C_3H_8:O_2 = 1:50

Catalysts prepared by non-aqueous impregnation and calcined at 400 ºC in static air

Stability tests over the most representative catalysts were performed at low conversion such that the reaction was kinetically controlled. Figure 4.14 shows the conversion of propane as a function of reaction time over 1 wt. % Pt/TiO_2 (A-R) at 350 °C and 1 wt. % Pt/TiO_2-SiO_2 (16 % mol Si, A-R) at 250 °C. After 10 hours, the rate of propane conversion reaches a steady state and no deactivation was observed during *ca.* 50 h on line.
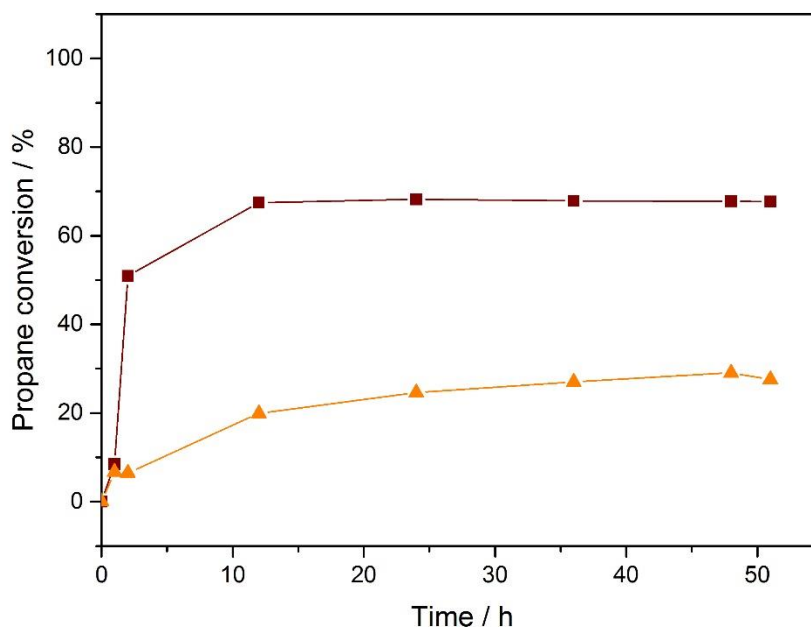
■ 1 wt. % Pt/TiO$_2$ (A-R) at **350 °C**   ▲ 1 wt. % Pt/TiO$_2$-SiO$_2$ (16 % mol Si, A-R) at **250 °C**

Figure 4.14. Total oxidation of propane as a function of time over supported platinum catalysts

Reaction conditions: Flow reactor, GHSV = 50,000 h^{-1}, C$_3$H$_8$:O$_2$ = 1:50

Catalysts prepared by non-aqueous impregnation and calcined at 400 ºC in static air

It should be noted that in Figure 4.14, 1 wt. % Pt/TiO$_2$ (A-R) shows higher propane conversion than 1 wt. % Pt/TiO$_2$-SiO$_2$ (A-R), whilst the opposite was shown in Figure 4.13. This is because the time on-line curve for 1 wt. % Pt/TiO$_2$ (A-R) was carried out at a higher temperature of 350 °C, as this catalyst showed negligible propane conversion at 250 °C in Figure 4.13. Although up to 10 hours were required to reach a steady state for both catalysts, they present different activity profiles. At steady state, 1 wt. % Pt/TiO$_2$ (A-R) showed *ca.* 68 % propane conversion (at 350 ºC, Figure 4.14). This differs significantly from the 42 % propane conversion which was observed at the same temperature in the light off curve in Figure 4.13 On the other hand, the degree of propane conversion observed at steady state

over 1 wt. % Pt/TiO_2-SiO_2 (A-R) (at 250 ^{o}C) is consistent with Figure 4.12, at *ca*. 20 %. Stability tests at the same temperature for each of the catalysts should be performed.

Reaction rates and turnover frequency (TOF) of propane oxidation were calculated from the conversion-time curves. Turnover frequencies for the platinum catalysts were calculated by dividing the reaction rate ($\mu mol_{propane}$ / ($g_{catalyst}$·s)) by propane uptake ($\mu mol_{propane}$/ $g_{catalyst}$). The turnover frequency of 1 wt. % Pt/TiO_2-SiO_2 (16 % mol Si, A-R) at 250 °C is 77.12 mol_{C3H8}·mol_{Pt}^{-1}·h^{-1}.

● 1 wt. % Pt/TiO_2 (A)   ★ 1 wt. % Pt/TiO_2-SiO_2 (10 % mol Si, A)

Figure 4.15. Total oxidation of propane over supported platinum catalysts

Reaction conditions: Flow reactor, GHSV = 50,000 h^{-1}, C_3H_8:O_2 = 1:50

Catalysts prepared by non-aqueous impregnation and calcined at 400 ^{o}C in static air

Light-off curves for propane oxidation over the anatase- only TiO_2 based platinum catalysts are shown in Figure 4.15.

In contrast to the results previously presented for mixed phase TiO_2 (A-R) catalysts, the introduction of 10 % mol of SiO_2 into TiO_2 (A) does not result in a major change in catalytic activity. In fact, catalytic activity is comparable to that of the most active TiO_2 (A-R) catalysts studied (1 wt. % Pt/TiO_2-SiO_2 (16 % mol Si, A-R)).

It is worthwhile to compare the activity of platinum supported on different titania supports (with no SiO_2 content). As presented in Figure 4.16, 1 wt. % Pt/TiO_2 (A) (pink curve) showed excellent activity for the total oxidation of propane. This was much higher than that of 1 wt. % Pt/TiO_2 (A-R) (red curve) and similar to that of the most active catalyst studied in the previous section, 1 wt. % Pt/TiO_2-SiO_2 (16 % mol Si, A-R). TiO_2 (A) exhibits a higher surface area, 1.5 times that of TiO_2 (A-R), and it is well known that a higher support surface area favours the reaction, improving the dispersion of platinum and the extent of reactant adsorption. In order to determine the degree which the support crystalline phase composition and surface area affects the reaction, 1 wt. % Pt catalysts were prepared using commercially available 100 % anatase TiO_2 (55 m^2/g surface area) and 100 % rutile TiO_2 (2 m^2/g surface area). Propane oxidation results over these catalysts are shown in Figure 4.16. As reported previously in the literature [19], the activity of Pt/TiO_2 (100 % anatase) is comparable with the activity of Pt/TiO_2 (100 % rutile) at low conversions and slightly higher at conversions over 20 %, which implies that the observed significant enhancement of Pt activity in TiO_2 (A) is not, to a great extent, due to the crystalline phase and surface area of the titania support. The pore structure of the support is equally important because the distribution of the pores may affect conversion by impeding diffusion of reactants and products throughout the porous medium. Accordingly, studies to analyse the pore size distribution of the bare supports and the platinum catalysts would be needed.

   ■ 1 wt. % Pt/TiO$_2$ (A-R)   ● 1 wt. % Pt/TiO$_2$ (A)

□ 1 wt. % Pt /TiO$_2$ (100 % RUTILE)   ○ 1 wt. % Pt /TiO$_2$ (100 % ANATASE)
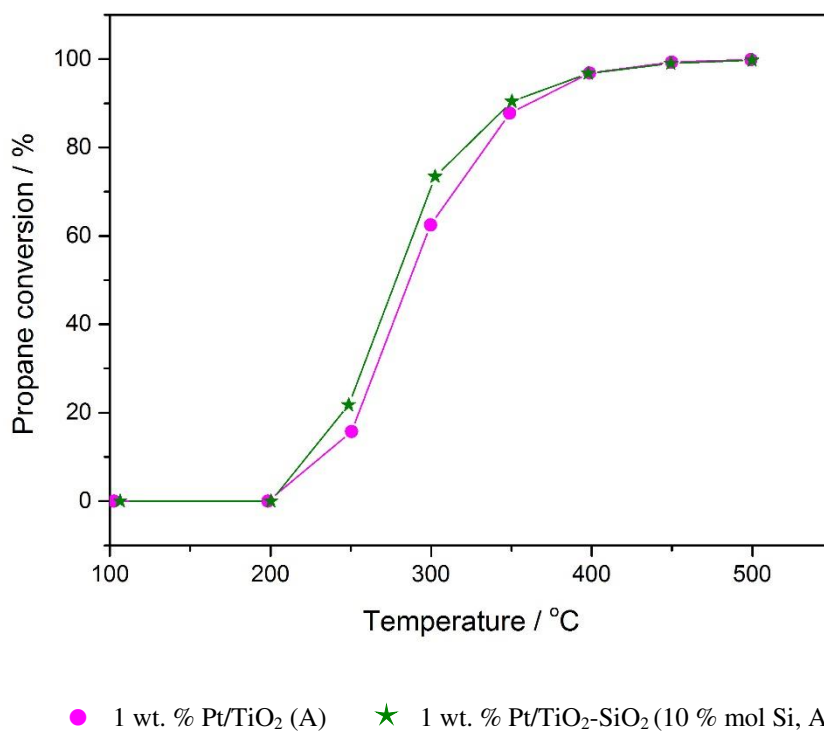
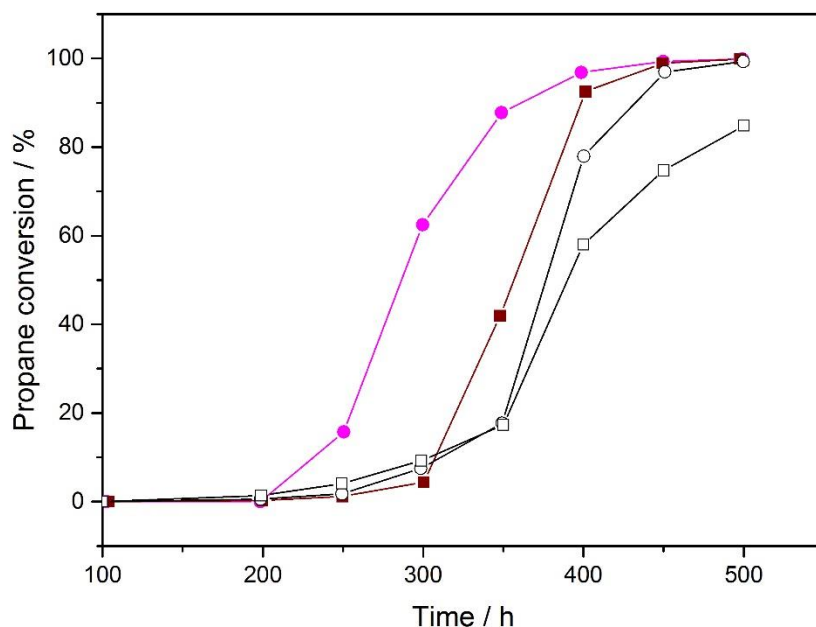**Figure 4.16.** Total oxidation of propane over supported platinum catalysts

Reaction conditions: Flow reactor, GHSV = 50,000 h^{-1}, C$_3$H$_8$:O$_2$ = 1:50

Catalysts prepared by non-aqueous impregnation and calcined at 400 ºC in static air

The performance of the platinum catalysts for total oxidation of propane improves considerably with the addition of SiO$_2$ to the TiO$_2$ (A-R) support. The same effect is found with the addition of SiO$_2$ to Al$_2$O$_3$, as shown in Figure 4.17. 1 wt. % Pt/Al$_2$O$_3$-SiO$_2$ (violet curve) is much more active than 1 wt. % Pt/Al$_2$O$_3$ (black curve), with up to 50 % higher conversion of propane, and presents similar activity to the 1 wt. % Pt/TiO$_2$-SiO$_2$ (5 % mol Si, A-R) catalyst (Figure 4.12).
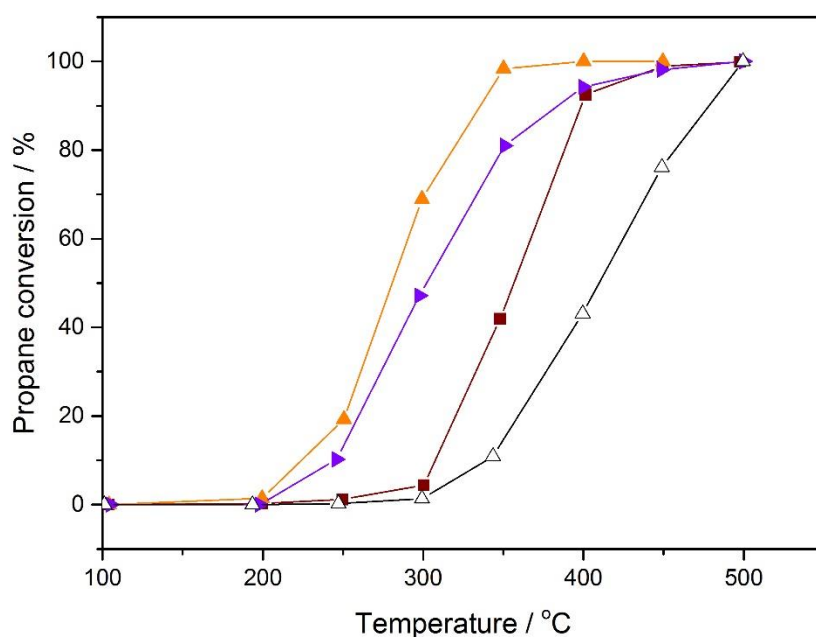
Figure 4.17. Total oxidation of propane over supported platinum catalysts

Reaction conditions: Flow reactor, GHSV = 50,000 h^{-1}, C_3H_8:O_2 = 1:50

Catalysts prepared by non-aqueous impregnation and calcined at 400 ºC in static air

A summary of the catalytic activity, where T_{10} and T_{50} are the reaction temperatures at which 10 % and 50 % propane conversion was achieved, is presented in Figure 4.18. Of the supported 1 wt. % platinum catalysts studied, the propane oxidation activity follows the sequence:

Pt/TiO$_2$ (A-R)   <   Pt/TiO$_2$-SiO$_2$ (5 %, A-R) ≈ Pt/Al$_2$O$_3$-SiO$_2$ (10 %)   <   Pt/TiO$_2$ (A)

<   Pt/TiO$_2$-SiO$_2$ (16 %, A-R) ≈ Pt /TiO$_2$-SiO$_2$ (10 %, A)
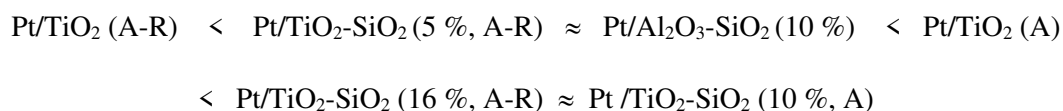
The catalytic activity is found to increase considerably with increasing SiO_2 content in the TiO_2 (A-R) support, the shift of the T_{50} towards lower temperatures exceeds 70 ºC when the SiO_2 content reaches 16 % mol. Platinum supported on anatase- only TiO_2 is more active than that supported on biphase anatase-rutile TiO_2 with T_{50} shifted 65 ºC towards lower temperatures. Platinum supported on SiO_2-Al_2O_3 presents similar activity to the 1 wt. % Pt/TiO_2-SiO_2 (5 % mol Si, A-R) catalyst, with T_{50} shifted towards lower temperatures by 55 ºC when compared with the TiO_2 (A-R) catalyst. These differences in conversion temperatures (50 – 70 ºC) are significant and represent a major energy saving as, under real conditions, DOCs require the heating of great amounts of air to function.

Figure 4.18. Temperature in degrees Celsius for 10 % propane conversion (T_{10}) and 50 % propane conversion (T_{50}) over supported platinum catalysts (1 wt. % Pt) prepared by non-aqueous impregnation and calcined at 400 ºC in static air

These results agree with those obtained in previous studies [9] [52], where catalytic activity for propane oxidation under an oxidising atmosphere was found to increase considerably with

an increase in SiO_2 content of TiO_2 based supports. Kobayashi *et al*. reported a T_{50} of 250 ºC when 2 wt. % of platinum was supported on TiO_2-SiO_2 (20 % mol Si). Yazawa *et al*. reported a T_{50} of 257 ºC when 2 wt. % of platinum was supported on SiO_2-Al_2O_3 (13 % mol Al).

■   1 wt. % Pt/TiO_2 (A-R)   ▲   1 wt. % Pt/TiO_2-SiO_2 (16 % mol Si, A-R)
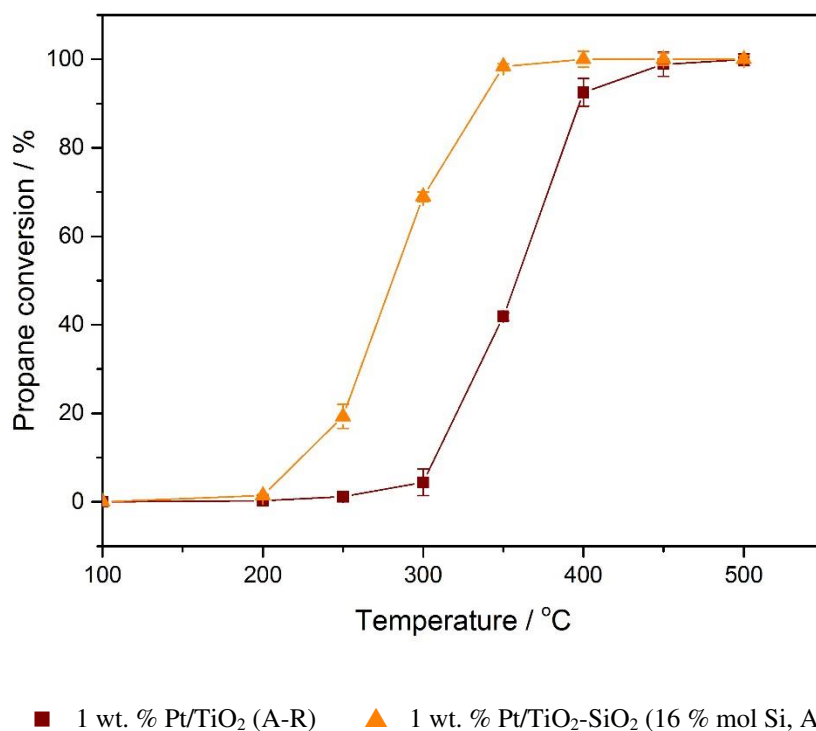
Figure 4.19. Total oxidation of propane over supported platinum catalysts with reaction error bars

Reaction conditions: Flow reactor, GHSV = 50,000 h^{-1}, C_3H_8:O_2 = 1:50

Catalysts prepared by non-aqueous impregnation and calcined at 400 ºC in static air

To quantify the error associated with the testing methodology, two catalysts (1 wt.% Pt/TiO_2 (A-R) and 1 wt. % Pt/TiO_2-SiO_2 (16 % mol Si, A-R)) were tested twice, with the standard error shown in Figure 4.19. Whilst the testing error (Figure 4.19) is negligible, the errors associated with the preparation of the platinum catalysts are considerable, as shown in Figure 4.20. Although catalytic activity always follows the same trend, increasing with the SiO_2 content of the support, Figure 4.20 shows the error bars

obtained by testing the same catalyst prepared in different batches under the same conditions. Reproducibility of catalyst performance was difficult, especially in the case of platinum supported on TiO_2 (A-R) which showed an error in propane conversion of up to 60 % depending on the temperature.
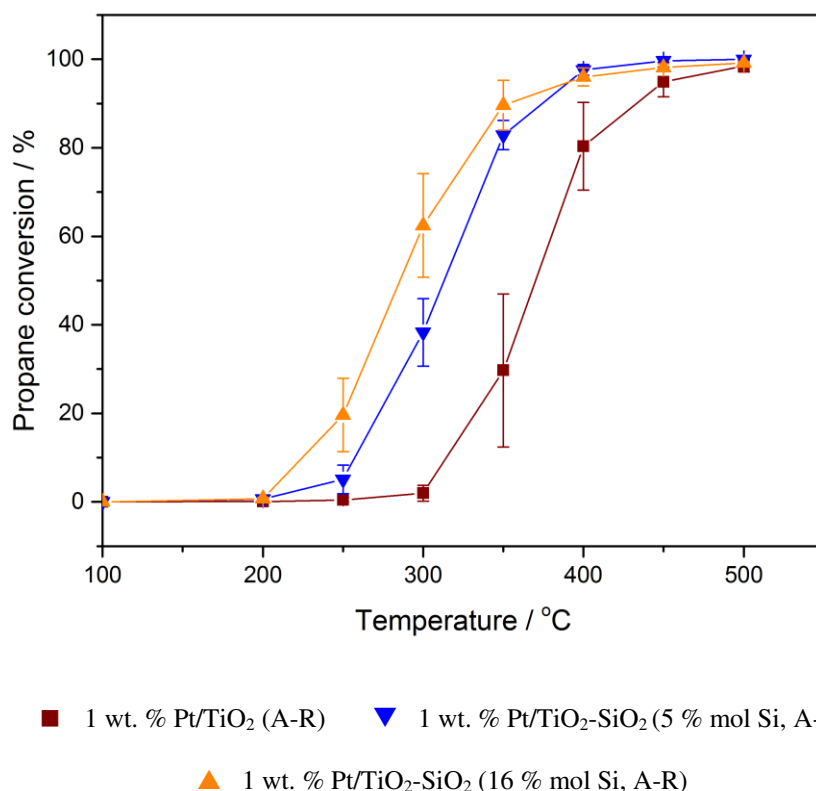
Figure 4.20. Total oxidation of propane over supported platinum catalysts, preparation error bars

Reaction conditions: Flow reactor, GHSV = 50,000 h^{-1}, C_3H_8:O_2 = 1:50

Catalysts prepared by non-aqueous impregnation and calcined at 400 ºC in static air

The effect of Pt loading on catalyst performance was investigated. Figure 4.21 compares the performance of supported platinum catalysts of various platinum loadings (0.5, 1 and 1.5 wt %). As expected, the catalytic activity for total oxidation of propane is, in general, enhanced with increasing platinum loading. This is the case for all the catalysts except

Pt/TiO_2 (A). An increase in the platinum content from 1 wt. % to 1.5 wt. % does not have a significant effect in the catalytic activity when supported on anatase- only TiO_2, and even decreases slightly. This could be due to sintering of platinum particles at higher loadings.
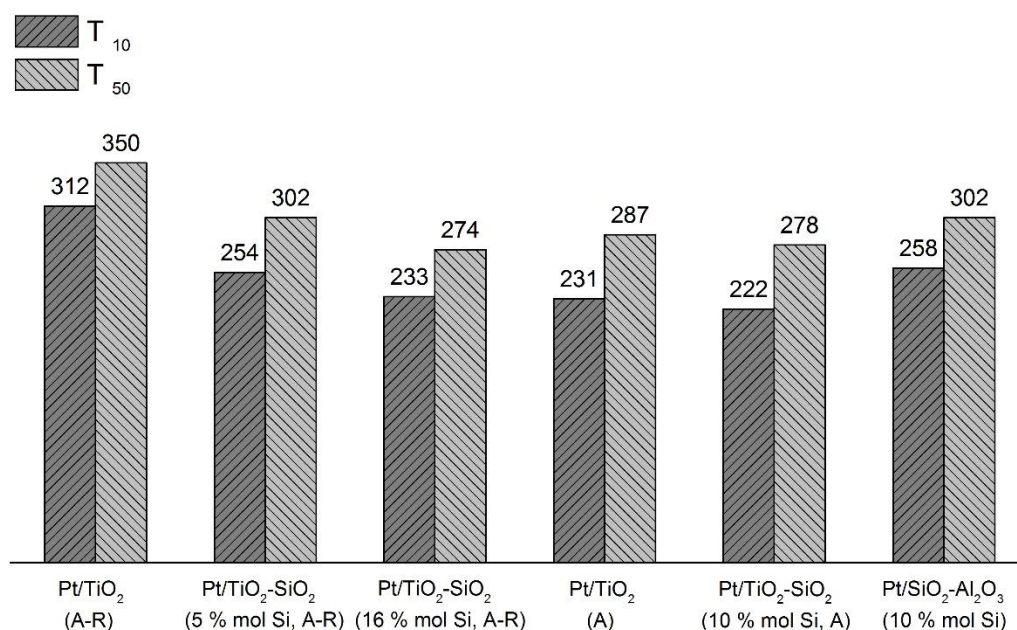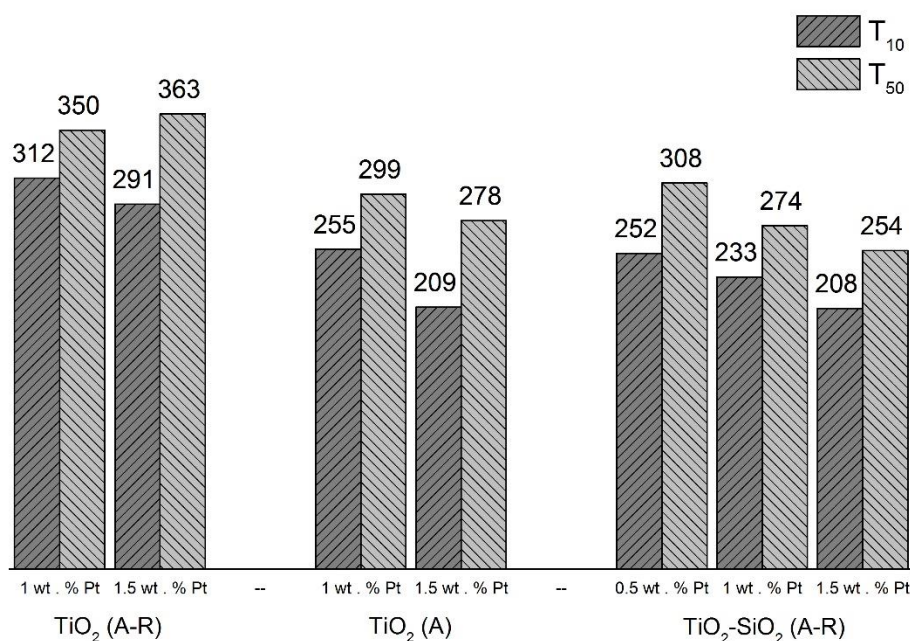

Figure 4.21. Temperature in degrees Celsius for 10 % propane conversion (T_{10}) and 50 % propane conversion (T_{50}) over supported platinum catalysts (different platinum loadings) prepared by non-aqueous impregnation and calcined at 400 ºC in static air

Many studies have focused on identifying differences on the oxidation properties of platinum catalysts and correlate these with the catalytic activity for propane oxidation. In order to understand how the support varies the activity of the catalyst, the effect of the TiO_2 and TiO_2-SiO_2 mixed supports on the structural and electronic properties of platinum was studied.

As listed in Table 4.5, and, compared to the bare supports surface areas decrease after the impregnation of platinum. This is in agreement with the literature [16, 32, 53]. Deposition of 1 wt. % Pt on the TiO_2 (A-R) and TiO_2 (A) based supports results in 1-6 % reduction of the BET surface area.

Table 4.5. Physicochemical properties of the supported platinum catalysts

Catalyst	Surface area (m²/g) [a]	Density (g/mL)	Pt Av. Crystallite size (Å)[b]	Pt Dispersion (%)[b]	Pt surface area (m²/g) [b]
1 wt. % Pt/TiO₂ (A-R)	50	0.55	24	47	1.2
1 wt. % Pt/TiO₂-SiO₂ (5 % mol Si, A-R)	83	0.45	69	16	0.4
1 wt. % Pt/TiO₂-SiO₂ (16 % mol Si, A-R)	71	0.40	n.d	n.d	n.d
1 wt. % Pt/TiO₂ (A)	75	0.55	46	25	0.6
1 wt. % Pt/TiO₂-SiO₂ (10 % mol Si, A)	96	0.45	94	12	0.3
1 wt. % Pt/Al₂O₃-SiO₂ (10 mol % Si)	222	0.25	17	66	1.6

[a] Surface area measured by N_2 physisorption, density

[b] CO chemisorption. Pretreatment: 300^0C, 2 h, H_2. CO chemisorption performed at room temperature using 77 μL pulses of CO. Sample mass used *ca*. 500 mg

Based on the CO Chemisorption data in Table 4.5, higher contents of SiO_2 in the support (shown to lead to more active catalysts) give rise to larger Pt particles and a lower degree of dispersion. An adsorption stoichiometry of Pt/CO = 1 was assumed. The least active

catalyst, 1 wt. % Pt/TiO_2 (A-R), displays the highest dispersion (≈ 47 %) and the smallest crystallite size among the TiO_2-SiO_2 based catalysts. It is worth pointing out that these results are inconsistent with those obtained from microscopy and should be considered carefully for the following reasons; whilst platinum supported on TiO_2 presents the typical CO uptake, platinum on supports containing SiO_2 present a "u-shaped" CO uptake indicating possible reduction of the catalyst by the CO, Appendix B. Calculations based in the "u-shaped" CO uptake can therefore lead to incorrect dispersion values.

FTIR spectra of the 1 wt. % Pt/TiO_2 (A-R) and 1 wt. % Pt/TiO_2-SiO_2 (16 % mol Si, A-R) are shown in Figure 4.22. The bands centred at 1620 cm^{-1} and 3350 cm^{-1} correspond to the bending and stretching vibrational modes of the hydroxyl groups, characteristic of surface-adsorbed water. The sharp peaks at 3700 cm^{-1} and 3750 cm^{-1} are characteristic of Ti-OH and Si-OH coordination vacancies [54]. Several weak peaks associated with vibrational modes of TiO_2 are observed in the region between 500 and 800 cm^{-1}. For the TiO_2 (A-R) spectrum, the band observed at 925 cm^{-1} is associated with the stretching and bending vibration modes of the Ti-O-Ti bonds. For the TiO_2-SiO_2 spectrum, the band observed at 970 cm^{-1} is associated with Si-O-Ti vibration [35, 55, 47, 38] and the two strong bands at 1100 cm^{-1} and 860 cm^{-1} are associated with asymmetric and symmetric Si-O-Si stretching vibrations [13, 35, 54, 55, 13, 38]. The FTIR spectrum of 1 wt. % Pt/TiO_2-SiO_2 shows the hydroxyl species specific to pure TiO_2 and SiO_2, indicating that the addition of SiO_2 to TiO_2 does not alter the type of hydroxyl sites significantly.

(---) 1 wt. % Pt/TiO$_2$ (A-R)   (---) 1 wt. % Pt/TiO$_2$-SiO$_2$ (16 % mol Si, A-R)
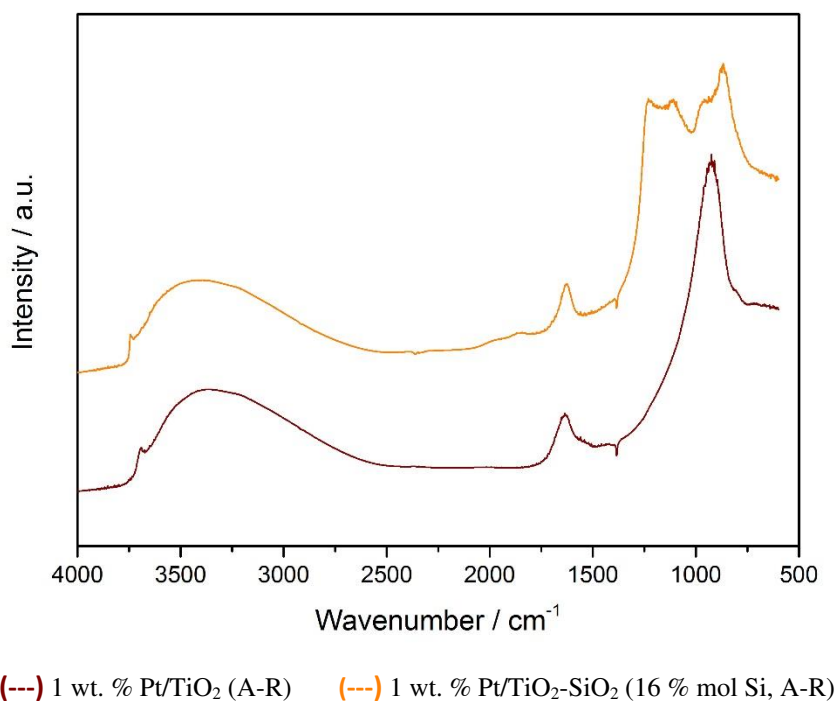
Figure 4.22. DRIFT spectra of the supported Pt catalysts

Figure 4.23 shows the IR spectra of CO chemisorbed onto the surface of these catalysts. The band in the region of 2150-2200 cm^{-1} is assigned to gaseous CO. Three overlapping bands at 2030, 2050 and 2080 cm^{-1} are observed with both catalysts, and can be assigned to linear CO adsorbed on platinum (Pt^0) terrace and step sites and on partially oxidised platinum (Pt$^{\delta+}$) sites [56] [32] [57] [58]. Although the analysis is only qualitative, it is possible to compare the relative intensity of the bands. The relative intensity of the band for CO associated with oxidised platinum sites (2080 cm^{-1}) is higher on 1 wt. % Pt/TiO$_2$ (A-R), indicating that platinum species on this support are more electron-deficient. The broad band at 1840 cm^{-1} is attributed to bridging CO adsorbed on Pt^0 particles [53], for which the relative intensity is much lower for 1 wt. % Pt/TiO$_2$–SiO$_2$ than on 1 wt.% Pt/TiO$_2$ (A-R).

(---) 1 wt. % Pt/TiO$_2$ (A-R)   (---) 1 wt. % Pt/TiO$_2$-SiO$_2$ (16 % mol Si, A-R)
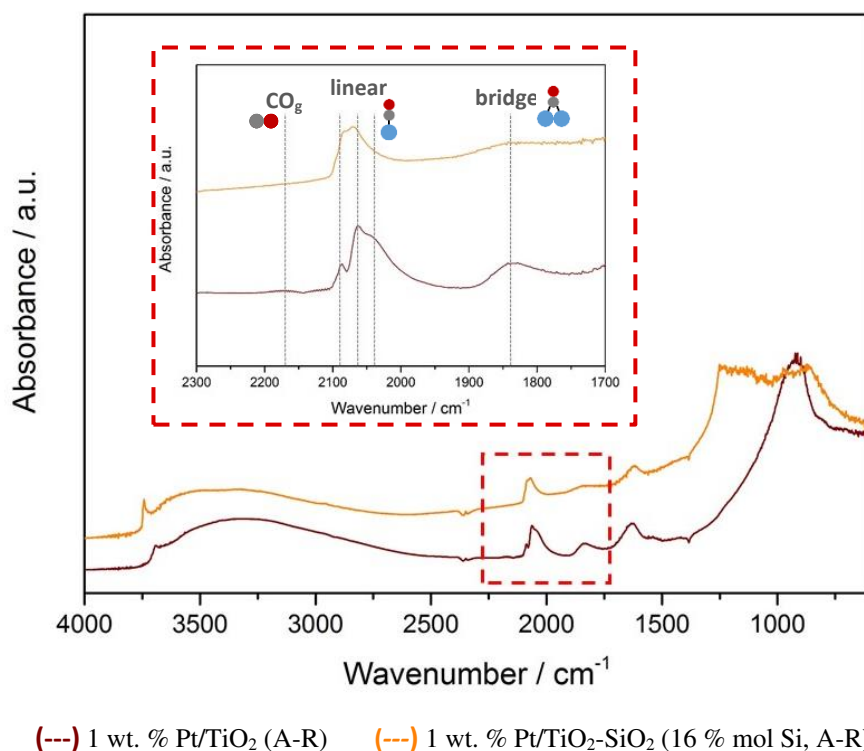
Figure 4.23. DRIFT spectra of CO adsorption at 25 °C on Pt/TiO$_2$ and Pt/TiO$_2$-SiO$_2$ after reducing with 10% H$_2$ in N$_2$ at 300 °C

From the DRIFTS results it can be concluded that CO chemisorption occurs in both catalysts studied and that more reducible Pt$^{\delta+}$ species are found on the Pt/TiO$_2$ (A-R) catalyst. This correlates with the results obtained for the CO chemisorption pulse studies, which showed that PtO is the predominant species on the TiO$_2$ (A-R) support, with Pt^{2+} not completely reduced by H$_2$ during the pretreatment. This platinum may be reduced by CO during the first pulses.

The surface state of the catalysts was investigated by XPS. Figure 4.24 shows the Pt 4f region of XPS spectra of the supported platinum catalysts.
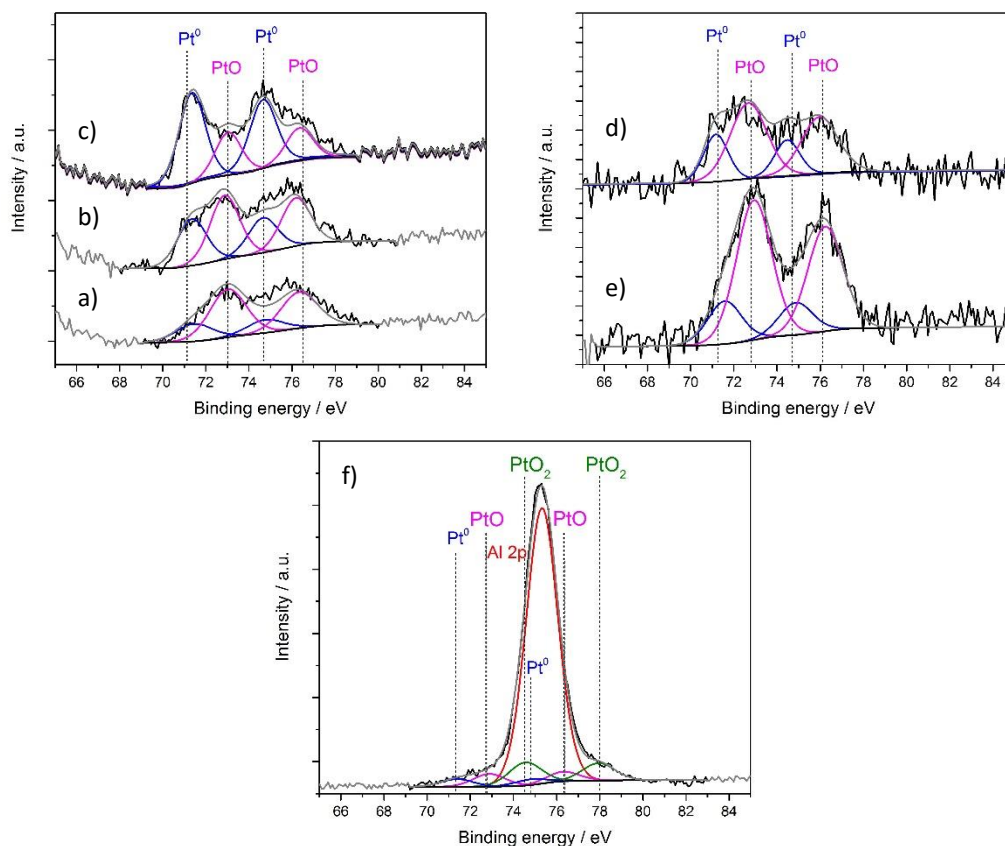
Figure 4.24. XPS spectra in the Pt 4f binding energy region of the 1 wt. % platinum catalysts

a) Pt/TiO$_2$ (A-R), b) Pt/TiO$_2$-SiO$_2$ (5 mol % Si, A-R), c) Pt/TiO$_2$-SiO$_2$ (16 mol % Si, A-R),

d) Pt/TiO$_2$ (A), e) Pt/TiO$_2$-SiO$_2$ (10 mol % Si, A) and f) Pt/ SiO$_2$-Al$_2$O$_3$ (10 % mol Si)

The spectra can be fitted with two or three pairs of overlapping Gaussian-Lorentzian curves. The Pt 4f7/2 and Pt 4f5/2 lines appearing at 71.4 eV and 74.7 eV are attributed to metallic platinum (Pt^0). The second pair appearing at 72.9 eV and 76.3 eV is assigned to platinum (II) oxide (PtO) and the third pair appearing at 74.6 eV and 77.9 eV is assigned to platinum (IV) oxide (PtO$_2$). In the figure, the relative heights indicate that metallic platinum is favoured, in general, with increasing SiO$_2$ content and that platinum oxide is predominant in both titania materials, TiO$_2$ (A) and TiO$_2$ (A-R). These results agree with

those obtained in previous work [9], which showed that the oxidation-resistance of platinum is significantly enhanced by addition of SiO_2 to the TiO_2 support.

Table 4.6. Quantitative analysis of the supported platinum catalysts obtained from the XPS spectra

Catalyst	Pt		Pt^0	Pt^{2+}	Pt^{4+}
	At %	Wt. %	Conc. %	Conc. %	Conc. %
1 wt. % Pt/TiO$_2$ (A-R)	0.42	3.07	26.70	73.30	0
1 wt. % Pt/TiO$_2$-SiO$_2$ (5 % mol Si, A-R)	0.26	2.03	42.09	57.90	0
1 wt. % Pt/TiO$_2$-SiO$_2$ (16 % mol Si, A-R)	0.23	1.93	67.49	32.52	0
1 wt. % Pt/TiO$_2$ (A)	0.18	1.36	30.03	69.97	0
1 wt. % Pt/TiO$_2$-SiO$_2$ (10 % mol Si, A)	0.22	1.82	22.65	77.35	0
1 wt. % Pt/Al$_2$O$_3$-SiO$_2$ (10 mol % Si)	0.01	0.13	45.83	32.29	21.88

Nevertheless, XPS analysis (not shown here) reveals that metallic platinum is the predominant species in all the 1.5 wt. % supported platinum catalysts.

Characteristic X-ray diffraction planes of platinum appear at 2θ of 39° (111), 46° (200) and 67° (220) [59]. However, as reported in previous studies [53], the absence of diffraction lines corresponding to platinum within the XRDs of the supported platinum catalysts in Appendix C, indicates that the relatively low loading of platinum is highly dispersed, with a small average particle size. Therefore, it was not possible to calculate the average size of platinum particles from XRD using the Debye-Scherrer equation.

To confirm the high dispersion of Pt over the support surface, the size and crystalline structure of the catalysts was analysed using microscopy imaging experiments coupled with EDX analysis. Many areas of the samples were analysed, and representative images are shown in Figure 4.25.

Selected SEM micrographs of the supported platinum catalysts are presented in Figure 4.25 and Figure 4.26. Whereas the BET surface area of Pt catalysts is comparable with that of the bare supports, the morphology and particle size distribution of 1 wt. % Pt/TiO$_2$ (A-R), but not that of 1 wt. % Pt/TiO$_2$ (A), changes following impregnation of platinum and calcination. For 1 wt. % Pt/TiO$_2$ (A-R), irregular agglomerates with a large window size range of 2 - 120 μm are formed.
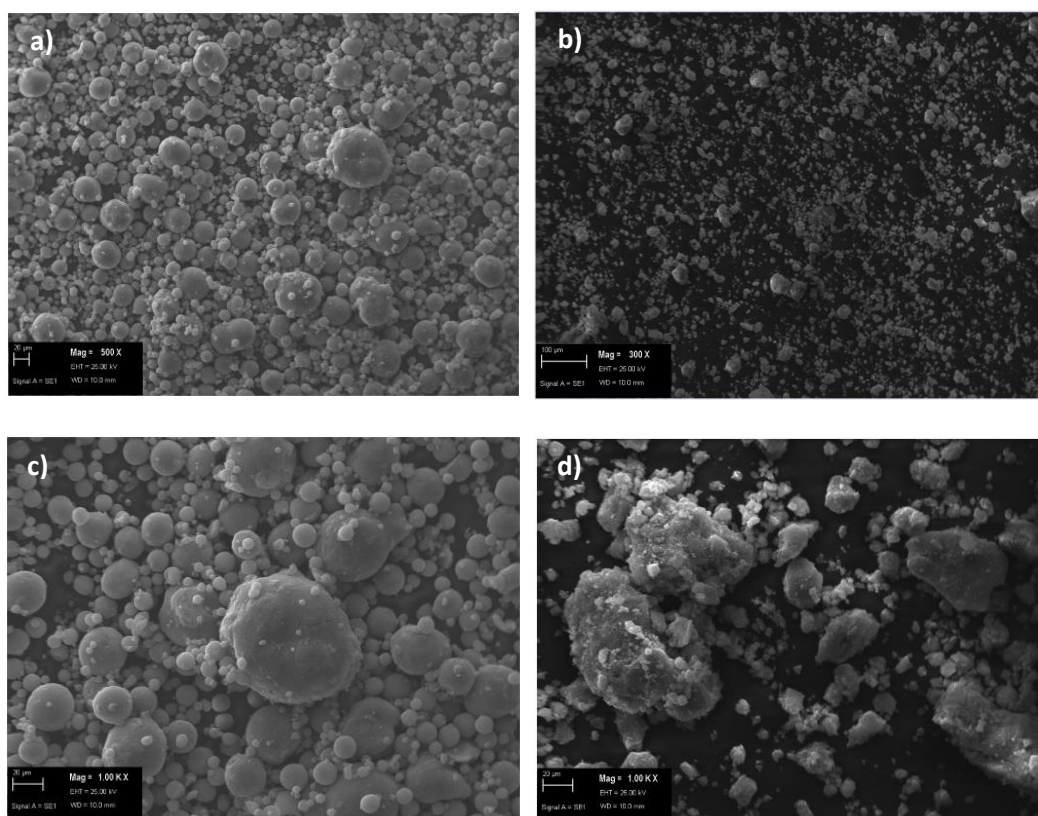
Figure 4.25 SEM images of the TiO$_2$ (A-R) support

a), c) before impregnation and b), d) after impregnation and calcination

The presence of large particles (2-6 μm) with bright contrast, corresponding to PtO, heterogeneously distributed over this support is confirmed by Energy-dispersive X-ray spectroscopy (EDX) in Figure 4.26. The large oblong platinum- containing clusters observed over this support are completely absent over the TiO_2-SiO_2 supports.
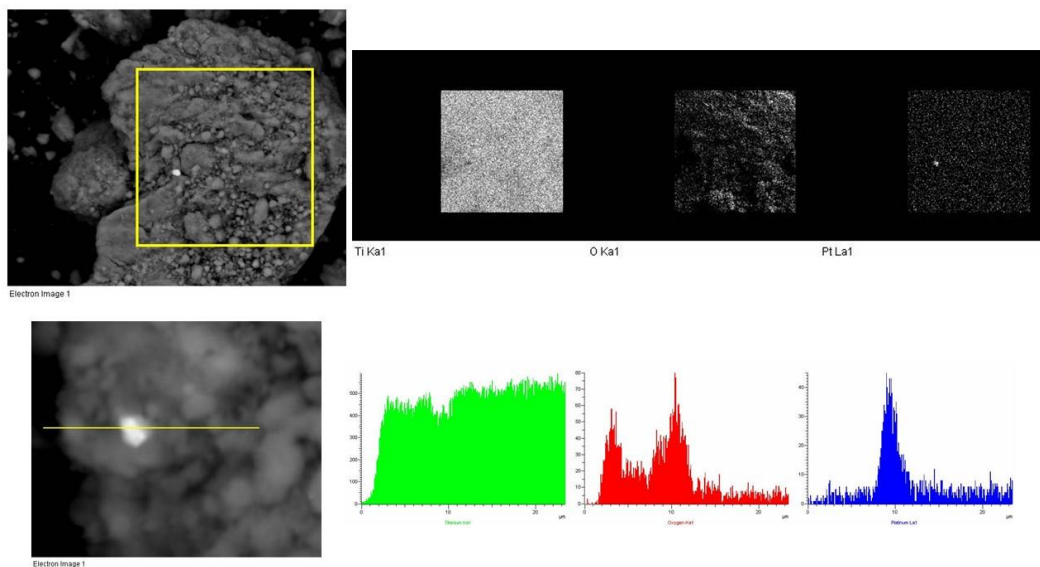
Figure 4.26 Selected SEM images and an EDX map and line scan of the 1 wt. % Pt/TiO_2 (A-R) catalyst

Figures 4.27 and 4.28 show high-resolution transmission electron microscopy (HRTEM) images of 1 wt. % Pt/TiO_2 (A-R) and 1 wt. % Pt/TiO_2-SiO_2 (16 % mol Si, A-R) following calcination at 400 °C in static air. On the TiO_2-SiO_2 (A-R) support, figure 4.28, small segregated Pt particles (dark coloured spherical particles) with a particle size of ≈ 2-5 nm are observed. On the other hand, platinum particles are rarely observed on the surface of the TiO_2 (A-R) support in figure 4.27, though some with a particle size of *ca*. 10 nm are identified by STEM images and EDX analysis.
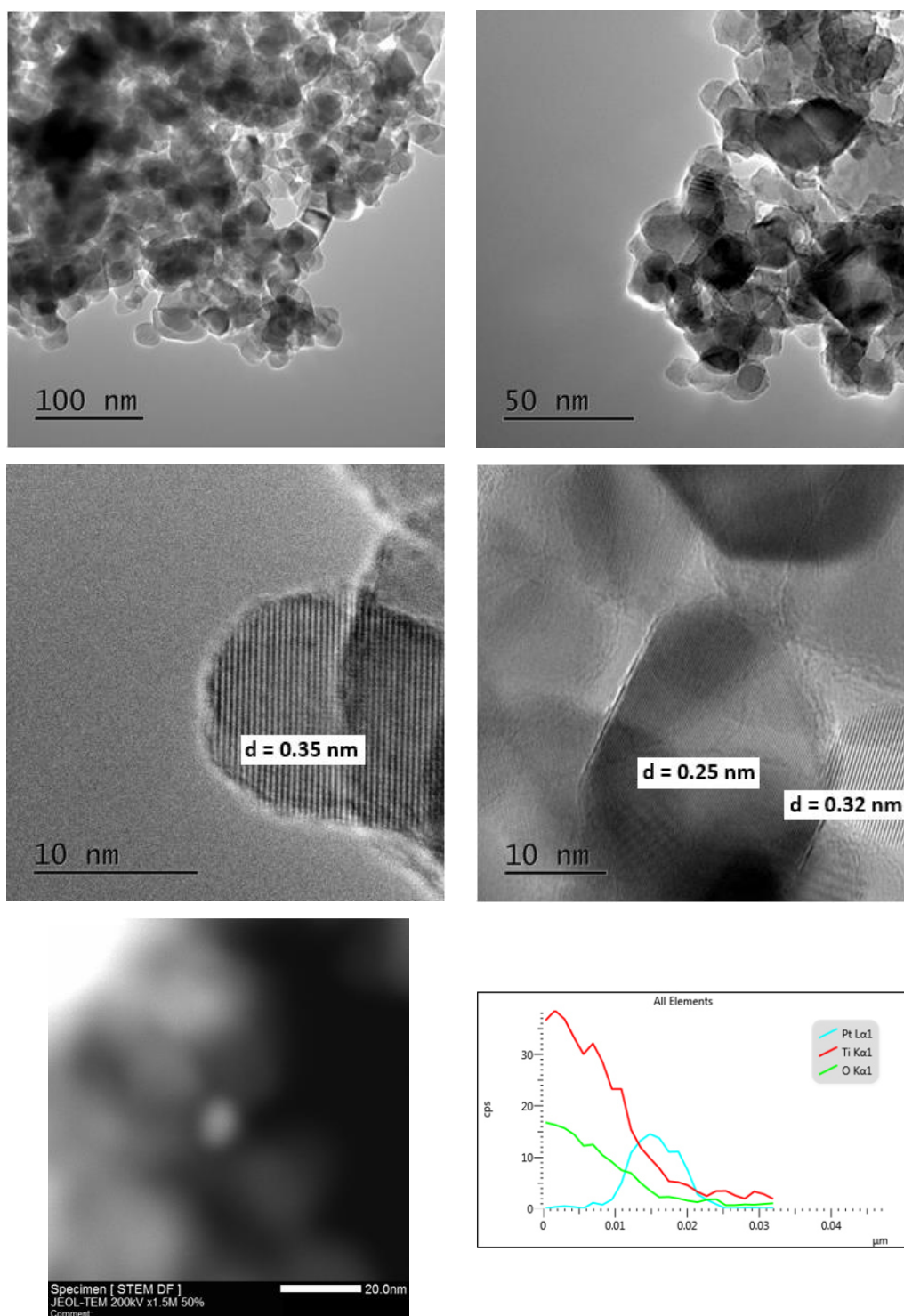
Figure 4.27. Selected HRTEM and STEM images and an EDX line scan of the

1 wt. % Pt/TiO$_2$ (A-R) catalyst
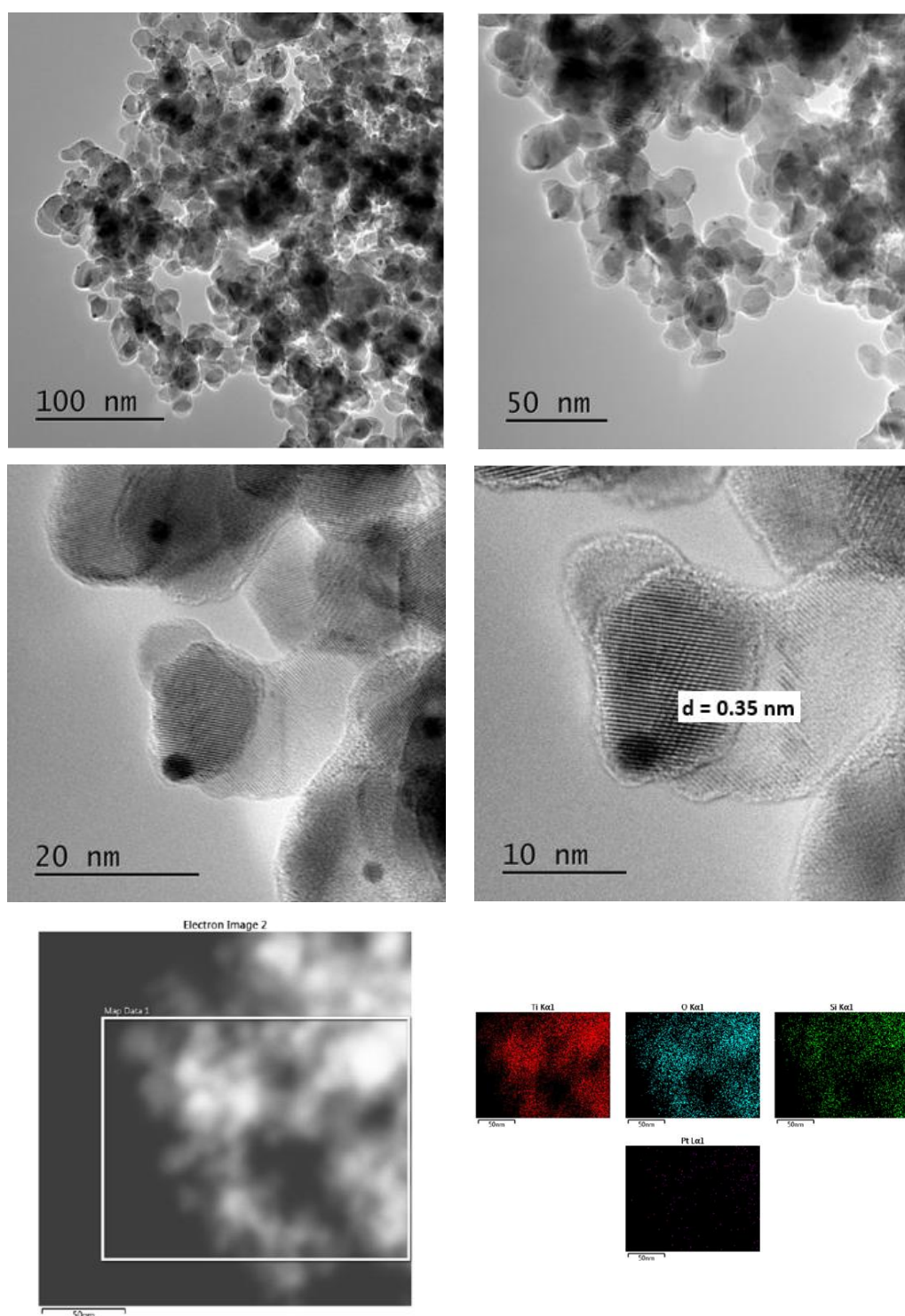
Figure 4.28. Representative HRTEM and STEM and EDX map scan of the

1 wt. % Pt/TiO$_2$-SiO$_2$ (16 % mol Si, A-R) catalyst

In such Z-contrast images, due to the higher atomic mass of Pt compared with Ti, Si and O, the metallic particles can be clearly identified as they display a high degree of contrast against the support. Although the STEM images do not allow clear discrimination between Pt and PtO particles, imaging coupled with EDX analysis provides complementary information to identify the metallic and oxide particles.

Titania consists of aggregated primary particles formed of aggregates. Aggregates of 30 μm and 1.5 μm are observed for the anatase and anatase-rutile phases respectively, whilst the primary particles have a mean diameter of *ca*. 20 nm. As shown in Figure 4.27, the lattice spacing measurements confirm the presence of anatase ((101), d = 0.35 nm) and rutile ((101), d = 0.25 nm, (110), d = 0.32 nm) [60][61], in accordance with XRD and Raman results in Figures 4.6 and 4.7.

After analysing multiples areas on 1 wt. % Pt/TiO_2-SiO_2 (5 % mol Si, A-R) and 1 wt. % Pt/TiO_2-SiO_2 (16 % mol Si, A-R), the resulting particle size distribution is presented in Figure 4.29. The majority of the distribution falls into the 1.5 - 3.5 nm size range and some minor extent particles with a lower population in the 0 - 1 nm and 4 - 7 nm ranges.

TEM images indicate that the platinum dispersion increases and particle size decreases notably with the addition of SiO_2 to the support. This data contrasts with the particle size obtained from the CO Chemisorption experiments in Table 4.5, in which the addition of SiO_2 to the TiO_2 support tends to decrease the dispersion of platinum particles.

This correlates with previous work that concluded that using a mixed metal oxide support, such as TiO_2-SiO_2 improves the dispersion of platinum and other metal/metal oxides by enhancing the interaction between the nanoparticles and the support [59][62][63][64].
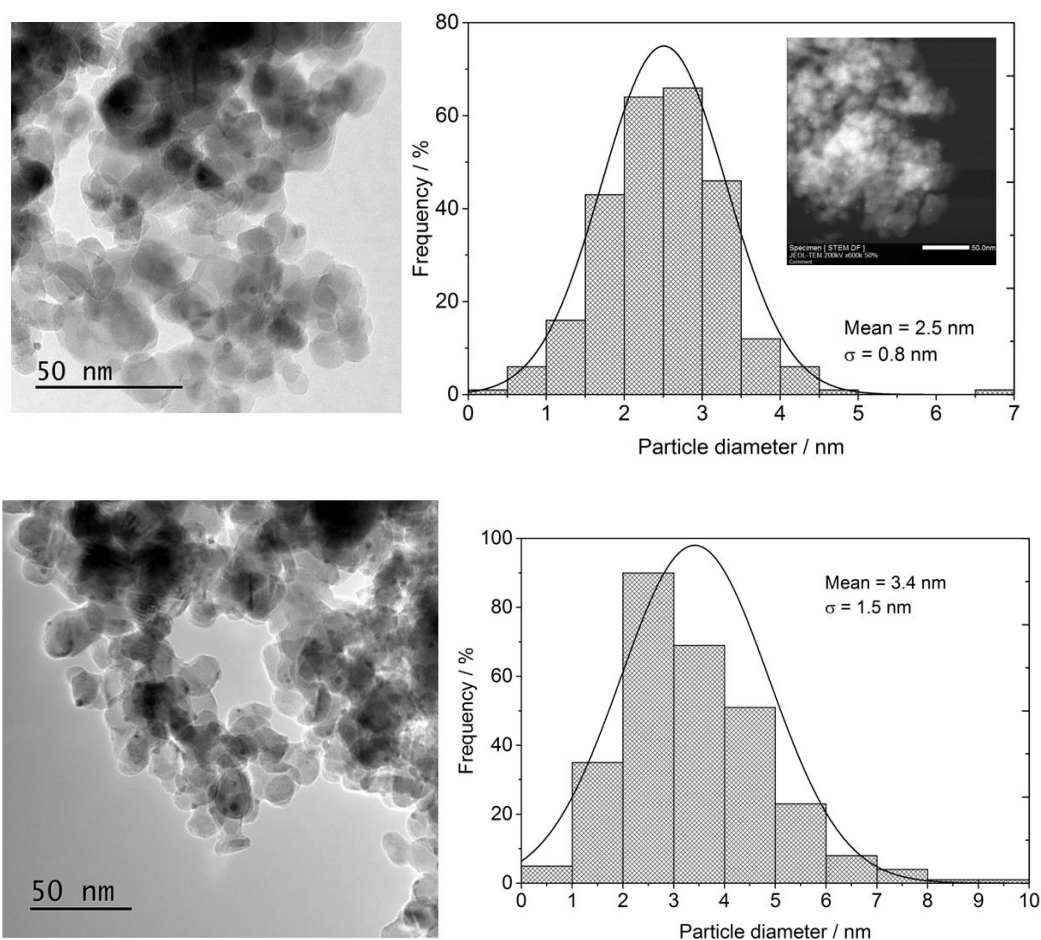
Figure 4.29. Selected HRTEM and STEM images and platinum particle size distribution

a) 1 wt. % Pt/TiO$_2$-SiO$_2$ (5 mol % Si, A-R) and b) 1 wt. % Pt/TiO$_2$-SiO$_2$ (16 mol % Si, A-R)

Representative HRTEM and STEM images from 1 wt. % Pt/TiO$_2$ (A) are shown in Figure 4.30. In this sample, some particles with size of 4 - 8 nm are observed. The dispersion of the platinum is somewhat enhanced when supported on anatase- only titania instead of anatase-rutile titania.

HRTEM images in Figure 4.31 show the presence of numerous dark spherical particles smaller than 1 nm which could be attributed to platinum particles. This supposition cannot be confirmed by STEM as the particles do not show high image contrast against the support. This is potentially due to the small particle size.
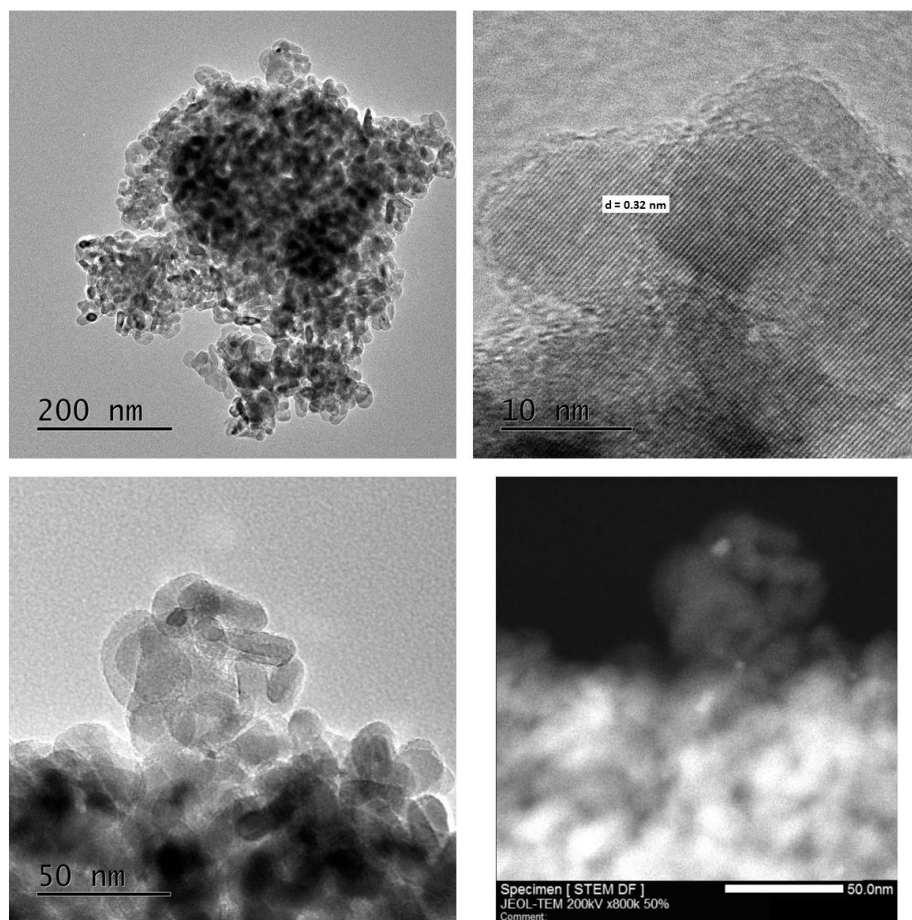
Figure 4.30. Selected HRTEM and STEM images of the 1 wt. % Pt/TiO$_2$ (A) catalyst
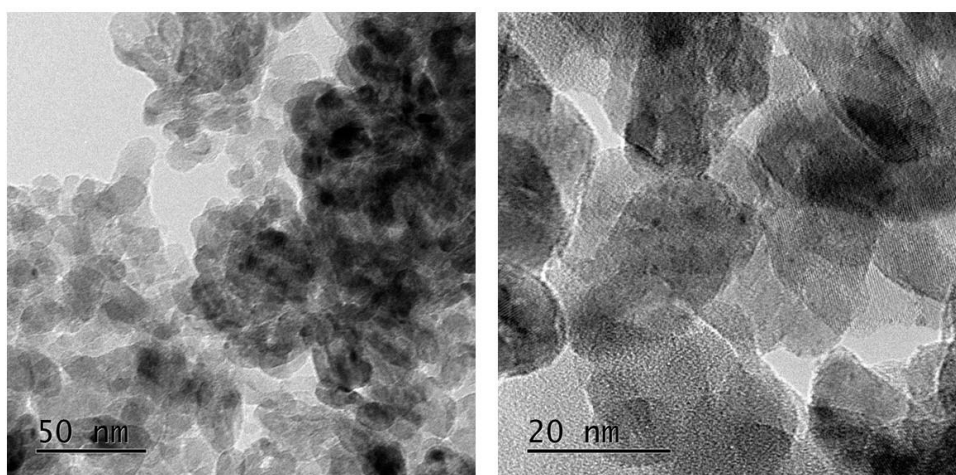
Figure 4.31. Selected HRTEM images of the 1 wt. % Pt/TiO$_2$-SiO$_2$ (10 % mol Si, A-R) catalyst

Figure 4.32 shows that the platinum is evenly distributed on the SiO_2-Al_2O_3 support with a particle size range of 1 - 3 nm.
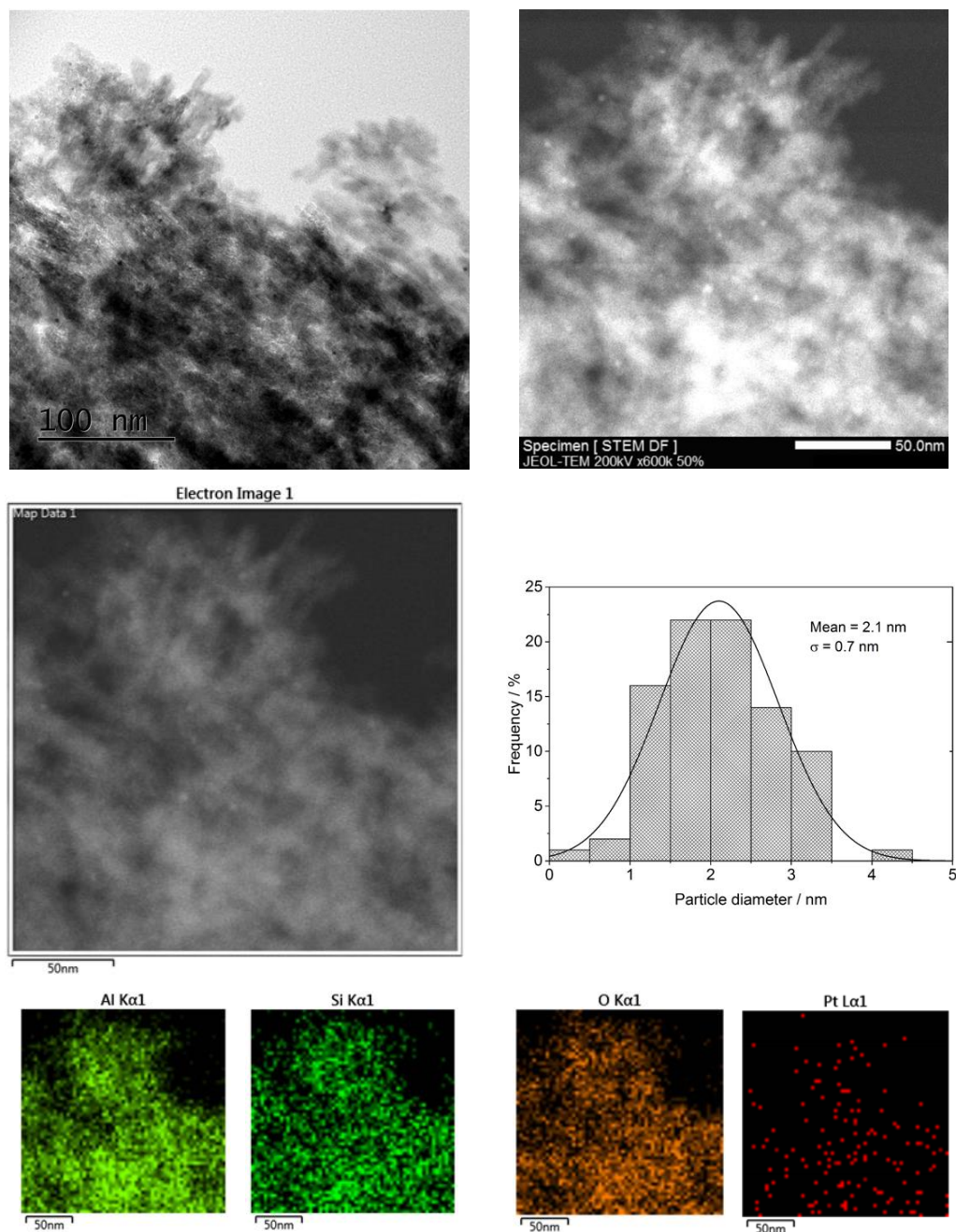
Figure 4.32. Selected HRTEM and STEM images, EDX map scan and platinum particle size distribution of the 1 wt. % Pt/SiO_2-Al_2O_3 (10 % mol Si)

Quantitative analysis obtained from different techniques; XPS and microscopy coupled with EDX, is presented in Table 4.7.

Table 4.7. Quantitative analysis of the supported platinum catalysts obtained from the XPS spectra and from the SEM and TEM imaging coupled with EDX

Catalyst		Ti wt. %	Al wt. %	Si wt. %	O wt. %	Pt wt. %
1 wt. % Pt/TiO$_2$ (A-R)	XPS	55.46	0	0	41.51	3.07
	SEM-EDX	50,04	0	0	49.28	0.68
	TEM-EDX	X	X	X	X	X
1 wt. % Pt/TiO$_2$-SiO$_2$ (5 % mol Si, A-R)	XPS	46.52	0	6.97	44.48	2.03
	SEM-EDX	X	X	X	X	X
	TEM-EDX	56.01	0	2.68	40.46	0.85
1 wt. % Pt/TiO$_2$-SiO$_2$ (16 % mol Si, A-R)	XPS	30.60	0	18.27	49.20	1.93
	SEM-EDX	48.90	0	8.19	41.98	0.93
	TEM-EDX	50.20	0	7.16	41.67	0.98
1 wt. % Pt/TiO$_2$ (A)	XPS	52.80	0	2.32	43.52	1.36
	SEM-EDX	58.87	0	0.32	39.69	1.12
	TEM-EDX	54.28	0	4.12	40.95	0.65
1 wt. % Pt/TiO$_2$-SiO$_2$ (10 % mol Si, A)	XPS	39.98	0	11.67	46.53	1.82
	SEM-EDX	X	X	X	X	X
	TEM-EDX	45.94	0	10.49	42.62	0.95
1 wt. % Pt/Al$_2$O$_3$-SiO$_2$ (10 mol % Si)	XPS	0	12.50	37.29	50.08	0.13
	SEM-EDX	X	X	X	X	X
	TEM-EDX	0	39.04	11.74	48.08	1.14

Variations in the silicon concentration calculated by techniques which differ by analysis depth suggest a non-homogeneity of the anatase-rutile based supports' composition. Whilst the surface silicon concentration measured by XPS ($\approx$ 10 nm penetration) correlates with the loading provided by the support supplier, the silicon content decreases considerably when measured by EDX ($\approx$ 1 - 2 μm penetration). This indicates the presence of a silicon gradient with a higher concentration of SiO$_2$ at the surface. On the other hand, the silicon concentration remains constant at different depths for the anatase- only based catalysts,

which present a different morphology and have a higher surface area, demonstrating a homogeneous composition of the support.

The heterogeneity of the composition becomes even more relevant for the Al_2O_3-SiO_2 support, which presents a concentration gradient for both SiO_2 and Al_2O_3 phases. For this support the silicon concentration is three times higher at the catalyst surface than at 2 μm depth, and the aluminium concentration is three times lower at the catalyst surface than at 2 μm depth.

In cases, a higher concentration of platinum species is found on the surface of the catalysts, exceeding the theoretical loading of ≈ 1 wt %. Whilst the bulk- sensitive analysis (EDX) shows platinum loadings similar to the theoretical values when platinum is supported on the mixed metal oxides; TiO_2-SiO_2 and Al_2O_3-SiO_2, the loading is lower on anatase- only and anatase-rutile TiO_2. This could be attributed to the poor dispersion of the platinum on the titania supports, as observed in Figure 4.27 for TiO_2 (A-R) and 4.30 for TiO_2 (A). As mentioned previously (Figure 4.24), quantitative results obtained from the XPS data for 1 wt. % Pt/Al_2O_3-SiO_2 should be considered carefully because the intense Al 2p signal overlaps with that of the Pt 4f.

Although these techniques can give a general idea about catalyst composition, elemental analysis via a different technique such as ICP-MS would be necessary in order to obtain a more representative quantification of the elements present within the supports and catalysts.

4.2.1.3 Discussion

Based on detailed characterisation studies, it has been possible to propose a model to describe the structural and electronic properties of the catalysts.

In general, the shape of the platinum particles is spherical. Platinum dispersion is enhanced with the addition of SiO_2 to both titanias; anatase and anatase-rutile. Meanwhile, small nanoparticles (2-5 nm) are highly dispersed on the TiO_2-SiO_2 supports, whilst large, poorly dispersed platinum particles ($\approx$ 10 nm) are found on SiO_2- free supports. Increasing the SiO_2 content of TiO_2 supports increases surface area and it is well known that an increment of the support surface area improves the dispersion of nanoparticles.

Although it is observed that the more active SiO_2 - containing catalysts have smaller platinum particles, the presence of silica also modifies the electronic properties of the supported platinum catalysts. Electronic properties depend on the Pt-support interactions and have been shown to have a significant influence towards increasing catalytic activity for hydrocarbon combustion.

The oxidation state of platinum varies with the support material. For the anatase-rutile TiO_2 based supports, the presence of metallic platinum becomes more favourable with increasing SiO_2 content; such that platinum is predominantly present in metallic state on TiO_2-SiO_2 (16 % mol Si, A-R) and exists as platinum oxide on TiO_2 (A-R). This tendency was consistent with previous studies [9] [10] [30] [52]. Changes in catalytic activity upon varying of support materials comes from the chemical modification of supported platinum catalysts, with the oxidation resistance of the noble metal being improved by more acidic/ electrophilic supports, i.e. with the SiO_2 content.

As illustrated in Figure 4.33 there is a clear relationship between the platinum oxidation state and propane conversion. A decrease in the Pt^{2+}/Pt^0 ratio corresponds to a significant improvement in catalytic activity.
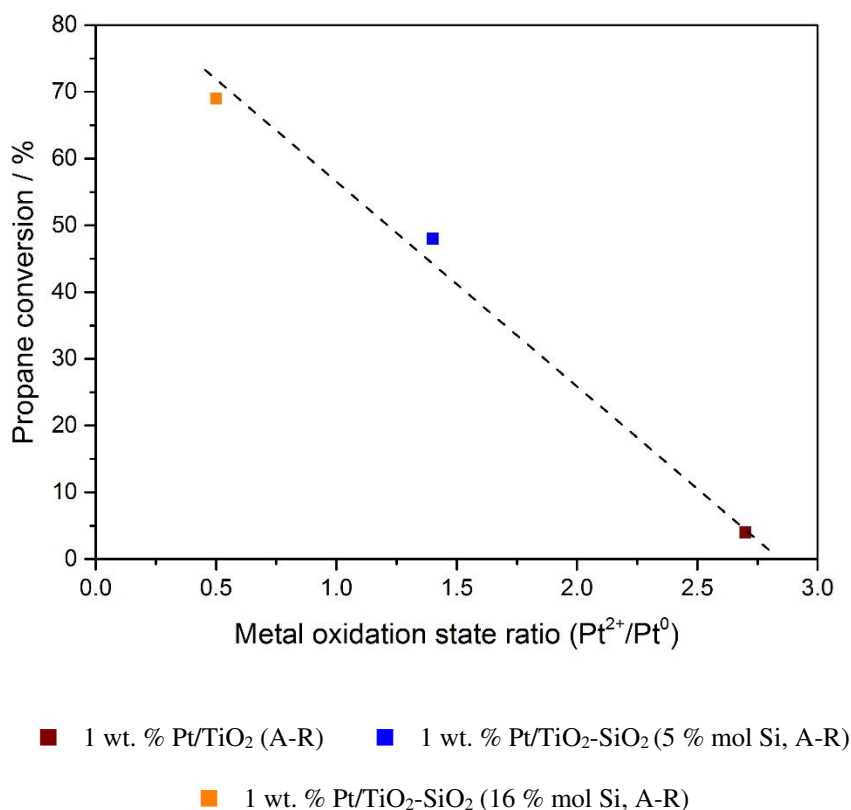
Figure 4.33. Activity of the supported platinum catalysts for total oxidation of propane at 300 °C as a function of the Pt^{2+}/Pt^0 ratio

However, based on the results obtained here, there is not a clear relationship between the platinum oxidation resistance and support acidity. NH$_3$ TPD experiments show the opposite to previous studies [30], as the total acidity of the anatase-rutile titania based mixed oxide supports decreases with the SiO$_2$ content. Garetto *et al*. [65] reported that the superior activity shown by platinum supported on acidic zeolites for propane combustion was due to the

increase in the density of adsorbed propane molecules rather than acid strength of the support materials. Hence, propane uptake on the supported catalysts should be measured.

Yazawa *et al*. [52] reported that the catalytic activity of supported platinum catalysts for low temperature propane combustion varied not only with the acid strength of support materials but also with the platinum dispersion, thus, the turnover frequency increased with increasing support acidity and with a decrease in platinum dispersion. They concluded that variation in catalytic activity with platinum dispersion is linked to the oxidation state of platinum, since large platinum particles are less readily oxidised than small ones[52]. These results are contrary to those obtained in this thesis, where catalytic activity is enhanced with the SiO_2 content of the support, which it is linked not only to an improvement in the oxidation resistance but also the dispersion of the platinum nanoparticles.

In the case of the anatase- only based supports, the presence of metallic Pt^0 does not increase with the SiO_2 content and platinum is predominantly present as the oxide (PtO) on both TiO_2 (A) and TiO_2-SiO_2 (10 % mol Si, A). The platinum loading, dispersion and oxidation state are comparable in both of these supports but platinum supported on TiO_2 (A) is much more active than that supported on TiO_2 (A-R). Surface area, morphology and phase composition differ between these two supports.

Although it is well known that anatase TiO_2 possesses a higher surface area than rutile TiO_2 and that an increase in the surface area of the support improves nanoparticle dispersion, it has already been proven, via experiments using commercial titania and rutile supports, that the significant enhancement of the activity is not, to a great extent, due to these factors. Figure 4.34 shows a fair relationship between the surface area of the support and propane conversion under the conditions studied. However, as shown in the TEM micrographs in

Figure 4.30, the dispersion of platinum on TiO_2 (A) is poor and comparable with that obtained for platinum on TiO_2 (A-R), figure 4.26 and 4.27.

■ 1 wt. % Pt/TiO_2 (A-R)   ■ 1 wt. % Pt/TiO_2-SiO_2 (5 % mol Si, A-R)

■ 1 wt. % Pt/TiO_2-SiO_2 (16 % mol Si, A-R)

■ 1 wt. % Pt/TiO_2 (A)   ■ 1 wt. % Pt/TiO_2-SiO_2 (10 % mol Si, A)
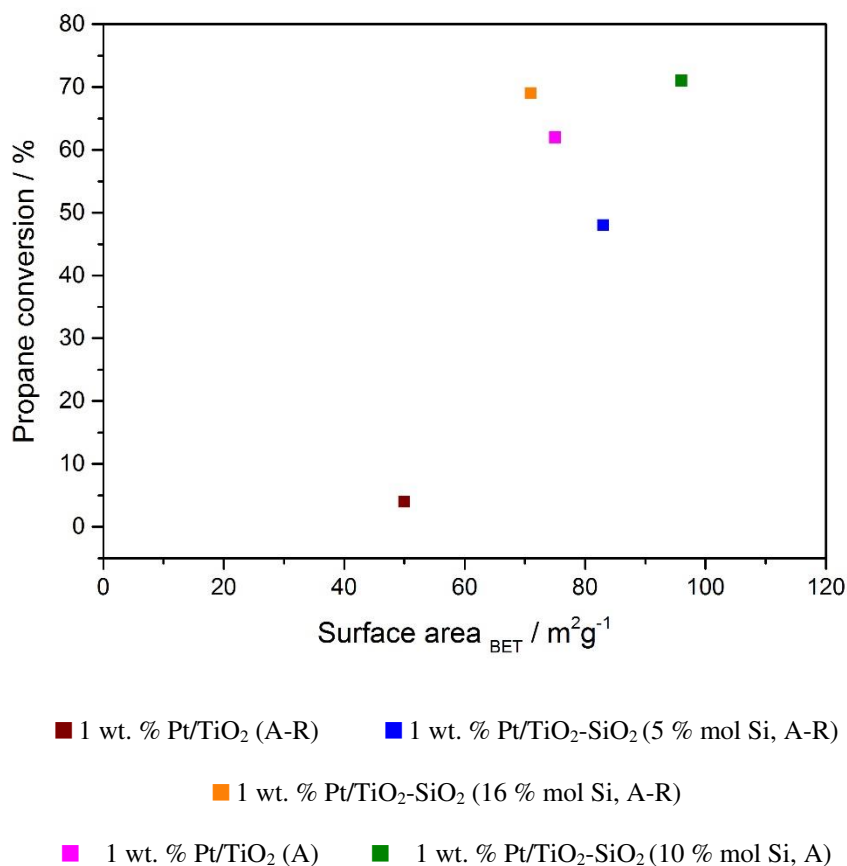
Figure 4.34. The activity of supported platinum catalysts for the total oxidation of propane at 300 °C as a function of BET surface area

In conclusion, the potential influence of the anatase- only TiO_2 support on the catalytic activity of supported platinum catalysts for propane oxidation remains unclear.

4.2.2 The effect of the transient temperature cycle

Results for stability tests over the most representative catalysts have already been shown in Figure 4.14 of this chapter. To help investigate the light-off characteristics of a catalyst under more realistic conditions, which simulate changes in engine load, experiments with a transient temperature cycle were carried out. The main objective is to demonstrate that even with a constant exhaust composition, activation or deactivation phenomena can be observed.

Propane oxidation reactions using different temperature cycles, consisting of both upwards and downwards ramps, were performed. Platinum catalysts tested under a transient temperature cycle exhibit hysteresis behaviour, indicating that the catalytic activity during the cool-down exceeds the activity of the first heat-up cycle.

Figure 4.35. Temperature in degrees Celsius for 10 % propane conversion (T_{10}) and 50 % propane conversion (T_{50}) during hysteresis: Heat-up, cool-down and heat-up cycles

Supported platinum catalysts (1 wt. % Pt) prepared by non-aqueous impregnation and

calcined at 400 ºC in static air

Figure 4.35 shows the T_{10} and T_{50} temperatures for 1 wt. % platinum supported on commercial TiO$_2$ P25, SiO$_2$ and Al$_2$O$_3$ during up – down - up temperature cycles. Whilst the T_{50} temperature decreases by 65 ºC and 35 ºC for the TiO$_2$ and Al$_2$O$_3$ catalysts respectively upon cycling back up, no variation in the T_{10} and T_{50} is observed for the SiO$_2$ catalyst.

- ■ - 1 wt. % Pt/TiO$_2$ (A-R) UP,   ¨ ■ ¨ 1 wt. % Pt/TiO$_2$ (A-R) DOWN

- □ - 1 wt. % Pt/TiO$_2$ (A-R) UP AGAIN
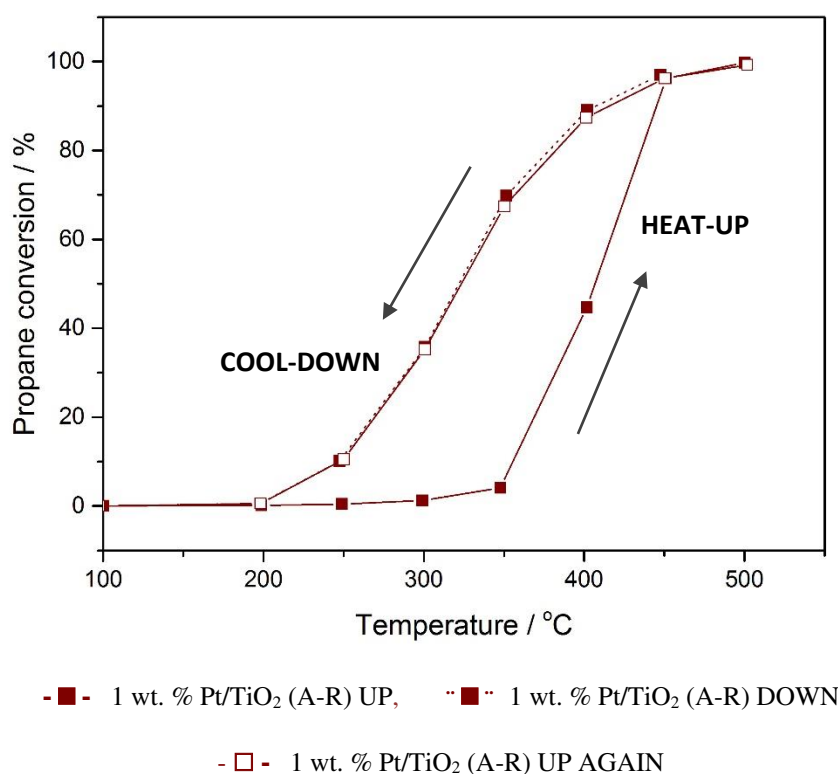
Figure 4.36. Total oxidation of propane over supported platinum catalysts

Hysteresis: Heat-up (solid line) and cool-down (dashed line) light-off curves

Reaction conditions: Flow reactor, GHSV = 50,000 h^{-1}, C$_3$H$_8$:O$_2$ = 1:50

Catalysts prepared by non-aqueous impregnation and calcined at 400 ºC in static air

Figure 4.36 shows propane conversion as a function of temperature in an experiment where the temperature was ramped from 100 ℃ up to 500 ℃, back to 100 ℃ and up to 500 ℃ again. In accordance with the results in Figure 4.35, the conversion of propane is higher during the negative ramp than during the first positive ramp. If the cycle is repeated, the conversion closely follows that of the first negative ramp.

Repeated temperature cycling significantly improves catalytic activity of 1 wt. % Pt/TiO_2 (A-R). Initially, 5 % propane conversion was observed at 350 ℃. This increased to 70 % after the second and third cycles at 500 ℃. This can be explained by a self-activation of the catalyst under reaction conditions.

Compared to the transient temperature cycle Figure 4.14, if the catalyst is operated at the same temperature (350 ℃) for a longer time, a steady state is observed that corresponds to the higher conversion during the hysteresis cycle.

The T_{10} and T_{50} temperatures observed for different supported platinum catalysts during up-down- up temperature hysteresis are illustrated in Figure 4.37. The catalytic activity enhancement is of great importance for 1 wt.% Pt/TiO_2 (A-R) catalyst, with a decrease in T_{50} of 86 ℃ but is not as significant for the platinum supported on TiO_2 (A) or any of SiO_2 – containing catalysts, with a decrease in T_{50} of only 10 ℃.
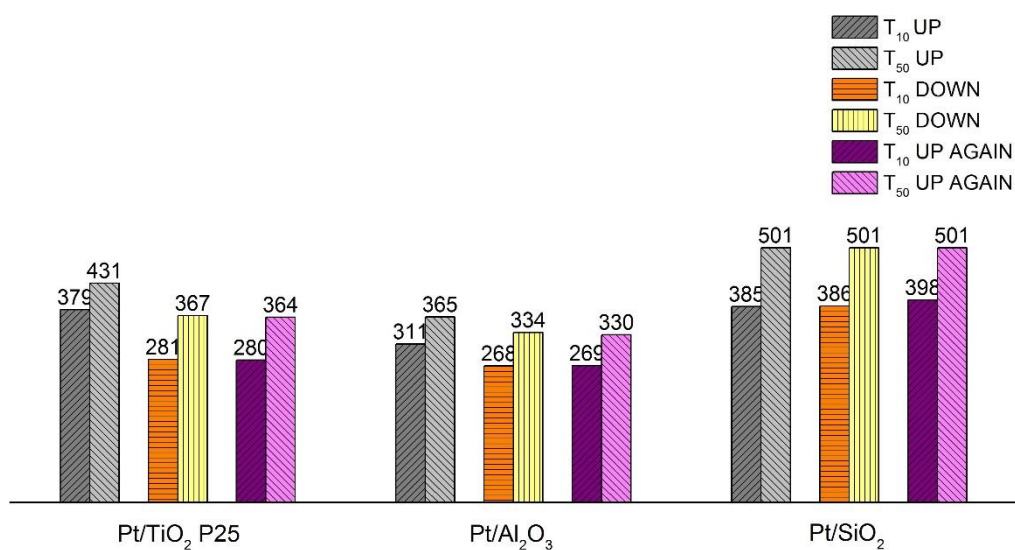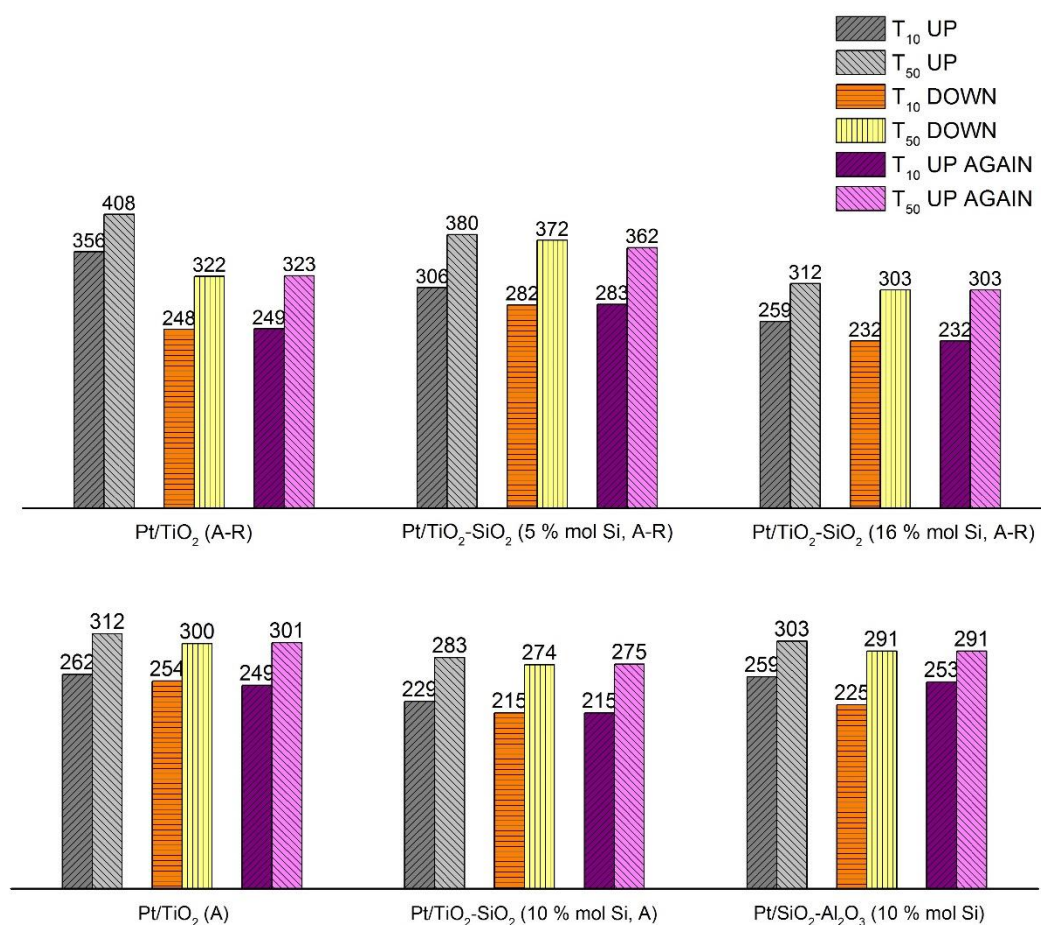
Figure 4.37. Temperature in degrees Celsius for 10 % propane conversion (T_{10}) and 50 % propane

conversion (T_{50}) during hysteresis: Heat-up, cool-down and heat-up cycles

Supported platinum catalysts (1 wt. % Pt) prepared by non-aqueous impregnation and

calcined at 400 ºC in static air

A similar phenomenon was reported in previous studies for CO oxidation on platinum [66,] [67], showing hysteresis behaviour with a higher degree of conversion during cool down than during heat up.

There are several physical and chemical effects which can cause regular hysteresis: (i) thermal inertia of the catalyst, (ii) multiple steady states due to the exothermic reaction and (iii) surface inhibition. The most likely explanation for the observed hysteresis behaviour in this study is an *in situ* reduction of the surface platinum.

Catalysts were analysed by XPS following temperature cycling experiments. Quantitative analysis of the Pt 4f binding energy region for these catalysts is presented in Table 4.8. The variation in the oxidation state of platinum can also explain the changes in activity during hysteresis cycles.

As illustrated in Figure 4.38, platinum in the metallic state is the predominant species after the first heat-up cycle, thus enhancing propane conversion. Whilst the Pt^{2+}/Pt^0 ratio in 1 wt. % Pt/TiO_2 (A-R) decreases considerably after the first propane oxidation reaction, from 2.8 to 0.24, the decrease is subtle for 1 wt. % Pt/TiO_2-SiO_2 (A-R), from 0.48 to 0.21.
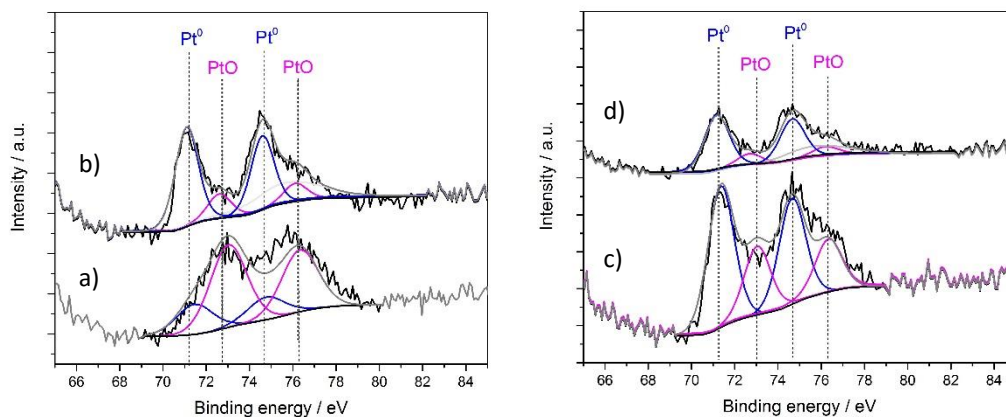
Figure 4.38. XPS spectra in the Pt 4f binding energy region of the 1 wt. % platinum catalysts:

Pt/TiO_2 (A-R):   a) Fresh   b) After Propane oxidation

Pt/TiO_2-SiO_2 (16 mol % Si, A-R):   c) Fresh   d) After Propane oxidation

It is thus proposed that at high temperatures, platinum is reduced by propane despite the large excess of oxygen in the gas feed. The metallic platinum is not oxidised back to its original state at lower temperatures, indicating that the new platinum species formed is stable.

Table 4.8. Quantitative analysis of the supported platinum catalysts, before and after reaction, obtained from the XPS spectra

Catalyst		Pt At %	Pt Wt %	Pt^0 Conc. %	Pt^{2+} Conc. %	Pt^{4+} Conc. %
1 wt. % Pt/TiO$_2$ (A-R)	Fresh	0.42	3.07	26.70	73.30	0
	After Propane ox.	0.15	1.34	80.68	19.32	0
1 wt. % Pt/TiO$_2$-SiO$_2$ (16 % mol Si, A-R)	Fresh	0.23	1.93	67.49	32.52	0
	After Propane ox.	0.16	1.42	82.66	17.24	0
1 wt. % Pt/TiO$_2$ (A)	Fresh	0.18	1.36	30.03	69.97	0
	After Propane ox.	0.17	1.29	12.23	51.28	36.49
1 wt. % Pt/TiO$_2$-SiO$_2$ (10 % mol Si, A)	Fresh	0.22	1.82	22.65	77.35	0
	After Propane ox.	0.14	1.14	100	0	0
1 wt. % Pt/Al$_2$O$_3$-SiO$_2$ (10 mol % Si)	Fresh	0.01	0.13	45.83	32.29	21.88

The difference in the Pt^{2+}/Pt^0 ratio before and after reaction and, therefore, the performance, is greater when the platinum is supported on TiO$_2$ (A-R) than when supported on TiO$_2$ -SiO$_2$ mixed oxides. These results also explain the enhancement in activity observed for 1 wt. % Pt/TiO$_2$ (A-R) during the time on-line experiment in Figure 4.14. The 62 % increase in propane conversion after 10 hours at 350 °C is potentially due to the *in situ* reduction of PtO to Pt^0.

Again, the anatase based catalysts do not follow the same trends, with no clear correlation between the catalytic performance and oxidation state of platinum. The concentration of metallic platinum decreases after the first heat-up cycle, from 30 to 12 %, but even then, the catalytic activity remains high.

These differences can be explained in terms of the redox properties and the reducibility of the platinum when supported on different materials.

4.2.3 The effect of the calcination conditions

The study and determination of the optimal conditions for catalyst preparation, pretreatment and activation is of great importance. The preparation of high surface area solid catalysts requires an oxidation or reduction step at elevated temperatures following metal impregnation. This is required to remove the precursor and obtain well dispersed metal nanoparticles. Calcination conditions influence the texture, specific surface area and morphology of the final catalyst and subsequently influence the catalytic performance. While calcination conditions have already been discussed in the experimental chapter, the effect of a range of calcination atmospheres on the catalysts and their performance was investigated.

In order to investigate the effect of the calcination atmosphere, each catalyst was calcined at 400 °C for 5 hours under: static air, flowing air and flowing helium. These catalysts were tested for propane oxidation.

Figures 4.39 and 4.40 show the effect of the calcination atmosphere on propane conversion.
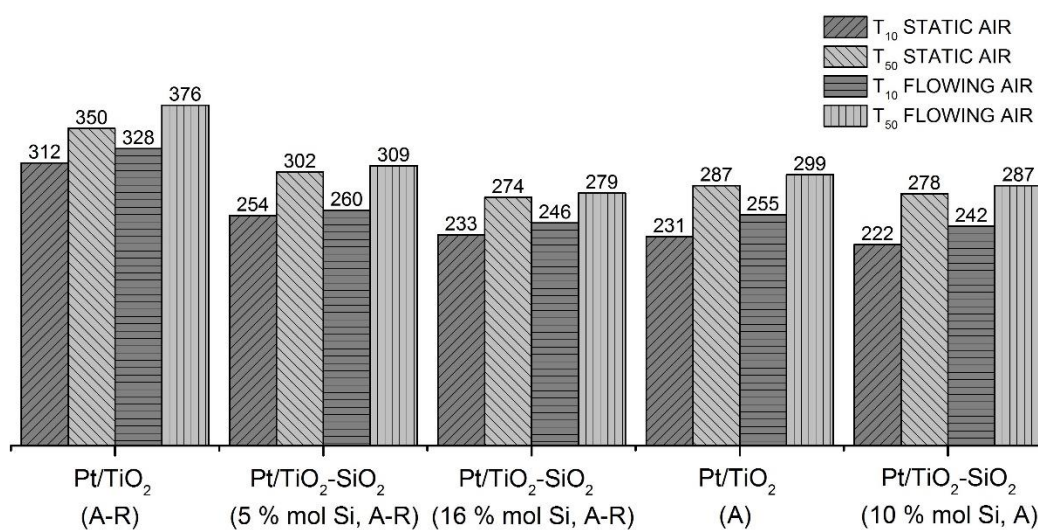
Figure 4.39. Temperature in degrees Celsius for 10 % propane conversion (T_{10}) and 50 % propane conversion (T_{50}) over supported platinum catalysts (1 wt. % Pt) prepared by non-aqueous impregnation, calcined at 400 ºC in static and flowing air
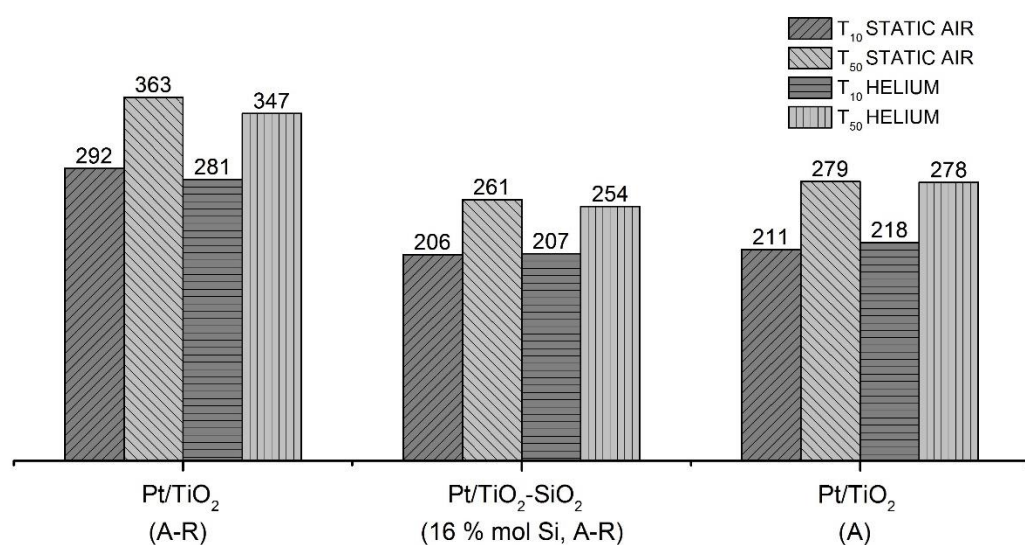
Figure 4.40. Temperature in degrees Celsius for 10 % propane conversion (T_{10}) and 50 % propane conversion (T_{50}) over supported platinum catalysts (1.5 wt. % Pt) prepared by non-aqueous impregnation, calcined at 400 ºC in static air and helium

It can be observed in Figure 4.39 that the catalysts calcined under flowing air present lower activity than those calcined under static air. This effect is more noticeable for the platinum supported on TiO_2 (A-R), with T_{50} shifted ≈ 26 °C towards higher temperatures.

The effect of using an inert atmosphere during the heat-treatment is illustrated in Figure 4.40. The catalysts calcined under helium presents enhanced performance compared with the catalyst calcined under static or flowing air. Again this effect is more apparent for the platinum supported on TiO_2 (A-R), with T_{50} shifted ≈ 16 °C towards lower temperatures.

With consideration of the obtained results, it can be concluded that whilst the changes are subtle, the performance of the catalysts is, in general, affected by the calcination atmosphere. Catalytic activity follows the order: helium > static air > flowing air.

Quantitative analysis of the supported platinum catalysts obtained from the XPS spectra, Pt 4f region, is presented in Table 4.9. Although it has been reported previously that the composition of the calcination atmosphere can affect the final oxidation state and surface metal centres, no clear change in the Pt^{2+}/Pt^0 ratio is observed in Table 4.9 when comparing the different calcination atmospheres. Whilst for the 1 wt. % Pt catalysts, metallic platinum becomes more favourable with increasing SiO_2 content of the support; for the   1.5 wt % Pt catalysts, metallic platinum is the predominant species independent of the support.

It is found that the calcination atmospheres studied have no significant effect upon the oxidation state of the platinum. The differences in performance for propane oxidation are therefore likely related to the nature of the support.

The oxidation activity of the 1 wt. % Pt catalysts depends strongly on oxidation state, with metallic platinum being the most active. To extend the understanding of the effect of the

platinum oxidation state on the catalytic activity for hydrocarbon oxidation, the effect of a reductive pretreatment on catalytic performance was studied.

Table 4.9. Quantitative analysis of the supported platinum catalysts, calcined under different atmospheres, obtained from the XPS spectra

Catalyst		Pt		Pt^0	Pt^{2+}
		At %	Wt %	Conc. %	Conc. %
1 wt. % Pt/TiO$_2$ (A-R)	Static air	0.42	3.07	26.70	73.30
	Flowing air	0.42	3.02	30.72	69..27
1.5 wt. % Pt/TiO$_2$ (A-R)	Static air	0.55	4.02	81.59	18.41
	Helium	0.65	4.67	77.09	22.91
1 wt. % Pt/TiO$_2$-SiO$_2$ (5 % mol Si, A-R)	Static air	0.26	2.03	42.09	57.90
	Flowing air	0.26	2.00	43.75	56.25
1 wt. % Pt/TiO$_2$-SiO$_2$ (16 % mol Si, A-R)	Static air	0.23	1.93	67.49	32.52
	Flowing air	0.24	2.02	63.01	36.98
1.5 wt. % Pt/TiO$_2$-SiO$_2$ (16 % mol Si, A-R)	Static air	0.29	2.45	74.99	25.01
	Helium	0.32	2.74	100	0.00
1 wt. % Pt/TiO$_2$ (A)	Static air	0.18	1.36	30.03	69.97
	Flowing air	0.21	1.60	36.65	63.35
1.5 wt. % Pt/TiO$_2$ (A)	Static air	0.37	2.80	65.63	34.37
	Helium	0.39	2.95	67.89	32.11
1 wt. % Pt/TiO$_2$-SiO$_2$ (10 % mol Si, A)	Static air	0.22	1.82	22.65	77.35
	Flowing air	0.22	1.80	17.41	82.59

Since it has been demonstrated that the catalytic activity of supported platinum varies with its oxidation state, reduction at elevated temperature could be beneficial in the synthesis of supported metal catalysts. However, heating a supported metal catalyst can cause morphological changes in the metal particles depending upon the particular metal-oxide system. When using titania as the support some considerations should be taken into account. As reported by Hanaor *et al.* [68], phase transformation of titania from anatase to rutile occurs at temperatures above 600 °C and ambient pressure. This leads to a decrease in the support's surface area. In addition, the so called strong-metal-support-interaction (SMSI) exhibited when metals in group 8-10 are supported on reducible metal oxides, such as TiO_2, and reduced in hydrogen results in sintering, encapsulation, inter-diffusion and alloy formation that leads to important changes in catalytic activity and selectivity [69].

Figure 4.41 shows propane conversion as a function of temperature for the supported platinum catalysts following reduction under 5 % H_2/Ar at 400 °C for 5 hours. In accordance with previous results, the conversion of propane is enhanced by the SiO_2 content of the TiO_2 (A-R) support.
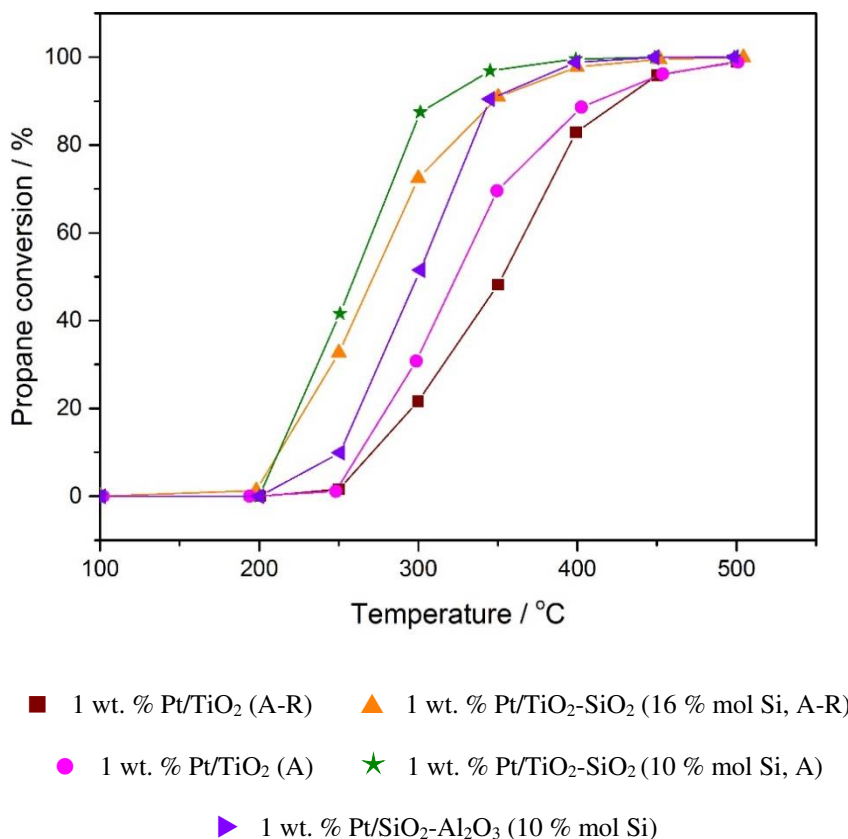
Figure 4.41 Total oxidation of propane over supported platinum catalysts

Reaction conditions: Flow reactor, GHSV = 50,000 h^{-1}, $C_3H_8:O_2$ = 1:50

Catalysts prepared by non-aqueous impregnation and reduced at 400 ºC in 5 % H_2/Ar

From the T_{10} and T_{50} values shown in Figure 4.42, it can be concluded that reductive pretreatment has a significant effect upon the catalytic activity of only one catalyst, 1 wt. % Pt/TiO$_2$ (A). For this catalyst, the catalytic activity decreases considerably with T_{50} shifted 37 °C towards higher temperatures. Whilst this catalyst presents high performance when calcined in an oxidising or inert atmosphere (Figure 4.40), its activity decreases when heat treated under a reducing atmosphere. Catalytic activity for propane oxidation is now similar for 1 wt.% Pt/TiO$_2$ (A) and 1 wt.% Pt/TiO$_2$ (A-R).
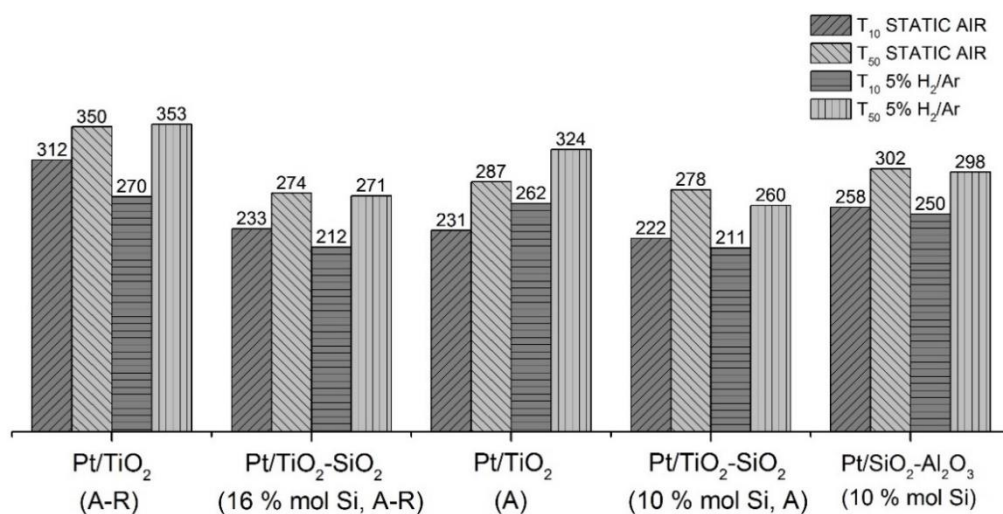
Figure 4.42. Temperature in degrees Celsius for 10 % propane conversion (T_{10}) and 50 % propane conversion (T_{50}) over supported platinum catalysts (1 wt. % Pt) prepared by non-aqueous impregnation, calcined at 400 ºC in static air and reduced at 400 ºC in 5 % H_2/Ar

Quantitative analysis of the reduced platinum catalysts obtained from the XPS spectra is shown in Table 4.10, revealing that metallic platinum is the predominant species in all catalysts, accounting for approximately 60 % of the total concentration for the TiO_2-SiO_2 based catalysts and 100% of platinum in the Al_2O_3-SiO_2 based catalyst. It should also be noted that a higher concentration of platinum species, 2.38 wt. %, is found on the surface of the 1 wt. % Pt/TiO_2 (A) catalyst after being reduced, overcoming the total loading of ≈ 1 wt %. This is also observed for the TiO_2 (A-R) based catalysts, independent of the calcination conditions.

Table 4.10. XPS quantitative analysis and Pt $4f_{7/2}$ core binding energies

of the supported platinum catalysts reduced at 400 ºC in 5 % H_2/Ar methods

(numbers in parentheses are the relative concentration of the platinum species)

Catalyst		Pt		Pt^0	Pt^{2+}	Pt^{4+}
		At %	Wt %	eV (%)	eV (%)	eV (%)
1 wt. % Pt/TiO$_2$ (A-R)	Static air	0.42	3.07	71.5 (26.7)	73.0 (73.3)	0
	5 % H$_2$/Ar	0.39	2.87	70.8 (54.6)	72.5 (45. 4)	0
1 wt. % Pt/TiO$_2$-SiO$_2$ (16 % mol Si, A-R)	Static air	0.23	1.93	71.4 (67.5)	73.0 (32.5)	0
	5 % H$_2$/Ar	0.16	1.39	71.6 (59.2)	73.6 (40.7)	0
1 wt. % Pt/TiO$_2$ (A)	Static air	0.18	1.36	71.4 (30.0)	72.8 (70.0)	0
	5 % H$_2$/Ar	0.31	2.38	71.5 (61.6)	73.2 (38.4)	0
1 wt. % Pt/TiO$_2$-SiO$_2$ (10 % mol Si, A)	Static air	0.22	1.82	71.6 (22.7)	72.9 (77.3)	0
	5 % H$_2$/Ar	0.14	1.20	71.6 (68.2)	73.0 (31.8)	0
1 wt. % Pt/Al$_2$O$_3$-SiO$_2$ (10 mol % Si)	Static air	0.01	0.13	71.4 (45.8)	72.9 (32.3)	74.5 (21.9)
	5 % H$_2$/Ar	0.01	0.03	71.8 (100)	0	0

Of particular interest is the shift towards a lower binding energy of the peak corresponding to metallic platinum for 1 wt. % Pt/TiO$_2$ (A-R) shown in Figure 4.43. Kobayashi *et al*. [9] also reported that the peak corresponding to Pt^0 was shifted 0.6 eV towards lower binding energy when a Pt/TiO$_2$-SiO$_2$ catalyst was pretreated in a reducing environment rather than in an oxidising one. This effect is only seen when platinum is supported on anatase-rutile and not on anatase- only TiO$_2$. Once again, the differences in performance for propane oxidation are mainly related to the nature of the support. Titania interacts with platinum, modifying the electronic state of surface species.
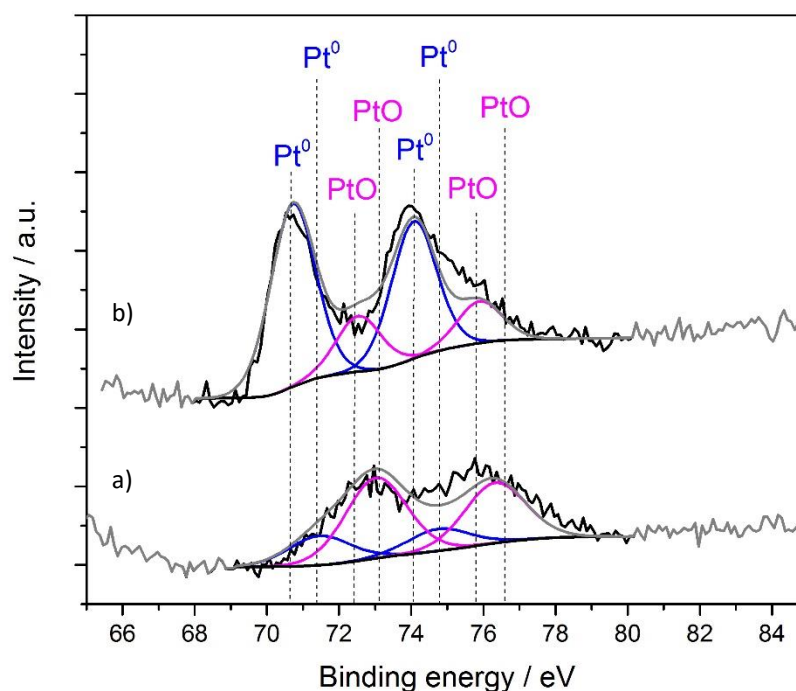
Figure 4.43. XPS spectra in the Pt 4f binding energy region of the Pt/TiO$_2$ (A-R) catalyst:

a) Static air   b) 5 % H$_2$ /Ar

Various studies have investigated the metal-support interaction in precious metal-TiO$_2$ and -Ce$_2$O$_3$ systems, using several characterisation techniques including TEM, XPS, FTIR and Raman [70] [71] [58] [72] [73] [74] [75] [76] [77] [78]. The Pt^0 peak shift towards lower binding energies in the XPS spectra in Figure 4.43 could be indicative of an SMSI effect. Electron transfer from TiO$_2$ to Pt forms electron rich (Pt)$_n^{\sigma-}$ species, resulting in a local charge density change and surface core level shifts in the Pt 4f$_{7/2}$ and Pt 4f$_{5/2}$. However, several authors [79] [80] [81] argued that the relation between activity and metal-support interaction is due to structural modification; a geometric effect, and proved by TEM analysis that the surface Pt is progressively covered/encapsulated by the reducible support when the catalyst is exposed to H$_2$ at high temperatures (T > 500 °C). In addition, Lewera *et al*. demonstrated that the observed binding energy shifts of core-level electrons were due to changes in the electronic

properties of platinum induced by not only charge transfer from the metal oxide but also changes in the lattice parameter due to alloy formation[76].

Encapsulation and electronic interactions might occur simultaneously but the electronic perturbation starts at lower reduction temperature than the geometric effect [82]. Haerudin *et al*. [83] found that reduction of titania begins at 200 °C and results in the formation of surface oxygen vacancies, Ti^{3+} ions and electrons. Hence, the reductive pretreatment at 400 °C performed in this study is likely to induce an electronic rather than geometric effect on the platinum.

In order to study the reducibility of the catalysts, temperature programmed reduction (TPR) experiments were performed using 10% H_2/Ar as the reducing agent. H_2-TPR profiles for the supported platinum catalysts are shown in Figure 4.44. In general, the profiles show a small peak below 100 °C and a series of weak overlapping uptake peaks in the temperature range 250 – 500 °C. Based on previous studies [53] [16], the peak at *ca*. 80°C can be assigned to reduction of PtO_x species to metallic platinum. The broad peak centred at 350 °C is attributed to the reduction of surface Ti^{4+} species to Ti^{3+} via H_2 spill-over. It should be noted that in Figure 4.44 d), the high temperature peak (Ti^{4+} - Ti^{3+}) for 1 wt.% Pt/TiO_2 (A) is more intense and is shifted 50 °C towards lower temperatures.
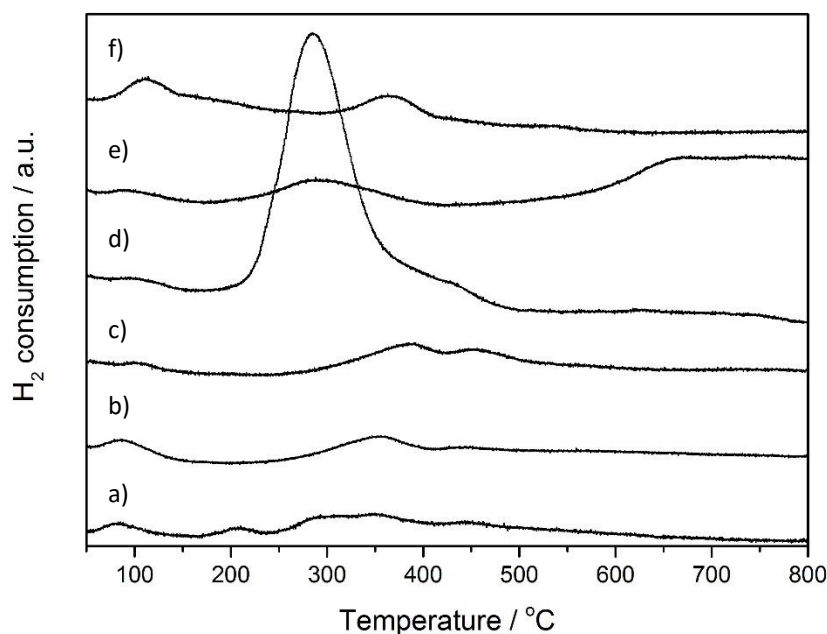
Figure 4.44. H_2-TPR curves of the 1 wt. % platinum catalysts calcined at 400 °C in static air:

a) TiO_2 (A-R), b) TiO_2-SiO_2 (5 mol % Si, A-R), c) TiO_2-SiO_2 (16 mol % Si, A-R),

d) TiO_2 (A), e) TiO_2-SiO_2 (10 mol % Si, A) and f) Al_2O_3-SiO_2 (10 mol % Al)

H_2-TPR profiles of both TiO_2 (A) and TiO_2 (A-R) are presented in Figure 4.45. Reduction

of bulk oxygen within TiO_2 has been reported to occur at temperatures of above 600 °C [84]

[85] [86]. Regarding the reducibility of the TiO_2 (A-R), no significant H_2 consumption peaks

were detected. In contrast, the anatase- only TiO_2 (A) exhibits one intense reduction peak

at 500 °C. This can be attributed to reduction of the surface capping oxygen in TiO_2 [86] [87] [88].

Such data is consistent with the general consideration that the temperature at which Ti^{4+}

sites were reduced in 1 wt.% Pt/TiO_2 (A) (Figure 4.44 d) is 200 °C lower than that of bare

TiO_2 (A) (Figure 4.45 b). Based on previous studies [53] [89], these results provide information

as to the influence of platinum on the reducibility of the supports, suggesting that platinum

facilitates the reduction of oxygen species on the TiO_2 surface. Platinum catalyses the

surface reduction of the support by lowering the temperature at which dissociative
adsorption of H_2 occurs [16].
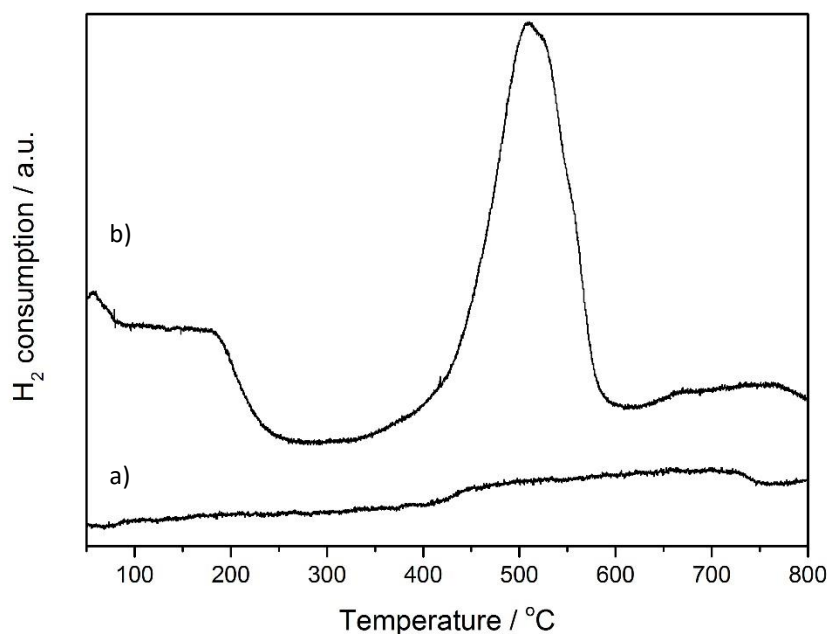
Figure 4.45. H_2-TPR curves of the as received titania supports:

a) TiO_2 (A-R)   b) TiO_2 (A)

The supports and catalysts' total hydrogen consumption determined from the TPR profiles
are presented in Table 4.11. The H_2 consumption for anatase titania on
1 wt. % Pt/TiO_2 (A) is 562 μmol H_2/g catalyst. This is 5 times greater than that obtained
for anatase-rutile titania in 1 wt. % Pt/TiO_2 (A-R). These values were determined by
calculating the theoretical amount of H_2 consumed in reducing the PtO (obtained from XPS
quantitative analysis) to Pt^0, and subtracting this from the total H_2 consumption. The
amount of H_2 consumed during the TPR of the anatase-rutile based supports is
approximately 28 μmol H_2/g catalyst. This value is comparable with that obtained for

Pt/TiO$_2$ P25 in previous studies [16]. In addition, the anatase support's hydrogen consumption is 322 μmol H$_2$/g catalyst.

Table 4.11 Hydrogen consumption obtained from the H$_2$-TPR profiles of the catalysts

Catalyst		Total H$_2$ consumption μmol H$_2$/g $_{catalyst}$	Support H$_2$ consumption μmol H$_2$/g $_{catalyst}$
TiO$_2$ (A-R)	Support	28	28
	1 wt. % Pt	152	114
TiO$_2$-SiO (5 % mol Si, A-R)	Support	28	28
	1 wt. % Pt	126	96
TiO$_2$-SiO (16 % mol Si, A-R)	Support	29	29
	1 wt. % Pt	133	116
TiO$_2$ (A)	Support	322	322
	1 wt. % Pt	598	562
TiO$_2$-SiO (10 % mol Si, A)	1 wt. % Pt	116	76
Al$_2$O$_3$-SiO$_2$ (10 mol % Si)	1 wt. % Pt	80	40

Figure 4.46 shows the TPR profiles for 1 wt. % Pt/TiO$_2$ following (a) calcination in static air (400 °C) and (b) reduction in 5 % H$_2$/Ar (400 °C). The peak at 300 °C is not present when the catalyst is heat-treated in a reducing atmosphere prior to the TPR experiment, indicating that this peak is, certainly, the result of a reduction reaction and not a thermal desorption. From these results and trends in Figure 4.42, it can be concluded that an increase in the concentration of surface capping oxygen species on the TiO$_2$ (A) support enhances the propane oxidation activity of 1 wt. % Pt/TiO$_2$ (A), as this catalyst shows much higher activity when calcined in static air than when reduced in 5 % H$_2$/Ar.
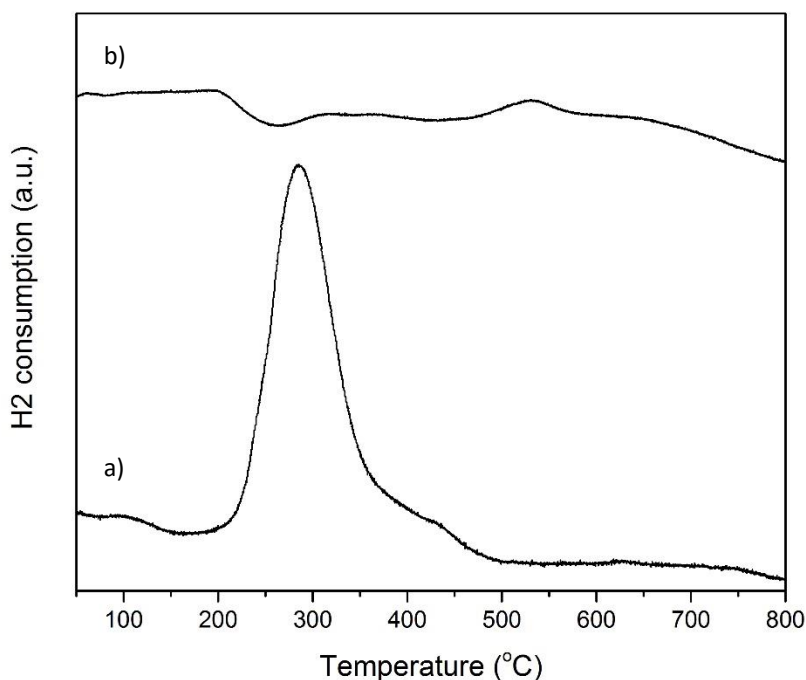
Figure 4.46. H_2-TPR curves of the 1 wt. % platinum catalysts calcined in different atmospheres:

Pt/TiO$_2$ (A):   a) Static air   b) 5 % H$_2$/Ar

The superior performance of the anatase over the anatase-rutile based catalyst, 1 wt. % Pt/TiO$_2$ (A) vs. 1 wt. % Pt/TiO$_2$ (A-R), may result from the fact that TiO$_2$ (A) serves as a reservoir of oxygen in the oxidation reaction. A number of studies have reported the reduction behaviour of other reducible supports, such as CeO$_2$, and their use as a redox/oxygen storage components in three-way-catalysts (TWC) [90 91 92 93 94 95 96 97 98]. In these materials, oxygen vacancy defects can be rapidly generated and eliminated, giving a high oxygen storage capacity (OSC). Activity depends on oxygen mobility and so called "weak" metal-oxygen bonds. A high concentration of surface oxygen with low binding energies on the catalyst surface has been reported to be required for catalyst activity. Oxygen species on the metal particles diffuse rapidly to the metal-support interface and result in the formation of the new active sites which are more active for the combustion

reaction, preserving the catalyst surface from over-oxidation. Those platinum species which react readily with the lattice oxygen of the support, are responsible for the increased propane oxidation activity. The highly reactive oxygen species are thought to be responsible for the high hydrocarbon total- oxidation activity shown by platinum and palladium- based catalysts [1], operating via a Mars-Van Krevelen type mechanism.

The reduction of CeO_2 depends strongly on the ceria crystallite size, with the oxygen transfer and reduction enhanced by the grain boundaries and defects in small ceria particles [99]. In the same way the "cloud-shape" morphology, high surface area and small particle size of the TiO_2 (A) studied, positively affects the reducibility and redox properties of TiO_2. In studies by Gao *et al.* [41], it was confirmed that highly dispersed surface titania species on silica exhibit completely different catalytic behaviour for methanol oxidation compared to bulk titania, due to redox products that are formed preferentially on the dispersed TiO_2.

TPR data has proven to be useful in understanding the performance of oxidation catalysts and the relation between catalytic activity and the redox properties of the supported platinum catalysts. The oxidation properties of supported platinum catalysts mainly depend upon the inherent reducibility of the pure oxide support. The structure, morphology and crystallite size of titania plays an important role in facilitating oxygen transfer from the support to the platinum.

To complete the study of the supports' redox properties, repeated TPR/O cycles, oxygen storage capacity and oxygen mobility experiments should be performed. In addition, propane oxidation tests over the bare supports would provide information as to what extent the metal oxide and mixed metal oxide supports, particularly TiO_2 (A), contribute to catalyst performance.

4.2.4 The effect of the preparation method

It is widely recognised that specific preparation methods can allow control of the physicochemical properties of catalysts, therefore influencing their stability and catalytic activity.

From the results presented in this study and in agreement with previous work, it can be concluded that the dispersion of platinum particles over the support has a significant effect on catalyst properties and catalytic activity.

Since Forde *et al*. [100] developed the chemical vapour impregnation (CVI), a simplified, facile, reproducible and easily controlled metal vapour deposition technique, it has been widely used within the group [101 102 103 104].

Supported platinum catalysts were prepared by chemical vapour impregnation using the same precursor, platinum (II) acetylacetonate.

Figure 4.47 shows propane conversion as a function of temperature for 1 wt. % Pt catalysts prepared by CVI and calcined at 400 °C for 5 hours in static air. Consistent with previous trends: propane conversion is clearly improved by increasing the support's SiO_2 content and platinum exhibits better performance when supported on anatase- only TiO_2/TiO_2-SiO_2 than when supported on anatase-rutile TiO_2/TiO_2-SiO_2 respectively.

Of the supported 1 wt. % platinum catalysts studied, the propane oxidation activity follows the sequence:

$$Pt/TiO_2 \text{ (A-R)} \quad < \quad Pt/Al_2O_3\text{-}SiO_2 \text{ (10 \%)} \quad < \quad Pt/TiO_2 \text{ (A)}$$

$$< \quad Pt/TiO_2\text{-}SiO_2 \text{ (16 \%, A-R)} \quad < \quad Pt/TiO_2\text{-}SiO_2 \text{ (10 \%, A)}$$
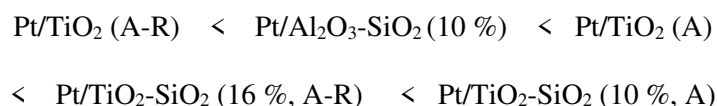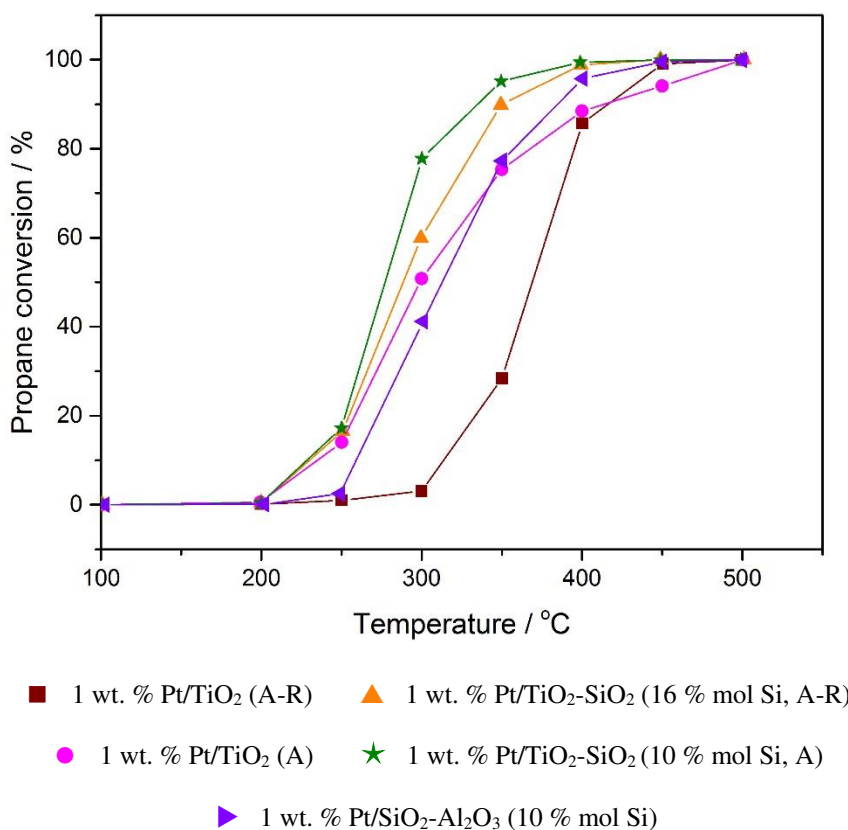
Figure 4.47. Total oxidation of propane over supported platinum catalysts

Reaction conditions: Flow reactor, GHSV = 50,000 h^{-1}, C_3H_8:O_2 = 1:50

Catalysts prepared by chemical vapour impregnation and calcined at 400 ºC in static air

Figure 4.48 compares the T_{10} and T_{50} of supported platinum catalysts prepared by non-aqueous impregnation and chemical vapour impregnation. Catalyst activity is not generally enhanced with the chemical vapour impregnation preparation method, though the difference in T_{10} and T_{50} is within the error associated with reproducibility of the catalyst preparation shown in Figure 4.20.
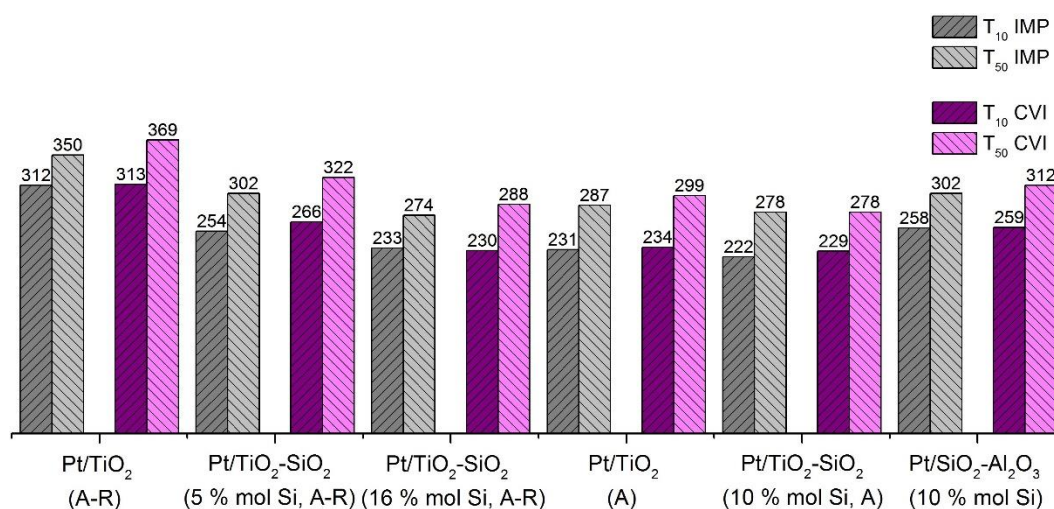
Figure 4.48 Temperature in degrees Celsius for 10 % propane conversion (T_{10}) and 50 % propane

conversion (T_{50}) over supported platinum catalysts (1 wt. % Pt) prepared by non-aqueous

impregnation (IMP) and chemical vapour impregnation (CVI), calcined at 400 ºC in static air

To study the effect of the support on the structural and electronic properties of platinum

catalysts prepared by CVI, XPS and TEM analysis were carried out.

From the deconvolution of the XPS curves in the Pt 4f binding energy region and

quantitative analysis, the concentration of the surface platinum species, Pt^0 and PtO was

determined. Results are presented in Table 4.12. In accordance with the conclusions

obtained for the catalysts prepared by non-aqueous impregnation, metallic platinum is

favoured with increasing SiO_2 content and PtO is the predominant species for both

TiO_2 (A) and TiO_2 (A-R) supports. The concentration of platinum species on the surface of

the catalysts prepared by CVI is even higher than that of the catalysts prepared by non-

aqueous impregnation, overcoming the total loading of 1 wt. %.

Table 4.12. XPS quantitative analysis and Pt $4f_{7/2}$ core binding energies

of the supported platinum catalysts, prepared by CVI

(numbers in parentheses are the relative concentration of the platinum species)

Catalyst	Pt		Pt^0	Pt^{2+}
	At %	Weight %	Conc. %	Conc. %
1 wt. % Pt/TiO$_2$ (A-R)	0.60	4.33	36.63	63.38
1 wt. % Pt/TiO$_2$-SiO$_2$ (5 % mol Si, A-R)	0.37	2.86	49.67	50.33
1 wt. % Pt/TiO$_2$-SiO$_2$ (16 % mol Si, A-R)	0.25	2.10	70.74	29.26
1 wt. % Pt/TiO$_2$ (A)	0.19	1.51	36.66	63.34
1 wt. % Pt/TiO$_2$-SiO$_2$ (10 % mol Si, A)	0.24	1.98	24.69	75.31
1 wt. % Pt/Al$_2$O$_3$-SiO$_2$ (10 mol % Si)	1.46	12.93	49.02	50.97

Figures 4.49 and 4.50 show TEM micrographs of the supported platinum catalysts prepared by CVI. Platinum appears as dark particles in the HRTEM images and shows bright contrast in the STEM images. Although the number of images acquired was not sufficient to calculate accurate particle distributions, it can be concluded that increasing the SiO$_2$ content of the support enhances platinum dispersion.

Poorly dispersed platinum particles with a size of 5 – 10 nm are found on TiO$_2$ (A-R), Figure 4.49. a). This result diverges from that obtained by Forde *et al*. [100] who reported that when platinum was deposited onto TiO$_2$ P25 using CVI, a uniform distribution of metal nanoparticles with a reasonably narrow size distribution and mean particle size of 1.5 ± 0.3 nm was formed. It should be noted that the total platinum loading was higher than

that of the catalysts studied in the present thesis, 2.5 vs. 1 wt %, and that while in Forde's work the prepared materials were reduced in 5 % H_2/Ar at 400 ºC, the catalysts presented here were calcined in static air (at the same temperature). The higher platinum loading and reductive heat-treatment could explain the differences in dispersion of the metal nanoparticles between studies. On the other hand, well dispersed platinum particles, with mean particle size of 1.5 nm ± 0.1 nm and size range of 0 – 6 nm, are observed on the anatase-rutile TiO_2-SiO_2 support, Figure 4.49. b).

In agreement with the results obtained for supported platinum catalysts prepared by non-aqueous impregnation, some particles with mean size of 5 nm are detected on the TiO_2 (A), as shown in, Figure 4.49 c). No dark (HRTEM) or bright spots (STEM), attributed to platinum nanoparticles, appear in Figure 4.49 d) for platinum supported on the anatase-only TiO_2-SiO_2 support. Despite this, quantitative analysis by EDX confirms the presence of well dispersed platinum, accounting for 1 wt % of the total composition. It could be supposed then, that the platinum is homogeneously dispersed on the TiO_2-SiO_2 (A) support, mainly as PtO. Due to the small size, potentially subnanometric, and poor contrast it is not possible to observe the particles clearly at the resolution of the TEM instrument used.

Distinctively, the morphology in 1 wt. % Pt/Al_2O_3-SiO_2 prepared by CVI, shown in Figures 4.49 e) and f), varies from the equivalent catalyst prepared by non-aqueous impregnation (Figure 4.32). A large size window is characteristic of this support, with platinum particles and clusters in the range of 2 - 80 nm observed on the STEM micrographs in Figure 4.50. e) and f). For this support, the most distinctive feature is the appearance of large platinum crystallites with cubic morphology that were not found when the catalyst was prepared by impregnation.

a)   1 wt. % Pt/TiO₂ (A-R)   **b)   1 wt. % Pt/TiO₂-SiO₂ (A-R)**

c)   1 wt. % Pt/TiO₂ (A)   **d)   1 wt. % Pt/TiO₂-SiO₂ (A)**

e)   1 wt. % Pt/Al₂O₃-SiO₂   **f)   1 wt. % Pt/Al₂O₃-SiO₂**
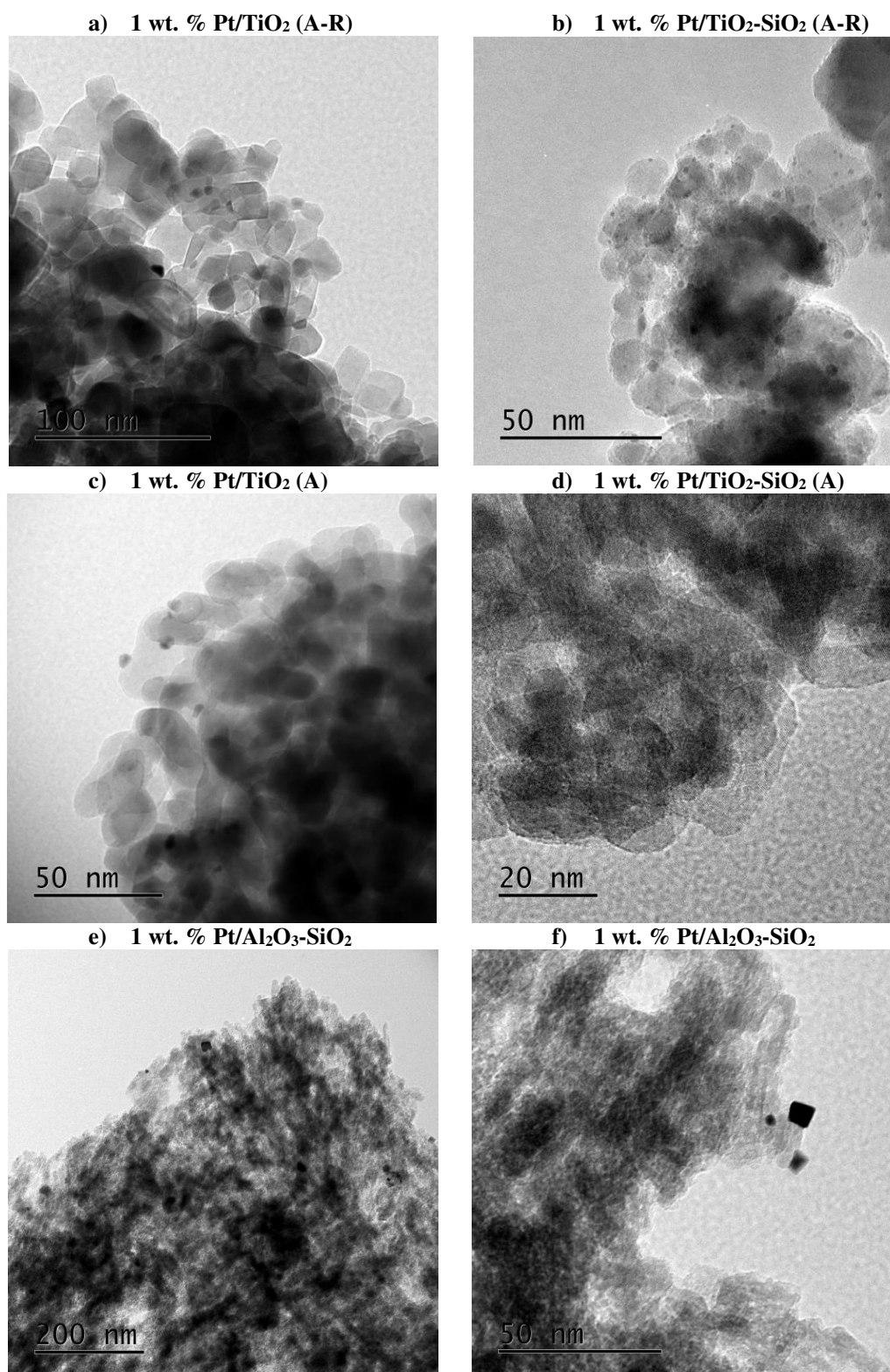
Figure 4.49. Selected HRTEM of the supported platinum catalysts prepared by CVI

a)　1 wt. % Pt/TiO₂ (A-R)　　　　　　**b)　1 wt. % Pt/TiO₂-SiO₂ (A-R)**

c)　1 wt. % Pt/TiO₂ (A)　　　　　　**d)　1 wt. % Pt/TiO₂-SiO₂ (A)**

e)　1 wt. % Pt/Al₂O₃-SiO₂　　　　　　**f)　1 wt. % Pt/Al₂O₃-SiO₂**
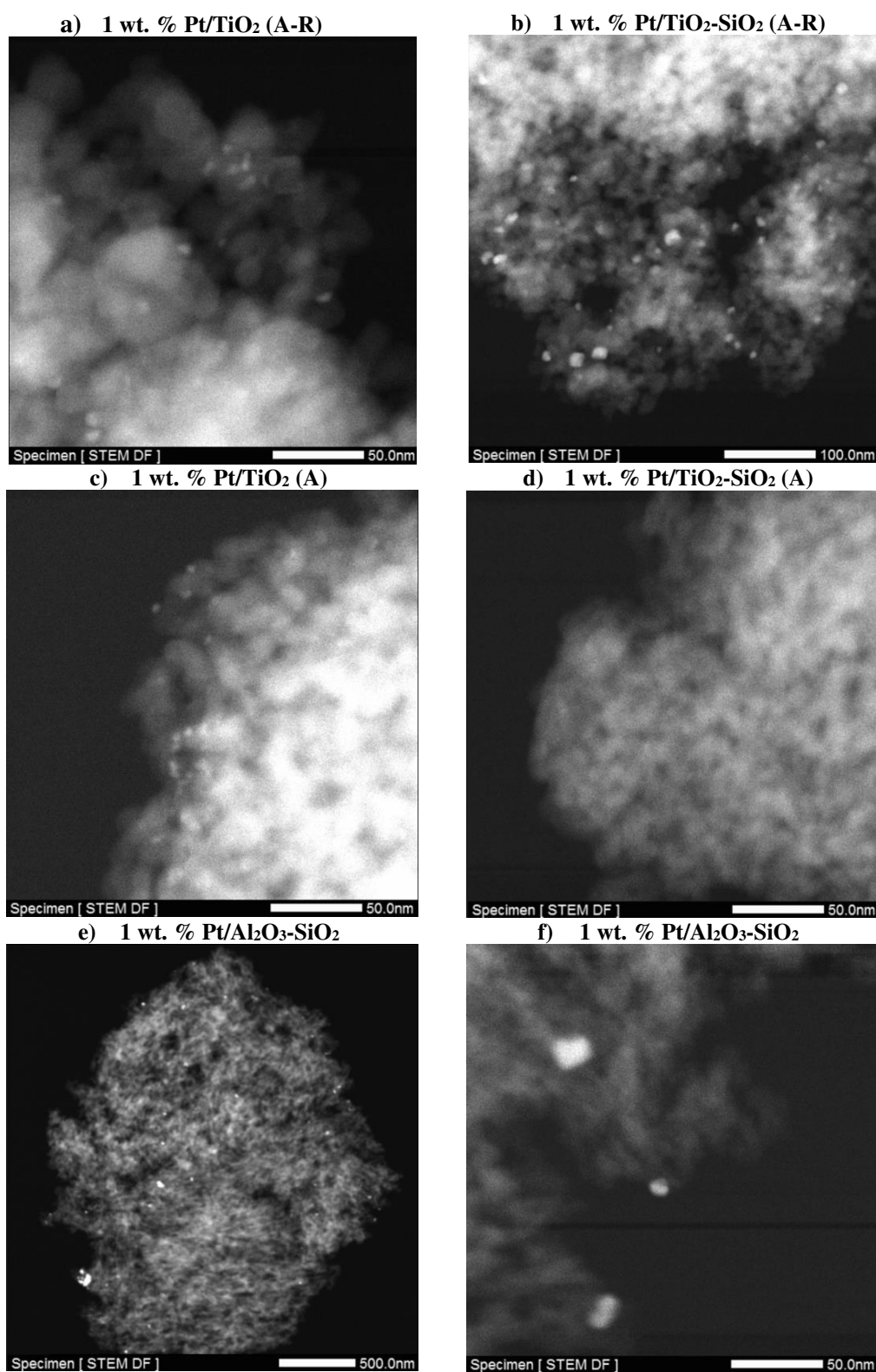
Figure 4.50. Selected STEM images of the supported platinum catalysts prepared by CVI

It can be concluded that, under the conditions studied, the oxidation properties of supported platinum catalysts are more greatly affected by the support material than by the preparation method. Previous studies reported that the change in catalytic activity with support materials comes from chemical modification of the catalysts' properties, the oxidation resistance of the noble metal and also the dispersion, which is improved with support acidity/electrophilicity [9] [30] [52]. Another factor is the hydrophobicity of the support. R. Armstrong (Cardiff Catalysis Institute, currently unpublished work) has shown that when preparing Cu/ZSM-5 catalysts by CVI, the hydrophobicity of the support plays an important role in enhancing dispersion and giving rise to smaller nanoparticles.

Meanwhile Al_2O_3 and TiO_2 P25 present a hydrophilic character caused by hydroxyl groups on the surface, amorphous SiO_2 possess a largely hydrophobic quality due to the absence of charged silanol groups on silica surfaces [105] [106]. Hence, increasing the SiO_2 content enhances the hydrophobic character of the support, the interaction with the hydrophobic precursor (platinum (II) acetylacetonate) and therefore, the platinum dispersion. Opposed to this, several studies showed that the addition of SiO_2 to TiO_2 films increases the acidity and also its hydrophilicity and photocatalytic activity [36] [107] [108].

Whilst Al_2O_3 and TiO_2 P25 present a hydrophilic character caused by hydroxyl groups on the surface, amorphous SiO_2 possess hydrophobic groups chemically bonded to the surface [105] [106]. Hence, increasing the SiO_2 content enhances the hydrophobic character of the support, the interaction with the hydrophobic precursor and therefore, the platinum dispersion. To measure the surface hydrophilicity/hydrophobicity of the support materials several suitable characterization methods could be used: surface adsorption, affinity coefficient and contact angle [109] [110].

Despite some slight differences, the electronic and structural properties of the supported platinum catalysts are comparable for both preparation methods. This explains the limited difference in catalytic activity shown in Figure 4.48 for catalysts prepared by non-aqueous impregnation and CVI.

4.2.5 The effect of the platinum precursor

The two methods used to prepare the platinum catalysts studied in this thesis; non-aqueous impregnation and chemical vapour impregnation, require conditions and metal precursors that differ from those applied widely in industry. Using an aqueous solution is characteristic of the preparation methods commonly employed to produce supported metal catalysts.

In order to compare the performance of the catalysts presented here, with those prepared frequently in the catalysis industry, platinum was supported on TiO_2 (A-R) by aqueous-impregnation and incipient wetness impregnation using platinum (IV) nitrate as the precursor. Figure 4.51 shows propane conversion as a function of temperature for the supported platinum catalysts prepared by these methods and calcined at 400 °C for 5 hours in static air.

     ■   1 wt. % Pt/TiO$_2$ (A-R) IMP   □   1 wt. % Pt/TiO$_2$ (A-R) IWI

              □   1 wt. % Pt/TiO$_2$ (A-R) modified IWI
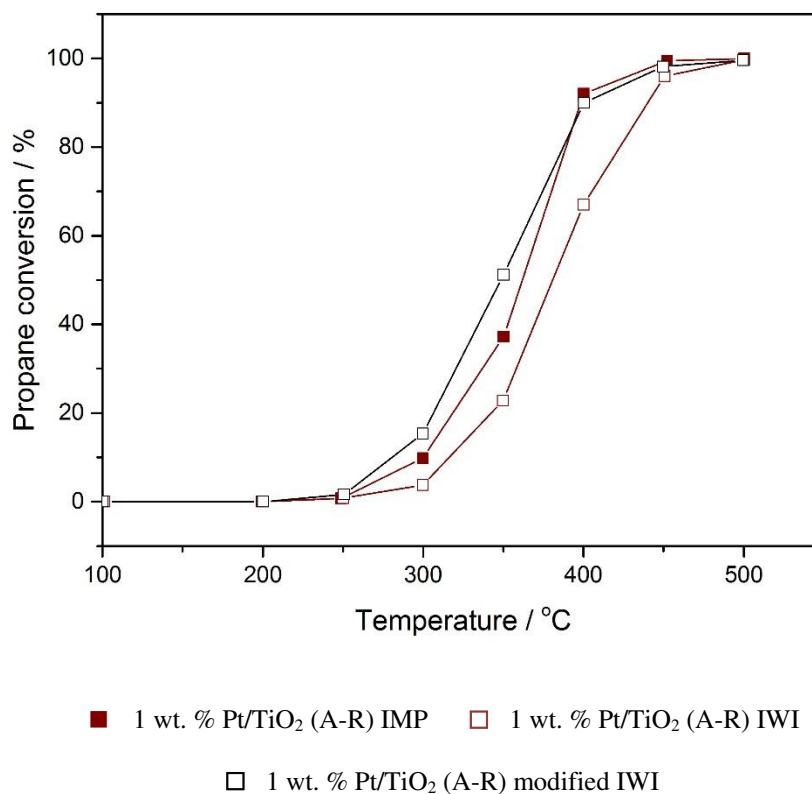
Figure 4.51. Total oxidation of propane over supported platinum catalysts

Reaction conditions: Flow reactor, GHSV = 50,000 h^{-1}, C$_3$H$_8$:O$_2$ = 1:50

Catalysts prepared by aqueous impregnation (IMP) and incipient wetness impregnation (IWI)

using Pt(NO$_3$)$_4$ as precursor and calcined at 400 ºC in static air

The performance of the Pt/TiO$_2$ (A-R) catalysts is comparable for the three preparation methods.

The T$_{10}$ and T$_{50}$ of the Pt/TiO$_2$ (A-R) catalyst prepared by different methods; aqueous and non-aqueous, are shown in Figure 4.52. Catalytic activity is equivalent across the group and differences in performance are within the error shown in Figure 4.20.
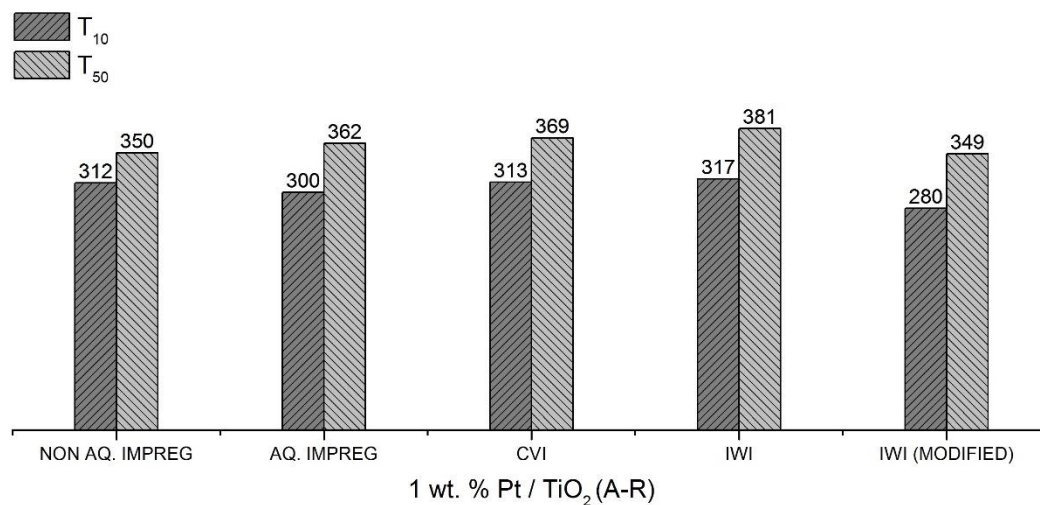
Figure 4.52. Temperature in degrees Celsius for 10 % propane conversion (T_{10}) and 50 % propane conversion (T_{50}) over 1 wt. % Pt supported on TiO_2 (ANATASE-RUTILE) prepared by different methods and calcined at 400 ºC in static air

XPS was used to investigate the oxidation state of the surface platinum species and their relative populations. Spectra in the Pt 4f binding energy are shown in Figure 4.53. They are fitted with two pairs of Gaussian-Lorenzian curves with Pt $4f_{7/2}$ binding energies between 71.8 and 72.0 eV and between 73.5 and 74.9 eV. The assignment of these is not completely clear. Based on XPS analysis of reference materials and previous studies [111] [112], bulk metallic platinum appears at 71.2 eV, platinum (II) oxide appears at 72.5 eV and platinum (IV) oxide at 74.5 eV. Hence, for the 1 wt. % Pt/TiO_2 (A-R) catalysts prepared by aqueous and incipient wetness impregnations, the XPS spectral lines are shifted by $\approx 0.6 - 1$ eV to binding energies between the characteristic values of metal and metal oxides. This shift is more pronounced for the aqueous impregnation than for the incipient wetness impregnation, where the volume of water during the preparation is drastically reduced, approximately equal to the pore volume of the support. The Pt $4f_{7/2}$ binding energy of the first pair of curves is relatively high for Pt^0 and as explained previously, a strong platinum-titania interaction could lead to a shift towards lower binding energies. Accordingly, it has

been proposed that platinum is in an oxidised form and that the peak at 71.8 – 72.0 eV corresponds to PtO and that at 73.5 – 73.9 eV to PtO_2. This should be considered carefully, as previous studies have confirmed that platinum supported on titania at a pH of 5-7, contains both metallic platinum (70.8 eV) and PtO (72.2 eV) [113]. In addition, various investigations [114] [115] have shown that variations in platinum particle size could also shift the binding energy and thus, the position of the lines. It was found that for platinum supported on TiO_2, SiO_2 and Al_2O_3, the Pt $4f_{7/2}$ line is shifted towards higher binding energies, which corresponds to a decrease in platinum particle size.
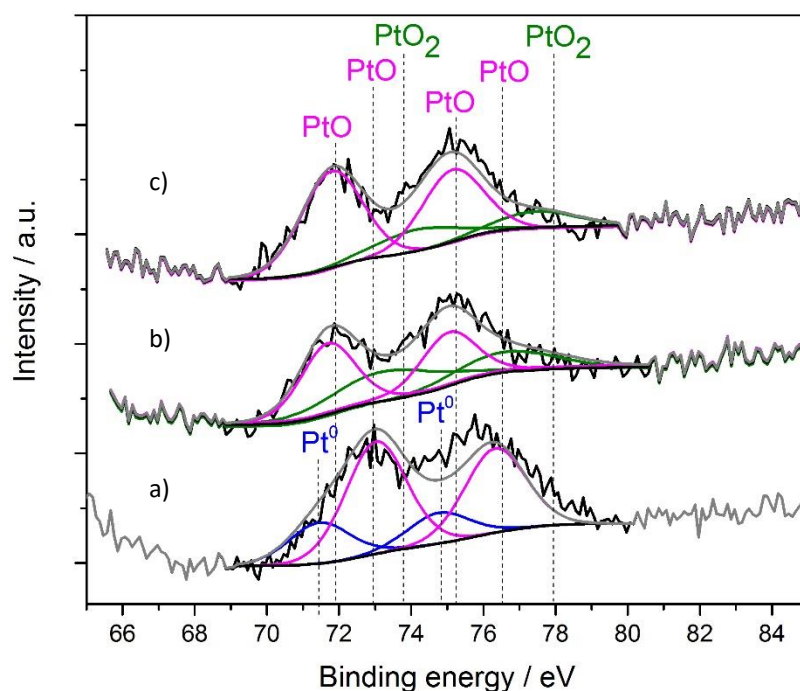
Figure 4.53. XPS spectra in the Pt 4f binding energy region of the 1 wt. % Pt/TiO_2 (A-R) prepared by: a) Non-aqueous impregnation   b) Aqueous Impregnation   c) Incipient Wetness Impregnation

Binding energy values and platinum species concentrations for 1 wt. % Pt/TiO_2 (A-R) prepared by non-aqueous and aqueous methods are summarised in Table 4.13. Both PtO and PtO_2 are present for the catalyst prepared by the three aqueous preparation methods. Of these, the concentration of PtO is higher ($\approx$ 78%) when platinum is supported on TiO_2 (A) by IWI, a preparation method which keeps the volume of water to a minimum. This indicates that platinum species in a higher oxidation state are favoured when a high concentration of water is present during the preparation. Note that although the surface platinum concentration overcomes the total loading of 1 wt. %, it is lower than that of the same catalyst prepared by a non-aqueous method.

Table 4.13. XPS quantitative analysis and Pt $4f_{7/2}$ core binding energies

of the Pt/TiO_2 (A-R) catalyst prepared by different methods

(numbers in parentheses are the relative concentration of the platinum species)

1 wt. % Pt/TiO$_2$ (A-R)	Pt		Pt^0	Pt^{2+}	Pt^{4+}
	At %	Wt %	eV (%)	eV (%)	eV (%)
CVI	0.60	4.33	71.6 (36.6)	72.6 (63.4)	0
NON AQ. IMP	0.42	3.07	71.5 (26.7)	73.0 (73.3)	0
AQ. IMP	0.24	1.82	0	71.8 (54.4)	73.5 (45.6)
IWI	0.32	2.39	0	72.0 (78.1)	74.0 (21.9)
IWI (modified)	0.38	2.83	0	72.1 (58.5)	73.9 (41.5)

HRTEM images in Figure 4.54. and 4.55 indicate that the size of the platinum particles decreases markedly when 1 wt. % Pt/TiO_2 (A-R) is prepared by aqueous and incipient wetness impregnation using $Pt(NO_3)_4$.
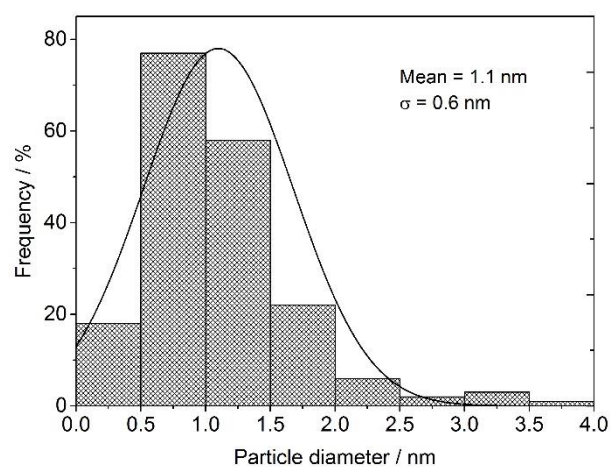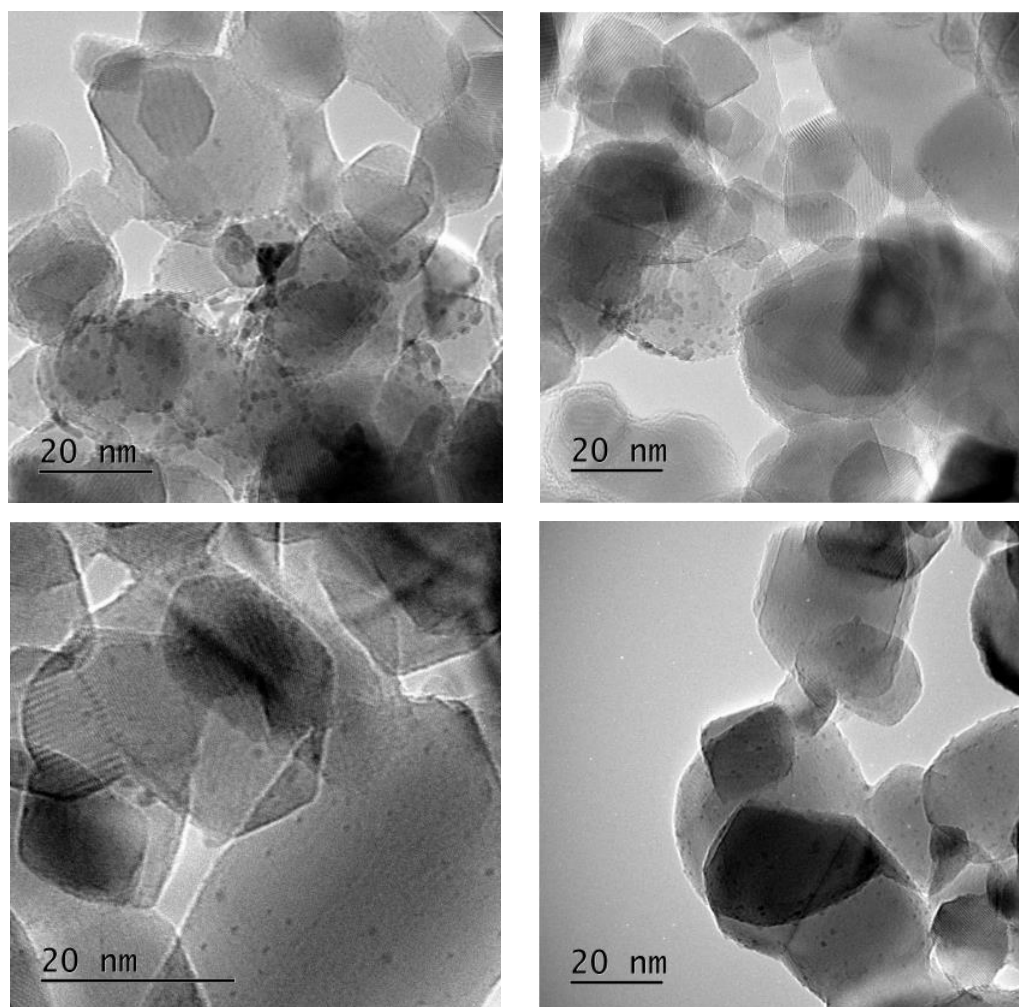
Figure 4.54. Selected HRTEM images and particle size distribution of the Pt/TiO$_2$ (A-R) catalyst

prepared by aqueous impregnation
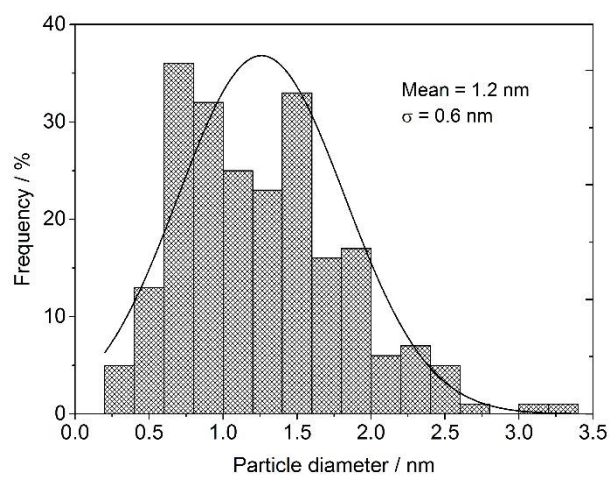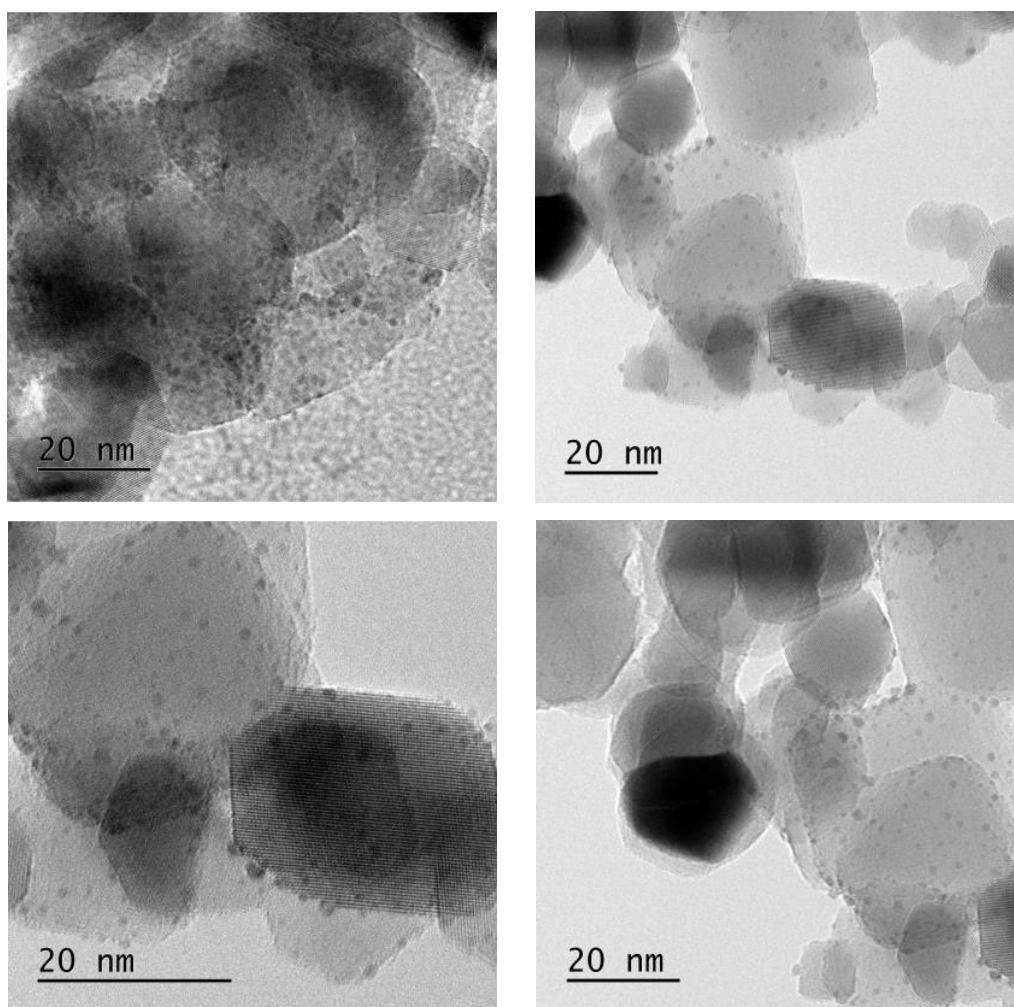
Figure 4.55. Selected HRTEM images and particle size distribution of 1 wt. % Pt/TiO_2 (A-R) prepared by incipient wetness impregnation

From the particle size distribution, a mean platinum particle size of 1.1 ± 0.6 is obtained for both aqueous preparation methods, this differs considerably from the poorly dispersed, large platinum particles found when the same catalyst was prepared by aqueous impregnation or chemical vapour impregnation. Despite the small particle size, platinum is not highly dispersed over the support's surface, but appears concentrated in certain regions of the titania.

Based on the results, it can be concluded that the metal precursor has a significant effect on the electronic and structural properties of platinum supported on TiO_2 (A-R), but not on the catalytic activity for propane oxidation under an oxidising atmosphere. It should be mentioned that not only the precursor but also the solvent was different, hence, this study compares platinum catalysts prepared via a non-ionic system, $Pt(acac)_2$ in toluene, with those prepared via an ionic system, $Pt(NO_3)_4$ in H_2O.

Platinum dispersion is enhanced when the catalyst is prepared in an aqueous environment, which gives rise to small nanoparticles. This could be explained in terms of the hydrophilicity of the system; as the hydrophilic platinum precursor will have a stronger interaction with the support due to the hydrophilic character of the titania. Besides, the binding energy of the Pt $4f_{7/2}$ in the XPS spectrum for the catalysts prepared in an aqueous solution is shifted towards higher values, lying between the characteristic values of bulk metallic platinum and its oxides. There are two possible explanations for this shift: (i) a strong metal support interaction will result in charge transfer from the support, modifying its electronic surface species and thus, the binding energy position and (ii) nanoparticle size can also affect the position of the peaks. Despite differences in these properties of the catalysts, no significant variation in catalytic performance is observed, probably because platinum is in an oxidised state.

4.3 Oxidation of nitric oxide to nitrogen dioxide

4.3.1 The effect of the support

The oxidation of nitric oxide (NO) to nitrogen dioxide (NO_2) on supported platinum catalysts under lean-burn conditions plays an important role in Diesel exhaust aftertreatment technologies [116] [117] [118] [119] [120]. The Diesel Particulate Filter (DPF) requires NO_2 for the oxidation of soot; Selective Catalytic Reduction (SCR) is promoted in a mixture of NO/NO_2 and the oxidation of NO is an essential first step of the storage mechanism for NO_x storage catalysts.

It is known that the activity of platinum catalysts towards NO oxidation is strongly influenced by the support [121] [122] [123]. Hence, the effect of the support on the oxidation of NO to NO_2 in the temperature range between 100 and 450 °C was assessed using the same platinum catalysts as tested for total the oxidation of propane. Conversion profiles for NO are presented in Figure 4.56. The main product for NO oxidation was NO_2 and formation of other nitrogen-containing products, such as N_2O, was negligible. As reported previously [124] [125], the catalytic conversion of NO to NO_2 is kinetically-controlled at low temperatures (T < 350 °C) and operates under equilibrium control at higher temperatures (T > 350 °C). After reaching thermodynamic equilibrium, the conversion of NO to NO_2 follows the thermodynamic equilibrium curve.

All the catalysts present the same conversion profile, with NO conversion and thus, the concentration of NO_2, reaching a maximum at 350 °C. Conversion then decreases at higher temperature, as the reaction is limited by the thermodynamic equilibrium.
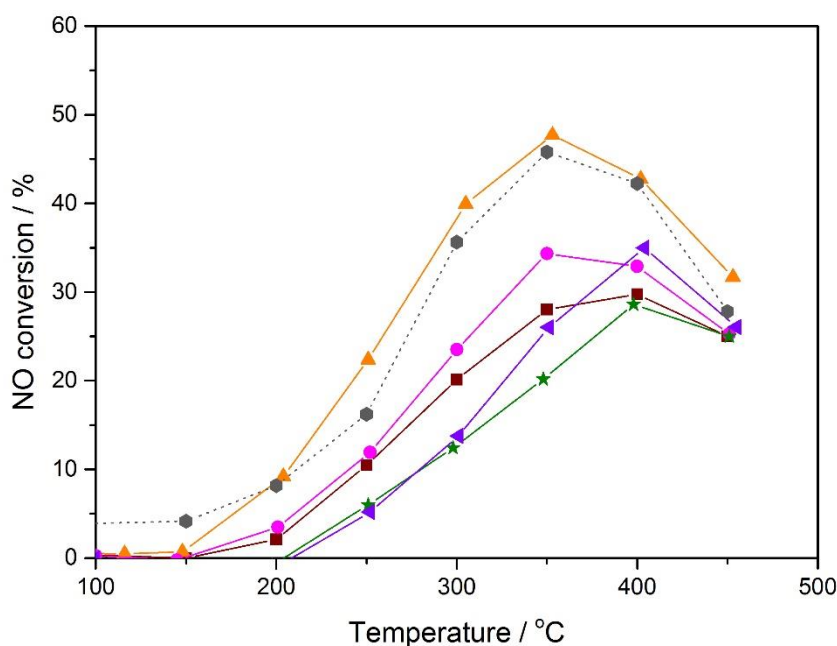
Figure 4.56. Oxidation of nitric oxide to nitrogen dioxide over supported platinum catalysts

Reaction conditions: Flow reactor, GHSV = 50,000 h^{-1}, NO:O$_2$ = 1:75

Catalysts prepared by non-aqueous impregnation and calcined at 400 $^{\circ}$C in static air

The activities of the 1 wt. % Pt catalysts for NO oxidation are significantly dependent on the supports. For the supported platinum catalysts studied, the activity order is:

1 wt. % Pt/TiO$_2$-SiO$_2$ (A)   <   1 wt. % Pt/Al$_2$O$_3$-SiO$_2$ (10 %)   <   1 wt. % Pt/TiO$_2$ (A-R)

<   1 wt. % Pt/TiO$_2$ (A)   <   2 wt. % Pt/γ-Al$_2$O$_3$ ≈ 1 wt. % Pt/TiO$_2$-SiO$_2$ (16 %, A-R)
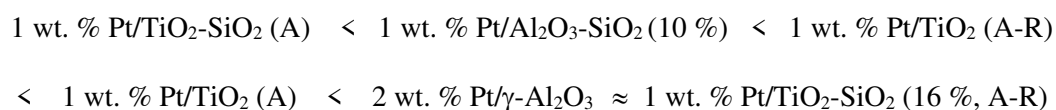
Figure 4.57 shows the degree of NO conversion observed over the supported platinum catalysts at 350 °C. 1 wt. % Pt/TiO_2-SiO_2 (16 % mol Si, A-R) (orange solid line in Figure 4.56) is the most active among the supported platinum catalysts studied with 48 % NO conversion to NO_2 shown at 350 °C. Its performance is comparable with that observed for a typical commercial oxidation catalyst, 2 wt. % Pt/Al_2O_3 (grey dashed line in Figure 4.56.) which presents 46 % conversion of NO to NO_2 at 350 °C.
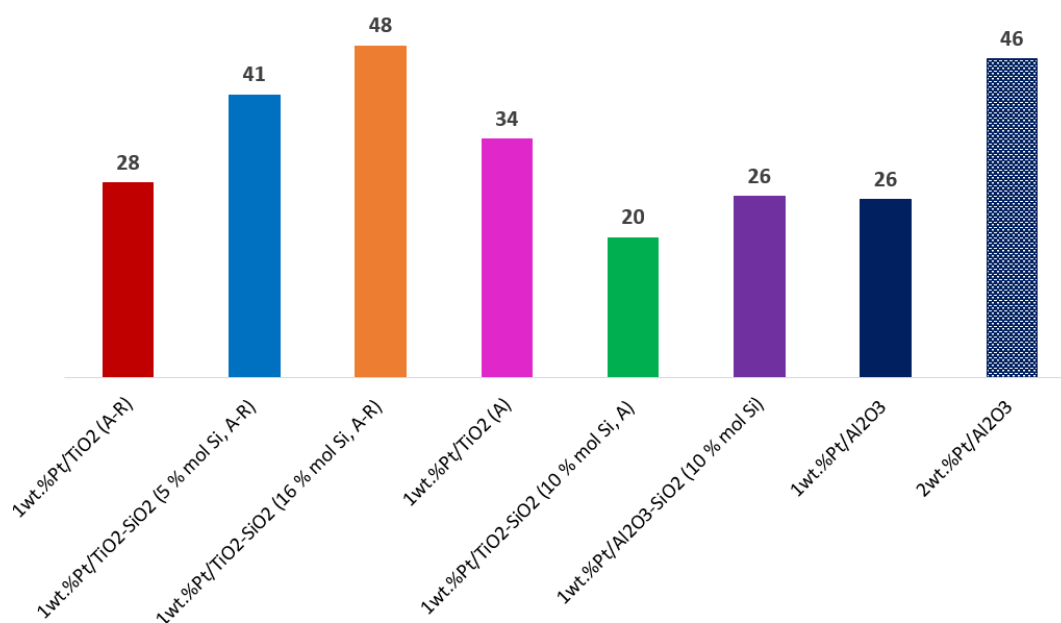
Figure 4.57. NO conversion in % for oxidation of NO to NO_2

over supported platinum catalysts at 350 °C

Reaction conditions: Flow reactor, GHSV = 50,000 h^{-1}, NO:O_2 = 1:75

In agreement with those results obtained for the total oxidation of propane, for the anatase-rutile based catalysts, catalytic activity for NO oxidation was promoted by addition of SiO_2 to the support. While 1 wt. % Pt/TiO_2 (A-R) gives 28 % conversion of NO to NO_2, 1 wt. % Pt/TiO_2-SiO_2 (16% mol Si, A-R) gives 48 % conversion. In fact, oxidation activity is almost doubled when the SiO_2 content of the support reaches 16 mol %.

Contrary to earlier data for total oxidation of propane, addition of SiO_2 to the Al_2O_3 support does not result in an improvement in NO oxidation activity, with 1 wt. % Pt/Al_2O_3-SiO_2 (10 %) presenting 26 % conversion at 350 °C. This is equal to that obtained for silica- free 1 wt. % Pt/Al_2O_3.

Once again, those catalysts obtained from the impregnation of platinum on anatase- only based supports, Pt/TiO_2-(SiO_2) (A), perform differently for NO oxidation when compared with their analogous anatase-rutile based catalysts, Pt/TiO_2-(SiO_2) (A-R). 1 wt. % Pt/TiO_2 (A-R) gives 34 % NO conversion at 350 °C and 1 wt. % Pt/TiO_2 (A) gives only 28 % conversion. Hence, platinum supported on anatase- only supports is more active than that supported on biphase anatase-rutile TiO_2 containing supports, although the difference in activity is not as significant as that observed for the total oxidation of propane. More interestingly, 1 wt. % Pt/TiO_2-SiO_2 (10% mol Si, A) presents the lowest oxidation activity among the catalysts studied, with 20 % NO conversion at 350 °C. Whilst addition of SiO_2 to the TiO_2 (A) support had no effect upon propane oxidation activity, this support modification led to a 41 % decrease in NO conversion at 350 °C

Many investigations have ascribed the oxidation activity of supported platinum catalysts to the presence of metallic platinum [122][126], and it is well known that oxygen poisoning of the catalyst inhibits NO oxidation and that conversion drops considerably when platinum is oxidised [123][127][128][129][130][131][132][133]. As illustrated in Figure 4.58, there is a linear relationship between oxidative NO conversion and the concentration of metallic platinum present in the catalyst at the beginning of the experiment. In general, an increase in the SiO_2 content of the support enhances the oxidation-resistance of platinum.
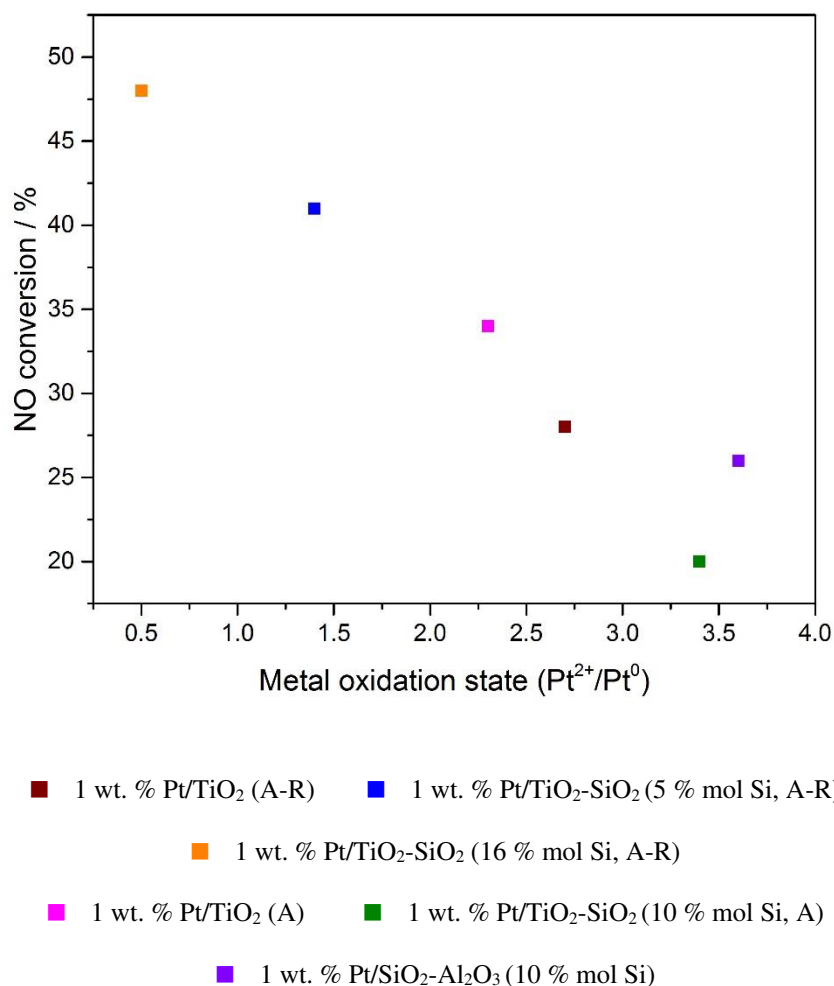
Figure 4.58 Activity of the supported platinum catalysts for oxidation of NO to NO_2 at 350 °C

as a function of the Pt^{2+}/Pt^0 ratio

The structure sensitive nature of NO oxidation has been investigated in previous work [123] [132] [133] [134] [135] [136]. It has been reported that Pt particle size influences the rate of NO oxidation and that when the dispersion is decreased, giving larger particles, the conversion of NO to NO_2 is promoted. This increase in activity with particle size is ascribed to the fact that small platinum particles are easier to oxidise than larger ones. Boubnov *et al* [136] studied structure-performance relationships for the catalytic oxidation of CO and NO over Pt/Al_2O_3 catalysts. They found that CO oxidation is size sensitive, with optimal conversion shown with

platinum particles of 2-3 nm. Lower conversion was observed with particles either smaller or larger than this. For NO oxidation, conversion increases with particle size, indicating that particles larger than *ca*. 5 nm possess a greater population of active sites for NO oxidation.

Based on the results presented in this thesis it is not possible to reach a clear conclusion as to whether NO oxidation is a structure sensitive reaction, under the conditions studied. Figure 4.27 shows that 1 wt. % Pt/TiO_2 (A-R) contains poorly dispersed, large platinum particles, and Figures 4.28 and 4.29 show highly dispersed small nanoparticles (2-5 nm) on 1 wt. % Pt/TiO_2-SiO_2 (16% mol Si, A-R). Platinum dispersion is enhanced with the SiO_2 content of the support, as is NO conversion, potentially due to the high concentration of metallic platinum on this catalyst. Platinum supported on the anatase-based mixed support, 1 wt. % Pt/TiO_2-SiO_2 (10% mol Si, A), is an interesting case study. Its performance for NO oxidation is poor (green line in Figure 4.56), which could be explained in terms of the oxidation state of the platinum, which is shown in Figure 4.58 to predominately present as its oxidised form (PtO). In addition, TEM analysis shown in Figure 4.31 confirms the presence of small platinum nanoparticles; 1 nm and subnanometer, on the TiO_2-SiO_2 (10% mol Si, A) support. The smaller size of the nanoparticles could be leading to the low conversion of this catalyst for NO oxidation but not for total oxidation of propane. The $NO/NO_2/O_2$ mixture could be more effective in oxidising the catalyst than the O_2, as the formation of surface oxides from oxygen is kinetically limited [128]. Hence, under the experimental conditions used for NO oxidation tests (0.1 % NO, 7.5 % O_2, He as balance) the small platinum particles are likely to be readily oxidised.

The existence of a strong relationship between the redox nature and activity of different platinum surface sites has been confirmed. The activity of a DOC changes during the NO

oxidation reaction; NO_2, because of its highly oxidising nature, promotes the formation of platinum oxides which thereby decreases catalyst activity. The formation of surface platinum oxide is reversible, with PtO reduced to Pt^0 above 350 °C due to thermal decay and also by NO at low temperatures [137].

Initial studies to determine the performance of the most active catalyst, 1 wt. % Pt/TiO_2-SiO_2 (16% mol Si, A-R), under real working conditions were carried out. Quantitative analysis obtained from XPS spectra of the catalyst before and after NO oxidation is presented Table 4.14. The concentration of metallic platinum does not decrease after reaction indicating that there is no irreversible formation of PtO during the NO oxidation reaction. Based on its performance in total oxidation of propane, it could be suggested that this catalyst will perform well under the transient temperature conditions characteristic of exhaust aftertreatment.

Table 4.14. Quantitative analysis of the supported platinum catalysts, before and after reaction, obtained from the XPS spectra

Catalyst		Pt		Pt^0	Pt^{2+}	Pt^{4+}
		At %	Wt %	Conc. %	Conc. %	Conc. %
1 wt. % Pt/TiO_2-SiO_2 (16 % mol Si, A-R)	Fresh	0.23	1.93	67.49	32.52	0
	After NO ox.	0.15	1.29	71.26	28.74	0

In order to study the activity- loss of supported platinum catalysts under strong oxidising conditions and assess the structure sensitive nature of the reaction, hysteresis experiments with characterisation before and after reaction should be performed.

4.3.2 *In situ* DRIFTS studies

To identify reaction intermediates at the catalyst surface, an in-situ FTIR study of NO oxidation over the supported platinum catalysts was performed.

Diffuse reflectance infrared fourier transform (DRIFT) spectra of surface adsorbed species on Pt catalysts under NO + O$_2$, and their evolution with temperature from 30 °C to 450 °C, are shown in Figure 4.59. A baseline spectrum was acquired prior to introducing the reactant gas mixture, which contained 0.45 % NO and 10 % O$_2$, in N$_2$ as diluent.

The adsorbed species on all catalysts are mainly nitrates and nitrites. It is clearly shown in Figure 4.59 that adsorption of NO leads to formation of nitrite species (NO$_2^-$) which are further oxidised to form nitrate species (NO$_3^-$). These reactions occur simultaneously, and the intensity of these bands decreases considerably at temperatures above 300 °C. Although the work presented here is only qualitative, as quantitative analysis requires response factors based on normalized areas determined using chemisorption, it is possible to analyse and compare the data in terms of relative peaks intensities.

1 wt. % Pt/TiO$_2$ (A-R) shows chelating nitrate at 1580 cm^{-1}, and bridging nitrate at 1610 cm^{-1}. There is also a broad peak centred at 1490 cm^{-1} due to linear nitrite. In addition, bridging nitrites appear at 1250 cm^{-1} and 1290 cm^{-1} respectively [138] [139]. The almost negligible peak at 1790-1810 cm^{-1} can be attributed to linear and gaseous NO. Increasing the temperature to 400 °C results in a gradual decrease in the intensity of bands corresponding to nitrates (chelating and bridging) and nitrites (linear and bridging). At 200 °C, a low intensity band at 1550 cm^{-1} is observed, which can be assigned to monodentate nitrate. This disappears at 400 °C. The spectrum of NO adsorbed on 1 wt. % Pt/TiO$_2$-SiO$_2$ (16 % mol Si, A-R) shows the peaks at 1580 cm^{-1} and 1610 cm^{-1}

previously assigned to chelating and bridging nitrate. Increasing the temperature leads the

bands to diminish, disappearing entirely at 300 °C.

1 wt. % Pt/TiO$_2$ (A-R)　　　　　**1 wt. % Pt/TiO$_2$-SiO$_2$ (16 % mol Si, A-R)**

1 wt. % Pt/TiO$_2$ (A)　　　　　**1 wt. % Pt/TiO$_2$-SiO$_2$ (10 % mol Si, A)**
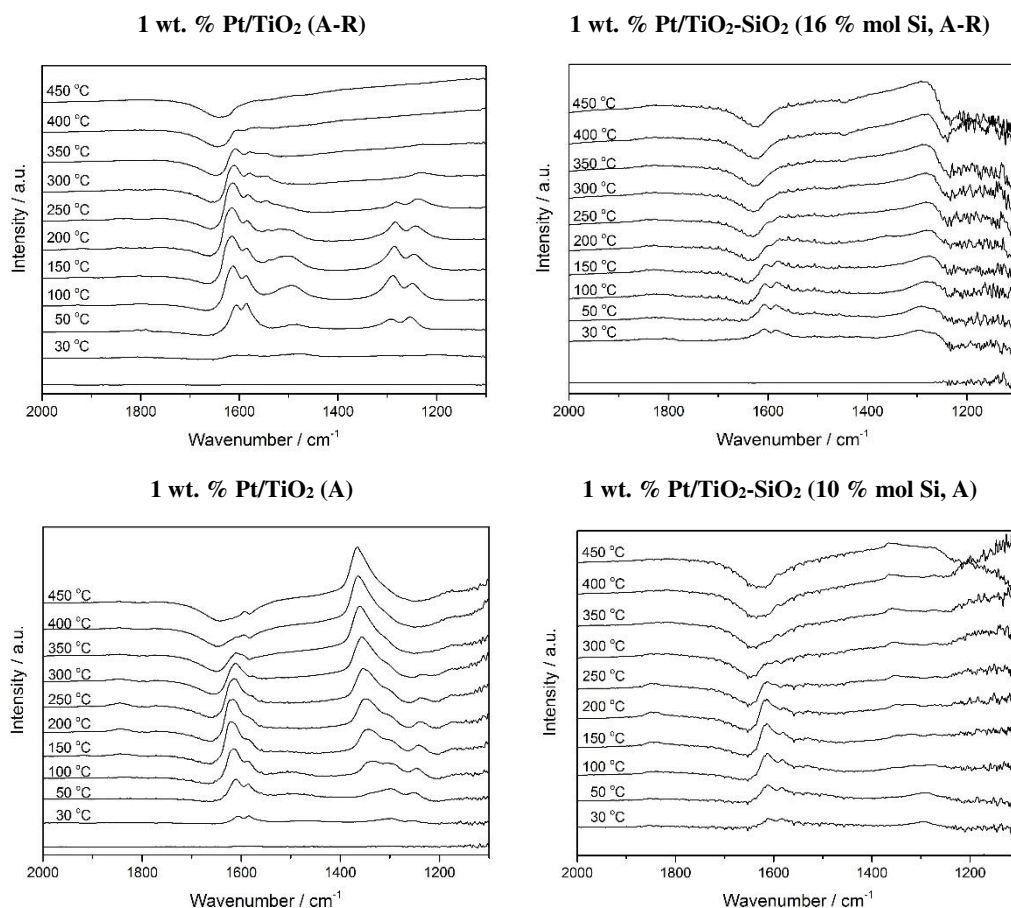
Figure 4.59 DRIFTS of NO adsorption at 30 - 450 °C on supported platinum catalysts
under NO + O$_2$ (0.5 % NO, 10 % O$_2$, N$_2$ balance)

The DRIFT spectra for 1 wt. % Pt/TiO$_2$ (A) are similar to those obtained for the anatase-

rutile based catalyst, 1 wt. % Pt/TiO$_2$ (A-R). Peaks previously assigned to nitrate (chelating,

bridging and monodentate) and nitrite (bridging) are observed, as is a new spectral band at

1350-1360 cm^{-1} which corresponds to free nitrate ion, NO$_3^-$ [140][141]. The relative intensity of

this NO$_3^-$ peak increases with temperature, and is still present at 450 °C. This implies that

at high temperatures, as reported previously with ceria based catalysts [140], the TiO$_2$ (A)

provides active oxygen for the oxidation of nitrites to nitrates and the transformation of different nitrate species from lower stability species to higher ones (from bidentate to monodentate and then to ionic nitrates). Hence, as discussed earlier in this chapter (Figure 4.46), anatase phase titania, TiO_2 (A), possesses highly reactive oxygen species that, in this case, promote the formation of ionic nitrate on the surface but not the oxidation of NO to NO_2.

In the case of 1 wt. % Pt/TiO_2-SiO_2 (10 % mol Si, A), DRIFT spectra are similar to those obtained for the anatase-rutile analogue, 1 wt. % Pt/TiO_2-SiO_2 (16 % mol Si, A-R). Distinctively, note that the peaks assigned to chelating and bridging nitrate (1580 cm^{-1} and 1610 cm^{-1}) are still present at temperatures above 250 °C. Also, a weak peak that corresponds to free nitrate ion, NO_3^-, is observed at high temperature.

The interpretation of DRIFTS data is not fully understood but the dramatic difference in the relative intensities is clear evidence that NO_x adsorption is limited by the oxidation of NO to NO_2. A strong chemisorption of nitrates and nitrites, which disfavour desorption due to their high thermal stability, could be related with a decrease in activity for NO oxidation. In this way the high NO oxidation activity of 1 wt. % Pt/TiO_2-SiO_2 (16 % mol Si, A-R) correlates with the fact that nitrate and nitrite bands are much weaker and almost absent above 150 °C.

Further DRIFTS experiments and the total uptake of NO_x should be measured in order to find routes involved in the NO_x adsorption and NO oxidation and therefore, propose a possible mechanism to explain the differences in the activity of these catalysts.

4.4 Conclusions

The oxidation properties of supported platinum catalysts and the effect of the support materials, in particular TiO_2-SiO_2 mixed metal oxides, were assessed.

It is found that the activity of supported platinum catalysts for total oxidation of propane and oxidation of NO to NO_2 is greatly affected by the support material. In general, their performance is enhanced by addition of SiO_2 to the TiO_2 support.

The order of activity for the supported 1 wt. % Pt catalysts, prepared by non-aqueous impregnation and calcined at 400 °C in static air, follows the sequence:

Pt/TiO_2 (A-R) < Pt/TiO_2-SiO_2 (5 %, A-R) ≈ Pt/Al_2O_3-SiO_2 (10 %) < Pt/TiO_2 (A)

< Pt/TiO_2-SiO_2 (16 %, A-R) ≈ Pt/TiO_2-SiO_2 (10 %, A)

for total oxidation of propane and

Pt/TiO_2-SiO_2 (10%, A) < Pt/Al_2O_3-SiO_2 (10 %) < Pt/TiO_2 (A-R) < Pt/TiO_2 (A)

< Pt/TiO_2-SiO_2 (5 %, A-R) < Pt/TiO_2-SiO_2 (16 %, A-R)

for oxidation of NO to NO_2

Among the oxidation platinum catalysts studied, 1 wt. % Pt/TiO_2-SiO_2 (16 % mol Si, A-R) is the most active. It is stable and gives high conversion for both oxidation reactions studied. Platinum is predominantly present in the metallic state and is highly dispersed over the support in the form of small (2-5 nm) spherical nanoparticles. No deactivation under steady and transient conditions is observed.

Evaluation of how the calcination atmosphere, preparation method and platinum precursor effect the catalytic activity was also performed. It can be concluded that these experimental

variables do not significantly affect catalytic activity and that it is the nature of the support used that led to variations in catalyst performance.

The activity of the platinum catalysts depends strongly on oxidation state, with platinum in metallic state being most active. However, it is not only the platinum oxidation state but the combination of several factors including metal dispersion, surface area, morphology and phase composition of the support that explains the variations in catalytic activity.

Addition of SiO_2 to TiO_2 supports results in an increase in support surface area and improved dispersion of platinum nanoparticles. Moreover, anatase- only TiO_2 presents a higher surface area than biphase anatase-rutile TiO_2 (A-R).

Platinum catalysts prepared using anatase-based supports, TiO_2-(SiO_2) (A), present high performance for total oxidation of propane but not for the oxidation of NO. These supports not only possess a high surface area but a "cloud shape" morphology with highly dispersed small TiO_2 crystallites. Morphology and phase composition play an active role in the redox properties of the support and its interaction with the metal particles.

It is widely recognised that platinum in metallic state is the most active species for the oxidation of hydrocarbons and NO with O_2. Results presented in this chapter show that there is a linear relationship between the oxidation state of platinum and catalytic activity for NO oxidation, with conversion clearly higher with an increasing presence of Pt^0. However, for the total oxidation of propane this relationship is not as unequivocal. While performance of anatase-rutile based catalysts, Pt/TiO_2-(SiO_2) (A-R), is enhanced with an increasing concentration of Pt^0, comparable activity is observed for anatase based catalysts, Pt/TiO_2-(SiO_2) (A), in which platinum exists predominantly as PtO.

Many studies have reported the structure sensitive nature of these oxidation reactions, with metal dispersion and particle size influencing conversion, as small platinum particles are more readily oxidised, thereby resulting in decreased catalyst performance. Contrarily, addition of SiO_2 to the TiO_2 support improves not only the platinum dispersion but also the metal oxidation resistance and thus small nanoparticles typical to the TiO_2-SiO_2 supports are less readily oxidised than those particles on the TiO_2 supports, which are generally larger. To assess the real effect of dispersion on catalytic activity, the oxidation activities of platinum catalysts which differ in metal dispersion and particle size, but are supported on the same metal oxide, should be evaluated.

Metal-support interactions are of great importance to understand the observed differences in catalytic activity. Through these interactions the support modifies the electronic and structural properties of the metal, creating unique active sites at the metal-support interface and even performing as an active participant in the reaction. Many examples covered during this chapter have demonstrated the relevance of such metal-support interactions. The most remarkable of these is that the extraordinary activity of 1 wt. % Pt/TiO_2 (A) is attributed to highly reactive oxygen species within the titania support, which promote the total oxidation of propane but not the oxidation of NO to NO_2.

Completion of this work will require further characterisation studies to fully understand the catalytic systems, and stability tests under realistic conditions for those promising catalysts found.

4.5 References

1.   Choudhary, T. V.; Banerjee, S.; Choudhary, V. R., Catalysts for combustion of methane and lower alkanes. *Applied Catalysis A: General* **2002,** *234* (1–2), 1-23.

2.   Taylor, M. N.; Zhou, W.; Garcia, T.; Solsona, B.; Carley, A. F.; Kiely, C. J.; Taylor, S. H., Synergy between tungsten and palladium supported on titania for the catalytic total oxidation of propane. *Journal of Catalysis* **2012,** *285* (1), 103-114.

3.   Okal, J.; Zawadzki, M.; Krajczyk, L., Light alkane oxidation over Ru supported on ZnAl2O4, CeO2 and Al2O3. *Catalysis Today* **2011,** *176* (1), 173-176.

4.   Taylor, M.; Ndifor, E. N.; Garcia, T.; Solsona, B.; Carley, A. F.; Taylor, S. H., Deep oxidation of propane using palladium–titania catalysts modified by niobium. *Applied Catalysis A: General* **2008,** *350* (1), 63-70.

5.   Garcia, T.; Solsona, B.; Murphy, D. M.; Antcliff, K. L.; Taylor, S. H., Deep oxidation of light alkanes over titania-supported palladium/vanadium catalysts. *Journal of Catalysis* **2005,** *229* (1), 1-11.

6.   Passos, F.; Oliveira, E.; Mattos, L.; Noronha, F., Effect of the support on the mechanism of partial oxidation of methane on platinum catalysts. *Catalysis Letters* **2006,** *110* (1-2), 161-167.

7.   Hoyle, N. D.; Kumarasamy, P.; Self, V. A.; Sermon, P. A.; Vong, M. S. W., Catalysis of H2, CO and alkane oxidation–combustion over Pt/Silica catalysts: evidence of coupling and promotion. *Catalysis Today* **1999,** *47* (1–4), 45-49.

8.   Wang, B.; Wu, X.; Ran, R.; Si, Z.; Weng, D., IR characterization of propane oxidation on Pt/CeO2–ZrO2: The reaction mechanism and the role of Pt. *Journal of Molecular Catalysis A: Chemical* **2012,** *356* (0), 100-105.

9.   Kobayashi, M.; Morita, A.; Ikeda, M., The support effect in oxidizing atmosphere on propane combustion over platinum supported on TiO2, TiO2–SiO2 and TiO2–SiO2–WO3. *Applied Catalysis B: Environmental* **2007,** *71* (1–2), 94-100.

10.   Yoshida, H.; Yazawa, Y.; Hattori, T., Effects of support and additive on oxidation state and activity of Pt catalyst in propane combustion. *Catalysis Today* **2003,** *87* (1–4), 19-28.

11.   Yazawa, Y.; Yoshida, H.; Takagi, N.; Komai, S.-i.; Satsuma, A.; Hattori, T., Acid Strength of Support Materials as a Factor Controlling Oxidation State of Palladium Catalyst for Propane Combustion. *Journal of Catalysis* **1999,** *187* (1), 15-23.

12.   Wang, B.; Wu, X.; Ran, R.; Si, Z.; Weng, D., Participation of sulfates in propane oxidation on Pt/SO42–/CeO2–ZrO2 catalyst. *Journal of Molecular Catalysis A: Chemical* **2012,** *361–362*, 98-103.

13.   Samantaray, S. K.; Parida, K., Modified TiO2–SiO2 mixed oxides: 1. Effect of manganese concentration and activation temperature towards catalytic combustion of volatile organic compounds. *Applied Catalysis B: Environmental* **2005,** *57* (2), 83-91.

14.   Kułażyński, M.; van Ommen, J. G.; Trawczyński, J.; Walendziewski, J., Catalytic combustion of trichloroethylene over TiO2-SiO2 supported catalysts. *Applied Catalysis B: Environmental* **2002,** *36* (3), 239-247.

15.   Kim, M.-Y.; Choi, J.-S.; Toops, T.; Jeong, E.-S.; Han, S.-W.; Schwartz, V.; Chen, J., Coating SiO2 Support with TiO2 or ZrO2 and Effects on Structure and CO Oxidation Performance of Pt Catalysts. *Catalysts* **2013,** *3* (1), 88-103.

16.   Avila, M. S.; Vignatti, C. I.; Apesteguía, C. R.; Garetto, T. F., Effect of support on the deep oxidation of propane and propylene on Pt-based catalysts. *Chemical Engineering Journal* **2014,** *241* (0), 52-59.

17.   Mitsui, T.; Tsutsui, K.; Matsui, T.; Kikuchi, R.; Eguchi, K., Catalytic abatement of acetaldehyde over oxide-supported precious metal catalysts. *Applied Catalysis B: Environmental* **2008,** *78* (1–2), 158-165.

18.   Tsou, J.; Magnoux, P.; Guisnet, M.; Órfão, J. J. M.; Figueiredo, J. L., Catalytic oxidation of volatile organic compounds: Oxidation of methyl-isobutyl-ketone over Pt/zeolite catalysts. *Applied Catalysis B: Environmental* **2005,** *57* (2), 117-123.

19.   Performance of doped Pt/TiO, (W6+) catalysts for combustion of volatile organic compounds (VOCs). *Applied Catalysis B: Environmental* **1998,** *15*, 75-92.

20.   γ-Alumina as a Support for Catalysts: A Review of Fundamental Aspects. *Eur. Journal Inorganic Chemistry* **2005**, 3393-3403.

21.   Argyle, M.; Bartholomew, C., Heterogeneous Catalyst Deactivation and Regeneration: A Review. *Catalysts* **2015,** *5* (1), 145.

22.   Gandhi, H. S.; Shelef, M., Effects of sulphur on noble metal automotive catalysts. *Applied Catalysis* **1991,** *77* (2), 175-186.

23.   Melchor, A.; Garbowski, E.; Mathieu, M. V.; Primet, M., Sulfur poisoning of Pt/Al2O3 catalysts, I. Determination of sulfur coverage by infrared spectroscopy. *Reaction Kinetics and Catalysis Letters 29* (2), 371-377.

24.   Nasri, N. S.; Jones, J. M.; Dupont, V. A.; Williams, A., A Comparative Study of Sulfur Poisoning and Regeneration of Precious-Metal Catalysts. *Energy & Fuels* **1998,** *12* (6), 1130-1134.

25.   Titanium Dioxide as a Catalyst Support in Heterogeneous Catalysis. *The Scientific World Journal* **2014**.

26.   Escandón, L. S.; Ordóñez, S.; Vega, A.; Díez, F. V., Sulphur poisoning of palladium catalysts used for methane combustion: Effect of the support. *Journal of Hazardous Materials* **2008,** *153* (1–2), 742-750.

27.   Matsumoto, S. i.; Ikeda, Y.; Suzuki, H.; Ogai, M.; Miyoshi, N., NOx storage-reduction catalyst for automotive exhaust with improved tolerance against sulfur poisoning. *Applied Catalysis B: Environmental* **2000,** *25* (2–3), 115-124.

28.   Sheu, H.-S.; Lee, J.-F.; Shyu, S.-G.; Chou, W.-W.; Chang, J.-R., Sulfur resistance enhancement by grafted TiO2 in SiO2-supported Pd catalysts: Role of grafted TiO2 and genesis of Pd clusters. *Journal of Catalysis* **2009,** *266* (1), 15-25.

29.   Min, B. K.; Santra, A. K.; Goodman, D. W., Understanding silica-supported metal catalysts: Pd/silica as a case study. *Catalysis Today* **2003,** *85* (2–4), 113-124.

30.   Yazawa, Y.; Takagi, N.; Yoshida, H.; Komai, S.-i.; Satsuma, A.; Tanaka, T.; Yoshida, S.; Hattori, T., The support effect on propane combustion over platinum catalyst: control of the oxidation-resistance of platinum by the acid strength of support materials. *Applied Catalysis A: General* **2002,** *233* (1–2), 103-112.

31.   Men, Y.; Kolb, G.; Zapf, R.; Pennemann, H.; Hessel, V., Total combustion of propane in a catalytic microchannel combustor. *Chemical Engineering Research and Design* **2009,** *87* (1), 91-96.

32.   Galisteo, F. C.; Mariscal, R.; Granados, M. L.; Fierro, J. L. G.; Daley, R. A.; Anderson, J. A., Reactivation of sintered Pt/Al2O3 oxidation catalysts. *Applied Catalysis B: Environmental* **2005,** *59* (3–4), 227-233.

33.   van den Tillaart, J. A. A.; Leyrer, J.; Eckhoff, S.; Lox, E. S., Effect of support oxide and noble metal precursor on the activity of automotive diesel catalysts. *Applied Catalysis B: Environmental* **1996,** *10* (1–3), 53-68.

34.   Structure, Surface Properties and Photocatalytic Activity of TiO2 and TiO2/SiO2 Catalysts Prepared at Different pH Values. *Acta Phys. -Chim. Sin.* **2011,** *27* (6), 1487-1492.

35.   Kemdeo, S. M.; Sapkal, V. S.; Chaudhari, G. N., TiO2–SiO2 mixed oxide supported MoO3 catalyst: Physicochemical characterization and activities in nitration of phenol. *Journal of Molecular Catalysis A: Chemical* **2010,** *323* (1–2), 70-77.

36.   Guan, K., Relationship between photocatalytic activity, hydrophilicity and self-cleaning effect of TiO2/SiO2 films. *Surface and Coatings Technology* **2005,** *191* (2–3), 155-160.

37.   Liu, T.-C.; Cheng, T.-I., Effects of SiO2 on the catalytic properties of TiO2 for the incineration of chloroform. *Catalysis Today* **1995,** *26* (1), 71-77.

38.   Properties of TiO2-SiO2 Mixed Oxides and Photocatalytic Oxidation of Heptane and Sulfur Dioxide.

39.   Liu, Z. F.; Tabora, J.; Davis, R. J., Relationships between Microstructure and Surface Acidity of Ti-Si Mixed Oxide Catalysts. *Journal of Catalysis* **1994,** *149* (1), 117-126.

40.   Doolin, P. K.; Alerasool, S.; Zalewski, D. J.; Hoffman, J. F., Acidity studies of titania-silica mixed oxides. *Catalysis Letters* **1994,** *25* (3-4), 209-223.

41.   Gao, X.; Bare, S. R.; Fierro, J. L. G.; Banares, M. A.; Wachs, I. E., Preparation and in-Situ Spectroscopic Characterization of Molecularly Dispersed Titanium Oxide on Silica. *The Journal of Physical Chemistry B* **1998,** *102* (29), 5653-5666.

42.   Tanabe, K.; Sumiyoshi, T.; Shibata, K.; Kiyoura, T.; Kitagawa, J., A New Hypothesis Regarding the Surface Acidity of Binary Metal Oxides. *Bulletin of the Chemical Society of Japan* **1974,** *47* (5), 1064-1066.

43.   Notari, B.; Willey, R. J.; Panizza, M.; Busca, G., Which sites are the active sites in TiO2–SiO2 mixed oxides? *Catalysis Today* **2006,** *116* (2), 99-110.

44.   Bonelli, B.; Cozzolino, M.; Tesser, R.; Di Serio, M.; Piumetti, M.; Garrone, E.; Santacesaria, E., Study of the surface acidity of TiO2/SiO2 catalysts by means of FTIR measurements of CO and NH3 adsorption. *Journal of Catalysis* **2007,** *246* (2), 293-300.

45.   Lu, J.; Kosuda, K. M.; Van Duyne, R. P.; Stair, P. C., Surface Acidity and Properties of TiO2/SiO2 Catalysts Prepared by Atomic Layer Deposition: UV–visible Diffuse Reflectance, DRIFTS, and Visible Raman Spectroscopy Studies. *The Journal of Physical Chemistry C* **2009,** *113* (28), 12412-12418.

46.   Ohtani, B.; Prieto-Mahaney, O. O.; Li, D.; Abe, R., What is Degussa (Evonik) P25? Crystalline composition analysis, reconstruction from isolated pure particles and photocatalytic activity test. *Journal of Photochemistry and Photobiology A: Chemistry* **2010,** *216* (2–3), 179-182.

47.   Zhang, X.; Zhang, F.; Chan, K.-Y., Synthesis of titania–silica mixed oxide mesoporous materials, characterization and photocatalytic properties. *Applied Catalysis A: General* **2005,** *284* (1–2), 193-198.

48.   Siuzdak, K.; Sawczak, M.; Klein, M.; Nowaczyk, G.; Jurga, S.; Cenian, A., Preparation of platinum modified titanium dioxide nanoparticles with the use of laser ablation in water. *Physical Chemistry Chemical Physics* **2014,** *16* (29), 15199-15206.

49.   Ou, H.-H.; Lo, S.-L., Effect of Pt/Pd-doped TiO2 on the photocatalytic degradation of trichloroethylene. *Journal of Molecular Catalysis A: Chemical* **2007,** *275* (1–2), 200-205.

50.   Burch, R.; Halpin, E.; Hayes, M.; Ruth, K.; Sullivan, J. A., The nature of activity enhancement for propane oxidation over supported Pt catalysts exposed to sulphur dioxide. *Applied Catalysis B: Environmental* **1998,** *19* (3–4), 199-207.

51.   Gluhoi, A. C.; Bogdanchikova, N.; Nieuwenhuys, B. E., Total oxidation of propene and propane over gold–copper oxide on alumina catalysts: Comparison with Pt/Al2O3. *Catalysis Today* **2006,** *113* (3–4), 178-181.

52.   Yazawa, Y.; Yoshida, H.; Hattori, T., The support effect on platinum catalyst under oxidizing atmosphere: improvement in the oxidation-resistance of platinum by the electrophilic property of support materials. *Applied Catalysis A: General* **2002,** *237* (1–2), 139-148.

53.   Zhang, C.; He, H.; Tanaka, K.-i., Catalytic performance and mechanism of a Pt/TiO2 catalyst for the oxidation of formaldehyde at room temperature. *Applied Catalysis B: Environmental* **2006,** *65* (1–2), 37-43.

54.   Karakas, G.; Yetisemiyen, P., Room Temperature Photocatalytic Oxidation of Carbon Monoxide Over Pd/TiO2–SiO2 Catalysts. *Topics in Catalysis* **2013,** *56* (18-20), 1883-1891.

55.   Arun Kumar, D.; Merline Shyla, J.; Xavier, F., Synthesis and characterization of TiO2/SiO2 nano composites for solar cell applications. *Appl Nanosci* **2012,** *2* (4), 429-436.

56.   Wu, X.; Zhang, L.; Weng, D.; Liu, S.; Si, Z.; Fan, J., Total oxidation of propane on Pt/WOx/Al2O3 catalysts by formation of metastable Ptdelta+ species interacted with WOx clusters. *J Hazard Mater* **2012,** *225-226*, 146-54.

57.   Jiang, Z.; Yang, Y.; Shangguan, W.; Jiang, Z., Influence of Support and Metal Precursor on the State and CO Catalytic Oxidation Activity of Platinum Supported on TiO2. *The Journal of Physical Chemistry C* **2012,** *116* (36), 19396-19404.

58.   Ruiz-Martinez, J.; Sepulveda-Escribano, A.; Anderson, J. A.; Rodriguez-Reinoso, F., Spectroscopic and microcalorimetric study of a TiO2-supported platinum catalyst. *Physical Chemistry Chemical Physics* **2009,** *11* (6), 917-920.

59.   Kim, M.-Y.; Choi, J.-S.; Toops, T.; Jeong, E.-S.; Han, S.-W.; Schwartz, V.; Chen, J., Coating SiO2 Support with TiO2 or ZrO2 and Effects on Structure and CO Oxidation Performance of Pt Catalysts. *Catalysts* **2013,** *3* (1), 88.

60.   Zhu, F.; Dong, H.; Wang, Y.; Wu, D.; Li, J.; Pan, J.; Li, Q.; Ai, X.; Zhang, J.; Xu, D., Dual-functional hetero-structured TiO2 nanotrees composed of rutile trunks and anatase branches for improved performance of quantum dot-sensitized solar cells. *Physical Chemistry Chemical Physics* **2013,** *15* (41), 17798-17803.

61.   Qing, Z.; Jieshu, Q.; Hao, P.; Luo, T.; Xingfu, Z., Synergistic manipulation of micro-nanostructures and composition: anatase/rutile mixed-phase TiO 2 hollow micro-nanospheres with hierarchical mesopores for photovoltaic and photocatalytic applications. *Nanotechnology* **2011,** *22* (39), 395703.

62.   Yang, Y.; Su, F.; Zhang, S.; Guo, W.; Yuan, X.; Guo, Y., Fabrication of metallic platinum doped ordered mesoporous titania–silica materials with excellent simulated sunlight and visible light photocatalytic activity. *Colloids and Surfaces A: Physicochemical and Engineering Aspects* **2012,** *415* (0), 399-405.

63.   Liu, Y.; Ma, X.; Wang, S.; Gong, J., The nature of surface acidity and reactivity of MoO3/SiO2 and MoO3/TiO2–SiO2 for transesterification of dimethyl oxalate with phenol: A comparative investigation. *Applied Catalysis B: Environmental* **2007,** *77* (1–2), 125-134.

64.   Min, B. K.; Wallace, W. T.; Goodman, D. W., Synthesis of a Sinter-Resistant, Mixed-Oxide Support for Au Nanoclusters†. *The Journal of Physical Chemistry B* **2004,** *108* (38), 14609-14615.

65.   Garetto, T. F.; Rincón, E.; Apesteguía, C. R., Deep oxidation of propane on Pt-supported catalysts: drastic turnover rate enhancement using zeolite supports. *Applied Catalysis B: Environmental* **2004,** *48* (3), 167-174.

66.   Salomons, S.; Hayes, R. E.; Votsmeier, M.; Drochner, A.; Vogel, H.; Malmberg, S.; Gieshoff, J., On the use of mechanistic CO oxidation models with a platinum monolith catalyst. *Applied Catalysis B: Environmental* **2007,** *70* (1–4), 305-313.

67.   Hegedus, L. L.; Oh, S. H.; Baron, K., MULTIPLE STEADY STATES IN AN ISOTHERMAL, INTEGRAL REACTOR - CATALYTIC-OXIDATION OF CARBON-MONOXIDE OVER PLATINUM-ALUMINA. *Aiche Journal* **1977,** *23* (5), 632-642.

68.   Hanaor, D. H.; Sorrell, C., Review of the anatase to rutile phase transformation. *J Mater Sci* **2011,** *46* (4), 855-874.

69.   Tauster, S. J.; Fung, S. C.; Garten, R. L., Strong metal-support interactions. Group 8 noble metals supported on titanium dioxide. *Journal of the American Chemical Society* **1978,** *100* (1), 170-175.

70.   Lin, W.; Herzing, A. A.; Kiely, C. J.; Wachs, I. E., Probing Metal−Support Interactions under Oxidizing and Reducing Conditions: In Situ Raman and Infrared Spectroscopic and Scanning Transmission Electron Microscopic−X-ray Energy-Dispersive Spectroscopic Investigation of Supported Platinum Catalysts. *The Journal of Physical Chemistry C* **2008,** *112* (15), 5942-5951.

71.   Aramendía, M. A.; Colmenares, J. C.; Marinas, A.; Marinas, J. M.; Moreno, J. M.; Navío, J. A.; Urbano, F. J., Effect of the redox treatment of Pt/TiO2 system on its photocatalytic behaviour in the gas phase selective photooxidation of propan-2-ol. *Catalysis Today* **2007,** *128* (3–4), 235-244.

72.   Iida, H.; Igarashi, A., Characterization of a Pt/TiO2 (rutile) catalyst for water gas shift reaction at low-temperature. *Applied Catalysis A: General* **2006,** *298*, 152-160.

73.   Mei, Z.; Li, Y.; Fan, M.; Zhao, L.; Zhao, J., Effect of the interactions between Pt species and ceria on Pt/ceria catalysts for water gas shift: The XPS studies. *Chemical Engineering Journal* **2015,** *259*, 293-302.

74.   Liotta, L. F.; Longo, A.; Macaluso, A.; Martorana, A.; Pantaleo, G.; Venezia, A. M.; Deganello, G., Influence of the SMSI effect on the catalytic activity of a Pt(1%)/Ce0.6Zr0.4O2 catalyst: SAXS, XRD, XPS and TPR investigations. *Applied Catalysis B: Environmental* **2004,** *48* (2), 133-149.

75.   Schierbaum, K. D.; Fischer, S.; Torquemada, M. C.; de Segovia, J. L.; Román, E.; Martín-Gago, J. A., The interaction of Pt with TiO2(110) surfaces: a comparative XPS, UPS, ISS, and ESD study. *Surface Science* **1996,** *345* (3), 261-273.

76.   Lewera, A.; Timperman, L.; Roguska, A.; Alonso-Vante, N., Metal–Support Interactions between Nanosized Pt and Metal Oxides (WO3 and TiO2) Studied Using X-ray Photoelectron Spectroscopy. *The Journal of Physical Chemistry C* **2011,** *115* (41), 20153-20159.

77.   Zhang, M.; Jin, Z.; Zhang, Z.; Dang, H., Study of strong interaction between Pt and TiO2 under oxidizing atmosphere. *Applied Surface Science* **2005,** *250* (1–4), 29-34.

78.   Ramaker, D. E.; de Graaf, J.; van Veen, J. A. R.; Koningsberger, D. C., Nature of the Metal–Support Interaction in Supported Pt Catalysts: Shift in Pt Valence Orbital Energy and Charge Rearrangement. *Journal of Catalysis* **2001,** *203* (1), 7-17.

79.   Santos, J.; Phillips, J.; Dumesic, J. A., Metal-support interactions between iron and titania for catalysts prepared by thermal decomposition of iron pentacarbonyl and by impregnation. *Journal of Catalysis* **1983,** *81* (1), 147-167.

80.   Bowker, M.; Stone, P.; Morrall, P.; Smith, R.; Bennett, R.; Perkins, N.; Kvon, R.; Pang, C.; Fourre, E.; Hall, M., Model catalyst studies of the strong metal–support interaction: Surface structure identified by STM on Pd nanoparticles on TiO2(110). *Journal of Catalysis* **2005,** *234* (1), 172-181.

81.   Raupp, G. B.; Dumesic, J. A., Effect of titania surface species on the chemisorption of carbon monoxide and hydrogen on polycrystalline nickel. *The Journal of Physical Chemistry* **1984,** *88* (4), 660-663.

82.   Belzunegui, J. P.; Sanz, J.; Rojo, J. M., Differentiation of two stages during establishment of strong metal-support interaction in rhodium/titania catalysts. *Journal of the American Chemical Society* **1990,** *112* (10), 4066-4068.

83.   Haerudin, H.; Bertel, S.; Kramer, R., Surface stoichiometry of 'titanium suboxide' Part I Volumetric and FTIR study. *Journal of the Chemical Society, Faraday Transactions* **1998,** *94* (10), 1481-1487.

84.   Xiaoyuan, J.; Guanghui, D.; Liping, L.; Yingxu, C.; Xiaoming, Z., Catalytic activities of CuO/TiO2 and CuO-ZrO2/TiO2 in NO + CO reaction. *Journal of Molecular Catalysis A: Chemical* **2004,** *218* (2), 187-195.

85.   Wang, J. A.; Cuan, A.; Salmones, J.; Nava, N.; Castillo, S.; Morán-Pineda, M.; Rojas, F., Studies of sol–gel TiO2 and Pt/TiO2 catalysts for NO reduction by CO in an oxygen-rich condition. *Applied Surface Science* **2004,** *230* (1–4), 94-105.

86.   de Resende, N. S.; Eon, J.-G.; Schmal, M., Pt–TiO2–γ Al2O3Catalyst: I. Dispersion of Platinum on Alumina-Grafted Titanium Oxide. *Journal of Catalysis* **1999,** *183* (1), 6-13.

87.   Epling, W. S.; Cheekatamarla, P. K.; Lane, A. M., Reaction and surface characterization studies of titania-supported Co, Pt and Co/Pt catalysts for the selective oxidation of CO in H2-containing streams. *Chemical Engineering Journal* **2003,** *93* (1), 61-68.

88.   Pérez-Hernández, R.; Gómez-Cortés, A.; Arenas-Alatorre, J.; Rojas, S.; Mariscal, R.; Fierro, J. L. G.; Díaz, G., SCR of NO by CH4 on Pt/ZrO2–TiO2 sol–gel catalysts. *Catalysis Today* **2005,** *107–108*, 149-156.

89.   Zhu, H.; Qin, Z.; Shan, W.; Shen, W.; Wang, J., Pd/CeO2–TiO2 catalyst for CO oxidation at low temperature: a TPR study with H2 and CO as reducing agents. *Journal of Catalysis* **2004,** *225* (2), 267-277.

90.   Yao, H. C.; Yao, Y. F. Y., Ceria in automotive exhaust catalysts. *Journal of Catalysis* **1984,** *86* (2), 254-265.

91.   Laachir, A.; Perrichon, V.; Badri, A.; Lamotte, J.; Catherine, E.; Lavalley, J. C.; El Fallah, J.; Hilaire, L.; Le Normand, F.; Quemere, E.; Sauvion, G. N.; Touret, O., Reduction of CeO2 by hydrogen. Magnetic susceptibility and Fourier-transform infrared, ultraviolet and X-ray photoelectron spectroscopy measurements. *Journal of the Chemical Society, Faraday Transactions* **1991,** *87* (10), 1601-1609.

92.   Bernal, S.; Calvino, J. J.; Cifredo, G. A.; Gatica, J. M.; Omil, J. A. P.; Pintado, J. M., Hydrogen chemisorption on ceria: influence of the oxide surface area and degree of reduction. *Journal of the Chemical Society, Faraday Transactions* **1993,** *89* (18), 3499-3505.

93.   El Fallah, J.; Boujana, S.; Dexpert, H.; Kiennemann, A.; Majerus, J.; Touret, O.; Villain, F.; Le Normand, F., Redox Processes on Pure Ceria and on Rh/CeO2 Catalyst

Monitored by X-Ray Absorption (Fast Acquisition Mode). *The Journal of Physical Chemistry* **1994,** *98* (21), 5522-5533.

94.   Cordatos, H.; Ford, D.; Gorte, R. J., Simulated Annealing Study of the Structure and Reducibility in Ceria Clusters. *The Journal of Physical Chemistry* **1996,** *100* (46), 18128-18132.

95.   Nunan, J. G.; Robota, H. J.; Cohn, M. J.; Bradley, S. A., Physicochemical properties of Ce-containing three-way catalysts and the effect of Ce on catalyst activity. *Journal of Catalysis* **1992,** *133* (2), 309-324.

96.   Oh, S. H.; Eickel, C. C., Effects of cerium addition on CO oxidation kinetics over alumina-supported rhodium catalysts. *Journal of Catalysis* **1988,** *112* (2), 543-555.

97.   Promoting Platinum metals by Ceria Platinum *Met. ReV.* **1988,** *32*, 73.

98.   Kašpar, J.; Fornasiero, P.; Graziani, M., Use of CeO2-based oxides in the three-way catalysis. *Catalysis Today* **1999,** *50* (2), 285-298.

99.   Cordatos, H.; Bunluesin, T.; Stubenrauch, J.; Vohs, J. M.; Gorte, R. J., Effect of Ceria Structure on Oxygen Migration for Rh/Ceria Catalysts. *The Journal of Physical Chemistry* **1996,** *100* (2), 785-789.

100.   Forde, M. M.; Kesavan, L.; bin Saiman, M. I.; He, Q.; Dimitratos, N.; Lopez-Sanchez, J. A.; Jenkins, R. L.; Taylor, S. H.; Kiely, C. J.; Hutchings, G. J., High Activity Redox Catalysts Synthesized by Chemical Vapor Impregnation. *ACS Nano* **2014,** *8* (1), 957-969.

101.   Forde, M. M.; Armstrong, R. D.; McVicker, R.; Wells, P. P.; Dimitratos, N.; He, Q.; Lu, L.; Jenkins, R. L.; Hammond, C.; Lopez-Sanchez, J. A.; Kiely, C. J.; Hutchings, G. J., Light alkane oxidation using catalysts prepared by chemical vapour impregnation: tuning alcohol selectivity through catalyst pre-treatment. *Chemical Science* **2014,** *5* (9), 3603-3616.

102.   Forde, M. M.; Armstrong, R. D.; Hammond, C.; He, Q.; Jenkins, R. L.; Kondrat, S. A.; Dimitratos, N.; Lopez-Sanchez, J. A.; Taylor, S. H.; Willock, D.; Kiely, C. J.; Hutchings, G. J., Partial Oxidation of Ethane to Oxygenates Using Fe- and Cu-Containing ZSM-5. *Journal of the American Chemical Society* **2013,** *135* (30), 11087-11099.

103.   Armstrong, R. D.; Freakley, S. J.; Forde, M. M.; Peneau, V.; Jenkins, R. L.; Taylor, S. H.; Moulijn, J. A.; Morgan, D. J.; Hutchings, G. J., Low temperature catalytic partial oxidation of ethane to oxygenates by Fe– and Cu–ZSM-5 in a continuous flow reactor. *Journal of Catalysis* **2015,** *330*, 84-92.

104.   Su, R.; Forde, M. M.; He, Q.; Shen, Y.; Wang, X.; Dimitratos, N.; Wendt, S.; Huang, Y.; Iversen, B. B.; Kiely, C. J.; Besenbacher, F.; Hutchings, G. J., Well-controlled metal co-catalysts synthesised by chemical vapour impregnation for photocatalytic hydrogen production and water purification. *Dalton Transactions* **2014,** *43* (40), 14976-14982.

105.   Isaienko, O.; Borguet, E., Hydrophobicity of Hydroxylated Amorphous Fused Silica Surfaces. *Langmuir* **2013,** *29* (25), 7885-7895.

106.   Zhuravlev, L. T., The surface chemistry of amorphous silica. Zhuravlev model. *Colloids and Surfaces A: Physicochemical and Engineering Aspects* **2000,** *173* (1–3), 1-38.

107.   Maeda, M.; Yamasaki, S., Effect of silica addition on crystallinity and photo-induced hydrophilicity of titania–silica mixed films prepared by sol–gel process. *Thin Solid Films* **2005,** *483* (1–2), 102-106.

108.   Luo, Z.; Cai, H.; Ren, X.; Liu, J.; Hong, W.; Zhang, P., Hydrophilicity of titanium oxide coatings with the addition of silica. *Materials Science and Engineering: B* **2007,** *138* (2), 151-156.

109.   Xiao, Y.; Wiesner, M. R., Characterization of surface hydrophobicity of engineered nanoparticles. *Journal of Hazardous Materials* **2012,** *215–216*, 146-151.

110.   Das, T.; Becker, T.; Nair, B. N., Measurements on hydrophobic and hydrophilic surfaces using a porous gamma alumina nanoparticle aggregate mounted on Atomic Force Microscopy cantilevers. *Thin Solid Films* **2010,** *518* (10), 2769-2774.

111.   Peuckert, M.; Bonzel, H. P., Characterization of oxidized platinum surfaces by X-ray photoelectron spectroscopy. *Surface Science* **1984,** *145* (1), 239-259.

112.   Zafeiratos, S.; Papakonstantinou, G.; Jacksic, M. M.; Neophytides, S. G., The effect of Mo oxides and TiO2 support on the chemisorption features of linearly adsorbed CO on Pt crystallites: an infrared and photoelectron spectroscopy study. *Journal of Catalysis* **2005,** *232* (1), 127-136.

113.   Zhang, F.; Chen, J.; Zhang, X.; Gao, W.; Jin, R.; Guan, N.; Li, Y., Synthesis of Titania-Supported Platinum Catalyst: The Effect of pH on Morphology Control and Valence State during Photodeposition. *Langmuir* **2004,** *20* (21), 9329-9334.

114.   Şen, F.; Gökağaç, G., Different Sized Platinum Nanoparticles Supported on Carbon: An XPS Study on These Methanol Oxidation Catalysts. *The Journal of Physical Chemistry C* **2007,** *111* (15), 5715-5720.

115.   Smirnov, M. Y.; Kalinkin, A. V.; Bukhtiyarov, V. I., X-ray photoelectron spectroscopic study of the interaction of supported metal catalysts with NOx. *J Struct Chem* **2007,** *48* (6), 1053-1060.

116.   Shelef, M.; McCabe, R. W., Twenty-five years after introduction of automotive catalysts: what next? *Catalysis Today* **2000,** *62* (1), 35-50.

117.   Heck, R. M.; Farrauto, R. J., Automobile exhaust catalysts. *Applied Catalysis A: General* **2001,** *221* (1–2), 443-457.

118.   Jobson, E., Future Challenges in Automotive Emission Control. *Topics in Catalysis* **2004,** *28* (1-4), 191-199.

119.   Twigg, M. V., Progress and future challenges in controlling automotive exhaust gas emissions. *Applied Catalysis B: Environmental* **2007,** *70* (1–4), 2-15.

120.   Gandhi, H. S.; Graham, G. W.; McCabe, R. W., Automotive exhaust catalysts. *Journal of Catalysis* **2003,** *216*, 433-442.

121.   Zhu, R.; Guo, M.; He, J., NO reactions over Ir-based catalysts under oxygen-rich conditions. *Fuel Processing Technology* **2013,** *108* (0), 63-68.

122.   Leistner, K.; Nicolle, A.; Da Costa, P., Modelling the kinetics of NO oxidation and NOx storage over platinum, ceria and ceria zirconia. *Applied Catalysis B-Environmental* **2012,** *111*, 415-423.

123.   Xue, E.; Seshan, K.; Ross, J. R. H., Roles of supports, Pt loading and Pt dispersion in the oxidation of NO to NO2 and of SO2 to SO3. *Applied Catalysis B: Environmental* **1996,** *11* (1), 65-79.

124.   Li, L.; Qu, L.; Cheng, J.; Li, J.; Hao, Z., Oxidation of nitric oxide to nitrogen dioxide over Ru catalysts. *Applied Catalysis B: Environmental* **2009,** *88* (1–2), 224-231.

125.   Olsson, L.; Westerberg, B.; Persson, H.; Fridell, E.; Skoglundh, M.; Andersson, B., A Kinetic Study of Oxygen Adsorption/Desorption and NO Oxidation over Pt/Al2O3 Catalysts. *The Journal of Physical Chemistry B* **1999,** *103* (47), 10433-10439.

126.   Wang, H.-F.; Guo, Y.-L.; Lu, G.; Hu, P., NO Oxidation on Platinum Group Metals Oxides: First Principles Calculations Combined with Microkinetic Analysis. *The Journal of Physical Chemistry C* **2009,** *113* (43), 18746-18752.

127.   Hauff, K.; Tuttlies, U.; Eigenberger, G.; Nieken, U., Platinum oxide formation and reduction during NO oxidation on a diesel oxidation catalyst – Experimental results. *Applied Catalysis B: Environmental* **2012,** *123–124*, 107-116.

128.   Hauptmann, W.; Votsmeier, M.; Gieshoff, J.; Drochner, A.; Vogel, H., Inverse hysteresis during the NO oxidation on Pt under lean conditions. *Applied Catalysis B: Environmental* **2009,** *93* (1–2), 22-29.

129.   Bhatia, D.; McCabe, R. W.; Harold, M. P.; Balakotaiah, V., Experimental and kinetic study of NO oxidation on model Pt catalysts. *Journal of Catalysis* **2009,** *266* (1), 106-119.

130.   Fridell, E.; Amberntsson, A.; Olsson, L.; Grant, A. W.; Skoglundh, M., Platinum oxidation and sulphur deactivation in NOx storage catalysts. *Topics in Catalysis* **2004,** *30-1* (1-4), 143-146.

131.   Després, J.; Elsener, M.; Koebel, M.; Kröcher, O.; Schnyder, B.; Wokaun, A., Catalytic oxidation of nitrogen monoxide over Pt/SiO2. *Applied Catalysis B: Environmental* **2004,** *50* (2), 73-82.

132.   Olsson, L.; Fridell, E., The Influence of Pt Oxide Formation and Pt Dispersion on the Reactions NO2⇔NO+1/2 O2 over Pt/Al2O3 and Pt/BaO/Al2O3. *Journal of Catalysis* **2002,** *210* (2), 340-353.

133.   Mulla, S. S.; Chen, N.; Cumaranatunge, L.; Blau, G. E.; Zemlyanov, D. Y.; Delgass, W. N.; Epling, W. S.; Ribeiro, F. H., Reaction of NO and O2 to NO2 on Pt: Kinetics and catalyst deactivation. *Journal of Catalysis* **2006,** *241* (2), 389-399.

134.   Schmitz, P. J.; Kudla, R. J.; Drews, A. R.; Chen, A. E.; Lowe-Ma, C. K.; McCabe, R. W.; Schneider, W. F.; Goralski Jr, C. T., NO oxidation over supported Pt: Impact of precursor, support, loading, and processing conditions evaluated via high throughput experimentation. *Applied Catalysis B: Environmental* **2006,** *67* (3–4), 246-256.

135.   Matam, S. K.; Kondratenko, E. V.; Aguirre, M. H.; Hug, P.; Rentsch, D.; Winkler, A.; Weidenkaff, A.; Ferri, D., The impact of aging environment on the evolution of Al2O3 supported Pt nanoparticles and their NO oxidation activity. *Applied Catalysis B: Environmental* **2013,** *129*, 214-224.

136.   Boubnov, A.; Dahl, S.; Johnson, E.; Molina, A. P.; Simonsen, S. B.; Cano, F. M.; Helveg, S.; Lemus-Yegres, L. J.; Grunwaldt, J.-D., Structure–activity relationships of Pt/Al2O3 catalysts for CO and NO oxidation at diesel exhaust conditions. *Applied Catalysis B: Environmental* **2012,** *126*, 315-325.

137.   Hauff, K.; Dubbe, H.; Tuttlies, U.; Eigenberger, G.; Nieken, U., Platinum oxide formation and reduction during NO oxidation on a diesel oxidation catalyst—Macrokinetic simulation. *Applied Catalysis B: Environmental* **2013,** *129*, 273-281.

138.   Toops, T. J.; Smith, D. B.; Partridge, W. P., NOx adsorption on Pt/K/Al2O3. *Catalysis Today* **2006,** *114* (1), 112-124.

139.   Toops, T. J.; Smith, D. B.; Epling, W. S.; Parks, J. E.; Partridge, W. P., Quantified NOx adsorption on Pt/K/gamma-Al2O3 and the effects of CO2 and H2O. *Applied Catalysis B: Environmental* **2005,** *58* (3–4), 255-264.

140.   Wang, L.; Ran, R.; Wu, X.; Li, M.; Weng, D., In situ DRIFTS study of NOx adsorption behavior on Ba/CeO2 catalysts. *Journal of Rare Earths* **2013,** *31* (11), 1074-1080.

141.   Prinetto, F.; Ghiotti, G.; Nova, I.; Lietti, L.; Tronconi, E.; Forzatti, P., FT-IR and TPD Investigation of the NOx Storage Properties of BaO/Al2O3 and Pt–BaO/Al2O3 Catalysts. *The Journal of Physical Chemistry B* **2001,** *105* (51), 12732-12745.

5

NO$_x$ storage on metal-exchanged zeolites

5.1 Introduction

Nitrogen oxides NO$_x$ (NO + NO$_2$) which are present in exhaust emissions are a major pollutant of the atmosphere, with a direct harmful effect upon the environment and human health. NO$_x$ are a major source of acid rain, photochemical smog and ozone depletion. Accordingly, more stringent emission standards have been introduced to lower the concentrations of these pollutants.

NO$_x$ abatement is crucial, especially in diesel engines where controlling NO$_x$ is extremely difficult as oxygen is always in excess. There are two ways of converting NO$_x$ to N$_2$ under lean conditions [1] (i) NO$_x$ storage-reduction (NSR), where the engine is operated in a mixed lean/rich operation mode and (ii) selective catalytic reduction (SCR) with ammonia (NH$_3$) or hydrocarbons (HC), where reduction of NO$_x$ is achieved even in large excess of oxygen.

As introduced earlier in this thesis, the objective of this chapter is to find an adsorption catalyst that stores NO$_x$ at low temperature (T < 250 °C) and releases it at high temperatures. Investigations of NO$_x$ adsorption-desorption on metal-exchanged zeolites have been reported in a large number of publications [2 3 4 5 6 7 8 9 10 11 12 13 14 15 16 17 18 19 20 21 22 23 24], however, further studies are needed to succeed in finding a catalytic system sufficiently active, selective and stable. The overall aim is to find an optimum zeolite-based system for NO$_x$ storage. Preparation and evaluation of a variety of metal-exchanged zeolites with different compositions and structures was performed to study the effect of the silicon/aluminium ratio, internal channels and inclusion of base and precious metals.

5.2 NO$_x$ adsorption-desorption studies

The first part of this study was the designing, construction and commissioning of a flow reactor to evaluate NO$_x$ storage over different catalytic systems. A detailed description of the experimental procedure is given in Chapter 3, Section 3.3.2.1. In summary, quantitative analysis of NO$_x$ adsorption-desorption processes was carried out by continuously monitoring the effluent gas composition using a FTIR spectrometer.

Nitrogen oxides (NO$_x$) are a mixture containing mostly nitrogen monoxide (NO) and between 5 and 10 % of nitrogen dioxide (NO$_2$). Hence, 1000 ppm of NO balanced in Helium (He) was used as a model flue gas and He (100 %) was used as the purge gas.

--- Temperature in °C (dashed line)   (---) H$_2$O v. %   (---) CO$_2$ v. %   (---) CO ppm

(---) N$_2$O ppm   (---) NO ppm   (---) NO$_2$ ppm

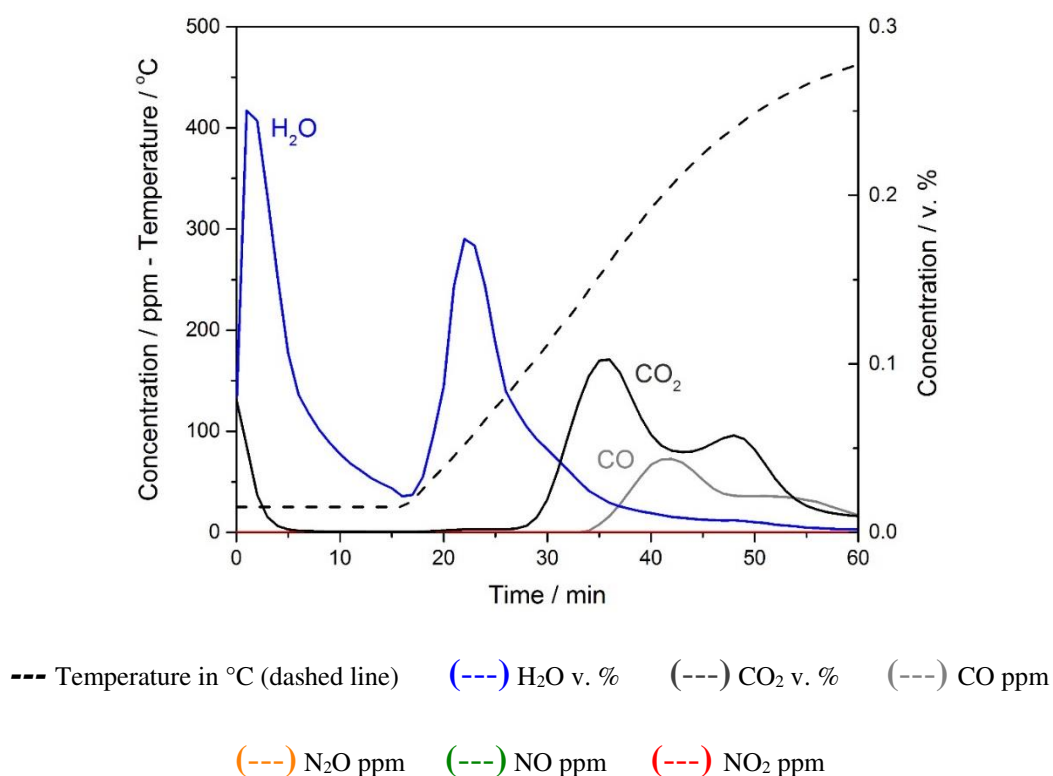**Figure 5.1.** Typical concentration profile over the zeolite-based catalysts during pretreatment

Reaction conditions: Flow reactor, GHSV = 35,000 h^{-1}, He

The microporous structure of the zeolites makes them adsorbents with a high affinity for water. Before adsorption-desorption experiments, zeolites catalysts were pretreated to remove water and other species from the surface. The pretreatment profile for Cu/ZSM-5 (30) is shown in Figure 5.1. Analysis of the gas effluent shows that desorption of H_2O, CO_2 and CO occurs up to 500 °C during pretreatment in He. H_2O presents two desorption peaks; at room temperature and 100 °C, corresponding to free and surface adsorbed water. CO_2 desorption occurs at room temperature, 250 °C and 400 °C. CO desorption is also observed at temperatures above 250 °C.

The storage capacity of zeolite-based systems was investigated using 0.1 % NO (1000 ppm) in He. The combined adsorption-desorption profile for Cu/ZSM-5 (30) is shown in Figure 5.2. The first 15 minutes correspond to the adsorption of NO at 30 °C. Initially, the concentration of NO decreases considerably, indicating that NO is being adsorbed by the catalyst. The NO concentration then slowly increases, tending towards the NO inlet concentration of ≈ 1000 ppm. After 10 minutes the catalyst becomes saturated, with the NO concentration reaching steady state. During the storage period CO_2 is desorbed. This has been reported in previous studies and corresponds to decomposition of carbonates, which are unstable in the presence of NO/O_2 [25].

After 15 minutes of adsorption, the catalyst bed is bypassed and the gas feed is switched to He (100 %) so the FTIR cell is flushed until an NO concentration of 0 ppm is observed. NO is desorbed at 30 °C (15 minutes) in He followed by a temperature programmed desorption (TPD) from 30 °C to 500 °C (10 °C min^{-1}). NO, H_2O, CO_2 and a low concentration of CO are detected during the desorption. It should be noted that even if a zeolite catalyst has been pretreated to remove surface H_2O, it rehydrates during the storage process as the gas feed is not completely dry. NO$_x$ is desorbed as NO, N_2O is not detected

and trace amounts of NO_2 are identified. NO desorption peaks at 30 °C and 100 °C correspond to physisorption and weak chemisorption of NO at the surface.

--- Temperature in °C (dashed line)   **(---)** H_2O v. %   **(---)** CO_2 v. %   **(---)** CO ppm

(---) N_2O ppm   **(---)** NO ppm   **(---)** NO_2 ppm

Figure 5.2. Typical concentration profile over the zeolite-based catalysts during

NO adsorption at 30 °C and TPD with He up to 500 °C

Reaction conditions: Flow reactor, GHSV = 35,000 h^{-1}, 0.1 % NO in He

Since the inlet concentration of NO is quantified, the amount of adsorbed/desorbed NO_x can be quantified by integration of the area under the corresponding curves and correlation with the response factor. Figure 5.3 shows the same adsorption-desorption experiment, for Cu/ZSM-5 (30), including only the NO_x profiles and the integrated areas.
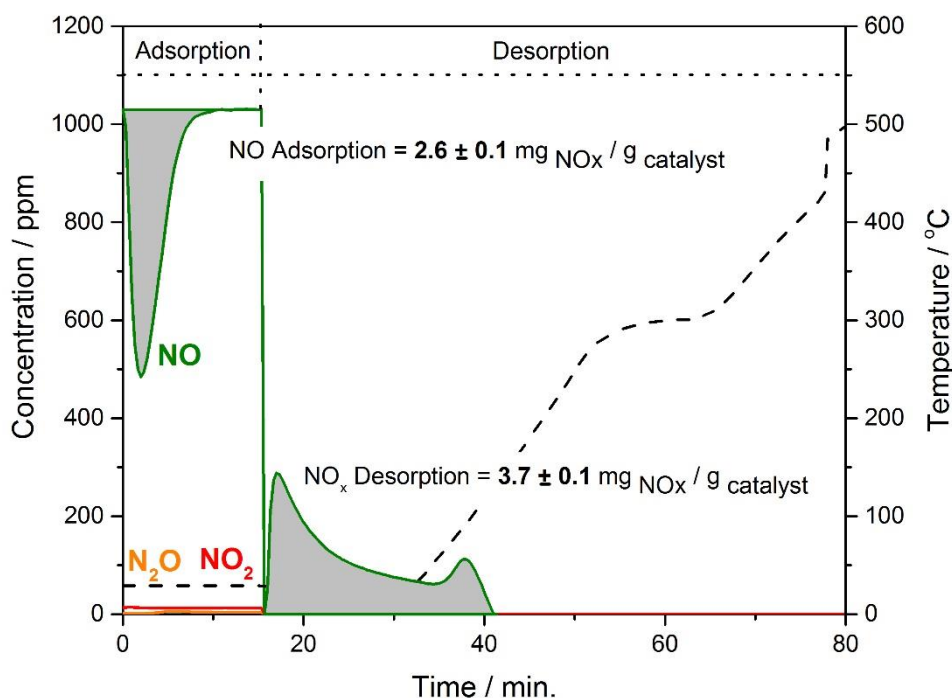
--- Temperature in °C (dashed line)   (---) N$_2$O ppm   (---) NO ppm   (---) NO$_2$ ppm
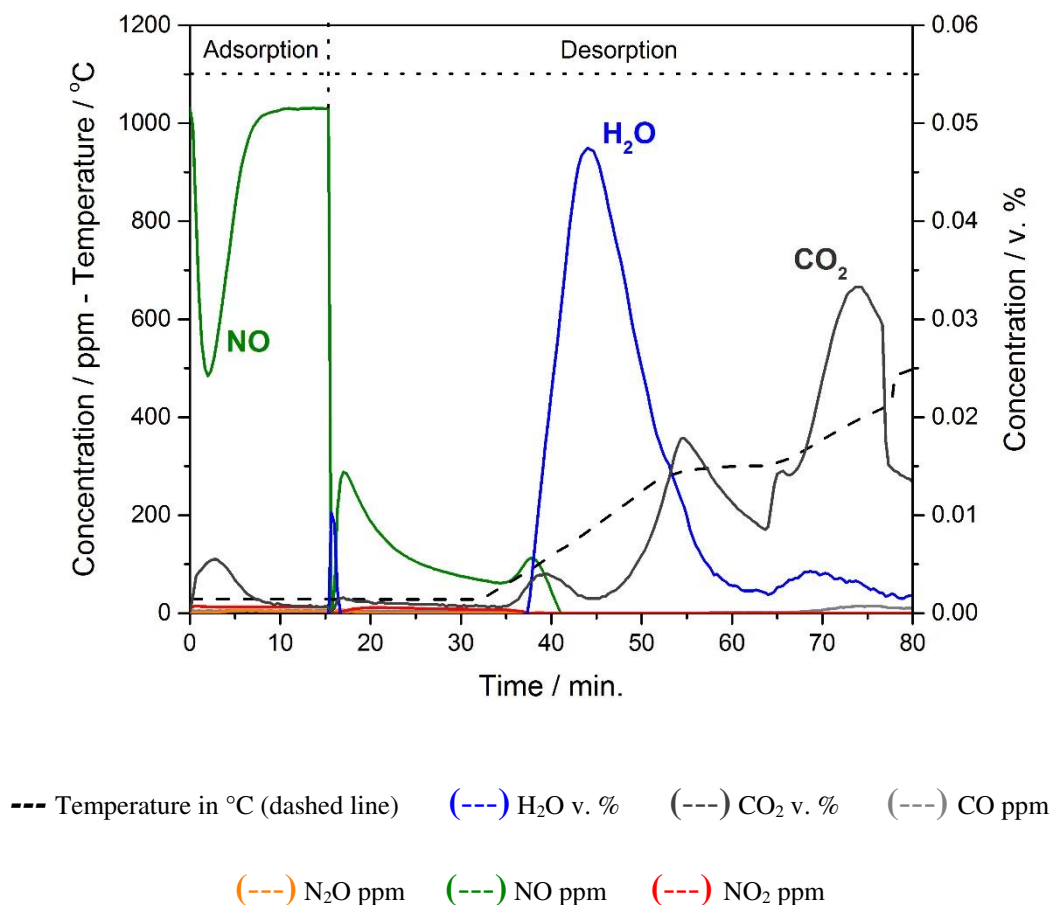
Figure 5.3. Typical NO$_x$ concentration profile over the zeolite-based catalysts during

NO adsorption at 30 °C and TPD with He up to 500 °C

Reaction conditions: Flow reactor, GHSV = 35,000 h^{-1}, 0.1 % NO in He

Results are expressed as mg of NO$_x$ (NO, NO$_2$ or NO$_x$) per g of catalyst. The standard

deviation, calculated by repeating the same adsorption/desorption experiment three times,

is found to be ± 0.1 mg/g.

It was not possible to obtain an accurate nitrogen balance. The shaded regions in Figure 5.3

represent total adsorbed and desorbed NO. Both areas should be equal or, if as reported

previously in the literature [9] [10], irreversible adsorption occurs: NO desorbed should be less

than NO adsorbed. Contrarily, the total amount of NO desorbed (3.7 mg NO$_x$/g catalyst)

exceeds the total amount of NO adsorbed (2.6 mg NO$_x$/g catalyst). This can be explained according to the following two points:

i)   The amount of NO calculated from the area under the desorption peak at 30 °C is the result of physisorbed NO but also residual NO that is confined in the reactor tube. Nevertheless, adsorption/desorption experiments performed over a blank adsorbent bed confirm that the residual NO only accounts for a maximum of 0.15 mg NO$_x$/g catalyst, this amount is much lower than the difference between NO adsorbed and desorbed obtained (1.1 mg NO$_x$/g catalyst).

ii)   The key limitation to consider is that the total amount of NO adsorbed is underestimated. The FTIR cell volume is 0.4 L and the gas flow used is 200 mL/min, thus, a few minutes are needed to reach a constant NO concentration. NO$_x$ adsorption occurs rapidly and is hindered by the volume of NO already present in the FTIR cell.

Based on these considerations, while NO$_x$ adsorption results are valid in comparing the adsorption capacity of different catalysts, the quantification is not completely accurate, as adsorption values are underestimated. On the other hand, the total amount of NO$_x$ desorbed is considered to be precise as the cell is flushed with He prior to desorption.

Due to the nature of the FTIR detector, analysis of N$_2$ is not possible. However, reduction of NO$_x$ to N$_2$ under these conditions is unlikely.

No NO$_x$ desorption is observed above 100 °C. It is widely known that NO is more weakly adsorbed on zeolites than NO$_2$ and that the oxidation of NO to NO$_2$ is necessary to improve storage capacity [10] [15] [25] [26]. Oxidation of NO to NO$_2$ under the oxygen- free gas feed conditions studied does not occur. Hence, the storage capacities of the zeolite-based

systems were also evaluated in the presence of excess oxygen: 0.1 % NO, 7.5 % O$_2$ balanced in He. The combined adsorption-desorption profile for Cu/ZSM-5 (30) is shown in Figure 5.4.

After pretreatment at 500 °C under He, the zeolite-based catalyst is exposed to the gas mixture of model flue and oxygen (0.1 % NO, 7.5 % O$_2$ balanced in He) at 30 °C for 30 minutes. Concordant with the adsorption profile in the absence of oxygen (Figure 5.3), the concentration of NO decreases considerably early in the adsorption period, indicating that NO is being adsorbed by the catalyst. After 5 minutes of adsorption the NO concentration begins to gradually increase. In contrast to the profile obtained in the absence of oxygen (Figure 5.3), a constant concentration of NO is not reached after 20 minutes and the NO concentration does not equal the inlet NO concentration. In the presence of oxygen, not only NO but also NO$_2$ adsorption occurs. During the first 10 minutes of the adsorption period, the detected outlet concentration of NO$_2$ is *ca*. 40 ppm lower than the inlet NO$_2$ concentration. After catalyst saturation, the NO$_2$ concentration increases until it exceeds the inlet value. After 30 minutes of adsorption, the outlet NO concentration ($\approx$ 400 ppm) is lower than the inlet NO concentration ($\approx$ 900 ppm) and the outlet concentration of NO$_2$ ($\approx$ 600 ppm) is much higher than the inlet NO$_2$ concentration ($\approx$ 50 ppm), the N$_2$O concentration does not change ($\approx$ 1.8 ppm) and the N$_2$ balance is 100 % $\pm$ 11 %. This indicates that NO is oxidised to NO$_2$ by the catalyst. Again, the presence of CO$_2$ confirms carbonate decomposition during the adsorption of NO and NO$_2$.

After 30 minutes of adsorption, the NO and O$_2$ feeds are interrupted and the FTIR cell is flushed with He (100 %) until the NO$_x$ concentration reaches a stable 0 ppm. Following a purge with He (15 minutes, 30 °C) a TPD is carried out, from 30 °C to 500 °C. NO, NO$_2$, H$_2$O, CO$_2$ and a low concentration of CO are detected during the TPD. Desorption profiles for NO, H$_2$O and CO$_2$ are similar to those obtained in the absence of oxygen (Figure 5.2).

NO desorption peaks at 30 °C and 100 °C correspond to physisorbed and weakly chemisorbed NO on the surface. Distinctively, NO_x desorption occurs mainly in the form of NO_2. Four NO_2 desorption peaks are observed, at 30 °C, 100 °C, 250 °C and 350 °C. The desorptions at 30 and 100 °C are attributed to desorption of NO_2 physisorbed over the catalyst surface. The desorption at 250 °C is due to moderately thermally stable species and the highest temperature desorption (350 °C) to nitrate species. This profile is comparable to that obtained in previous work [8] .
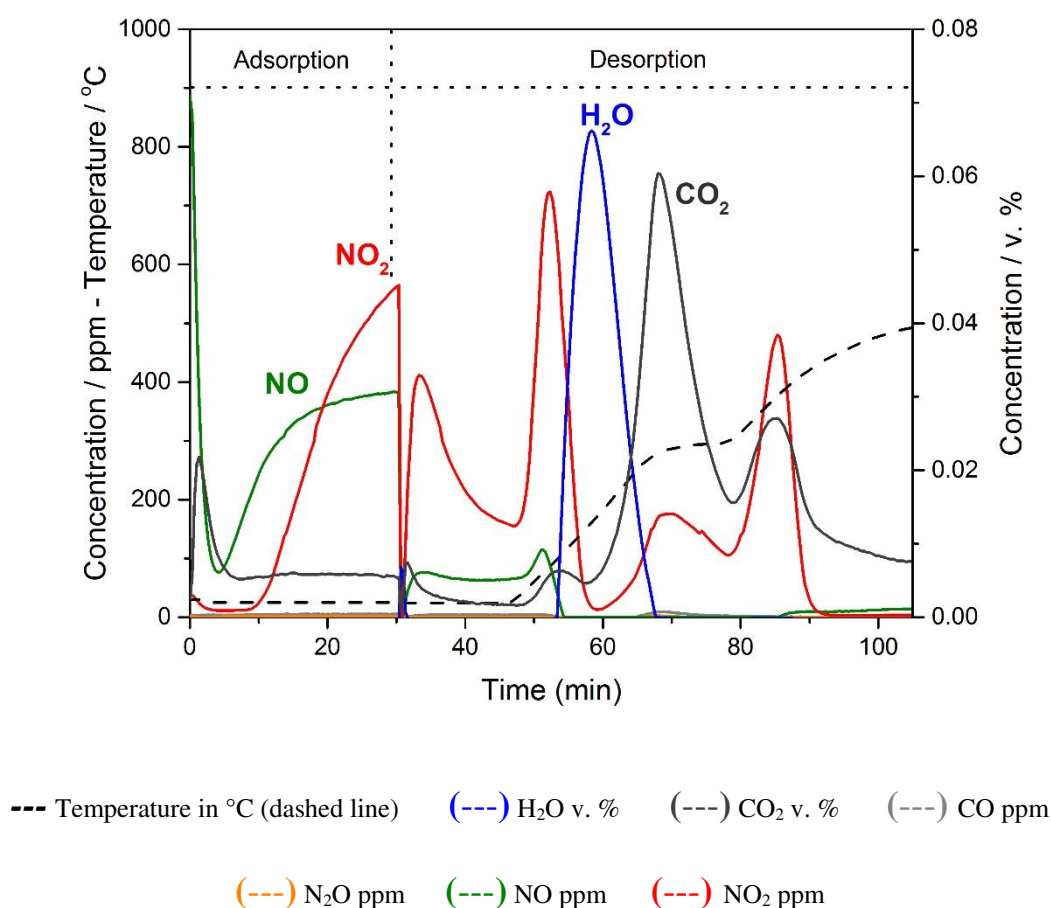
Figure 5.4. Typical concentration profile over the zeolite-based catalysts during

NO_x adsorption at 30 °C ($NO:O_2 = 1:75$) and TPD with He up to 500 °C

Reaction conditions: Flow reactor, GHSV = 35,000 h^{-1}, 0.1 % NO + 7.5 % O_2 in He

Figure 5.5 shows the same adsorption-desorption experiment, for Cu/ZSM-5 (30), including only the NO$_x$ profiles and the integrated areas for quantification. The evolution of NO and NO$_2$ during the TPD is a measure of the thermal stability of stored and adsorbed NO$_x$ species.
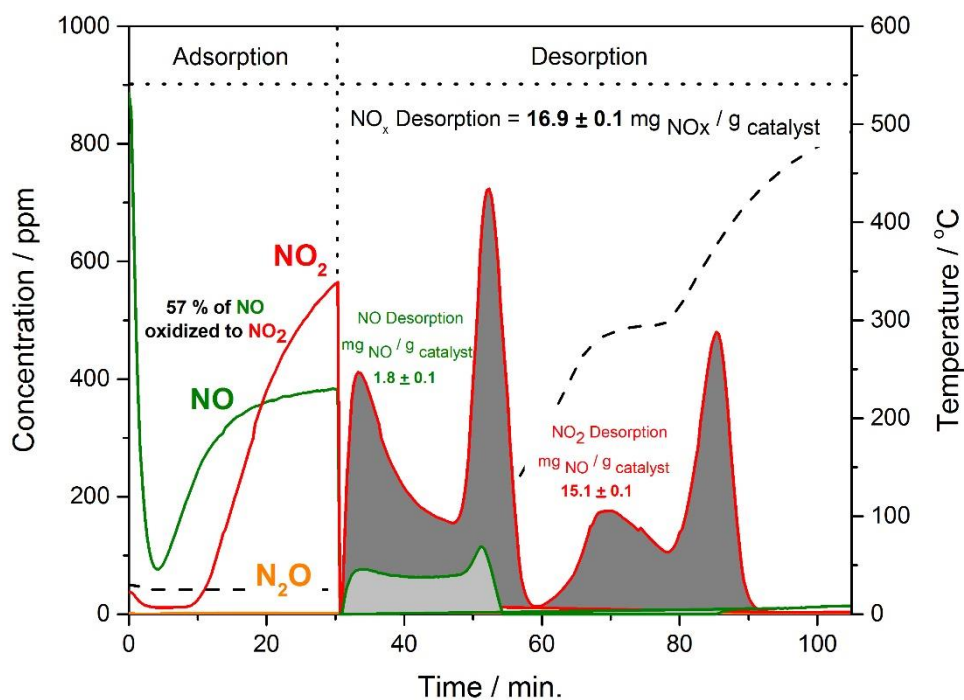
--- Temperature in °C (dashed line)   (---) N$_2$O ppm   (---) NO ppm   (---) NO$_2$ ppm

Figure 5.5. Typical NO$_x$ concentration profile over the zeolite-based catalysts during

NO$_x$ adsorption at 30 °C (NO:O$_2$ = 1:75) and TPD with He up to 500 °C

Reaction conditions: Flow reactor, GHSV = 35,000 h^{-1}, 0.1 % NO + 7.5 % O$_2$ in He

In the presence of oxygen, desorption at high temperatures is ascribed to formation of more thermally stable nitrate species, promoted by the initial oxidation of NO to NO$_2$.

This thesis chapter is dedicated to screening the NO$_x$ storage capacity of a variety of zeolite-based catalysts in the presence and absence of O$_2$. This is quantified through performing

isothermal NO_x adsorption followed by TPD in He. While the total amount of NO_x adsorbed/desorbed differs significantly between different catalysts, their adsorption/desorption profiles are similar to those explained in Figures 5.2 and 5.4. The NO_x storage capacities of zeolite catalysts are summarised in separate figures which illustrate quantified values for the total amount of NO_x (NO_2 and NO) adsorbed/desorbed and the % of NO converted to NO_2.

Results are expressed as mg NO_x/g catalyst. Total NO_x desorption does not include the reversibly adsorbed NO_x, meaning that the physisorbed NO_x which desorbs at 30 °C (prior to the TPD) is excluded from calculations. As explained previously, the total amount of NO_x adsorbed is under-quantified due to limitations of the experimental method. However, the total amount of NO_x desorbed during the TPD is an accurate estimation of the storage capacity. Since oxidation of NO is an essential first step in the storage mechanism and the NO_x adsorption capacities are under-quantified, only the % of NO converted to NO_2 is included in the results for experiments performed in the presence of O_2.

When comparing the storage capacities of the different zeolite-based catalysts, non-exchanged H^+-ZSM-5 ($SiO_2/Al_2O_3 = 30$) is used as a baseline and a commercial diesel NO_x abatement autocatalyst prototype is used as the reference. Quantified NO_x adsorption/desorption results obtained for these two systems are presented in Table 5.1. The storage capacity of the reference catalyst prototype in Table 5.1, is much higher than that of the baseline catalyst, H^+-ZSM-5 (30). The objective then, is to find a zeolite-based system with superior performance to the prototype. It should be mentioned that it is not only the absolute storage capacity but also the NO_x desorption distribution at different temperatures which should be compared to determine the performance of a catalyst. An ideal storage system should possess both the ability to oxidise NO to NO_2 and to store the NO_2 formed up to high temperatures.

Table 5.1. NO_x storage capacity of the baseline and reference catalyst obtained for adsorption/desorption experiments performed in the presence and absence of O_2

NO STORAGE (0.1 % NO, He balance)

	NO Adsorption (mg/g)	NO Desorption (mg/g)	NO₂ Desorption (mg/g)	NOₓ Desorption (mg/g)
H^+-ZSM-5 (30)	0.60 ± 0.46	0.29 ± 0.30	0.08 ± 0.03	0.37 ± 0.29
PROTOTYPE	2.09 ± 0.08	1.48 ± 0.11	0.33 ± 0.06	1.81 ± 0.18

NO_x STORAGE (0.1 % NO, 7.5 % O_2, He balance)

	NO Conversion (%)	NO Desorption (mg/g)	NO₂ Desorption (mg/g)	NOₓ Desorption (mg/g)
H^+-ZSM-5 (30)	27 ± 4	0.16 ± 0.08	2.96 ± 0.01	3.13 ± 0.08
PROTOTYPE	38 ± 2	1.14 ± 0.03	6.12 ± 0.04	7.26 ± 0.08

The chemical composition, structure and extra-framework cations of zeolites greatly influence molecular adsorption and interaction with the active sites, thus influencing catalytic and storage properties.

The nomenclature used for zeolite-based catalysts is defined as follows;

$$M^X / ZEO (Y)_{PREP} \quad where;$$

M = metal ion-exchanged/supported,

X = oxidation state of the metal in the metal precursor,

ZEO = zeolite name, associated with its structure,

Y = zeolite SiO_2/Al_2O_3 ratio, associated with its acidity,

PREP = preparation method.

Whilst the zeolite-based catalysts used in this study are named as metal-exchanged zeolites, it should be noted that both ion-exchanged and supported metal species are present on the zeolite support. Hence, M/ZEO is used instead of M-ZEO.

5.3 Monometallic zeolitic systems

5.3.1 Wet ion exchange

There are several techniques to modify zeolites by ion exchange. Among them, wet ion exchange (WIE) is the most common as it is simple and feasible for industrial applications, involving few steps and with easily controlled experimental variables.

A detailed description of the WIE procedure is given in Chapter 3, Section 3.2.2.1. Extra-framework cations are introduced by ion-exchange of the H$^+$ form zeolite with an aqueous solution of the metal precursor.

Because of the reversible nature of the exchange process, multiple exchanges are necessary to accomplish complete exchange. Thus, the metal exchange level should be determined by a bulk chemical analysis technique such as ICP-AES.

5.3.1.1 Exchanged metal

Cu/ZSM-5 catalysts have been reported to show good performance for NO$_x$ SCR with HC [26][27][28][29][30] and NH$_3$ [31], and NO decomposition [32][33][34][35][36][37][38][39][40][33]. Fe/ZSM-5 catalysts are also very active for NO$_x$ SCR with HC [41][42][43][44][45][46][47][48][49] and NH$_3$ [50][51][46], as well as for N$_2$O decomposition [52][53][54][55][56][57][58][59]. Pt/ZSM-5 catalysts have also been investigated for HC SCR [60][61][62][63]. Deeba *et al.* reported that Pt/ ZSM-5 enhances NO$_x$ conversion due to a cooperative effect between acid sites and Pt [64]. The Pt sites enhance the formation of active intermediates such as NO$_2$. NO must be oxidised to NO$_2$ prior to reduction. Additionally, as NO is much more weakly adsorbed onto zeolites than NO$_2$, this oxidation also enhances total NO$_x$ storage. In fact, commercial NSR catalysts are composed of an adsorbent, such as BaO, combined with an oxidation component, such as Pt, that favours the oxidation of NO to NO$_2$ [65][66][67][68][69].

Fe/ and Cu/ZSM-5 are promising catalysts, with durability at high temperatures and resistance to poisoning. Meanwhile supported Pt catalysts possess favourable oxidation properties. Hence, the storage capacities of a series of base (Fe and Cu), and precious (Pt), metal-exchanged zeolites were evaluated.

The physicochemical properties of the metal-exchanged zeolites prepared by wet ion exchange and calcined at (550 °C for 3 hours in static air) are summarised in Table 5.2.

Table 5.2. Physicochemical properties of the metal-exchanged zeolites:

	Surface area BET [a]	Pore volume [a]	Acidity [b]			H$_2$ Consumption[c]
			Total	250 °C	450 °C	
	m^2/g	mL/g	μmol NH$_3$/g			μmol H$_2$/g
H$^+$-ZSM-5 (30)	412	0.383	1299	260	350	181
Cu^{II}/ZSM-5 (30) $_{WIE}$	394	0.282	1439	707	100	192
Fe^{III}/ZSM-5 (30) $_{WIE}$	350	0.381	1064	207	188	20
Fe^{II}/ZSM-5 (30) $_{WIE}$	X	X	1128	233	172	77
Pt^{IV}/ZSM-5 (30) $_{WIE}$	X	X	1477	263	182	81

[a] Surface area and pore volume measured by N$_2$ physisorption, [b] acidity measured by NH$_3$-TPD and [c] hydrogen consumption obtained from H$_2$-TPR profiles

All adsorption isotherms were characteristic of Type 1 according to the IUPAC classification [70]. The surface area of the unmodified support, H$^+$-ZSM-5 (30), is 412 ± 8 m^2/g, in good agreement with the value provided by the supplier (400 m^2/g). Incorporation of metal oxide particles diminishes the total surface area by 4.4 % for Cu and 15 % for Fe.

The pore volume distribution calculated from the nitrogen adsorption isotherms using the DFT & Monte-Carlo method is described in Table 5.3. It is known that incorporation of

metal oxide particles can lead to blockage of the zeolite channels and decrease the adsorption properties. Results show that the pore volume distribution does change after exchange, however the decrease in total pore volume is more significant for the Cu^{II}/ZSM-5 (30) $_{WIE}$ catalyst. Reduction of the micro-, meso- and macro- porous volume indicates that CuO is distributed inside the pores, leading to the diminution in surface area and pore volume. In the case of the Fe^{III}/ZSM-5 (30) $_{WIE}$ catalyst, only the microporous volume is reduced (by 15 %).

Table 5.3. Pore volume distribution of the metal-exchanged zeolites:

	Pore volume/mL · g^{-1}			
	Total	Microporous (< 2 nm)	Mesoporous (2 nm – 50 nm)	Macroporous (> 50 nm)
H$^+$-ZSM-5 (30)	0.383	0.142	0.209	0.033
Cu^{II}/ZSM-5 (30) $_{WIE}$	0.282	0.110	0.169	0.003
Fe^{III}/ZSM-5 (30) $_{WIE}$	0.381	0.121	0.219	0.040

The acidity of the zeolite-based catalysts was probed using NH$_3$-TPD, with NH$_3$ adsorbed at 30 °C. The NH$_3$-TPD profiles are shown in Figure 5.6. In agreement with previous work [51] [71] [72] [73] [74] the profile presents two main NH$_3$ desorptions, at 250 °C and 450 °C. These represent different acid sites strengths, with the peak at 250 °C attributed to desorption of NH$_3$ from weak Brønsted and Lewis acid sites and that at 450 °C assigned to desorption of NH$_3$ from strong Brønsted acid sites. Quantification of the concentration of acid sites was obtained by integration of the curves and correlation with the response factor. Results reported in Table 5.2 are given as total acid site density (µmol NH$_3$/g support) and acid density at 250 °C and 450 °C. The total amount of acid sites is proportional to the Al content of the zeolite. The loading of different metals onto H$^+$-ZSM-5 (30) reduces the strong Brønsted acid- site density. The high temperature peak is shifted 50 °C higher and its

intensity decreases due to loss of Brønsted acid sites through metal ion exchange. In addition, the profile for Cu^{II}/ZSM-5 (30) $_{WIE}$, Figure 5.6 b), shows that the peak at 250 °C is broader and more intense. The shoulder at 320 °C, suggests that Cu-exchange generates new medium strength acid sites, attributed to desorption of NH_3 from $Cu(NH_3)_2{}^{2+}$ complexes [72].

Figure 5.6. NH_3-TPD profiles of the metal-exchanged zeolites:

a) H^+-ZSM-5 (30)   b) Cu^{II}/ZSM-5 (30) $_{WIE}$ c) Fe^{III}/ZSM-5 (30) $_{WIE}$

d) Fe^{II}/ZSM-5 (30) $_{WIE}$ e) Pt^{IV}/ZSM-5 (30) $_{WIE}$

For a complete characterisation of the acidity of zeolite-based catalysts it is necessary to determine the distribution of acid sites (Lewis and Brønsted) on the surface. Therefore, IR spectra of adsorbed pyridine should be collected.

In metal-exchanged zeolites, the redox properties of the metal species are an important factor in determining catalytic performance. Reducibility of the zeolite-based catalysts was investigated via H_2-TPR and H_2 uptake profiles are shown in Figure 5.7. Quantified hydrogen consumption (μmol H_2/g catalyst) determined from the TPR profiles is included in Table 5.2.
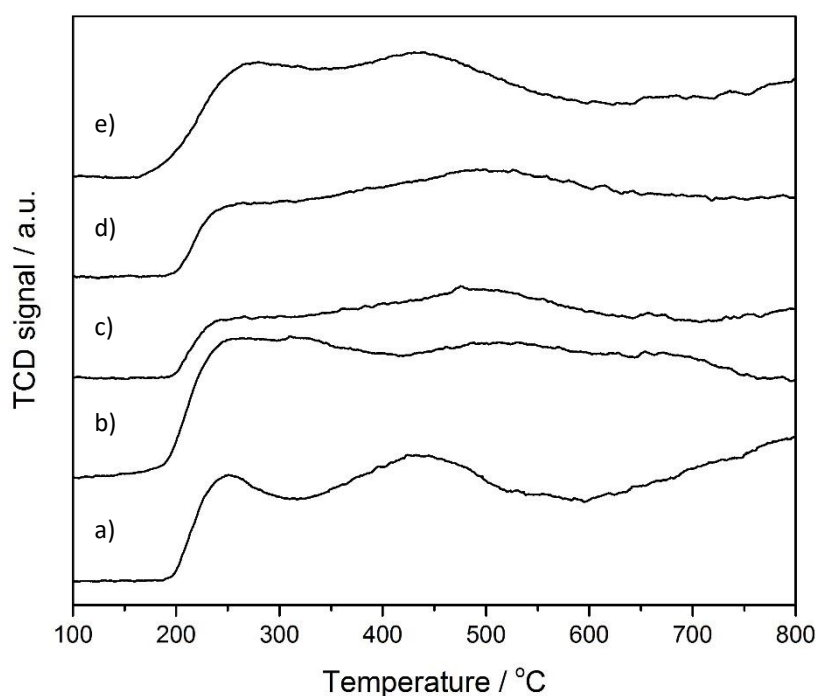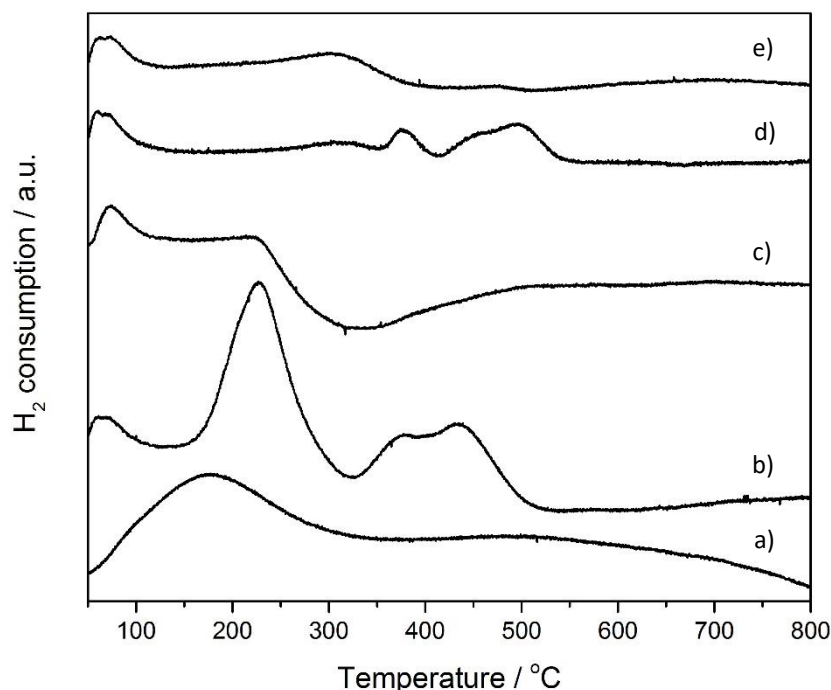

Figure 5.7. H_2-TPR profiles of the metal-exchanged zeolites:

a) H^+-ZSM-5 (30)   b) Cu^{II}/ZSM-5 (30) $_{WIE}$ c) Fe^{III}/ZSM-5 (30) $_{WIE}$

d) Fe^{II}/ZSM-5 (30) $_{WIE}$ e) Pt^{IV}/ZSM-5 (30) $_{WIE}$

The small reduction peak that appears between 30 °C and 100 °C is an artefact and can be attributed to residual Ar. Cu^{II}/ZSM-5 (30) $_{WIE}$, Figure 5.7 b), exhibits two distinct reduction events. The first reduction peak, at 225 °C, is attributed to reduction of Cu^{2+} cations located at exchanged sites and supported CuO species, to Cu^+. The second reduction event is broad and centred at 400 °C, corresponding to reduction of Cu^+ to Cu^0 [71 72 75]. This could be

deconvoluted into two different peaks, at 375 °C and 450 °C. For Fe-exchanged ZSM-5 systems [76] [77] [78] [57] [79], the first TPR peak, at 375 °C, corresponds to the reduction of Fe_2O_3 to Fe_3O_4, and the second, at 500 °C, is assigned to the reduction of Fe_3O_4 to Fe^0. Reduction of Fe_3O_4 to Fe^0 proceeds via FeO, thus, the shoulder at 450 °C could be attributed to the reduction of FeO [80]. Fe^{II}/ZSM-5 (30) $_{WIE}$ (Figure 5.7 d) exhibits the typical TPR profile, suggesting that Fe is present as a mixture of Fe^{2+} and Fe^{3+} species. Contrarily, as shown in Figure 5.7 c), the H_2-TPR for Fe^{III}/ZSM-5 (30) $_{WIE}$, Fe-exchanged ZSM-5 obtained through WIE using $FeCl_3$ does not show the Fe_2O_3 and Fe_3O_4 reduction peaks but rather a negative peak centred around 300 °C. Reduction of PtO_x species to Pt^0 occurs at $\approx$ 80 °C. Due to the low temperature desorption of residual Ar it is not possible to distinguish those reduction peaks attributed to Pt in Figure 5.7 e), whilst the reduction events observed at higher temperatures are similar to those obtained for the unmodified H^+-ZSM-5 (30) which correspond to reduction of the zeolite.

The nature and distribution of Cu and Fe species was investigated using diffuse-reflectance UV-Vis spectroscopy. The UV-Vis spectra are presented in Figure 5.8. It is known that for Fe-exchanged zeolites [51] [59] [81] [82] [83] [84] [85] [86] [87] [88] [77], $Fe^{3+} \leftarrow$ O charge-transfer (CT) bands (200-350 nm) and weak Fe^{3+} ($3d^5$) d-d transitions (350-550 nm) are expected. The first band (200-250 nm) is attributed to isolated Fe^{3+} species in the zeolite framework. The second band (250 nm - 350 nm) corresponds to isolated or small oligonuclear Fe_xO_y extra-framework species. Larger Fe_xO_y clusters appear between 350 and 450 nm and those bands at wavelengths over 450 nm correspond to surface Fe_xO_y nanoparticles. In the case of Cu-exchanged zeolites, d-d transitions of Cu^{2+} ($3d^9$) appear over 700 nm, hence electronic spectra analysis is only possible using UV-Vis-NIR spectroscopy [89] [90].

Fe^{III}/ZSM-5 (30) $_{WIE}$, Figure 5.8 c), presents a mixture of Fe species. The two bands at 225 and 250 nm are attributed to $t_1 \rightarrow t_2$ and $t_1 \rightarrow e$ CT transitions [59], confirming the presence

of tetrahedral and octahedral Fe^{3+} species. Additionally, the spectrum suggests the presence of extra-framework Fe_xO_y species in the micropores, which is in agreement with a decrease in micropore volume after Fe-exchange, as shown in Table 5.3. Fe is also distributed as larger clusters and iron crystallites on the external surface of the zeolite. Those UV bands observed for the unmodified H^+-ZSM-5 (30), Figure 5.8 a), are attributed to CT transitions of the contaminant iron, intrinsic within commercial zeolites. It has been reported that commercial zeolites contain trace levels of Fe and Ti within the MFI structure that are highly active for oxidation reactions [83]. The spectrum of the Cu^{II}/ZSM-5 (30) $_{WIE}$ catalyst differs from that obtained for the non-exchanged H^+-ZSM-5 and exhibits one absorption band at 200-260 nm which could be assigned to charge-transfer from O^{2-} to Cu^+ or Cu^{2+} [29 35 91], and also to Fe^{3+} ions in the framework.
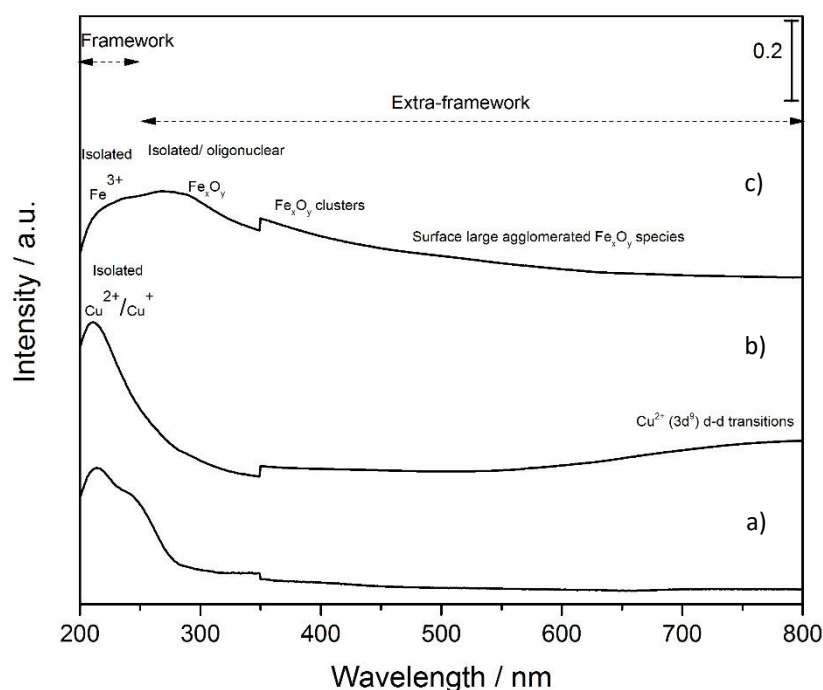

Figure 5.8. UV-Vis spectra of the metal-exchanged zeolites:

a) H^+-ZSM-5 (30)   b) Cu^{II}/ZSM-5 (30) $_{WIE}$ c) Fe^{III}/ZSM-5 (30) $_{WIE}$

Characteristic absorption bands of the parent zeolite [5], H⁺-ZSM-5 (30), are observed in the FTIR spectrum shown in Figure 5.9. The spectrum in the surface hydroxyl (OH) vibrational region (inset) contains three main bands at 3560, 3660 and 3750 cm⁻¹. The band at 3560 cm⁻¹ is associated with Brønsted acid groups; bridging hydroxyl groups with tetrahedrally coordinated framework aluminium (-Si-OH-Al-), the band at 3660 cm⁻¹ is associated with hydroxyls of extra-framework aluminium (Al-OH), and the sharp peak at 3750 cm⁻¹ with terminal silanol groups (Si-OH) inside the zeolite channels and on the surface [75] [83] [87].
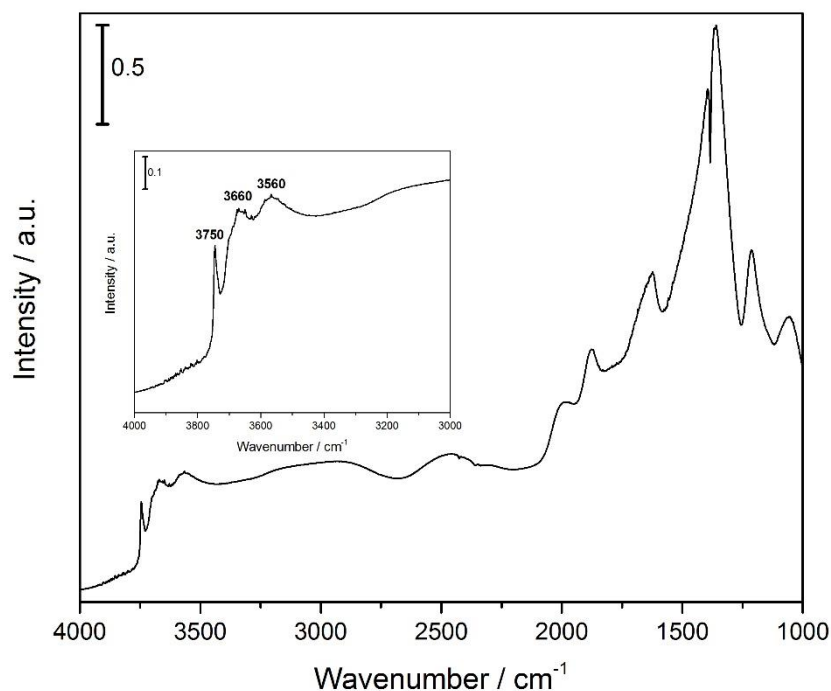

Figure 5.9. DRIFT spectra of the parent zeolite: H⁺-ZSM-5 (30)

FTIR spectra in the OH vibrational region of the metal-exchanged zeolites are shown in Figure 5.10. As reported in the literature [76] [92], exchange of H⁺ with metal cations results in differences in the relative concentration of the different –OH groups. The relative intensity

of the band associated with bridging hydroxyl groups decreases after metal ion-exchange. Although the resolution of the spectra is not good enough, it seems that the relative intensity of the band at 3560 cm^{-1} is lower for Cu^{II} and Fe^{III}-exchanged ZSM-5, Figure 5.10 b) and c). This suggests that the level of exchange is much lower for these last two metal ion-exchanged ZSM-5 catalysts. Fe/ZSM-5 (30) catalysts present a new band at 3715 cm^{-1} which is attributed to the stretching vibration of hydrolysed Fe species.
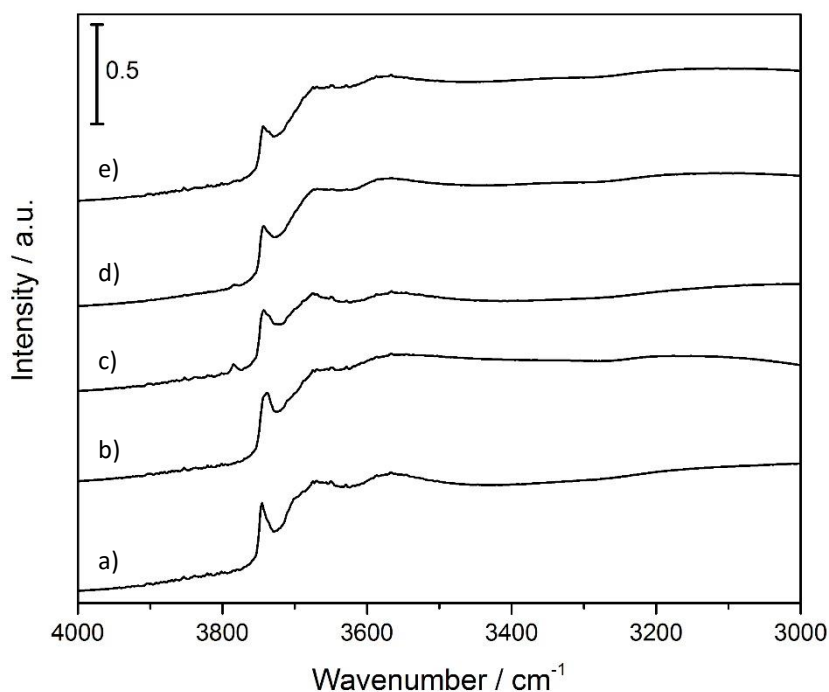
Figure 5.10. DRIFT spectra in the OH vibrational region of the metal-exchanged zeolites:

a) H$^+$-ZSM-5 (30)   b) Cu^{II}/ZSM-5 (30) $_{WIE}$ c) Fe^{III}/ZSM-5 (30) $_{WIE}$

d) Fe^{II}/ZSM-5 (30) $_{WIE}$ e) Pt^{IV}/ZSM-5 (30) $_{WIE}$

The NO$_x$ storage capacities of the metal-exchanged ZSM-5 (30) catalysts were evaluated in the presence and absence of O$_2$. Figure 5.11 shows the NO$_x$ adsorption capacities in the absence of O$_2$ and quantification of the amount of NO$_x$ species desorbed during the TPD.
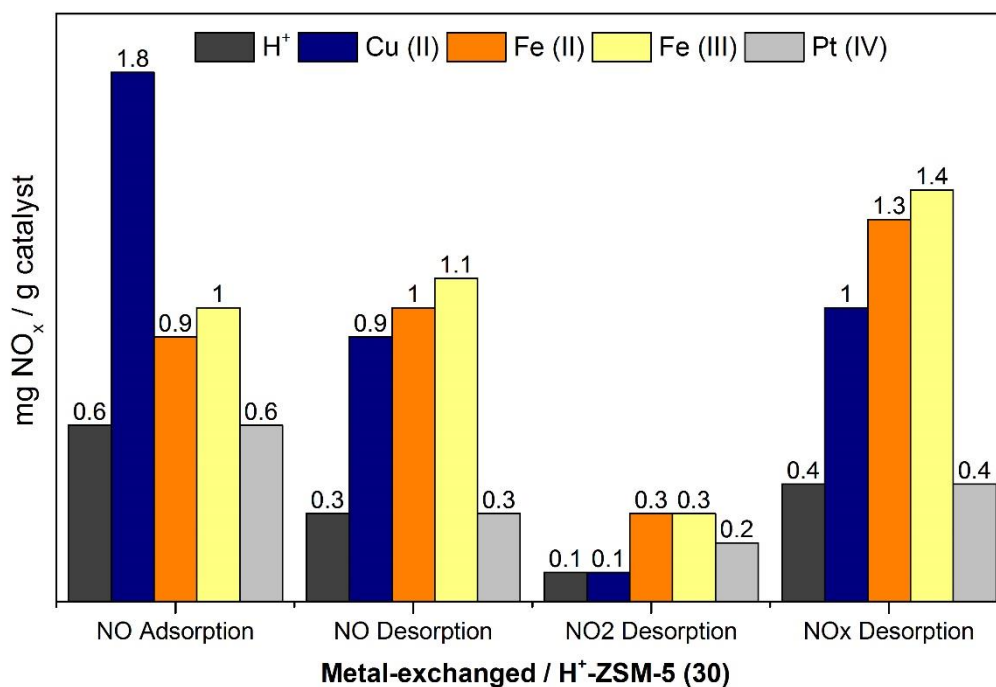
Figure 5.11. NO$_x$ storage capacities of metal-exchanged / H$^+$-ZSM-5 (30) catalysts

NO adsorption at 30 °C and TPD with He up to 500 °C

Reaction conditions: Flow reactor, GHSV = 35,000 h^{-1}, 0.1 % NO in He / He

Catalysts prepared by WIE at 25 °C for 24 h and calcined at 550 °C for 3 h in static air

After adsorbing NO in the absence of O$_2$, desorption occurs mainly in the form of NO and at temperatures below 250 °C.

Two kinds of NO$_x$ adsorption sites are present on metal ion-exchanged zeolites: weak adsorption sites, attributed to the parent zeolite, and strong adsorption sites, attributed to the metal species exchanged and supported on the zeolite [15].

The NO$_x$ adsorption and desorption capacity of the parent zeolite (H$^+$-ZSM-5) is lower than that of the metal-exchanged ZSM-5 (30) catalysts.

Among the different metal-exchanged zeolites, Cu^{II}/ZSM-5 (30) $_{WIE}$ exhibits the highest NO adsorption capacity at three times that of unmodified H^+-ZSM-5 (30). While the NO$_x$ desorption capacity is also around three times greater than the parent zeolite, it is similar to that of the Fe-exchanged zeolites. This indicates that NO adsorption on the Cu^{II}/ZSM-5 (30) $_{WIE}$ catalyst is mainly reversible, with most of the NO being desorbed at the adsorption temperature (30 °C). As discussed previously, the desorption capacity represented in the bar graphs does not include the amount of NO$_x$ desorbed at 30 °C. These results correlate with earlier studies in which Cu/ZSM-5 showed greater reversible NO adsorption compared to a series of metal-exchanged ZSM-5 zeolites[24].

The NO$_x$ adsorption and desorption behaviour of both Fe-exchanged zeolites, Fe^{II}/ZSM-5 (30) $_{WIE}$ and Fe^{III}/ZSM-5 (30) $_{WIE}$, is similar. This is despite variations in the redox properties of the supported Fe species shown in Figure 5.7, and suggests that the storage capacity is not affected by the Fe precursor, $Fe(SO_4)$ or $FeCl_3$, used for WIE.

Pt^{IV}/ZSM-5 (30) $_{WIE}$ presents the lowest adsorption and desorption capacity, comparable with that of unmodified H^+-ZSM-5 (30). A potential explanation is low exchange of Pt achieved during WIE. Characterisation of Pt^{IV}/ZSM-5 (30) $_{WIE}$ shows minor changes in the acid and redox properties when compared with the unmodified zeolite. In addition, the platinum solution used is much less concentrated (0.5 mM) than the copper and iron solutions (50 mM).

In the absence of O_2, limited desorption is observed at temperatures above 150 °C. It is known that NO is more weakly adsorbed on zeolites than NO_2. Therefore, to improve the storage capacity, NO should be converted to NO_2. The NO$_x$ storage capacities of the metal-exchanged ZSM-5 (30) catalysts were evaluated in the presence of O_2. Figure 5.12 shows the amount of NO$_x$ desorbed after NO was adsorbed in the presence of O_2.
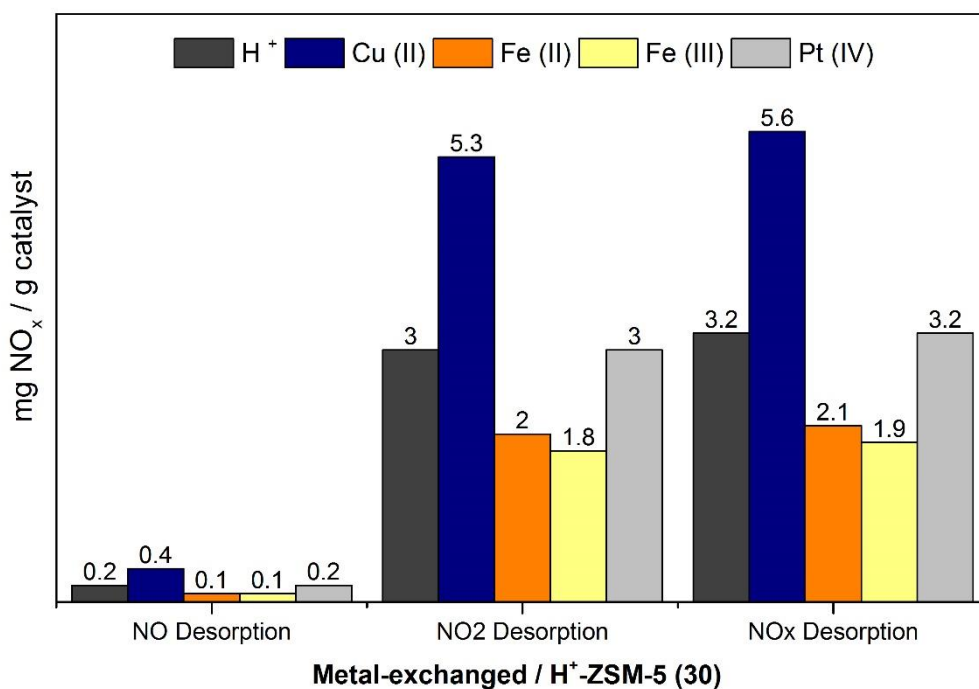
Figure 5.12. NO_x storage capacity of metal-exchanged / H^+-ZSM-5 (30) catalysts

NO_x adsorption at 30 °C ($NO:O_2$ = 1:75) and TPD with He up to 500 °C

Reaction conditions: Flow reactor, GHSV = 35,000 h^{-1}, 0.1 % NO + 7.5 % O_2 in He / He

Catalysts prepared by WIE at 25 °C for 24 h and calcined at 550 °C for 3 h in static air

NO_x is mainly desorbed in the form of NO_2. Cu^{II}/ZSM-5 (30) $_{WIE}$ exhibits the highest NO_x desorption, double of unmodified H^+-ZSM-5 (30). On the other hand, the storage capacity of the parent zeolite, H^+-ZSM-5 (30) is not changed after Pt ion-exchange in Pt^{IV}/ZSM-5 (30) $_{WIE}$. In contrast to the results obtained for adsorption in absence of O_2, Fe-exchanged zeolites present the lowest NO_x desorption capacity at 33 % below the baseline value set by unmodified H^+-ZSM-5 (30).

In the absence of O_2, NO adsorbed over metal ion-exchanged zeolites is converted to N_2O and N_2O_3 via a disproportionation reaction. The N_2O is easily desorbed and the N_2O_3

species, appearing as a NO$^+$-NO$_2^-$ ion pair, are more strongly chemisorbed. In the presence of O$_2$, NO oxidises to NO$_2$, which forms N$_2$O$_4$. This then ionizes into NO$^+$ and NO$_3^-$.

Hadjiivanov *et al*. [4] proposed that in the presence of O$_2$, NO adsorption on Cu/ZSM-5 at ambient temperature leads to the formation of nitrate and Cu^{2+}-NO species. In the presence of O$_2$, the NO species are converted via the following reaction sequence [4]:

$$NO \; \rightarrow \; N_2O_3 \; \rightarrow \; N_2O_4 \; \rightarrow \; NO_2 \; \rightarrow \; NO_3^- \qquad\qquad \text{Equation 5.1}$$

Hence, the presence of O$_2$ in the feed promotes the formation of nitrates [4,15,10,2,16,24]. As nitrates are more thermally stable, desorption of these species occurs at higher temperatures.

It has been reported that although the main role of the O$_2$ is to oxidise NO to NO$_2$ and convert the NO$_x$ into highly reactive surface nitrates [4], an excess of oxygen is also required to keep the catalyst surface clean from carbonaceous deposits and the metal ions in a high oxidation state [93].

A distribution of the NO$_x$ species desorbed at different temperatures is shown in Figure 5. 13.

Reversible adsorption at 30 °C is predominant over unmodified H$^+$-ZSM-5 (30). When compared with Cu and Fe ion-exchanged ZSM-5 catalysts, Pt^{IV}/ZSM-5 (30) $_{WIE}$ also exhibits considerable reversible adsorption, with a greater amount of NO$_x$ desorbed at 30 °C.

NO$_x$ desorption over the Fe ion-exchanged ZSM-5 catalysts occurs mainly at 250 °C, being non-significant at 100 °C and 350 °C.

Among the zeolite catalysts studied, only Cu^{II}/ZSM-5 (30) $_{WIE}$ exhibits a high degree of NO$_x$ desorption at 350 °C. This is attributed to formation of surface Cu(NO$_3$)$_2$ species that are more thermally stable.

Based on these results, Cu^{II}/ZSM-5 (30) $_{WIE}$ not only shows the highest activity for NO adsorption, but also a superior degree of NO$_x$ desorption at high temperatures than either Fe or Pt ion-exchanged ZSM-5 (30).
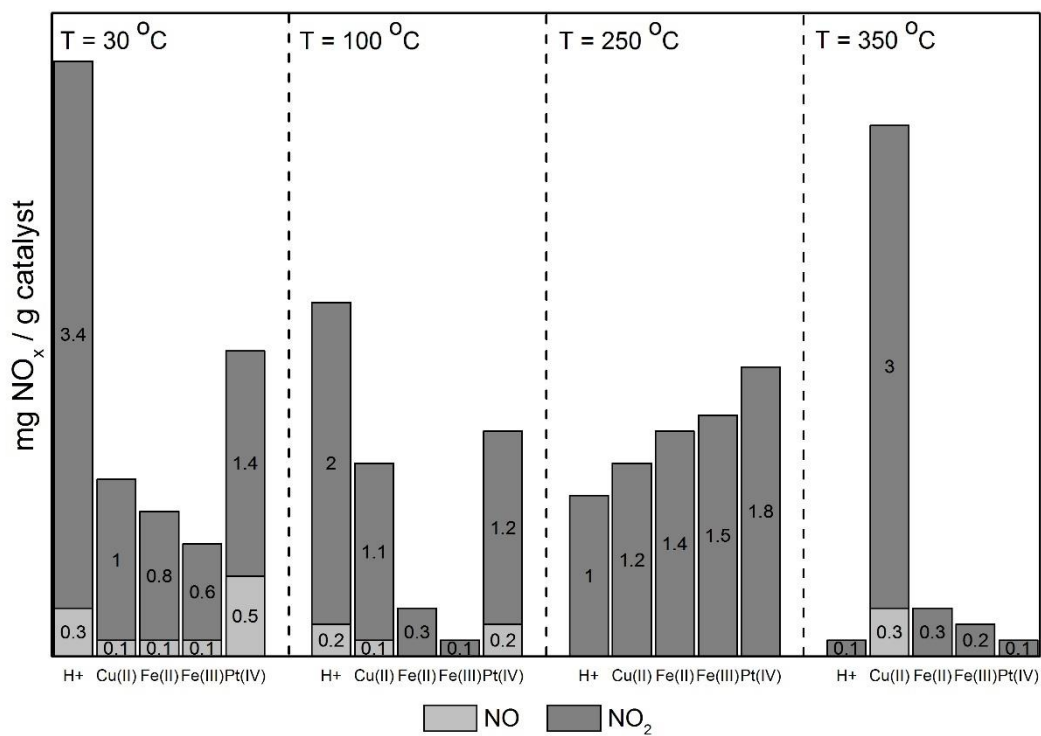

Figure 5.13. Total amount of NO$_x$ desorbed during the TPD carried out after NO$_x$ adsorption (0.1 % NO, 7.5 % O$_2$, He) on metal-exchanged / H$^+$-ZSM-5 (30) at each desorption temperature

5.3.1.2 Zeolite structure and aluminium content

The role of the zeolite framework in the adsorption/desorption process and effect of varying the Si/Al ratio, which determines a zeolites hydrophilic/hydrophobic character, was investigated. Cu and Fe ions were exchanged into different medium and large pore zeolites including; Y, ZSM-5 and BETA, by WIE.

Zeolite Y has a Faujasite- type structure and possesses highly ordered cavities, denoted as supercages, with a diameter of 13 nm [94]. It is also very hydrophilic.

Among the different zeolites available, ZSM-5 is widely used and studied. It has a MFI framework type and belongs to the pentasil family of zeolites. ZSM-5 is formed by 10 ring channels system with apertures of 0.51 nm x 0.55 nm and 0.53 nm x 0.56 nm. It ranges from moderately hydrophilic to hydrophobic, depending on the Si/Al ratio. Its acid resistance and thermal stability together with the special pore structure, possessing channel dimensions equal to the diameter of an aromatic ring [95], make ZSM-5 based catalysts suitable for multiple applications.

BETA is an attractive zeolite because of its widely open structure with a three dimensional channel system and narrow pore size distribution. With a disordered BEA framework type, it consists of 12 membered ring apertures with two perpendicular straight channels, each with a cross-section of 0.76 nm x 0.64 nm, and a sinusoidal channel of 0.56 nm x 0.56 nm. Within this type of open distorted framework, aluminium is present in a octahedral framework coordination site and as extra-framework species [96]. The open structure provides greater accessibility to aluminium sites and compensating extra-framework cations, and makes it promising for shape-selective reactions. NH_4^+-exchanged BETA is known to contain a substantial concentration of defects, which gives it unique acid properties. BETA contains nine types of different T sites and seventeen environments of

oxygen. In addition, compared to ZSM-5, zeolite BETA possesses high hydrothermal ability.

The channel dimensions of a zeolite not only affect its adsorption/desorption properties but also the effectiveness of metal ion-exchange. Larger channel dimensions could have a beneficial effect on WIE as it facilitates the diffusion of hydrated metal ions into the pores.
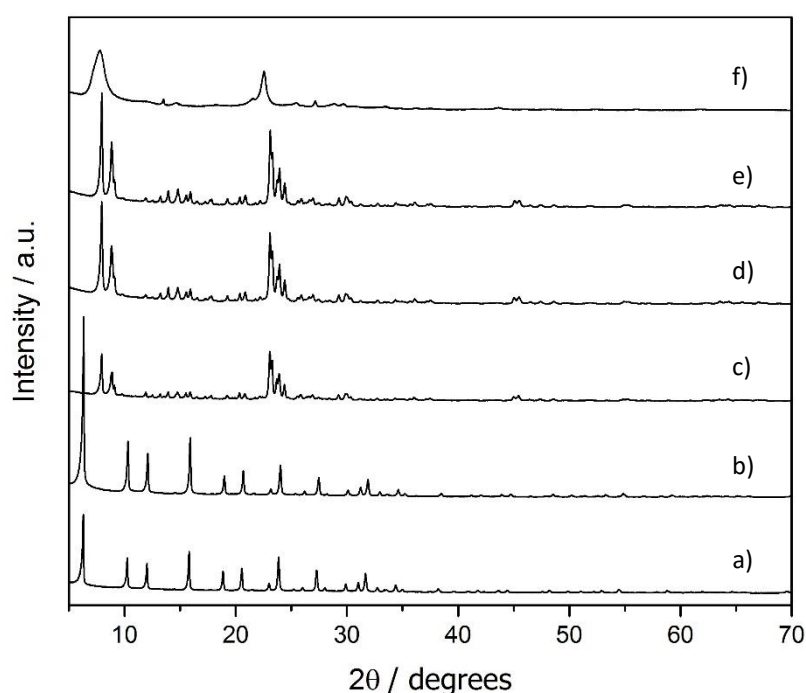
Figure 5.14. Powder X-Ray diffraction patterns of the parent zeolites:

a) H$^+$-Y (5.1)   b) H$^+$-Y (30)   c) H$^+$-ZSM-5 (23)   d) H$^+$-ZSM-5 (30)

e) H$^+$-ZSM-5 (50)   f) H$^+$-BETA (38)

XRD patterns in Figure 5.14 show the characteristic diffraction peaks of each framework type [97]. Figure 5.14 a) and b) show distinctive diffraction peaks at 2θ of 6.3°, 10.3°, 12.1°, 15.9° and 24.1°, typical of FAU-type zeolites. XRD pattern of ZSM-5, Figure 5.14 c), d) and e), is consistent with an MFI-type zeolite, with typical diffraction peaks at 2θ of 7.9°,

8.8°, 23.1°, 23.9°, and 24.4°.Typical diffraction peaks of H^+-BETA, Figure 5.14 f), appear at 2θ of 7.8°, 22.4°, 29.6° and 43.5°.

Figure 5.15 illustrates the effect of varying the zeolite framework and acidity on NO_x storage in the absence of O_2, over Cu-exchanged zeolites.

Figure 5.15. NO_x storage capacity of Cu-exchanged zeolites

NO adsorption at 30 °C and TPD with He up to 500 °C

Reaction conditions: Flow reactor, GHSV = 35,000 h^{-1}, 0.1 % NO in He / He

Catalysts prepared by WIE at 25 °C for 48 h and calcined at 550 °C for 3 h in static air

Both NO adsorption and desorption are dependent on the structure and aluminium content of the zeolites. As before, NO_x desorption occurs mainly in the form of NO at low temperatures. Two different peaks are observed in the desorption profile, corresponding to reversible adsorption of NO at 30 °C and NO desorption at 100 °C.

Cu-exchanged Y catalysts, Cu^{II}/Y (5.1) $_{WIE}$ and Cu^{II}/Y (30) $_{WIE}$, exhibit the lowest NO adsorption capacities. While NO adsorption over Cu^{II}/Y (30) $_{WIE}$ is mainly reversible, NO desorption (T > 30 °C) is more significant for the Cu^{II}/Y (5.1) $_{WIE}$ catalyst. Among the zeolite catalysts studied, $Cu^{II}/BETA$ (38) $_{WIE}$ presents the highest NO adsorption and desorption capacity. However, around 50 % of the NO adsorption is reversible and the amount of NO_x desorbed at 100 °C is similar to that of the Cu-exchanged ZSM-5 catalysts.

The NO adsorption performance of Cu-exchanged ZSM-5 catalysts increases with the SiO_2 content of the ZSM-5, though no clear trend is observed regarding their desorption capacity. Although the amount of NO desorbed at 100 °C is similar for both $Cu^{II}/ZSM-5$ (23) $_{WIE}$ and $Cu^{II}/ZSM-5$ (50) $_{WIE}$ catalysts ($\approx$ 1.6 mg NO_x/g), the desorption capacity of the $Cu^{II}/ZSM-5$ (30) $_{WIE}$ catalyst is lower. It should be noted that the catalysts denoted as ''$Cu^{II}/ZSM-5$ (30) $_{WIE}$'' in Figures 5.11 and 5.15 were prepared by WIE over 24 and 48 h respectively. The desorption capacity is comparable but not the NO adsorption, hence, these differences are related to the amount of reversible NO adsorption. Mass transfer limitations could affect the NO_x desorption at low temperatures [98], slowing the desorption of physisorbed NO_x at 30 °C.

Concordant with the results discussed here, Chang *et al.* [15] found that H^+-BETA zeolites perform better for adsorbing NO_x at 40 °C than Na^+-Y, H^+-ZSM-5, mordenite or activated carbon.

In order to study desorption at high temperatures, the NO_x storage capacities of Cu-exchanged ZSM-5 (30) catalysts were evaluated in the presence of O_2. Figure 5.16 shows the amount of NO_x desorbed after adsorption in the presence of O_2, as well as the NO oxidation activity.
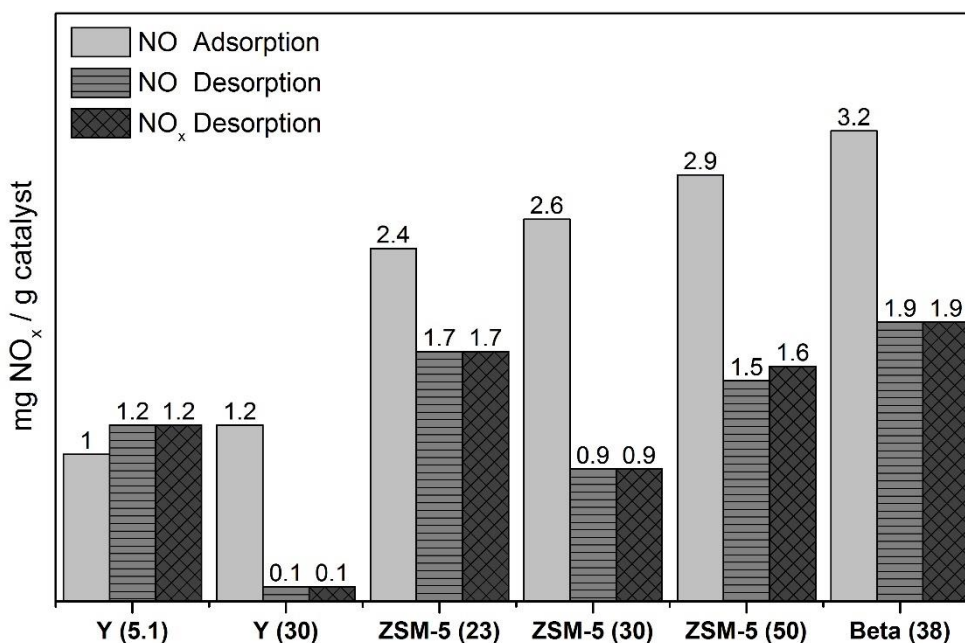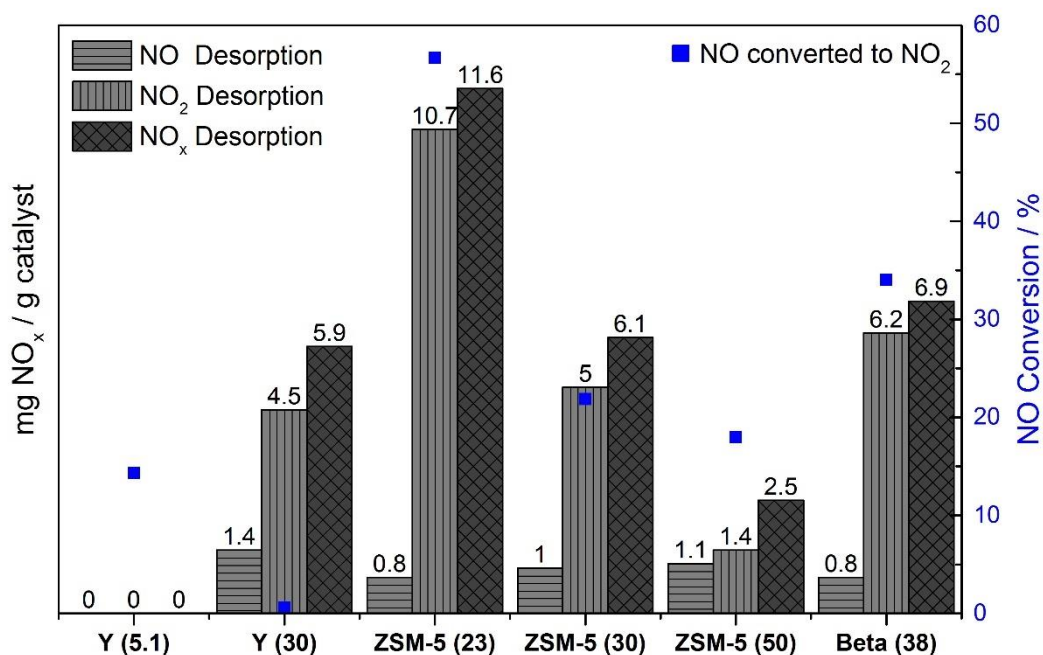
Figure 5.16. NO_x storage capacity of Cu-exchanged zeolites

NO_x adsorption at 30 °C ($NO:O_2$ = 1:75) and TPD with He up to 500 °C

Reaction conditions: Flow reactor, GHSV = 35,000 h^{-1}, 0.1 % NO + 7.5 % O_2 in He / He

Catalysts prepared by WIE at 25 °C for 48 h and calcined at 550 °C for 3 h in static air

Again, the main component of desorbed NO_x is NO_2 and desorption at high temperatures becomes significant.

Cu^{II}/ZSM-5 (23) $_{WIE}$ exhibits the highest NO_x desorption capacity. Among the Cu-exchanged ZSM-5 catalysts, desorption is clearly enhanced with the Al_2O_3 content of the ZSM-5 support. The amount of NO_x desorbed from Cu^{II}/ZSM-5 (23) $_{WIE}$ is more than 4 times that for Cu^{II}/ZSM-5 (50) $_{WIE}$. Hence, decreasing the SiO_2/Al_2O_3 ratio increases the NO_x storage capacity. This is potentially due to the fact that hydrophilicity and cation exchange capacity increase with the Al_2O_3 content of the zeolite. In order to correlate the

storage capacity with an improvement in the cation exchange properties, elemental analysis should be carried to determine the actual loadings of supported metals.

The total amount of NO_x desorbed over Cu^{II}/Y (30) $_{WIE,}$ Cu^{II}/ZSM-5 (30) $_{WIE}$ and $Cu^{II}/BETA$ (38) $_{WIE}$ is approximately 6 mg NO_x/g. Accordingly, the storage capacity of Cu-exchanged zeolites with different structure but similar acidity is comparable.

Interestingly, the superior acidity of Zeolite Y, which has a SiO_2/Al_2O_3 ratio of 5.1, is not beneficial for the storage capacity of Cu ion-exchanged catalysts. This is because NO_x adsorption over Cu^{II}/Y (5.1) $_{WIE}$ is exclusively reversible, with one peak observed at 30 °C attributed to desorption of physisorbed NO and NO_2.

As reported previously in the literature , the first reaction that takes place in the presence of NO and O_2 is the oxidation of NO to NO_2 [15]:

$$2\,NO \;+\; O_2 \;\leftrightarrow\; 2\,NO_2 \;\leftrightarrow\; NO^+ \;+\; NO_3^- \qquad\qquad\qquad \text{Equation 5.1}$$

In general, a high desorption capacity correlates with high oxidation activity. The amount of NO_x desorbed is greater for those catalysts which oxidise NO to NO_2 during the 30 °C adsorption period. Cu^{II}/ZSM-5 (23) $_{WIE}$ not only presents the greatest desorption capacity but also the highest conversion of NO to NO_2. Surprisingly, despite negligible NO oxidation, considerable desorption is observed for Cu^{II}/Y (30) $_{WIE}$.

Desorption over the H^+ form of zeolites is attributed to decomposition of surface HNO_3 species. Nitric acid could be formed by interaction of adsorbed NO_x with H_2O or via NO_2 disproportionation following:

$$ZEO\text{-}O\text{-}H^+ \;+\; NO^+ \;+\; NO_3^- \;\leftrightarrow\; ZEO\text{-}O\text{-}NO^+ \;+\; H^+NO_3^- \qquad\qquad \text{Equation 5.2}$$
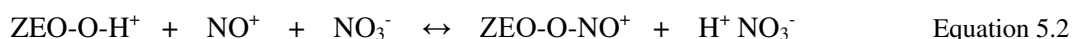
HNO$_3$ species formed through both reaction mechanisms have similar thermal stability. It has been reported that deposition of HNO$_3$ onto the surface of zeolites could induce contraction of the unit cell [98].

Over Cu-exchanged zeolites, NO$_x$ is adsorbed in the form of nitrates. The following reaction sequence has been previously proposed [15]:

$$2 \text{ ZEO-CuO} + 2 \text{ NO}^+ + 2 \text{ NO}_3^- \rightarrow \text{ZEO-Cu(NO}_2)_2 + \text{ZEO-Cu(NO}_3)_2$$
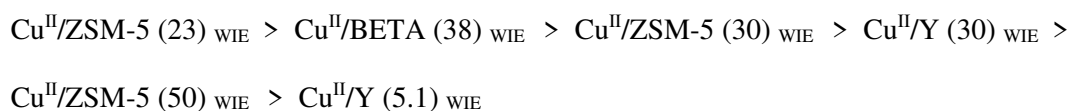$$\rightarrow 2 \text{ ZEO-Cu(NO}_2)_2 + 2 \text{ NO g} \qquad\qquad \text{Equation 5.3}$$
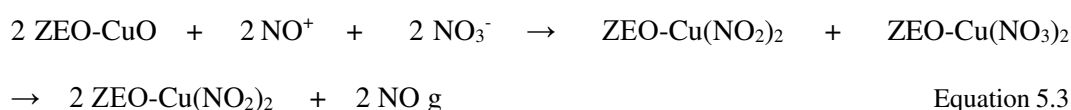
The distribution of NO$_x$ species desorbed at different temperatures is shown in Figure 5. 17.

The purpose of this work is to enhance the high temperature desorption of NO$_x$. Accordingly, based on the amount of NO$_x$ desorbed at temperatures above 200 °C, the storage capacity of the Cu-exchanged zeolites decreases as follows:

Cu^{II}/ZSM-5 (23) $_{WIE}$ > Cu^{II}/BETA (38) $_{WIE}$ > Cu^{II}/ZSM-5 (30) $_{WIE}$ > Cu^{II}/Y (30) $_{WIE}$ > Cu^{II}/ZSM-5 (50) $_{WIE}$ > Cu^{II}/Y (5.1) $_{WIE}$

Integration of desorption peaks at 250 °C and 350 °C allowed quantification of the amount on NO$_x$ desorbed from these catalysts. In this way, Cu^{II}/Y (30) $_{WIE}$ Cu^{II}/ZSM-5 (30) $_{WIE}$ and Cu^{II}/BETA (38) $_{WIE}$ show desorption of 4.7, 5.2 and 5.3 mg NO$_x$/g respectively. Thus, the storage capacity of Cu-exchanged zeolites with different frameworks but similar acidity is comparable, when comparing the total amount of NO$_x$ desorbed and the amount desorbed at high temperatures.

The amount of NO$_x$ desorbed at high temperature over Cu^{II}/ZSM-5 (23) $_{WIE}$ is 6 mg NO$_x$/g. This is 15 % higher than that of Cu^{II}/ZSM-5 (30) $_{WIE}$. However, when considering total NO$_x$ desorption across the whole temperature range, Cu^{II}/ZSM-5 (23) $_{WIE}$

shows double the amount of desorbed NO$_x$ compared to Cu^{II}/ZSM-5 (30) $_{WIE}$. This is attributed to the fact that Cu^{II}/ZSM-5 (23) $_{WIE}$ also presents a high concentration of weakly adsorbed NO$_x$ species, which desorb at 30 °C and 100 °C and account for up to 11.2 mg NO$_x$/g of the total desorption.
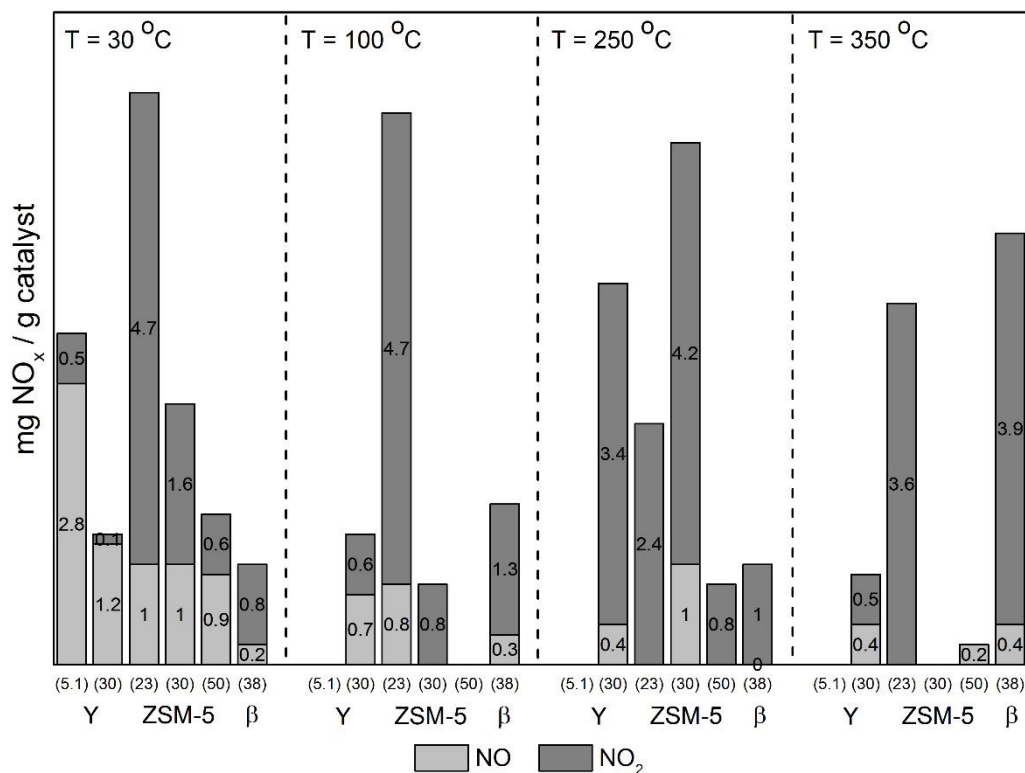
Figure 5.17. Total amount of NO$_x$ desorbed during the TPD carried out after NO$_x$ adsorption (0.1 % NO, 7.5 % O$_2$, He) on Cu-exchanged zeolites at each desorption temperature

The results in Figures 5.15 show that in the absence of O$_2$, the NO adsorption capacity is influenced by both the zeolite structure and acidity. Meanwhile Figure 5.17 shows that in the presence of O$_2$, while the oxidation activity is influenced by both the zeolite framework type and acidity, the NO$_x$ desorption capacity is found to be more dependent on the Brønsted acidity of the zeolite than on the framework structure.

The NO$_x$ storage capacity of Cu-exchanged zeolites depends on two factors: i) Selective adsorption sites attributed to ion-exchanged Cu^{2+}/Cu$^+$ and supported oxides (CuO) and ii) physical and weak chemical adsorption on the zeolite support itself, which correlates with its physicochemical properties including structure, acidity, surface area and micropore volume.

The superior total NO$_x$ desorption at 30 °C and 100 °C over the Cu^{II}/ZSM-5 (23) $_{WIE}$ catalyst could be attributed to intrinsic adsorption properties of the unmodified H$^+$-ZSM-5 (23). H$^+$-ZSM-5 (23) possesses relatively high Brønsted acidity due to the higher aluminium content. This promotes the formation of surface HNO$_3$ species through the reactions shown in Equation 5.2. Adsorption/desorption studies over the bare H-form zeolites are required to determine the extent to which the support contributes to the storage capacity of   Cu-exchanged catalysts. This will also determine whether there is a synergistic effect between the zeolite support and CuO species.

The impact of the oxidation state and redox properties of Cu^{n+} ions upon NO$_x$ storage capacity has been studied in previous work [24] [37] [75] [99]. In general, catalysts where Cu^{2+} is more readily reduced to Cu$^+$ are more active in generating intermediates for deNO$_x$ reactions, such as the oxidation of NO to NO$_2$, which favours the formation of more thermally stable adsorbed nitrate species. Additionally, higher activity is observed for catalysts with more stable Cu$^+$ species, which show a higher Cu$^+$ to Cu^0 reduction temperature.

The H$_2$-TPR profiles of the Cu-exchanged zeolites are shown in Figure 5.18.

As discussed previously, Cu-exchanged zeolites generally exhibit two reduction peaks, at 225 °C and 400 °C. The first reduction peak is attributed to reduction of Cu^{2+} to Cu$^+$ located at cation-exchange sites and supported CuO species.

$$Cu^{2+} + H_2 \rightarrow Cu^0 + H_2O \qquad\qquad \text{Equation 5.4}$$
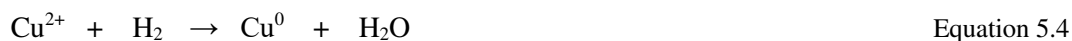
The second peak corresponds to reduction of Cu^+ to Cu^0.

$$Cu^+ + \tfrac{1}{2} H_2 \rightarrow Cu^0 + \tfrac{1}{2} H_2O \qquad\qquad \text{Equation 5.5}$$
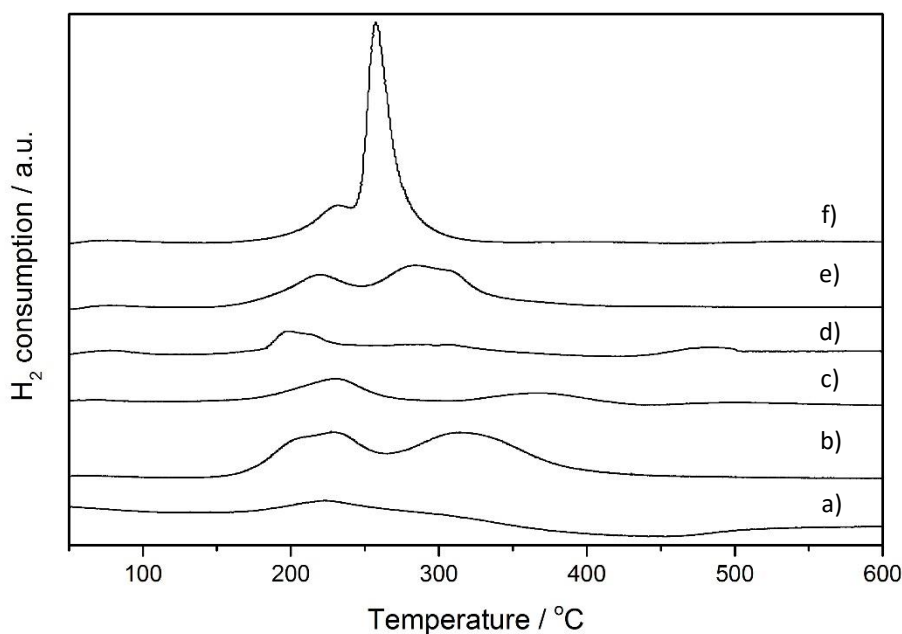
Figure 5.18. H_2-TPR profiles of Cu-exchanged zeolites:

a) Cu^{II}/Y (5.1) WIE   b) Cu^{II}/Y (30) WIE   c) Cu^{II}/ZSM-5 (23) WIE   d) Cu^{II}/ZSM-5 (30) WIE

e) Cu^{II}/ZSM-5 (50) WIE   f) Cu^{II}/BETA (38) WIE

The reduction profile is highly dependent on the support as the reduction temperature is affected by the interaction of the Cu ions with the zeolite. The temperature at which Cu^{2+} is reduced to Cu^+ depends on the presence of Cu^{2+} located at exchange sites and as supported CuO species. In addition, the reduction temperature is known to be affected by the acidity of the support. Cu ions exchanged on a low SiO_2/Al_2O_3 ratio zeolite are likely

to be reduced at a higher temperature, as the high negative framework charge means that Cu cations are more strongly bonded to the framework oxygen.

Total hydrogen consumption, determined from the TPR profiles, is shown in Table 5.4. Despite variations in the total amount of H_2 consumed, reduction profiles are comparable for all catalysts, except Cu^{II}/BETA (38) $_{WIE}$.

Table 5.4. Hydrogen consumption obtained from the H_2-TPR profiles of Cu-exchanged zeolites:

	H_2 consumption μmol H_2/g	High/Low temperature area ratio
Cu^{II}/Y (5.1) $_{WIE}$	256	0.0
Cu^{II}/Y (30) $_{WIE}$	499	1.4
Cu^{II}/ZSM-5 (23) $_{WIE}$	310	0.5
Cu^{II}/ZSM-5 (30) $_{WIE}$	219	0.5
Cu^{II}/ZSM-5 (50) $_{WIE}$	477	2.0
Cu^{II}/BETA (38) $_{WIE}$	491	4.0

Cu supported on H^+-BETA (38) presents a distinctive reduction profile with a small peak appearing at 235 °C and a sharp intense peak at 255 °C. It should be noted that the high/low temperature area ratio of this catalyst is 4, much higher than that of Cu supported on H^+-Y and H^+-ZSM-5. The TPR profile for Cu^{II}/BETA (38) $_{WIE}$ is similar to that observed for over-exchanged zeolites in previous work [100], where the reduction peak at 250 °C is assigned to cationic oligomers located at exchanged sites. Although compositional analysis is required to determine the Cu loadings, TPR results suggest that the level of exchange is superior in the case of Cu supported on H^+-BETA (38). The superior NO adsorption capacity, Figure 5.15, and NOₓ desorption at high temperature, Figure 5.17, could be attributed to a high level of metal ion-exchange.

The NO_x storage capacity of Fe-exchanged zeolites prepared by WIE using $FeCl_3$, was also investigated.

Figure 5.19 illustrates the effect of the zeolite structure and acidity on NO_x storage, in the absence of O_2, over Fe-exchanged zeolites.

Figure 5.19. NO_x storage capacity of Fe-exchanged zeolites

NO adsorption at 30 °C and TPD with He up to 500 °C

Reaction conditions: Flow reactor, GHSV = 35,000 h^{-1}, 0.1 % NO in He / He

Catalysts prepared by WIE at 25 °C for 48 h and calcined at 550 °C for 3 h in static air

Fe^{III}/BETA (38) $_{WIE}$ exhibits the highest NO adsorption and desorption capacity, 6.3 and 3.6 mg NO_x/g. This is superior to its Cu analogue catalyst Cu^{II}/BETA (38) $_{WIE}$, and nearly 8 times that of Fe exchanged onto H^+/ZSM-5 (30). Unlike the results obtained for

Cu-exchanged zeolites, in the absence of O_2 Fe/ZSM-5 catalysts present poor NO storage activity, with performance comparable with that of the unmodified zeolites. Additionally, an increase in the amount of NO adsorbed at 30 °C is observed for Fe/Y catalysts when compared with Cu analogues in Figure 5.15.

Figure 5.20 shows the degree of NO conversion and amount of NO_x desorbed following adsorption in the presence of NO and O_2.

In agreement with the trend found for Cu-exchanged ZSM-5 catalysts, NO_x desorption is clearly enhanced with the Al_2O_3 content of the ZSM-5 support. The amount of NO_x desorbed for the Fe^{III}/ZSM-5 (23) $_{WIE}$ catalyst is more than 7 that of the Fe^{III}/ZSM-5 (50) $_{WIE}$ catalyst. The total NO_x desorption capacity of the two more active catalysts; Fe^{III}/ZSM-5 (23) $_{WIE}$ and Fe^{III}/BETA (38) $_{WIE}$, is comparable with that of their Cu analogues, Cu^{II}/ZSM-5 (23) $_{WIE}$ and Cu^{II}/BETA (38) $_{WIE}$.

For Fe-exchanged zeolites, the NO_x storage capacity is also influenced by the zeolite structure. Both the amount of NO adsorbed on the catalyst in the absence of O_2 and the amount of NO_x desorbed following adsorption in the presence of O_2 are affected by the zeolite structure. Figure 5.20 shows that there is a significant change in the NO_x desorption capacity of catalysts with comparable SiO_2/Al_2O_3 ratio but different zeolite frameworks, being Fe^{III}/BETA (38) $_{WIE}$ > Fe^{III}/ZSM-5 (30) $_{WIE}$ > Fe^{III}/Y (30) $_{WIE}$. However, Fe supported on BETA zeolite does not always present superior NO_x storage performance compared to Fe supported on ZSM-5. Pan *et al.* [14] reported that Fe/ZSM-5 (30) presents higher NO_x adsorption capacity than Fe/BETA (25), under 470 ppm of NO and 5 % of O_2 at 300 °C.
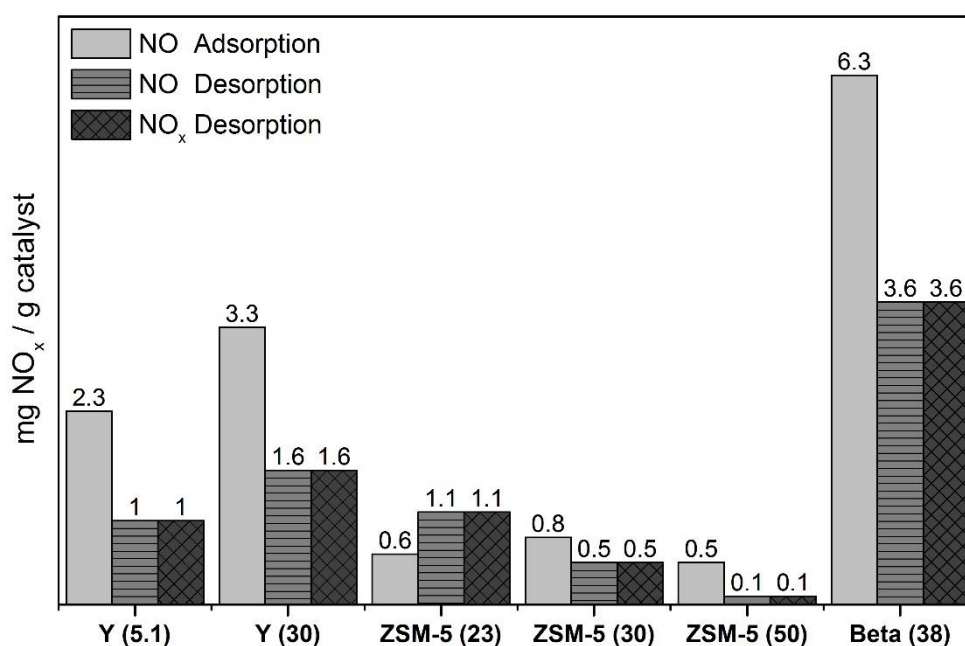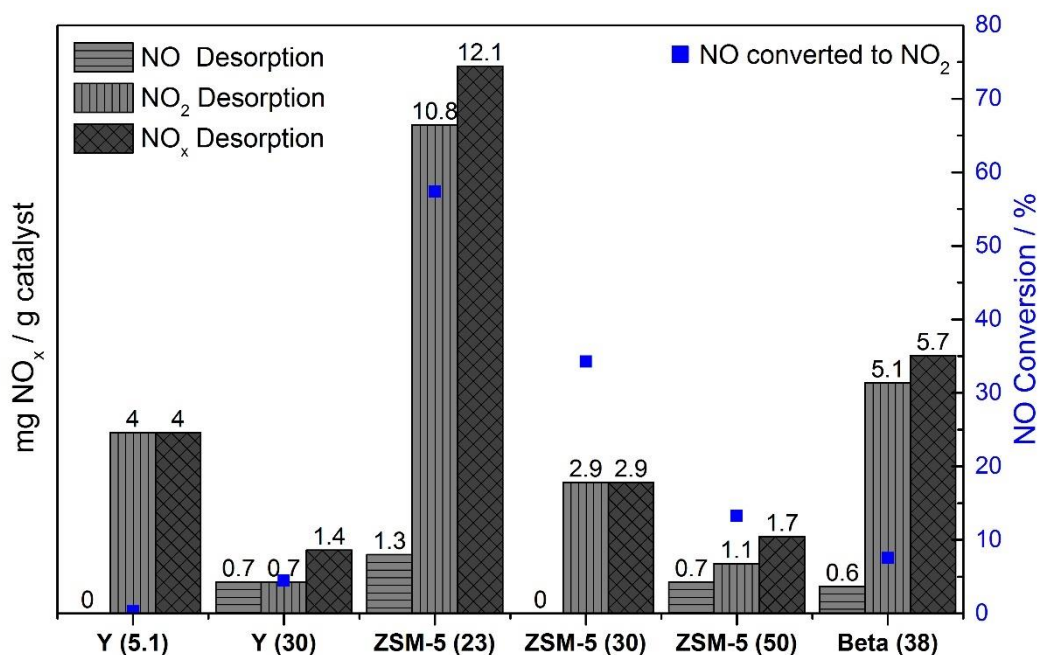
Figure 5.20. NO_x storage capacity of Fe-exchanged zeolites

NO_x adsorption at 30 °C (NO:O_2 = 1:75) and TPD with He up to 500 °C

Reaction conditions: Flow reactor, GHSV = 35,000 h^{-1}, 0.1 % NO + 7.5 % O_2 in He / He

Catalysts prepared by WIE at 25 °C for 48 h and calcined at 550 °C for 3 h in static air

The distribution of NO_x species desorbed from Fe-exchanged zeolites at different temperatures is shown in Figure 5. 21.

It is important to highlight the decrease in the amount of total NO_x desorbed at high temperature, especially at 350 °C, when comparing Fe-exchanged zeolites with analogous Cu catalysts (Figure 5.17). While, the amount of NO_x desorbed at 350 °C is 4.3 mg NO_x/g over Cu^{II}/BETA (38) $_{WIE}$, this value decreases to 1.3 mg NO_x/g for Fe^{III}/BETA (38) $_{WIE}$. However the difference in the total amount of NO_x desorbed at high

temperatures (T > 200 °C) over metal-exchanged BETA (38) is not as significant: 5.3 mg NO_x/g for Cu^{II}/BETA (38) $_{WIE}$ and 4.9 mg NO_x/g for Fe^{III}/BETA (38) $_{WIE}$.

Based on the amount of NO_x desorbed at temperatures above 200 °C, the storage capacity of the Fe-exchanged zeolites decreases as follows:

Fe^{III}/BETA (38) $_{WIE}$ > Fe^{III}/Y (5.1) $_{WIE}$ > Fe^{III}/ZSM-5 (23) $_{WIE}$ ≈ Fe^{III}/ZSM-5 (30) $_{WIE}$ > Fe^{III}/ZSM-5 (50) $_{WIE}$ > Fe^{III}/Y (30) $_{WIE}$
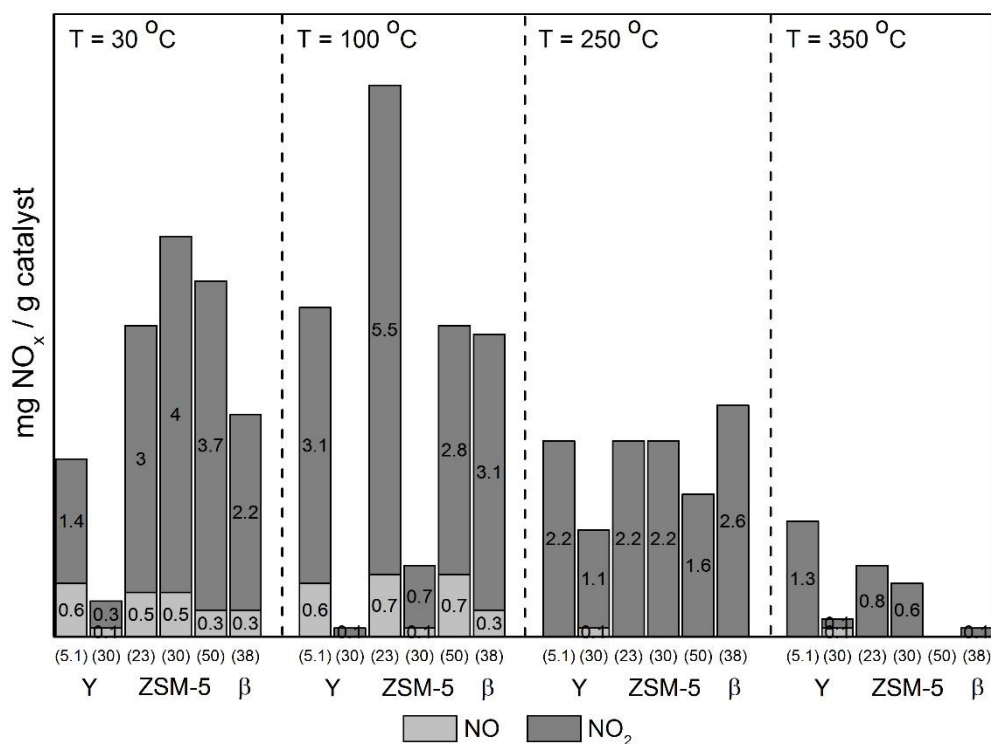
Figure 5.21. Total amount of NO_x desorbed during the TPD carried out after NO_x adsorption (0.1 % NO, 7.5 % O_2, He) on Fe-exchanged zeolites at each desorption temperature

Despite the superior desorption capacity of the Fe^{III}/ZSM-5 (23) $_{WIE}$ catalyst (12.1 mg NO_x/g), most NO_x is desorbed at 30 °C and 100 °C. As found for its Cu analogue, the large amount of NO_x desorbed at low temperature is attributed to intrinsic adsorption properties of the zeolite support (H^+-ZSM-5 (23)) and formation of surface HNO_3 species.

The nature of metal-exchanged ions and their redox properties greatly affect the NO$_x$ storage capacity of zeolite catalysts. H$_2$-TPR profiles of the Fe-exchanged zeolites are shown in Figure 5.22.
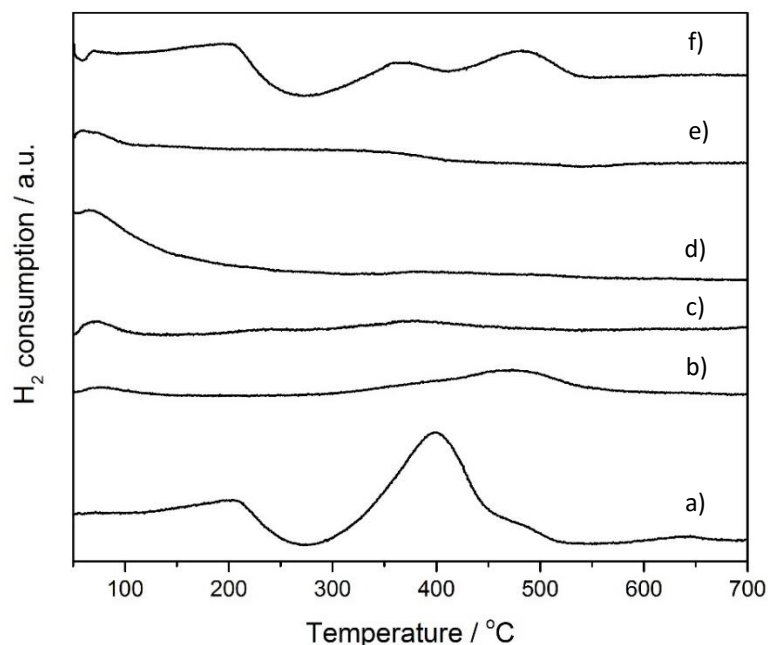
Figure 5.22. H$_2$-TPR profiles of Fe-exchanged zeolites:

a) Fe^{III}/Y (5.1) $_{WIE}$ b) Fe^{III}/Y (30) $_{WIE}$ c) Fe^{III}/ZSM-5 (23) $_{WIE}$ d) Fe^{III}/ZSM-5 (30) $_{WIE}$

e) Fe^{III}/ZSM-5 (50) $_{WIE}$ f) Fe^{III}/BETA (38) $_{WIE}$

As discussed previously, a typical reduction profile for Fe ion-exchanged zeolites presents two peaks. The first peak at 375 °C corresponds to the reduction of Fe$_2$O$_3$ to Fe$_3$O$_4$. The second peak, at 500 °C, is assigned to the reduction of Fe$_3$O$_4$ to Fe^0 via FeO. In addition to these characteristic Fe reduction peaks, a distinctive negative event centred around 250 °C is observed for Fe^{III}/Y (5.1) $_{WIE}$ and Fe^{III}/BETA (38) $_{WIE}$.

Total hydrogen consumption determined through integration of the H$_2$-TPR curves is included in Table 5.5. In concordance with the absence of intense reduction peaks in

Figure 5.22, H_2 consumption is much lower for Fe exchanged onto ZSM-5 zeolites. Elemental analysis of Fe loadings should be performed to determine if variations in H_2 consumption are due to the metal exchange level achieved, influenced by the zeolite structure, or to a change in the reducibility of the Fe species induced by the support.

Table 5.5. Hydrogen consumption obtained from the H_2-TPR profiles

of the Fe-exchanged zeolites:

	H_2 consumption $\mu mol\ H_2/g$
Fe^{III}/Y (5.1) $_{WIE}$	281
Fe^{III}/Y (30) $_{WIE}$	119
$Fe^{III}/ZSM-5$ (23) $_{WIE}$	49
$Fe^{III}/ZSM-5$ (30) $_{WIE}$	23
$Fe^{III}/ZSM-5$ (50) $_{WIE}$	44
$Fe^{III}/BETA$ (38) $_{WIE}$	93

Iron possesses high oxygen storage capacity and oxygen mobility because of its equilibrium:

$$Fe^{3+} \leftrightarrow Fe_3O_4 \leftrightarrow Fe^{2+}$$ Equation 5.6

Low storage capacity is related with a low content of Fe^{3+} as both the oxygen storage capacity and oxygen mobility are lower. It has been reported previously that the presence of Fe_2O_3 species plays a crucial role in the oxidation of NO to NO_2. Hence, the larger amount of H_2 consumed could explain the superior NO_x storage capacity of the $Fe^{III}/BETA$ (38) $_{WIE}$ catalyst, potentially due to a higher Fe^{3+} content.

5.3.2 Chemical vapour impregnation

The method by which metal ion-exchanged zeolites are prepared is crucial in optimising NO$_x$ storage capacity, through control of metal loadings, nature and distribution of active species and crystallite size.

Sublimation of FeCl$_3$ vapour onto the H$^+$ form of a zeolite is an effective method to introduce Fe into exchange sites [43] [49] [101] [102] [47]. Over-exchanged Fe-MFI prepared by sublimation shows high activity for deNO$_x$ technologies. Several authors have reported a method by which anhydrous FeCl$_3$ is sublimed onto H$^+$-ZSM-5, with Brønsted protons replaced by [FeCl$_2$]$^+$ according to the following reaction [43]:

$$H^+ \ + \ FeCl_3 \ \rightarrow \ [FeCl_2]^+ \ + \ HCl \qquad\qquad \text{Equation 5.7}$$

As introduced in Chapter 4, chemical vapour impregnation (CVI) is a simple, facile, reproducible and easily controlled metal vapour deposition technique developed by Forde *et al.* [103] It has been demonstrated that CVI is an effective technique to achieve highly dispersed metal oxide nanoparticles on H+-ZSM-5 [84] [104] [105]. A detailed description of the experimental procedure is found in Chapter 3, Section 3.2.2.2.

5.3.2.1 Exchanged metal

1 wt. % Cu-, Fe- and Pt-exchanged ZSM-5 (30) were prepared by CVI using copper (II) acetylacetonate, iron (III) acetylacetonate and platinum (II) acetylacetonate as metal precursors.

The physicochemical properties of the metal-exchanged zeolites, prepared by chemical vapour impregnation and calcined at 550 °C for 3 hours in static air are summarised in Table 5.6.

Table 5.6. Physicochemical properties of metal-exchanged zeolites prepared by CVI:

	Surface area $_{BET}$ [a]	Pore volume [a]	Acidity [b]			H$_2$ Consumption[c]
			Total	250 °C	450 °C	
	m^2/g	mL/g		μmol NH$_3$/g		μmol H$_2$/g
H$^+$-ZSM-5 (30)	412	0.383	1299	260	350	181
Cu^{II}/ZSM-5 (30) $_{CVI}$	337	0.319	1290	512	67	152
Fe^{III}/ZSM-5 (30) $_{CVI}$	375	0.357	1077	82	730	84
Pt^{II}/ZSM-5 (30) $_{CVI}$	307	0.208	X	X	X	69

[a] Surface area and pore volume measured by N$_2$ physisorption, [b] acidity measured by NH$_3$-TPD and [c] hydrogen consumption obtained from the H$_2$-TPR profiles

Impregnation of H$^+$-ZSM-5 (30) via CVI diminishes the total surface area by 18 % for Cu, 9 % for Fe and 25 % for Pt. The total pore volume also decreases after metal exchange. This pore blockage is extensive for the Pt^{II}/ZSM-5 (30) $_{CVI}$ catalyst, with a 46 % decrease in pore volume.

Table 5.7. Pore volume distribution of metal-exchanged zeolites prepared by CVI:

	Pore volume/mL·g^{-1}			
	Total	Microporous (< 2 nm)	Mesoporous (2 nm – 50 nm)	Macroporous (> 50 nm)
H$^+$-ZSM-5 (30)	0.383	0.142	0.209	0.033
Cu^{II}/ZSM-5 (30) $_{CVI}$	0.319	0.115	0.178	0.026
Fe^{III}/ZSM-5 (30) $_{CVI}$	0.357	0.129	0.196	0.032
Pt^{II}/ZSM-5 (30) $_{CVI}$	0.208	0.104	0.102	0.002

The pore volume distributions of the metal-exchanged ZSM-5 (30) catalysts prepared by CVI are presented in Table 5.7. A decrease in the micro- and meso-porous volume is common for Cu, Fe and Pt/ZSM-5 (30) catalysts.

Representative transmission electron microscopy images and particle size distribution for the Pt^{II}/ZSM-5 (30) $_{CVI}$ catalyst are shown in Figure 5.23. Highly dispersed Pt particles with a mean particle size of 6.2 ± 3.3 nm are observed. The majority of the distribution falls into the 2 - 10 nm size range, with a low population in the 0 -2 nm and 10 -18 nm ranges. The morphology of the nanoparticles should be considered, as not all particles present the same shape, spherical and larger cubic crystallites are observed. The homogeneously distributed Pt nanoparticles are likely the cause of the macro- porous volume reduction of the Pt^{II}/ZSM-5 (30) $_{CVI}$ catalyst in Table 5.7.

Quantitative analysis obtained from TEM coupled with EDX, presented in Table 5.8, confirms the presence of approximately 1 wt. % of Pt in Pt^{II}/ZSM-5 (30) $_{CVI}$. Thus, the actual metal loading achieved is equal to the theoretical total loading expected based on the amount of Pt precursor used during CVI. In addition, the SiO$_2$/Al$_2$O$_3$ ratio correlates with that of the commercial zeolite (30).

Table 5.8. Quantitative analysis of the Pt^{II}/ZSM-5 (30) $_{CVI}$ catalyst obtained from TEM imaging coupled with EDX

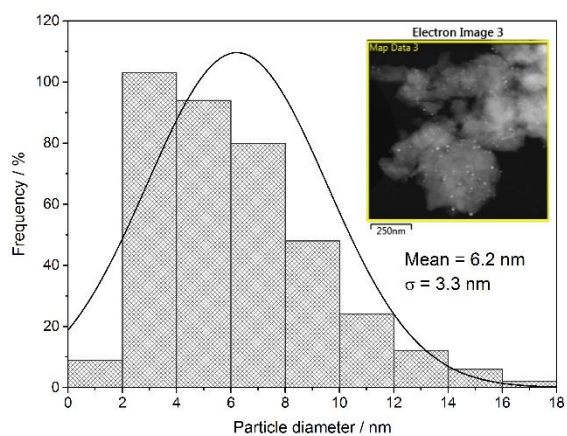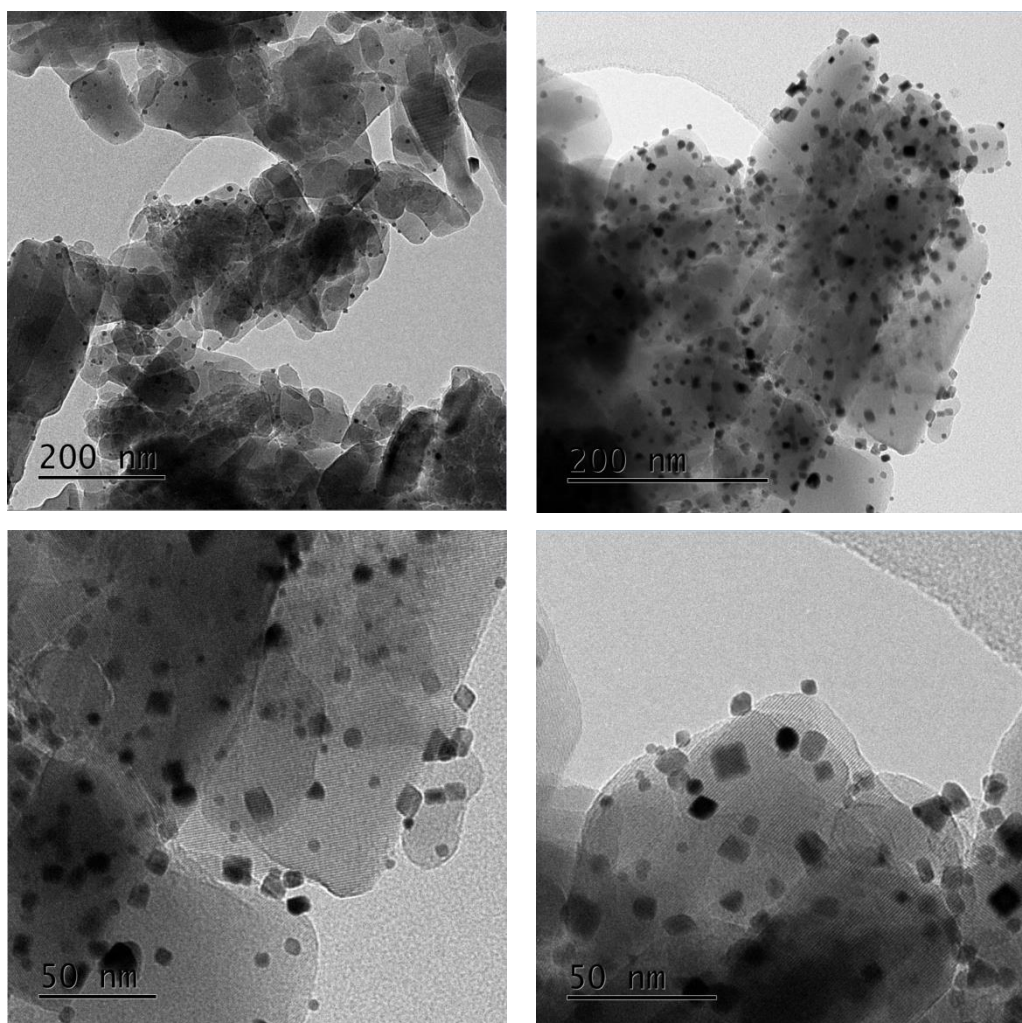|	Si		Al		O		Pt	
	wt. %	σ	wt. %	σ	wt. %	σ	wt. %	σ
Pt^{II}/ZSM-5 (30) $_{CVI}$	40.49	0.61	2.54	0.20	55.95	0.65	0.92	0.26

Figure 5.23. Selected HRTEM and STEM images and platinum particle size distribution

for Pt^{II}/ZSM-5 (30) $_{CVI}$

NH$_3$-TPD profiles for these catalysts are shown in Figure 5.24. The intensity of the peak at 450 °C, attributed to NH$_3$ chemisorbed at Brønsted acid sites, decreases considerably after Cu exchange. This is due to exchange of Brønsted acid protons. Fe^{III}/ZSM-5 (30) $_{CVI}$ presents a different profile with a characteristic event at low temperature and a peak centred at 350 °C suggesting that Fe exchange generates new medium-strength acid sites.
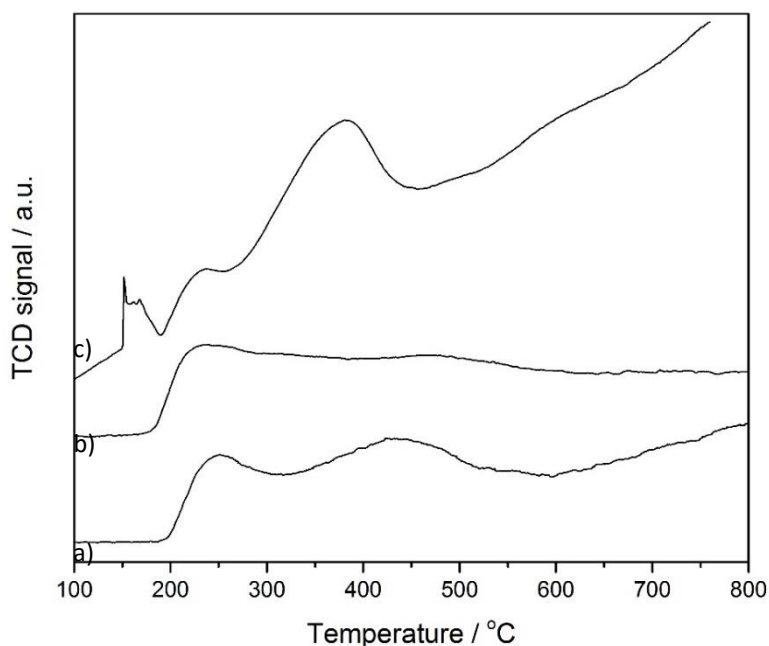

Figure 5.24. NH$_3$-TPD profiles of metal-exchanged zeolites prepared by CVI:

a) H$^+$-ZSM-5 (30)   b) Cu^{II}/ZSM-5 (30) $_{CVI}$ c) Fe^{III}/ZSM-5 (30) $_{CVI}$

H$_2$-TPR profiles of the metal-exchanged ZSM-5 (30) catalysts prepared by CVI are presented in Figure 5.25. Cu^{II}/ZSM-5 (30) $_{CVI}$ exhibits the typical reduction profile discussed previously for Figure 5.7, with two peaks at 225 °C and 400 °C attributed to the reduction of Cu^{2+} to Cu$^+$ at exchanged sites and supported CuO species to Cu^0. On the other hand, the TPR profile of Fe^{III}/ZSM-5 (30) $_{CVI}$ is formed by a broad peak centred at 300 °C with shoulders at 220 °C and 375 °C. No peak at 500 °C, assigned early in this chapter to reduction of Fe$_3$O$_4$ to Fe^0, is observed. This indicates that those Fe$_x$O$_y$ species formed by

CVI are more easily reduced as the reduction temperature is shifted towards lower values. Pt^{II}/ZSM-5 (30) $_{CVI}$ presents a sharp negative peak at 375 °C followed by a positive peak of similar intensity, these events represent H$_2$ uptake via a spillover mechanism which is characteristic of supported Pt species [106]. The low temperature reduction of PtO species at 80 °C is accompanied by H$_2$ uptake in Figure 5.25 d) [107].
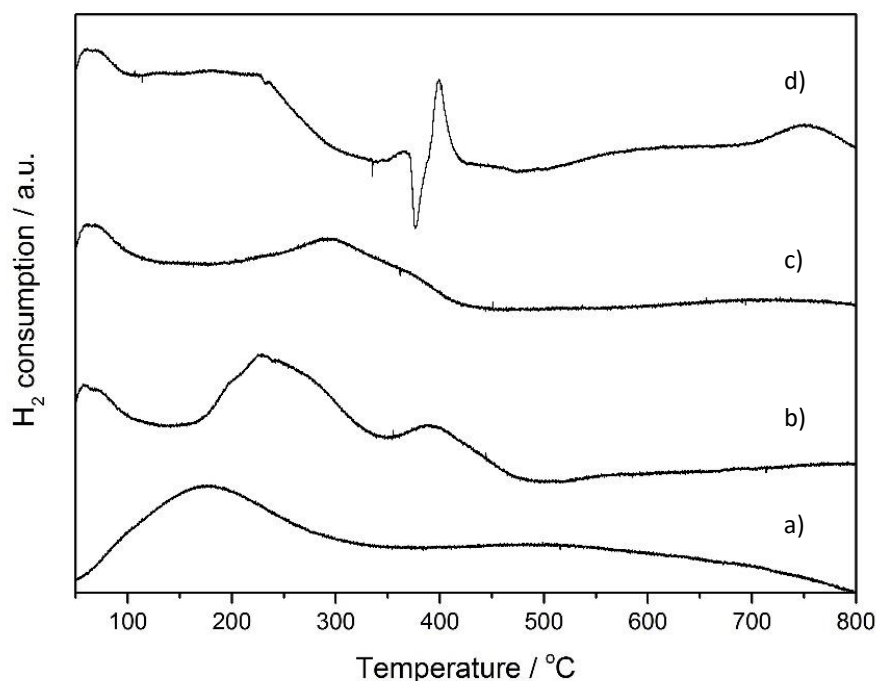
Figure 5.25. H$_2$-TPR profiles of metal-exchanged zeolites prepared by CVI:

a) H$^+$-ZSM-5 (30)   b) Cu^{II}/ZSM-5 (30) $_{CVI}$ c) Fe^{III}/ZSM-5 (30) $_{CVI}$

d) Pt^{II}/ZSM-5 (30) $_{CVI}$

FTIR spectra in the OH vibrational region are shown in Figure 5.26. Based on relative intensities of the bands, it is difficult to determine differences in the concentration of the different –OH groups. However, exchange of H$^+$ by metal ions is known to decrease the intensity of the band at 3560 cm^{-1}, associated with Brønsted acid groups.
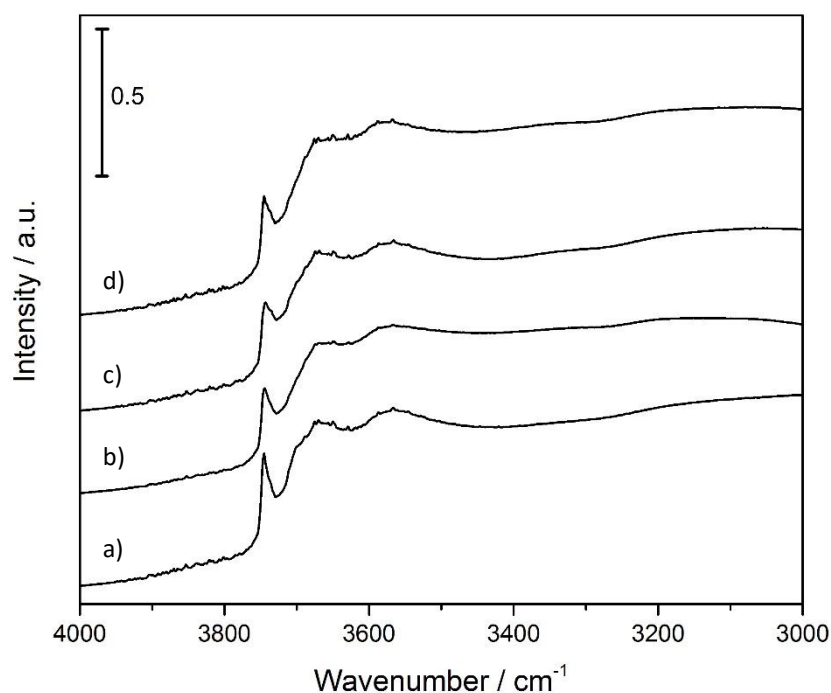
Figure 5.26. DRIFT spectra in the OH vibrational region of metal-exchanged zeolites prepared

by CVI:

a) H$^+$-ZSM-5 (30)   b) Cu^{II}/ZSM-5 (30) $_{CVI}$ c) Fe^{III}/ZSM-5 (30) $_{CVI}$

d) Pt^{II}/ZSM-5 (30) $_{CVI}$

The storage capacities of the Fe-, Cu- and Pt-exchanged ZSM-5 (30) catalysts prepared by

CVI were evaluated in the presence and absence of O$_2$.

Figure 5.27 compares the adsorption/desorption capacity in the absence of O$_2$.

Desorption of NO adsorbed at 30 °C in the absence of O$_2$ occurs in the form of NO at 30 °C

and 100 °C. The two desorption peaks correspond to reversible adsorption of NO and weak

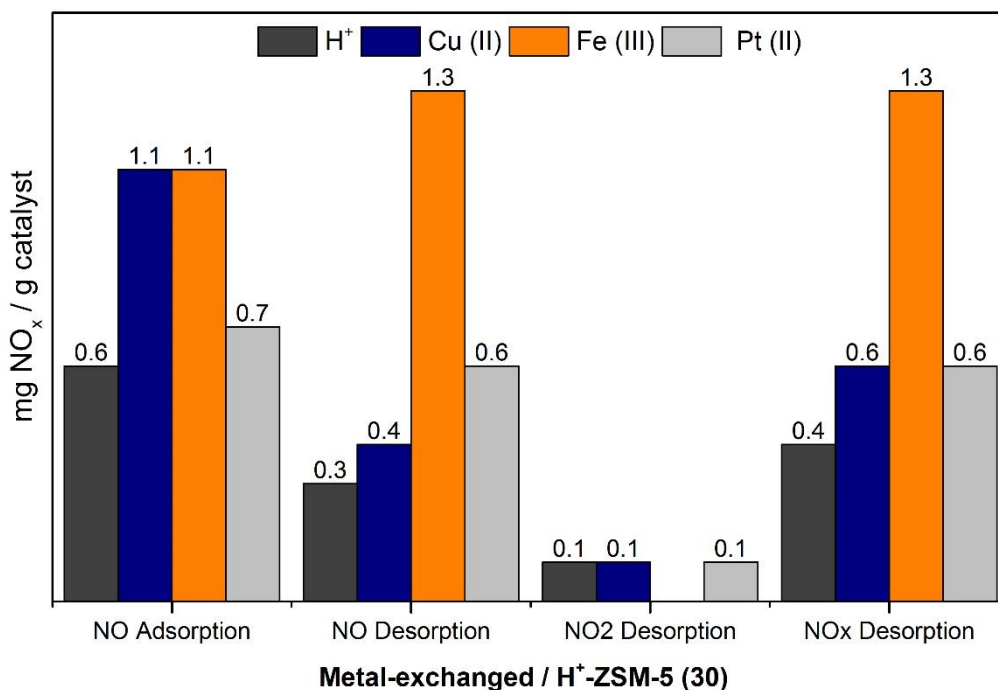physical adsorption of NO on the surface of the catalyst.

Figure 5.27. NOₓ storage capacity of metal-exchanged / H⁺-ZSM-5 (30) catalysts

NO adsorption at 30 °C and TPD with He up to 500 °C

Reaction conditions: Flow reactor, GHSV = 35,000 h⁻¹, 0.1 % NO in He / He

Catalysts prepared by CVI at 150 °C for 2 h and calcined at 550 °C for 3 h in static air

Whereas an equal NO adsorption capacity is observed for Cu^{II}/ZSM-5 (30) $_{CVI}$ and Fe^{III}/ZSM-5 (30) $_{CVI}$, Fe-exchanged ZSM-5 shows double the total NOₓ desorption. This indicates that NO adsorption over Cu^{II}/ZSM-5 (30) $_{CVI}$ is mainly reversible, as the amount of NO desorbed at 100 °C is similar to that of the parent zeolite H⁺/ZSM-5 (30). Pt^{II}/ZSM-5 (30) $_{CVI}$ exhibits very low storage capacity, not much larger than that of the unmodified ZSM-5 (30).

NOₓ desorption at high temperatures is related to formation of more thermally stable nitrates on the catalyst surface. Oxidation of NO to NO_2 is known to be the first and limiting

step in this storage mechanism. Hence, the storage capacity in the presence of O_2 was assessed. Figure 5.28 represents the NO_x desorption capacity following adsorption of NO in the presence of O_2.
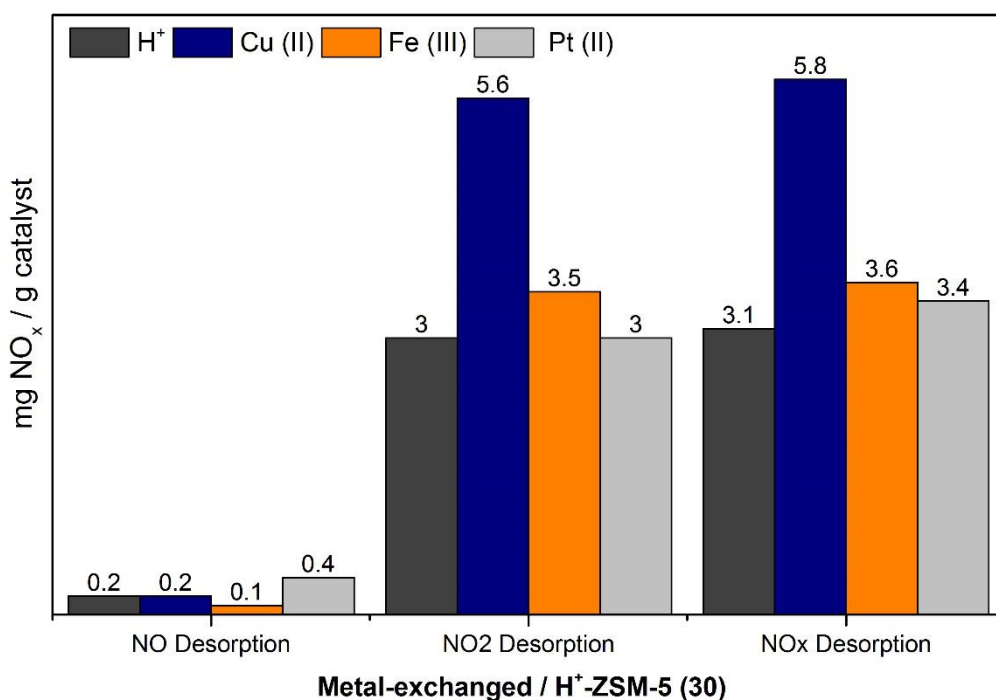
Figure 5.28. NO_x storage capacity of metal-exchanged/H+- ZSM-5 (30) catalysts

NO_x adsorption at 30 °C ($NO:O_2 = 1:75$) and TPD with He up to 500 °C

Reaction conditions: Flow reactor, GHSV = 35,000 h^{-1}, 0.1 % NO + 7.5 % O_2 in He / He

Catalysts prepared by CVI at 150 °C for 2 h and calcined at 550 °C for 3 h in static air

NO_x is desorbed mainly in the form of NO_2, at 30 °C, 100 °C 250 °C and 350 °C. The four desorption events represent adsorbed species of differing nature, reversible and weak physical adsorption of NO and adsorption of nitrates with different thermal stabilities.

Total NO_x desorption is greater for Cu^{II}/ZSM-5 (30) CVI (5.8 mg NO_x/g), which is comparable with that of the analogous catalyst prepared by WIE shown in Figure 5.12

(5.6 mg NO$_x$/g). Desorption is not improved by exchanging Fe or Pt ions onto H$^+$-ZSM-5 (30). Thus, results are similar to those obtained for metal-exchanged ZSM-5 (30) prepared by WIE.

The total distribution of NO$_x$ species desorbed at different temperatures is shown in Figure 5.29.
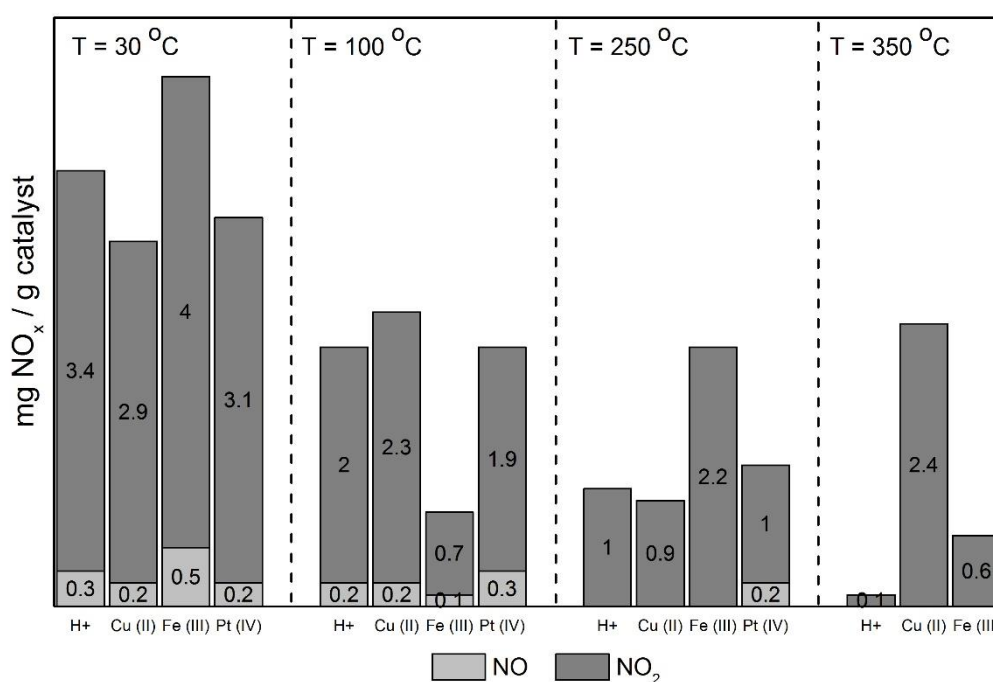
Figure 5.29. Total amount of NO$_x$ desorbed during the TPD carried out after NO$_x$ adsorption (0.1 % NO, 7.5 % O$_2$, He) on metal-exchanged/H$^+$-ZSM-5 (30) at each desorption temperature

Total NO$_x$ desorption at temperatures above 200 °C is similar for both Cu- and Fe-exchanged ZSM-5 (30), 3.3 and 2.8 mg NO$_x$/g respectively. Even so, the formation of thermally stable surface nitrates, which desorb at 350 °C, is only significant in the case of Cu^{II}/ZSM-5 (30) $_{CVI}$.

5.3.2.2 Zeolite structure and aluminium content

The role of the zeolite framework and acidity in NO$_x$ storage over metal-exchanged zeolites prepared by CVI was investigated. The study comprises of evaluating the NO$_x$ adsorption/desorption capacities of Cu Fe and Pt ions exchanged onto six different zeolites in the absence and presence of O$_2$. Assessed zeolite supports include Y, ZSM-5 and BETA. Nevertheless, for simplification, only the most relevant results will be discussed.

Cu-exchanged zeolites were the first set of catalysts assessed. Figure 5.30 includes their NO$_x$ adsorption and desorption capacities in the absence of O$_2$.
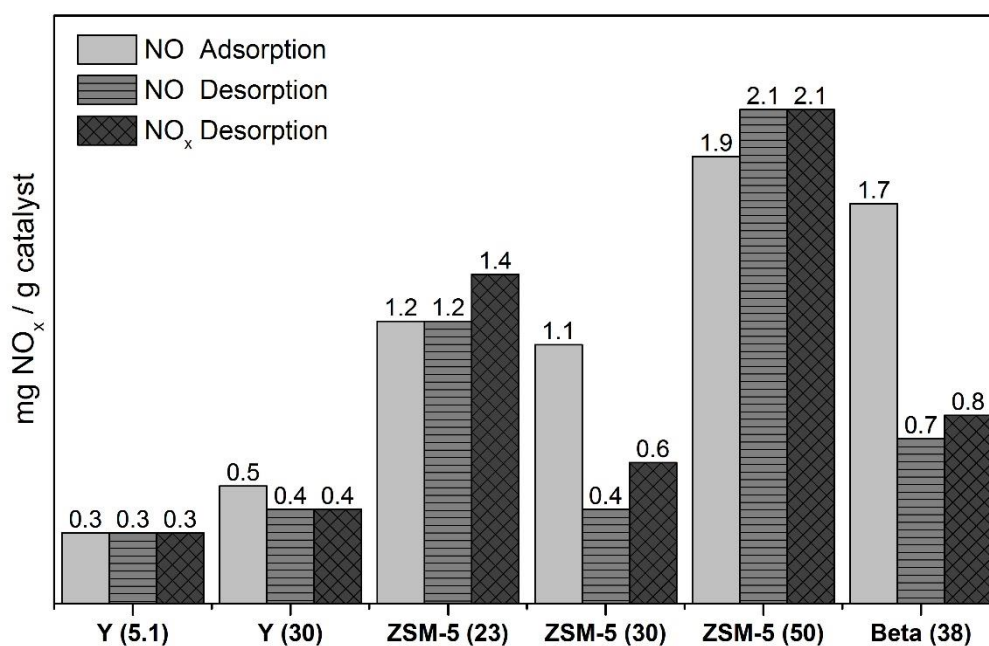

Figure 5.30. NO$_x$ storage capacity of Cu-exchanged zeolites

NO adsorption at 30 °C and TPD with He up to 500 °C

Reaction conditions: Flow reactor, GHSV = 35,000 h^{-1}, 0.1 % NO in He / He

Catalysts prepared by CVI at 150 °C for 2 h and calcined at 550 °C for 3 h in static air

The zeolite framework and SiO_2/Al_2O_3 ratio affect not only the total NO adsorption capacity but also the amount of reversibly adsorbed NO. As for Cu-exchanged zeolites prepared by WIE, a clear absolute trend is not found. However, some similarities are apparent. Cu^{II}/BETA (38) $_{CVI}$ exhibits the greatest NO adsorption but not desorption capacity due to the large amount of reversibly adsorbed NO. Among the ZSM-5 based catalysts Cu^{II}/ZSM-5 (50) $_{CVI}$, that with the highest SiO_2 content, shows superior storage performance. Meanwhile larger pore size zeolite Y has a detrimental effect on the NO storage capacity.
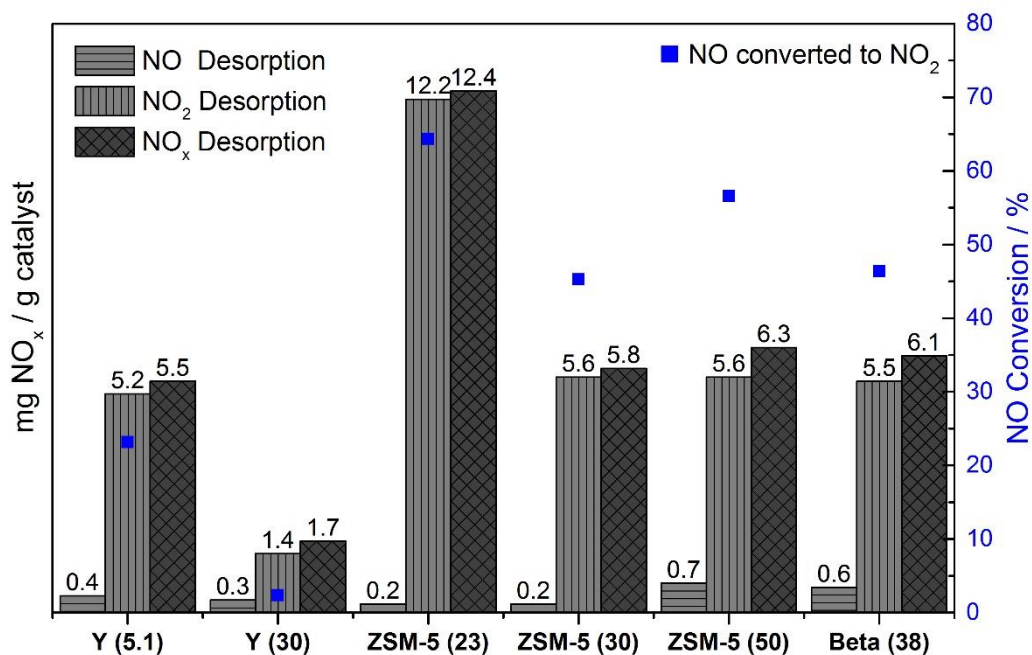

Figure 5.31. NOₓ storage capacity of Cu-exchanged zeolites

NOₓ adsorption at 30 °C (NO:O₂ = 1:75) and TPD with He up to 500 °C

Reaction conditions: Flow reactor, GHSV = 35,000 h⁻¹, 0.1 % NO + 7.5 % O₂ in He / He

Catalysts prepared by CVI at 150 °C for 2 h and calcined at 550 °C for 3 h in static air

Results obtained for NO$_x$ storage in the presence of O$_2$ are shown in Figure 5.31. The total amount of NO$_x$ desorbed is similar for all the catalysts but two. As for those Cu-exchanged zeolites prepared by WIE in Figure 5.16, superior NO$_x$ desorption is observed for Cu^{II}/ZSM-5 (23) $_{CVI}$. In addition, despite the lower NO oxidation activity of Cu^{II}/Y (5.1) $_{CVI}$, the amount of NO$_x$ desorbed is 5.5 mg NO$_x$/g, which is comparable with that of Cu^{II}/ZSM-5 (30) $_{CVI}$ (5.8 mg NO$_x$/g).

Based on the distribution of NO$_x$ species at different temperatures, shown in Figure 5.32, it can be concluded that the amount of NO$_x$ desorbed at temperatures above 200 °C is much higher for Cu^{II}/ZSM-5 (23) $_{CVI}$.
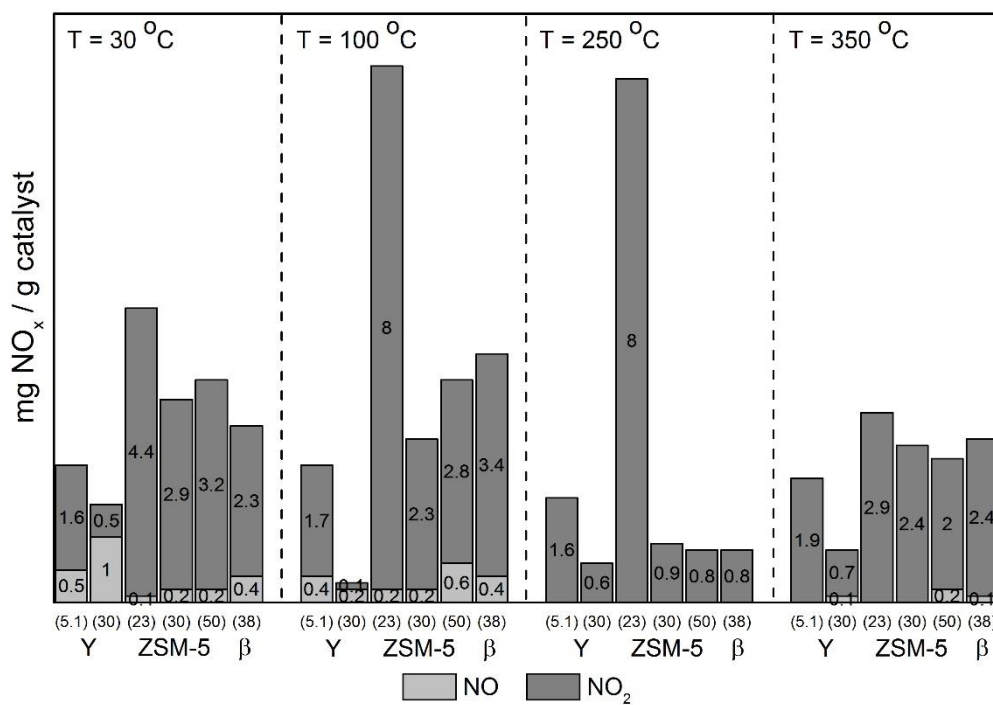

Figure 5.32. Total amount of NO$_x$ desorbed during the TPD carried out after NO$_x$ adsorption (0.1 % NO, 7.5 % O$_2$, He) on Cu-exchanged CVI zeolites at each desorption temperature

It should be noted that the distribution of adsorbed NO$_x$ species and their thermal stability differs between Cu^{II}/ZSM-5 (23) prepared by WIE (Figure 5.17) and CVI (Figure 5.32). Both catalysts present high NO$_x$ desorption capacity, with a large amount of NO$_x$ desorbed at high temperatures. Cu^{II}/ZSM-5 (23) prepared by WIE shows desorption of a similar amount of NO$_x$ at each temperature. Thus, not only reversibly adsorbed and physisorbed NO (desorbed at 30 °C) is detected, but also highly thermally stable nitrates - which are desorbed at 350 °C. On the other hand, when Cu^{II}/ZSM-5 (23) is prepared by CVI most of the NO$_x$ desorption occurs at 100 °C and 250 °C. This indicates that CVI favours the formation of active sites which form weakly adsorbed NO$_x$ species and nitrates of moderate thermal stability.
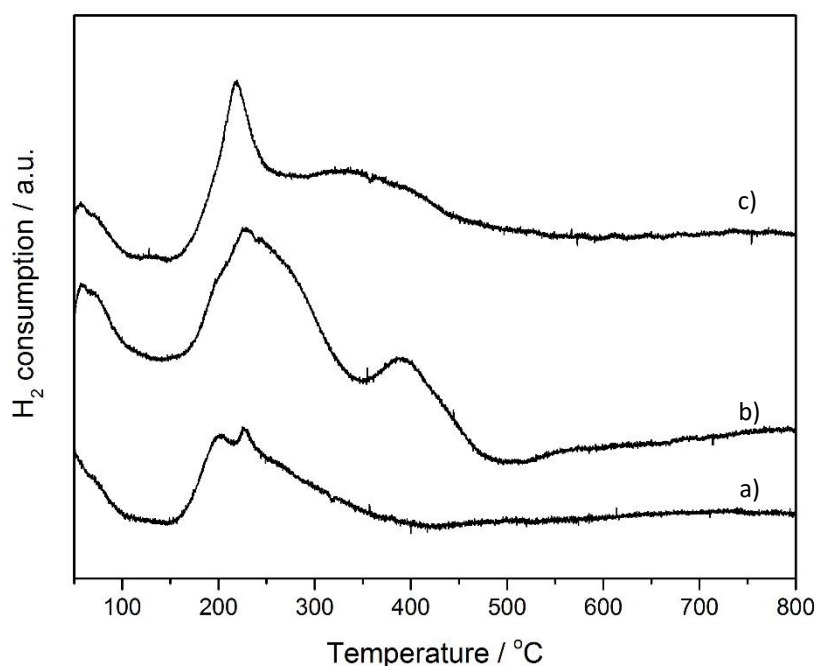
Figure 5.33. H$_2$-TPR profiles of Cu-exchanged zeolites:

a) Cu^{II}/Y (30) $_{CVI}$ b) Cu^{II}/ZSM-5 (30) $_{CVI}$ c) Cu^{II}/BETA (38) $_{CVI}$

H$_2$-TPR profiles of Cu-exchanged zeolites with different frameworks but similar acidity are shown in Figure 5.33. The zeolite framework is found to have a greater effect on the

redox properties of Cu sites in -exchanged zeolite catalysts prepared by CVI than those prepared by WIE (Figure 5.18). Similar reduction profiles are shown in Figure 5.33.The absence of a high temperature reduction peak in Cu^{II}/Y (30) $_{CVI}$ (Figure 5.33 a) suggests that Cu is mainly in the form of CuO and as less stable exchanged Cu ions, which are reduced at lower temperatures. The broad high temperature reduction peak observed at *ca.* 360 °C for $Cu^{II}/BETA$ (38) $_{CVI}$ is also less intense than that of $Cu^{II}/ZSM-5$ (30) $_{CVI}$.

Figure 5.34. NOₓ storage capacity of Fe-exchanged zeolites

NO adsorption at 30 °C and TPD with He up to 500 °C

Reaction conditions: Flow reactor, GHSV = 35,000 h⁻¹, 0.1 % NO in He / He

Catalysts prepared by CVI at 150 °C for 2 h and calcined at 550 °C for 3 h in static air

NO$_x$ storage was also evaluated over Fe-exchanged zeolites prepared by CVI. Figure 5.34 illustrates the effect of the zeolite framework and acidity on NO$_x$ adsorption/desorption capacity in the absence of O$_2$.

Contrary to the results obtained for metal-exchanged zeolites prepared by WIE, Fe exchanged on BETA (Fe^{III}/BETA (38) $_{CVI}$), does not show superior storage performance. In fact, the amount of NO adsorbed over this catalyst (1.6 mg NO$_x$/g) is 4 times lower than that of the WIE analogue (6.3 mg NO$_x$/g, Figure 5.19).
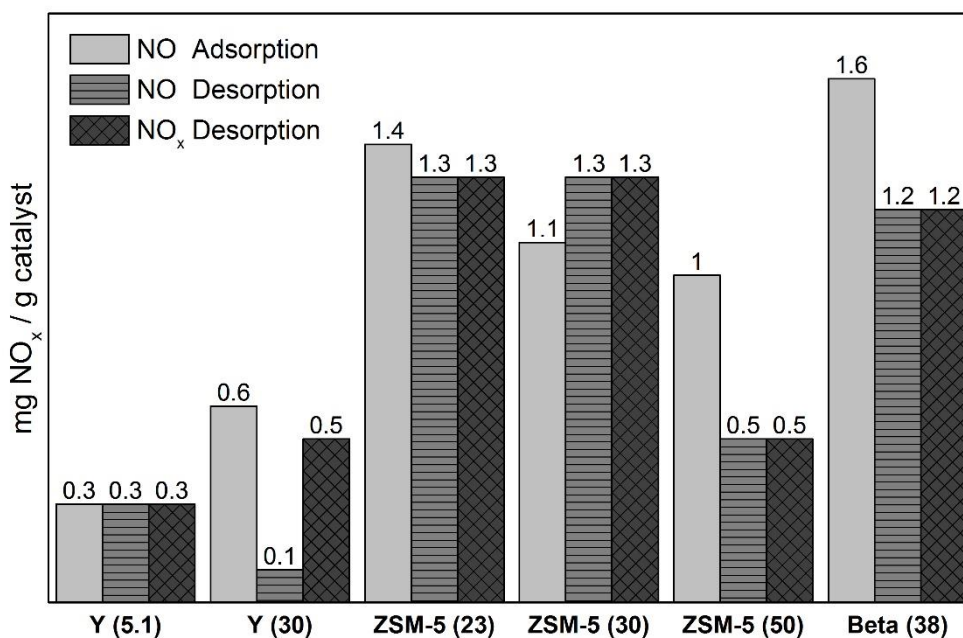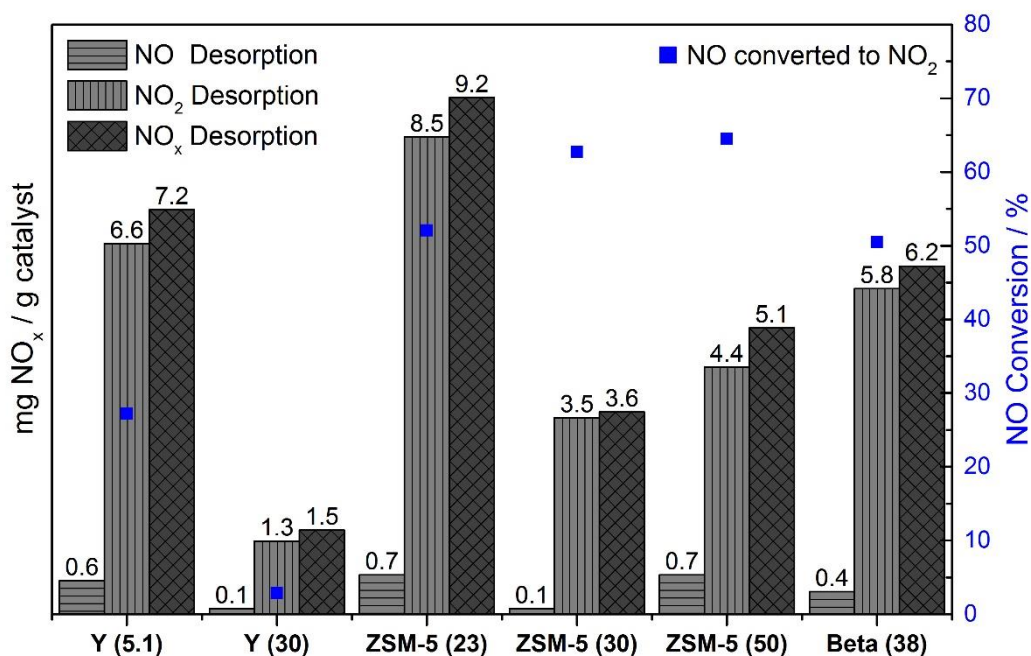

Figure 5.35. NO$_x$ storage capacity of Fe-exchanged zeolites

NO$_x$ adsorption at 30 °C (NO:O$_2$ = 1:75) and TPD with He up to 500 °C

Reaction conditions: Flow reactor, GHSV = 35,000 h^{-1}, 0.1 % NO + 7.5 % O$_2$ in He / He

Catalysts prepared by CVI at 150 °C for 2 h and calcined at 550 °C for 3 h in static air

Based on results obtained during NO$_x$ adsorption/desorption experiments in the presence of O$_2$, it can be concluded that the trends observed for Fe-exchanged zeolites prepared by CVI are similar to those observed in Figure 5.20 for their WIE analogues.
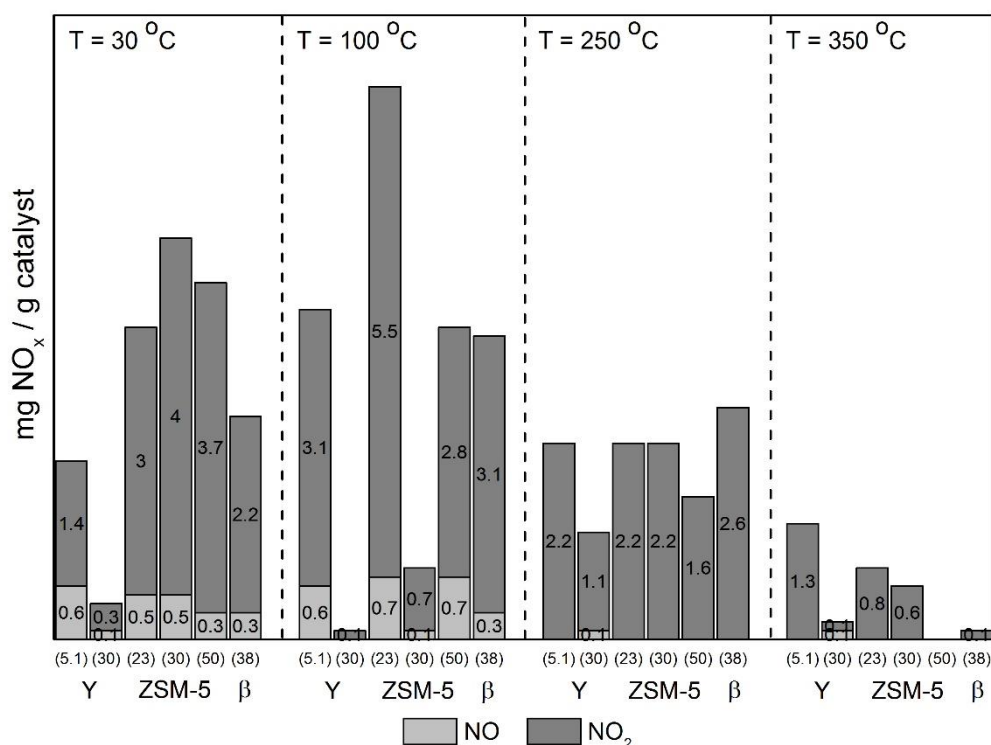
Figure 5.36. Total amount of NO$_x$ desorbed during the TPD carried out after NO$_x$ adsorption (0.1 % NO, 7.5 % O$_2$, He) on Fe-exchanged zeolites at each desorption temperature

High storage capacity is noted for Fe^{III}/ZSM-5 (23) $_{CVI}$, with 9.2 mg of NO$_x$ desorbed per g of catalyst. As shown in Figure 5.32, the majority of NO$_x$ desorption occurs at low temperature, indicating formation of weakly adsorbed surface species. In fact, NO$_x$ desorption at temperatures above 200 °C only accounts for 3 mg NO$_x$/g (33 % of total desorbed NO$_x$). Interestingly, Fe^{III}/Y (5.1) shows almost double the total NO$_x$ desorption when prepared by CVI (7.2 mg NO$_x$/g) compared with WIE (4 mg NO$_x$/g). Fe^{III}/Y (5.1) $_{CVI}$ shows a large amount of NO$_x$ desorption above 200 °C (3.5 mg NO$_x$/g), which exceeds the

amount desorbed by Fe^{III}/ZSM-5 (23) $_{CVI}$ (3.0 mg NO$_x$/g) or Fe^{III}/BETA (38) $_{CVI}$ (2.7 mg NO$_x$/g). The distributions of NO$_x$ species desorbed at different temperatures from Fe CVI catalysts are shown in Figure 5.36.
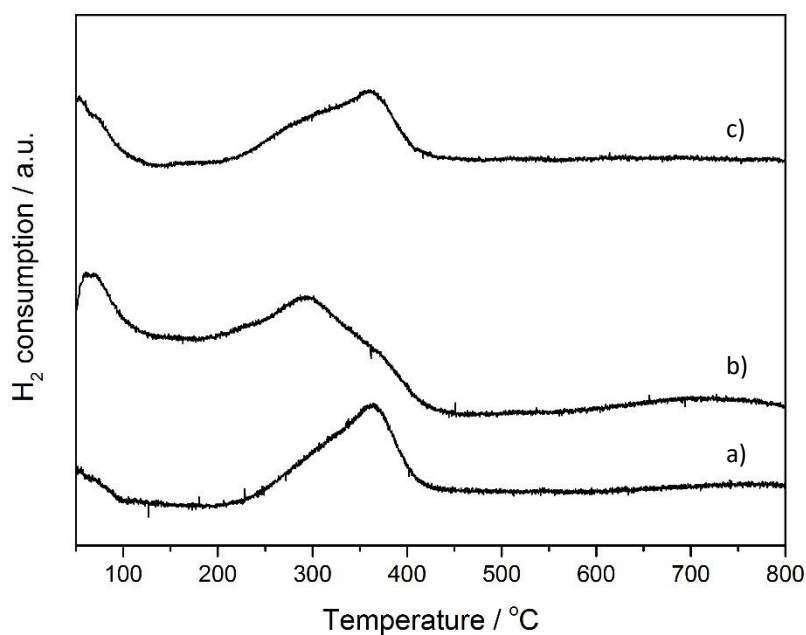
Figure 5.37. H$_2$-TPR profiles of Fe-exchanged zeolites:

a) Fe^{III}/Y (30)$_{CVI}$ b) Fe^{III}/ZSM-5 (30)$_{CVI}$ c) Fe^{III}/BETA (38)$_{CVI}$

As shown in Figure 5.37, H$_2$-TPR profiles of the Fe-exchanged zeolites prepared by CVI exhibit a broad reduction peak centred at 300 °C. This can be deconvoluted into a series of peaks corresponding to reduction of Fe following the sequence: Fe$_2$O$_3$ → Fe$_3$O$_4$ → FeO → Fe^0. The structure of the zeolite induces changes in the reducibility of the Fe species. The reduction event is shifted towards higher temperature for Fe^{III}/Y (30) $_{CVI}$, Figure 5.37 a). Reduction temperature shifts suggest variation in the relative Fe^{3+}/Fe^{2+} concentration and the stability of Fe ions. Hence, reduction occurring at higher temperatures could imply

a larger population of Fe species in a lower oxidation state and more strongly bonded Fe ions. Further characterisation is needed to confirm these suggestions.

NO_x adsorption/desorption experiments in the absence and presence of O_2, were also performed over Pt-exchanged zeolites prepared by CVI.

As presented in Figure 5.38, results for NO_x adsorption and desorption in the absence of O_2 are comparable with those of the unmodified zeolites (Figure 5.27), indicating that the storage capacity is not enhanced with exchange of H^+ by Pt ions on the parent zeolite.
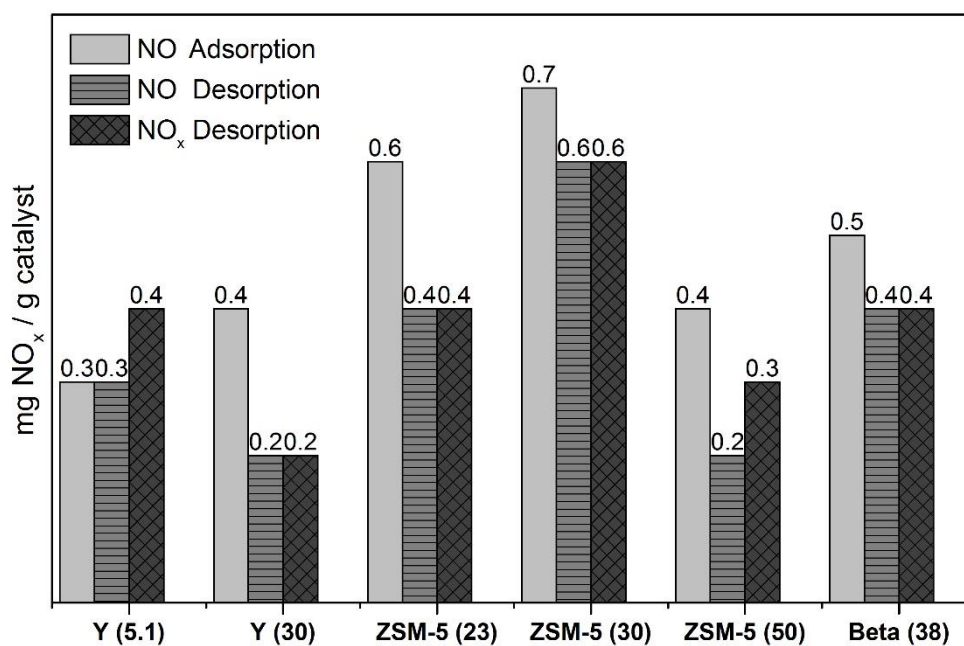
Figure 5.38. NO_x storage capacity of Pt-exchanged zeolites

NO adsorption at 30 °C and TPD with He up to 500 °C

Reaction conditions: Flow reactor, GHSV = 35,000 h^{-1}, 0.1 % NO in He / He

Catalysts prepared by CVI at 150 °C for 2 h and calcined at 550 °C for 3 h in static air

Although in absolute numbers, the NO$_x$ storage capacity in the presence of O$_2$ over Pt-exchanged zeolites is lower than that of the Cu and Fe catalysts, the same trends are observed. As presented in Figure 5.39, Pt^{II}/Y (5.1) $_{CVI}$ and Pt^{II}/ZSM-5 (23) $_{CVI}$ present the highest degree of NO$_x$ desorption. In the case of the Fe^{III}/ZSM-5 (23) $_{CVI}$ catalyst, most desorption occurs at low temperatures, associated with the intrinsic adsorption capacity of unmodified H$^+$-ZSM-5 (23). The distributions of NO$_x$ species desorbed at different temperatures are shown in Figure 5.40. The largest amount of NO$_x$ desorption at 250 °C is observed for Pt^{II}/Y (5.1) $_{CVI}$ (1.8 mg NO$_x$/g).
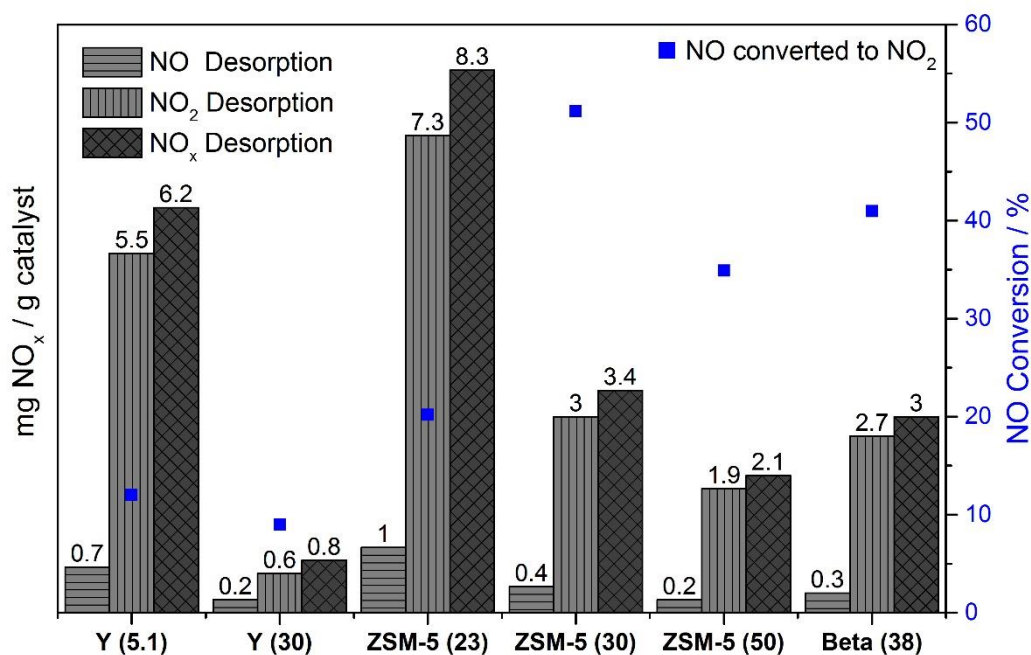
Figure 5.39. NO$_x$ storage capacity of Pt-exchanged zeolites

NO$_x$ adsorption at 30 °C (NO:O$_2$ = 1:75) and TPD with He up to 500 °C

Reaction conditions: Flow reactor, GHSV = 35,000 h^{-1}, 0.1 % NO + 7.5 % O$_2$ in He / He

Catalysts prepared by CVI at 150 °C for 2 h and calcined at 550 °C for 3 h in static air

The absence of NO_x desorption at 350 °C for Pt ion-exchanged zeolites in Figure 5.40 should be noted. This indicates that no highly thermally stable nitrates are formed.
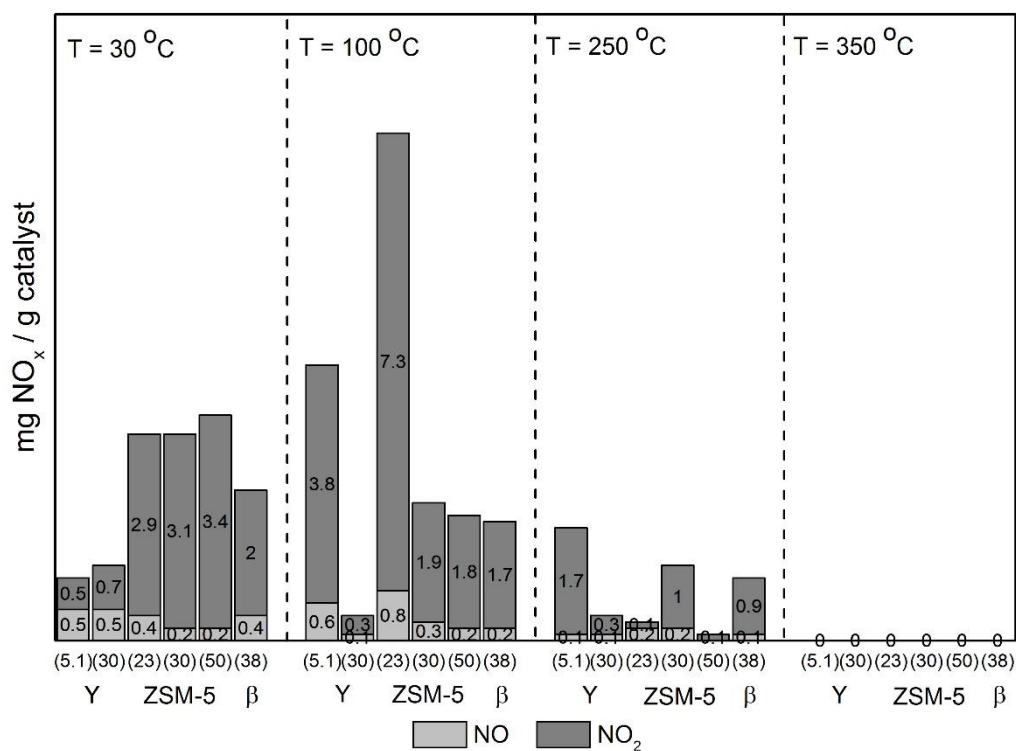
Figure 5.40. Total amount of NO_x desorbed during the TPD carried out after NO_x adsorption (0.1 % NO, 7.5 % O_2, He) on Pt-exchanged zeolites at each desorption temperature

5.4 Bimetallic and trimetallic zeolitic systems

The effect of the exchanged metal, zeolite framework, acidity and preparation method on the NO$_x$ storage capacity of monometallic ion-exchanged zeolites has already been assessed. Bimetallic zeolitic systems prepared by introducing a second metal cation using ion exchange have been reported to show superior performance in deNO$_x$ reactions [38b] [108] [109] [110]. Sultana *et al.* [110] reported that Cu-Fe/ZSM-5, prepared by consecutive wet ion exchanges, exhibits higher NO$_x$ conversion for NH$_3$ SCR compared with the monometallic analogues. This performance improvement was correlated to a change in redox properties of the constituent metals; that the presence of Cu increases the reducibility of Fe resulting in an increase in low temperature NO$_x$ conversion.

In order to study complementary and synergistic effects between Cu, Fe and Pt, a series of bimetallic and trimetallic zeolitic catalysts was prepared by CVI. Cu-Fe/ZSM-5 (30) $_{CVI}$, Cu-Pt/ZSM-5 (30) $_{CVI}$, Fe-Pt/ZSM-5 (30) $_{CVI}$ and Cu-Fe-Pt/ZSM-5 (30) $_{CVI}$ catalysts were prepared by simultaneous sublimation of the corresponding metal acetylacetonates precursors at 150 °C for 2 hours. These were then calcined in static air at 550 °C for 3 hours. NO$_x$ adsorption/desorption experiments, in the presence and absence of O$_2$, were carried out using these bimetallic and trimetallic zeolitic catalysts.

While the theoretical metal loading of monometallic zeolitic systems prepared by CVI is 1 wt. %, that of bimetallic and trimetallic zeolitic systems is up to 3 wt. %. The theoretical metal loading is calculated based on the amount of metal precursor used during CVI. Hence, in order to compare the storage capacity, results are expressed as mg of NO$_x$ adsorbed/desorbed per gram of metal loaded.

Results presented in Figure 5.41 show that NO$_x$ storage capacity is not significantly improved by impregnation of a second metal onto the ZSM-5 (30) support.
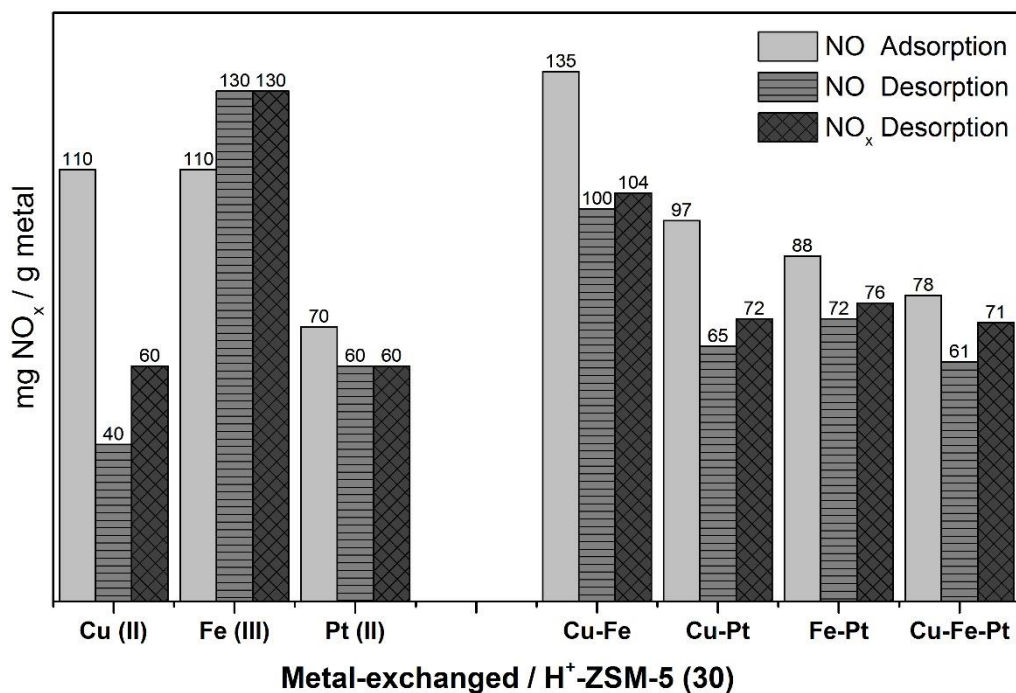
Figure 5.41. NOₓ storage capacity of mono-, bi- and tri-metallic zeolites

NO adsorption at 30 °C and TPD with He up to 500 °C

Reaction conditions: Flow reactor, GHSV = 35,000 h^{-1}, 0.1 % NO in He / He

Catalysts prepared by CVI at 150 °C for 2 h and calcined at 550 °C for 3 h in static air

On the contrary, the addition of Pt to either Cu/ZSM-5 (30) $_{CVI}$ or Fe/ZSM-5 (30) $_{CVI}$, results in a decrease in the amount of NOₓ adsorbed and desorbed. As presented in Figure 5.41, the amount of NO adsorbed in the absence of O₂ and subsequently desorbed decreases over the Cu-Pt/ZSM-5 (30) $_{CVI}$, Fe-Pt/ZSM-5 (30) $_{CVI}$ and Cu-Fe-Pt/ZSM-5 (30) $_{CVI}$ catalysts when compared with their monometallic analogues. A similarly detrimental effect is found in Figure 5.42 for NOₓ adsorption and desorption in the presence of O₂. Cu-Pt/ZSM-5 (30) $_{CVI}$, Fe-Pt/ZSM-5 (30) $_{CVI}$ and Cu-Fe-Pt/ZSM-5 (30) $_{CVI}$ present comparable NOₓ storage capacities to that of monometallic Pt/ZSM-5 (30) $_{CVI}$. It should be noted that the NO

oxidation activity is similar for all ZSM-5-based catalysts studied; mono-, bi- and trimetallic.
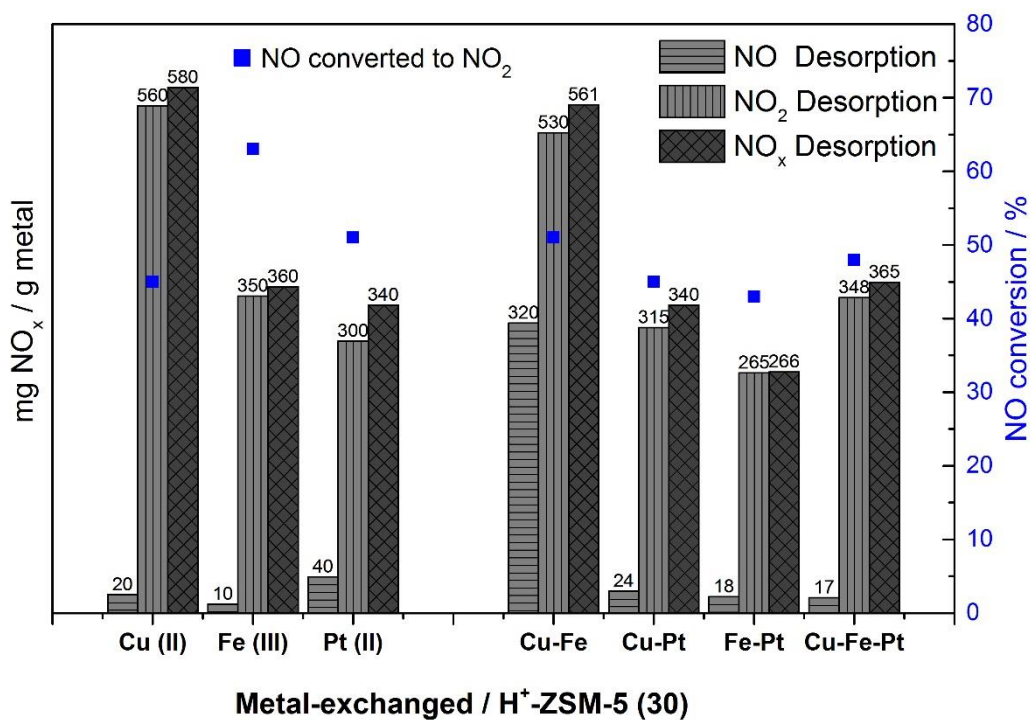
Figure 5.42. NO$_x$ storage capacity of mono-, bi- and tri-metallic zeolites

NO$_x$ adsorption at 30 °C (NO:O$_2$ = 1:75) and TPD with He up to 500 °C

Reaction conditions: Flow reactor, GHSV = 35,000 h^{-1}, 0.1 % NO + 7.5 % O$_2$ in He / He

Catalysts prepared by CVI at 150 °C for 2 h and calcined at 550 °C for 3 h in static air

A positive synergistic effect is only found for Cu-Fe/ZSM-5 (30) $_{CVI}$, for which the amount of NO$_x$ desorbed is increased by 10 % following adsorption in the absence of O$_2$, and by 20 % following adsorption in the presence of O$_2$, when compared with monometallic Cu/ZSM-5 (30) $_{CVI}$ or Fe/ZSM-5 (30) $_{CVI}$. However, as shown in Figure 5.43 the addition of Fe to Cu/ZSM-5 (30) $_{CVI}$ does not result in an improvement in the desirable high

temperature NO$_x$ desorption at 350 °C, which is associated with highly thermally stable

adsorbed species.

Figure 5.43. Total amount of NO$_x$ desorbed during the TPD carried out after NO$_x$ adsorption

(0.1 % NO, 7.5 % O$_2$, He) on mono-, bi- and tri-metallic zeolites

at each desorption temperature

As discussed previously, the reducibility of supported metals plays an important role in the

NO$_x$ storage capacity. The incorporation of a second metal cation affects the structure,

redox properties, stability and nature of the active sites on the zeolite. Hence,

characterisation studies of these bi- and trimetallic zeolitic systems are required.

5.5 High temperature NO$_x$ desorption from zeolite catalysts

As introduced previously in this chapter and in the thesis objectives in Chapter 1, the main goal of this study is to find an adsorption catalyst which stores NO$_x$ below 250 °C and releases it at high temperature (T > 250 °C). It has been shown that the oxidation of NO to NO$_2$ is crucial to form those highly thermally stable species which are desorbed at higher temperature. Hence, only adsorption/desorption experiments in the presence of O$_2$ are considered.

Figures 5.44 and 5.45 summarise the high temperature NO$_x$ desorption capacities of metal-exchanged zeolites prepared by WIE and CVI respectively. Results include the amount of NO$_x$ calculated from the integrated area of desorption peaks appearing at 250 °C and 350 °C.

Figure 5.44. The total amount of NO$_x$ desorbed during the TPD carried out after NO$_x$ adsorption

(0.1 % NO, 7.5 % O$_2$, He) on metal-exchanged zeolites prepared by WIE

at temperatures of above 100 °C

The high temperature NO_x desorption capacity of the baseline catalyst, unmodified H^+-ZSM-5 (30), is, in most cases, clearly enhanced following metal exchange by both methods, WIE and CVI. In fact, the amount of NO_x desorbed at high temperatures over a number of the catalysts studied even exceeds the 3.5 mg NO_x/g desorbed from the commercial catalyst prototype, defined as reference catalyst in Table 5.1. Whilst the zeolite framework and acidity plays a crucial role in the NO_x storage capacity and desorption at high temperatures, the effect is more significant for those zeolite-based catalysts prepared by WIE. In general, metal-exchanged zeolites prepared by WIE exhibit higher NO_x desorption at high temperatures than analogous catalysts prepared by CVI. Among the catalysts studied, several present high NO_x storage performance, though Cu^{II}/ZSM-5 (23) is of particular interest because of its intrinsic adsorption properties.
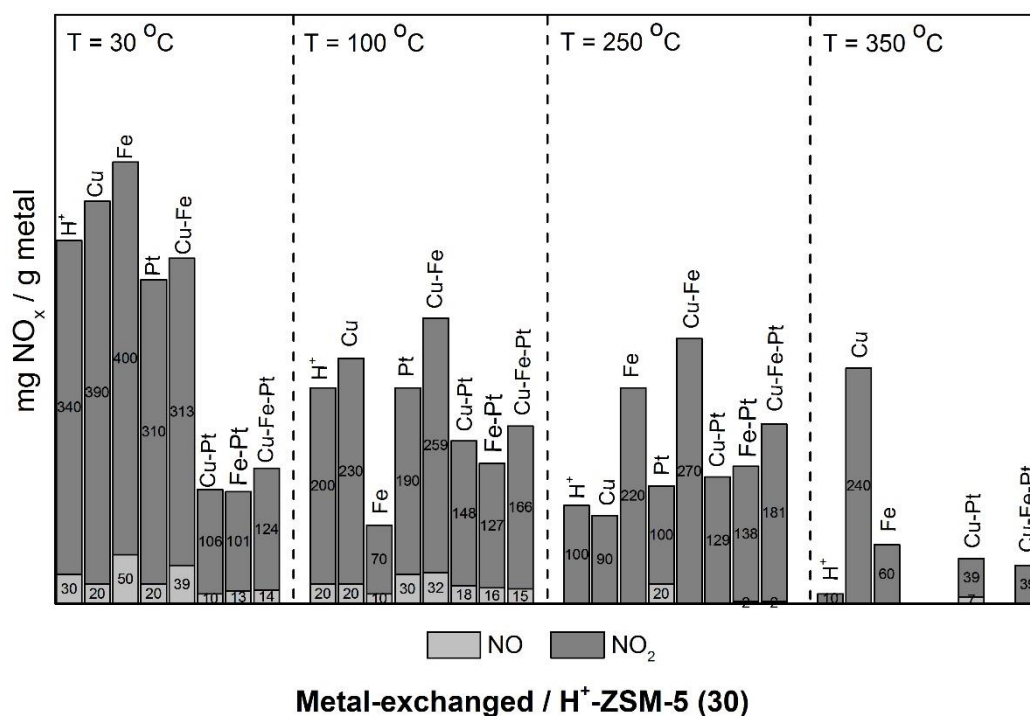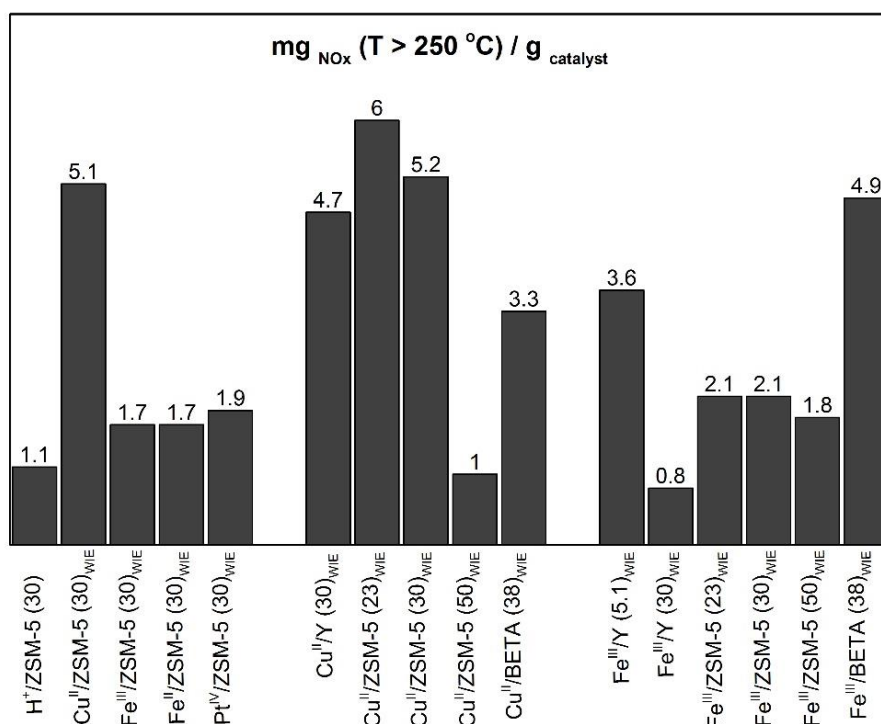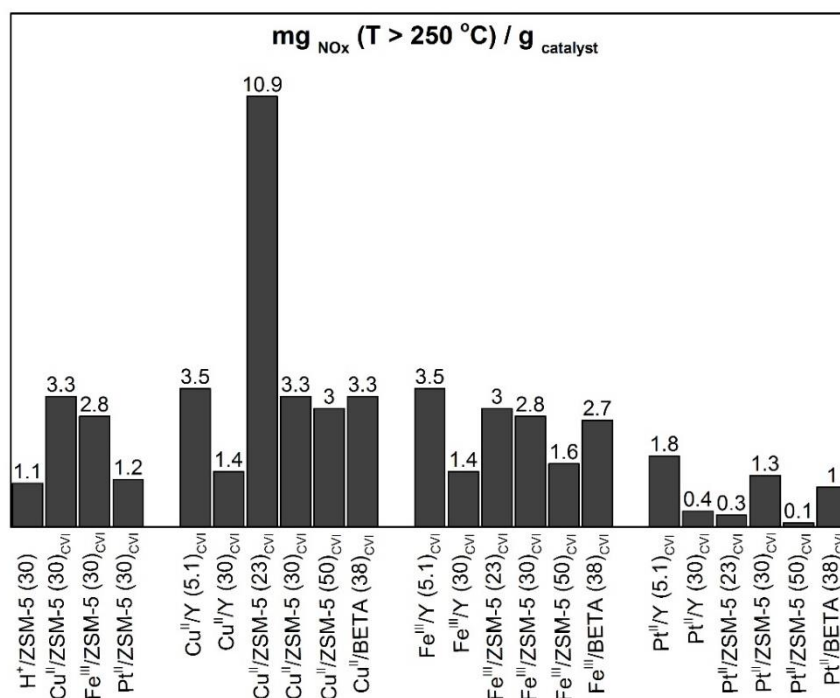

Figure 5.45. The total amount of NO_x desorbed during the TPD carried out after NO_x adsorption

(0.1 % NO, 7.5 % O_2, He) on metal-exchanged zeolites prepared by CVI

at temperatures of above 100 °C

5.6 Conclusions

This chapter is dedicated to initial screening of metal-exchanged zeolites for NO$_x$ storage under different conditions and to study the effect of the silicon/aluminium ratio, internal channels and inclusion of base and precious metals. Of particular interest is desorption that occurs at high temperature, above 200 °C, essential to use a NO$_x$ adsorption catalyst in real applications. A series of metal-exchanged zeolites have been prepared by two post synthesis exchange methods; wet ion exchange and chemical vapour impregnation, and evaluated for NO$_x$ storage under different model conditions. Cu, Fe and Pt was exchanged into different medium and large pore zeolites, including Y, ZSM-5 and BETA. Although several promising candidates, with great storage performance and large amount of NO$_x$ desorbed at high temperature, have been found, reproducibility and durability studies are needed to reach robust conclusions.

All zeolite-based catalysts exhibit a high adsorption capacity for NO at 30 °C in the presence and absence of O$_2$. He-TPD was conducted to investigate the desorption of NO$_x$ from these catalysts. During the desorption of NO$_x$, other than NO and NO$_2$ no other N-containing products such as N$_2$ or N$_2$O were observed. While in the absence of O$_2$, desorption occurs as NO at 30 °C and 100 °C; in the presence of O$_2$, desorption occurs mainly as NO$_2$ at four different desorption temperatures: 30 °C, 100 °C, 250 °C and 350 °C. Desorption at 30 °C is denoted as being reversible adsorption, associated with weakly physisorbed species on the catalyst surface. Variable temperature desorption studies suggest that NO$_x$ is adsorbed on different sites. High temperature desorption is attributed to formation of more thermally stable nitrates; NO is converted to nitrate species following the reaction sequence: NO $\rightarrow$ N$_2$O$_3$ $\rightarrow$ N$_2$O$_4$ $\rightarrow$ NO$_2$ $\rightarrow$ NO$_3$. Hence the concentration of O$_2$ in the gas feed has an important role, as the first reaction step involved in forming more strongly adsorbed, thermally stable species is the oxidation of NO to NO$_2$.

Two kinds of NO$_x$ adsorption sites are present on metal-exchanged zeolites: weak adsorption sites, attributed to the parent zeolite, and adsorption sites, attributed to the metal species exchanged and supported onto the zeolite.

When comparing the nature of the exchanged metal, in general, Cu- and Fe-exchanged zeolites present higher NO$_x$ storage capacity than Pt analogues, for which the storage capacity is comparable to that of the baseline catalyst H$^+$-ZSM-5 (30).

In agreement with previous work [14] [24] [47] [82], the zeolite framework and Si/Al ratio is found to play a crucial role in the NO$_x$ storage capacity of metal-exchanged zeolites. The framework and acidity of the zeolite have an influence not only on the total NO$_x$ adsorption/desorption capacity; but also on the amount of reversible and irreversible adsorption, on the degree of NO oxidation and on the distribution of NO$_x$ species desorbed at different temperatures. In addition, these behaviours are also dependent on the gas feed composition. Thus, relationships between the properties and storage capacities of zeolites are different for experiments carried out in the absence and presence of O$_2$.

The zeolite framework determines the NO$_x$ storage activity and thermal stability of the catalysts. The widely open structure and three directional channel system of BETA zeolite is advantageous for NO adsorption in the absence of O$_2$, as the superior storage performance of Cu^{II}/BETA (38) and Fe^{III}/BETA (38) suggests. Whereas, the medium and small average pore diameters of the ZSM-5 and BEA framework provide, in general, the most active catalysts; the larger pore sizes of Y zeolites have a detrimental effect on the NO storage capacity. This lower activity has been reported before for Cu/Y [111] and Fe/Y [47] [112], where only a fraction of cations are active due to species located in inaccessible sites, sodalite cages and hexagonal prisms. The pore geometry of the parent zeolites also influences NO$_x$ storage capacities when NO is adsorbed in the presence of O$_2$- narrow pore

zeolites are more active for the oxidation of NO to NO$_2$ and, therefore favour formation of more stable adsorbed species.

The Brønsted acidity of the zeolite support is also found to affect the NO$_x$ storage capacity. However, conflicting trends are found depending on the nature of the exchanged metal and the storage conditions. It has been found in previous work that whereas stability can be improved by using high SiO$_2$/Al$_2$O$_3$ ratios, a low SiO$_2$/Al$_2$O$_3$ ratio results in highly active systems [113] [114]. The amount of NO adsorbed/desorbed in the absence of O$_2$, over Cu-exchanged zeolites increases with a decreasing aluminium content of zeolites with the same framework topology. Contrarily, the storage capacity obtained in the absence of O$_2$ for Fe-exchanged zeolites increases with increasing aluminium content of ZSM-5 zeolites. When comparing zeolites with the same framework, a decrease in the SiO$_2$/Al$_2$O$_3$ ratio (increase in Brønsted acidity) is also beneficial for NO$_x$ desorption and NO oxidation during NO adsorption in the presence of O$_2$. Metal-exchanged ZSM-5 (23) catalysts exhibit high NO$_x$ storage capacity. Although desorption occurs mainly at low temperatures, due to the intrinsic adsorption capacity of the parent zeolite H$^+$-ZSM-5 (23), desorption at high temperatures is also significant. In addition, the high aluminium content zeolite Y studied, shows promising results for NO$_x$ storage in the presence of O$_2$, Cu^{II}/Y (5.1) and Fe^{III}/Y (5.1) prepared by CVI present a greater NO$_x$ desorption, even at high temperatures.

Consistent with previous reports, the preparation method and degree of exchange are also believed to influence the stability and activity of metal-exchanged zeolites for deNO$_x$ reactions [115]. Previous studies have reported the importance of achieving an optimum balance between the zeolite's Brønsted acidity and degree of metal exchange, in order to improve catalyst activity [114]. Whilst results presented in this chapter disagree as to which method produces the most active zeolites, the wet ion exchange preparation method is slightly favoured over CVI. Activity of metal, particularly Cu, -exchanged zeolites

prepared by WIE combine high NO adsorption capacity with high temperature NO_x desorption.

The important role of the redox behaviour of metal sites on a zeolite's storage performance is widely recognized [2]. NO_x adsorption and formation of stable surface nitrates is influenced by the initial catalyst redox state. The Cu^{2+}/Cu^{+} [2] [37] and Fe^{2+}/Fe^{3+} ratio [14] and bonding strength of the metal ions to the framework affect the reducibility of metal species and consequently the storage capacity.

Whilst initial reducibility studies have been performed; in order to identify the active sites, understand the storage capacity and propose a possible mechanism further characterisation is required. Complete characterisation of the zeolite catalysts should include an analysis of the structure, morphology, porosity, acidity, composition, degree of metal exchange, redox properties and distribution of metal species as well as identification of the adsorbed N-complexes.

5.7 References

1.   Twigg, M. V., Progress and future challenges in controlling automotive exhaust gas emissions. *Applied Catalysis B: Environmental* **2007,** *70* (1–4), 2-15.

2.   Colombo, M.; Nova, I.; Tronconi, E., NO2 adsorption on Fe- and Cu-zeolite catalysts: The effect of the catalyst red-ox state. *Applied Catalysis B-Environmental* **2012,** *111*, 433-444.

3.   Perdana, I.; Creaser, D.; Ohrman, O.; Hedlund, J., NOx adsorption over a wide temperature range on Na-ZSM-5 films. *Journal of Catalysis* **2005,** *234* (1), 219-229.

4.   Hadjiivanov, K.; Klissurski, D.; Ramis, G.; Busca, G., Fourier transform IR study of NOx adsorption on a CuZSM-5 DeNOx catalyst. *Applied Catalysis B: Environmental* **1996,** *7* (3–4), 251-267.

5.   Othman Ali, I., Preparation and characterization of copper nanoparticles encapsulated inside ZSM-5 zeolite and NO adsorption. *Materials Science and Engineering: A* **2007,** *459* (1–2), 294-302.

6.   Brilhac, J. F.; Sultana, A.; Gilot, P.; Martens, J. A., Adsorption and pressure swing desorption of NOx in NA-Y zeolite: Experiments and modeling. *Environmental Science & Technology* **2002,** *36* (5), 1136-1140.

7.   Wang, Y.; Lei, Z.; Chen, B.; Guo, Q.; Liu, N., Adsorption of NO and N2O on Fe-BEA and H-BEA zeolites. *Applied Surface Science* **2010,** *256* (12), 4042-4047.

8.   Landi, G.; Lisi, L.; Pirone, R.; Russo, G.; Tortorelli, M., Effect of water on NO adsorption over Cu-ZSM-5 based catalysts. *Catalysis Today* **2012,** *191* (1), 138-141.

9.   Iwasaki, M.; Shinjoh, H., NO evolution reaction with NO2 adsorption over Fe/ZSM-5: In situ FT-IR observation and relationships with Fe sites. *Journal of Catalysis* **2010,** *273* (1), 29-38.

10.   Despres, J.; Koebel, M.; Kröcher, O.; Elsener, M.; Wokaun, A., Adsorption and desorption of NO and NO2 on Cu-ZSM-5. *Microporous and Mesoporous Materials* **2003,** *58* (2), 175-183.

11.   Zhang, W.; Jia, M.; Yu, J.; Wu, T.; Yahiro, H.; Iwamoto, M., Adsorption Properties of Nitrogen Monoxide on Silver Ion-Exchanged Zeolites. *Chemistry of Materials* **1999,** *11* (4), 920-923.

12.   Labaki, M.; Issa, M.; Smeekens, S.; Heylen, S.; Kirschhock, C. E. A.; Villani, K.; Jeguirim, M.; Habermacher, D.; Brilhac, J. F.; Martens, J. A., Modeling of NOx adsorption-desorption-reduction cycles on a ruthenium loaded Na-Y zeolite. *Applied Catalysis B-Environmental* **2010,** *97* (1-2), 13-20.

13.   Liu, Y.; Harold, M. P.; Luss, D., Coupled NOx storage and reduction and selective catalytic reduction using dual-layer monolithic catalysts. *Applied Catalysis B: Environmental* **2012,** *121–122* (0), 239-251.

14.   Pan, H.; Guo, Y.; Bi, H. T., NOx adsorption and reduction with C3H6 over Fe/zeolite catalysts: Effect of catalyst support. *Chemical Engineering Journal* **2015,** *280*, 66-73.

15.   Chang, X.; Lu, G.; Guo, Y.; Wang, Y.; Guo, Y., A high effective adsorbent of NOx: Preparation, characterization and performance of Ca-beta zeolites. *Microporous and Mesoporous Materials* **2013,** *165* (0), 113-120.

16.   Wang, H.; Yu, Q.; Xiao, L.; Liu, T.; Yu, W.; Jiang, X.; Zhang, X.; Zheng, X., Superior Storage Performance for NO in Modified Natural Mordenite. *Chinese Journal of Chemistry* **2012,** *30* (7), 1511-1516.

17.   Wang, Y.; Lei, Z.; Zhang, R.; Chen, B., Adsorption of NO and N2O on Cu-BEA zeolite. *Journal of Molecular Structure-Theochem* **2010,** *957* (1-3), 41-46.

18.   Olsson, L.; Sjövall, H.; Blint, R. J., Detailed kinetic modeling of NOx adsorption and NO oxidation over Cu-ZSM-5. *Applied Catalysis B: Environmental* **2009,** *87* (3–4), 200-210.

19.   Rejmak, P.; Broclawik, E.; Gora-Marek, K.; Radon, M.; Datka, J., Nitrogen Monoxide Interaction with Cu(I) Sites in Zeolites X and Y: Quantum Chemical Calculations and IR Studies. *Journal of Physical Chemistry C* **2008,** *112* (46), 17998-18010.

20.   Szanyi, J.; Kwak, J. H.; Burton, S.; Rodriguez, J. A.; Peden, C. H. F., Characterization of NOx species in dehydrated and hydrated Na- and Ba-Y FAU zeolites formed in NO2 adsorption. *Journal of Electron Spectroscopy and Related Phenomena* **2006,** *150* (2-3), 164-170.

21.   Rudolf, T.; Böhlmann, W.; Pöppl, A., Adsorption and Desorption Behavior of NO on H-ZSM-5, Na-ZSM-5, and Na-A as Studied by EPR. *Journal of Magnetic Resonance* **2002,** *155* (1), 45-56.

22.   Gervasini, A., Desorption study of NO and O2 on Cu-ZSM-5. *Applied Catalysis B: Environmental* **1997,** *14* (3–4), 147-159.

23.   Zhang, W.-X.; Yahiro, H.; Iwamoto, M.; Izumi, J., Reversible and irreversible adsorption of nitrogen monoxide on cobalt Ion-exchanged ZSM-5 and mordenite zeolites at 273-523 K. *Journal of the Chemical Society, Faraday Transactions* **1995,** *91* (4), 767-771.

24.   Zhang, W. X.; Yahiro, H.; Mizuno, N.; Izumi, J.; Iwamoto, M., Removal of nitrogen monoxide on copper ion-exchanged zeolites by pressure swing adsorption. *Langmuir* **1993,** *9* (9), 2337-2343.

25.   Mahzoul, H.; Brilhac, J. F.; Gilot, P., Experimental and mechanistic study of NOx adsorption over NOx trap catalysts. *Applied Catalysis B: Environmental* **1999,** *20* (1), 47-55.

26.   Li, Y.; Hall, W. K., Stoichiometric catalytic decomposition of nitric oxide over copper-exchanged zeolite (CuZSM-5) catalysts. *The Journal of Physical Chemistry* **1990,** *94* (16), 6145-6148.

27.   Bennett, C. J.; Bennett, P. S.; Golunski, S. E.; Hayes, J. W.; Walker, A. P., Selective reduction of nitrogen oxides under oxidising exhaust-gas conditions. *Applied Catalysis A: General* **1992,** *86* (2), L1-L6.

28.   Li, L.; Guan, N., HC-SCR reaction pathways on ion exchanged ZSM-5 catalysts. *Microporous and Mesoporous Materials* **2009,** *117* (1–2), 450-457.

29.   Li, L.; Zhang, F.; Guan, N.; Richter, M.; Fricke, R., Selective catalytic reduction of NO by propane in excess oxygen over IrCu-ZSM-5 catalyst. *Catalysis Communications* **2007,** *8* (3), 583-588.

30.   Adelman, B. J.; Beutel, T.; Lei, G. D.; Sachtler, W. M. H., Mechanistic Cause of Hydrocarbon Specificity over Cu/ZSM-5 and Co/ZSM-5 Catalysts in the Selective Catalytic Reduction of NOx. *Journal of Catalysis* **1996,** *158* (1), 327-335.

31.   Deka, U.; Lezcano-Gonzalez, I.; Warrender, S. J.; Lorena Picone, A.; Wright, P. A.; Weckhuysen, B. M.; Beale, A. M., Changing active sites in Cu–CHA catalysts: deNOx selectivity as a function of the preparation method. *Microporous and Mesoporous Materials* **2013,** *166* (0), 144-152.

32.   Hasna, A. M., Reduction of NOX Gases Using Copper Zeolite Catalyst. In *World Congress on Engineering 2009, Vols I and Ii*, Ao, S. I.; Gelman, L.; Hukins, D. W. L.; Hunter, A.; Korsunsky, A. M., Eds. 2009; pp 657-661.

33.   Iwamoto, M.; Yokoo, S.; Sakai, K.; Kagawa, S., Catalytic decomposition of nitric oxide over copper(II)-exchanged, Y-type zeolites. *Journal of the Chemical Society, Faraday Transactions 1: Physical Chemistry in Condensed Phases* **1981,** *77* (7), 1629-1638.

34.   Lee, D., Quantification and redox property of the oxygen-bridged Cu2+ dimers as the active sites for the NO decomposition over Cu-ZSM-5 catalysts. *Korean J. Chem. Eng.* **2004,** *21* (3), 611-620.

35.   Teraoka, Y.; Tai, C.; Ogawa, H.; Furukawa, H.; Kagawa, S., Characterization and NO decomposition activity of Cu-MFI zeolite in relation to redox behavior. *Applied Catalysis A: General* **2000,** *200* (1–2), 167-176.

36.   Schay, Z.; Guczi, L.; Koppany, Z.; Nagy, I.; Beck, A.; Samuel, V.; Dongare, M. K.; Sabde, D. P.; Hegde, S. G.; Ramaswamy, A. V., Decomposition of NO over Cu-AITS-1 zeolites. *Catalysis Today* **1999,** *54* (4), 569-574.

37.   Wichterlová, B.; Dědeček, J.; Sobalík, Z.; Vondrová, A.; Klier, K., On the Cu Site in ZSM-5 Active in Decomposition of NO: Luminescence, FTIR Study, and Redox Properties. *Journal of Catalysis* **1997,** *169* (1), 194-202.

38.   (a) Pulido, A.; Nachtigall, P., Correlation Between Catalytic Activity and Metal Cation Coordination: NO Decomposition Over Cu/Zeolites. *Chemcatchem* **2009,** *1* (4), 449-453; (b) Dossi, C.; Fusi, A.; Recchia, S.; Psaro, R.; Moretti, G., Cu–ZSM-5 (Si/Al=66), Cu–Fe–S-1 (Si/Fe=66) and Cu–S-1 catalysts for NO decomposition: preparation, analytical characterization and catalytic activity. *Microporous and Mesoporous Materials* **1999,** *30* (1), 165-175.

39.   Varga, J.; Halasz, J.; Kiricsi, I., Modified ZSM-5 zeolite as DENOX catalyst. *Environmental Pollution* **1998,** *102*, 691-695.

40.   Price, G. L.; Kanazirev, V.; Church, D. F., FORMATION OF CU-MFI NO DECOMPOSITION CATALYST VIA REDUCTIVE SOLID-STATE ION-EXCHANGE. *Journal of Physical Chemistry* **1995,** *99* (3), 864-868.

41.   Yang, T. T.; Bi, H. T., Novel Fluidized Bed Reactor for Integrated NOx Adsorption-Reduction with Hydrocarbons. *Environmental Science & Technology* **2009,** *43* (13), 5049-5053.

42.   Feng, X.; Keith Hall, W., FeZSM-5: A Durable SCR Catalyst for NOxRemoval from Combustion Streams. *Journal of Catalysis* **1997,** *166* (2), 368-376.

43.   Chen, H.-Y.; Voskoboinikov, T.; Sachtler, W. M. H., Reduction of NOxover Fe/ZSM-5 Catalysts: Adsorption Complexes and Their Reactivity toward Hydrocarbons. *Journal of Catalysis* **1998,** *180* (2), 171-183.

44.   Schwidder, M.; Kumar, M. S.; Klementiev, K.; Pohl, M. M.; Bruckner, A.; Grunert, W., Selective reduction of NO with Fe-ZSM-5 catalysts of low Fe content - I. Relations between active site structure and catalytic performance. *Journal of Catalysis* **2005,** *231* (2), 314-330.

45.   Guzmán-Vargas, A.; Delahay, G.; Coq, B.; Lima, E.; Bosch, P.; Jumas, J.-C., Influence of the preparation method on the properties of Fe-ZSM-5 for the selective catalytic reduction of NO by n-decane. *Catalysis Today* **2005,** *107–108* (0), 94-99.

46.   Chen, H. Y.; Sun, Q.; Wen, B.; Yeom, Y. H.; Weitz, E.; Sachtler, W. M. H., Reduction over zeolite-based catalysts of nitrogen oxides in emissions containing excess oxygen - Unraveling the reaction mechanism. *Catalysis Today* **2004,** *96* (1-2), 1-10.

47.   Chen, H. Y.; Wang, X.; Sachtler, W. M. H., Reduction of NOx over various Fe/zeolite catalysts. *Applied Catalysis a-General* **2000,** *194*, 159-168.

48.   Chen, H. Y.; Voskoboinikov, T.; Sachtler, W. M. H., Reduction of NOx over Fe/ZSM-5 catalysts: mechanistic causes of activity differences between alkanes. *Catalysis Today* **1999,** *54* (4), 483-494.

49.   Chen, H. Y.; Voskoboinikov, T.; Sachtler, W. M. H., Reaction intermediates in the selective catalytic reduction of NOx over Fe/ZSM-5. *Journal of Catalysis* **1999,** *186* (1), 91-99.

50.   Brüggemann, T. C.; Keil, F. J., Theoretical Investigation of the Mechanism of the Selective Catalytic Reduction of Nitrogen Oxide with Ammonia on Fe-Form Zeolites. *The Journal of Physical Chemistry C* **2011,** *115* (48), 23854-23870.

51.   Iwasaki, M.; Yamazaki, K.; Banno, K.; Shinjoh, H., Characterization of Fe/ZSM-5 DeNOx catalysts prepared by different methods: Relationships between active Fe sites and NH3-SCR performance. *J. Catal.* **2008,** *260* (2), 205-216.

52.   Yamada, K.; Pophal, C.; Segawa, K., Selective catalytic reduction of N2O by C3H6 over Fe-ZSM-5. *Microporous and Mesoporous Materials* **1998,** *21* (4–6), 549-555.

53.   Kapteijn, F.; Marbán, G.; Rodriguez-Mirasol, J.; Moulijn, J. A., Kinetic Analysis of the Decomposition of Nitrous Oxide over ZSM-5 Catalysts. *Journal of Catalysis* **1997,** *167* (1), 256-265.

54.   Li, G.; Pidko, E. A.; Filot, I. A. W.; van Santen, R. A.; Li, C.; Hensen, E. J. M., Catalytic properties of extraframework iron-containing species in ZSM-5 for N2O decomposition. *Journal of Catalysis* **2013,** *308* (0), 386-397.

55.   Sobolev, V. I.; Koltunov, K. Y., Location, stability, and reactivity of oxygen species generated by N2O decomposition over Fe-ZSM-5 and Fe-Beta zeolites. *Journal of Molecular Catalysis a-Chemical* **2011,** *347* (1-2), 22-27.

56.   Liu, N.; Chen, B.; Li, Y.; Zhang, R.; Liang, X.; Li, Y.; Lei, Z., Charge Transfer Analysis on the Direct Decomposition of Nitrous Oxide over Fe-BEA Zeolite: An Experimental and Density Functional Study. *Journal of Physical Chemistry C* **2011,** *115* (26), 12883-12890.

57.   Chen, B.; Liu, N.; Liu, X.; Zhang, R.; Li, Y.; Li, Y.; Sun, X., Study on the direct decomposition of nitrous oxide over Fe-beta zeolites: From experiment to theory. *Catalysis Today* **2011,** *175* (1), 245-255.

58.   Sklenak, S.; Andrikopoulos, P. C.; Boekfa, B.; Jansang, B.; Novakova, J.; Benco, L.; Bucko, T.; Hafner, J.; Dedecek, J.; Sobalik, Z., N2O decomposition over Fe-zeolites: Structure of the active sites and the origin of the distinct reactivity of Fe-ferrierite, Fe-ZSM-5, and Fe-beta. A combined periodic DFT and multispectral study. *Journal of Catalysis* **2010,** *272* (2), 262-274.

59.   Pérez-Ramírez, J.; Santhosh Kumar, M.; Brückner, A., Reduction of N2O with CO over FeMFI zeolites: influence of the preparation method on the iron species and catalytic behavior. *Journal of Catalysis* **2004,** *223* (1), 13-27.

60.   Cortes, J. M. G.; Gomez, M. J. I.; de Lecea, C. S. M., The selective reduction of NOx with propene on Pt-beta catalyst: A transient study. *Applied Catalysis B-Environmental* **2007,** *74* (3-4), 313-323.

61.   Xin, M.; Hwang, I. C.; Kim, D. H.; Cho, S. I.; Woo, S. I., The effect of the preparation conditions of Pt/ZSM-5 upon its activity and selectivity for the reduction of nitric oxide. *Applied Catalysis B: Environmental* **1999,** *21* (3), 183-190.

62.   Takami, A.; Takemoto, T.; Iwakuni, H.; Yamada, K.; Shigetsu, M.; Komatsu, K., Zeolite-supported precious metal catalysts for NOx reduction in lean burn engine exhaust. *Catalysis Today* **1997,** *35* (1-2), 75-81.

63.   Guo, J.; Konno, M.; Chikahisa, T.; Murayama, T.; Iwamoto, M., NOx reduction characteristics of Pt-ZSM-5 catalyst with diesel engine exhaust. *JSAE Review* **1995,** *16* (1), 21-25.

64.   Deeba, M.; Feeley, J.; Farrauto, R., Lean NOx: dual sites for NOx reduction on Pt/H-ZSM-5. *Applied Catalysis A: General* **1999,** *188* (1–2), 219-227.

65.   Sedlmair, C.; Seshan, K.; Jentys, A.; Lercher, J. A., Elementary steps of NOx adsorption and surface reaction on a commercial storage–reduction catalyst. *Journal of Catalysis* **2003,** *214* (2), 308-316.

66.   Ottinger, N. A.; Toops, T. J.; Pihl, J. A.; Roop, J. T.; Choi, J.-S.; Partridge, W. P., Sulfate storage and stability on representative commercial lean NOx trap components. *Applied Catalysis B: Environmental* **2012,** *117–118* (0), 167-176.

67.   Leistner, K.; Nicolle, A.; Da Costa, P., Modelling the kinetics of NO oxidation and NOx storage over platinum, ceria and ceria zirconia. *Applied Catalysis B-Environmental* **2012,** *111*, 415-423.

68.   Clayton, R. D.; Harold, M. P.; Balakotaiah, V.; Wan, C. Z., Pt dispersion effects during NOx storage and reduction on Pt/BaO/Al2O3 catalysts. *Applied Catalysis B: Environmental* **2009,** *90* (3–4), 662-676.

69.   Dawody, J.; Skoglundh, M.; Wall, S.; Fridell, E., Role of Pt-precursor on the performance of Pt/BaCO3/Al2O3·NOx storage catalysts. *Journal of Molecular Catalysis A: Chemical* **2005,** *225* (2), 259-269.

70.   Balbuena, P. B.; Gubbins, K. E., Theoretical interpretation of adsorption behavior of simple fluids in slit pores. *Langmuir* **1993,** *9* (7), 1801-1814.

71.   Sultana, A.; Nanba, T.; Sasaki, M.; Haneda, M.; Suzuki, K.; Hamada, H., Selective catalytic reduction of NOx with NH3 over different copper exchanged zeolites in the presence of decane. *Catalysis Today* **2011,** *164* (1), 495-499.

72.   Putluru, S. S. R.; Riisager, A.; Fehrmann, R., Alkali resistant Cu/zeolite deNOx catalysts for flue gas cleaning in biomass fired applications. *Appl. Catal., B* **2011,** *101* (3-4), 183-188.

73.   Inaba, M.; Murata, K.; Takahara, I.; Inoue, K.-i., Production of olefins from ethanol by Fe and/or P-modified H-ZSM-5 zeolite catalysts. *Journal of Chemical Technology and Biotechnology* **2011,** *86* (1), 95-104.

74.   Nawaz, Z.; Qing, S.; Gao, J.; Tang, X.; Wei, F., Effect of Si/Al ratio on performance of Pt-Sn-based catalyst supported on ZSM-5 zeolite for n-butane conversion to light olefins. *Journal of Industrial and Engineering Chemistry* **2010,** *16* (1), 57-62.

75.   Kefirov, R.; Penkova, A.; Hadjiivanov, K.; Dzwigaj, S.; Che, M., Stabilization of Cu+ ions in BEA zeolite: Study by FTIR spectroscopy of adsorbed CO and TPR. *Microporous and Mesoporous Materials* **2008,** *116* (1-3), 180-187.

76.   Chen, H.-Y.; Sachtler, W. M. H., Activity and durability of Fe/ZSM-5 catalysts for lean burn NOx reduction in the presence of water vapor. *Catalysis Today* **1998,** *42* (1–2), 73-83.

77.   Ma, L.; Li, J.; Arandiyan, H.; Shi, W.; Liu, C.; Fu, L., Influence of calcination temperature on Fe/HBEA catalyst for the selective catalytic reduction of NOx with NH3. *Catalysis Today* **2012,** *184* (1), 145-152.

78.   Voskoboinikov, T. V.; Chen, H. Y.; Sachtler, W. M. H., On the nature of active sites in Fe/ZSM-5 catalysts for NOx abatement. *Applied Catalysis B-Environmental* **1998,** *19* (3-4), 279-287.

79.   Li, L.; Shen, Q.; Li, J.; Hao, Z.; Xu, Z. P.; Lu, G. Q. M., Iron-exchanged FAU zeolites: Preparation, characterization and catalytic properties for N2O decomposition. *Applied Catalysis a-General* **2008,** *344* (1-2), 131-141.

80.   Lobree, L. J.; Hwang, I.-C.; Reimer, J. A.; Bell, A. T., Investigations of the State of Fe in H–ZSM-5. *Journal of Catalysis* **1999,** *186* (2), 242-253.

81.   Hammond, C.; Dimitratos, N.; Jenkins, R. L.; Lopez-Sanchez, J. A.; Kondrat, S. A.; Hasbi ab Rahim, M.; Forde, M. M.; Thetford, A.; Taylor, S. H.; Hagen, H.; Stangland, E. E.; Kang, J. H.; Moulijn, J. M.; Willock, D. J.; Hutchings, G. J., Elucidation and Evolution of the Active Component within Cu/Fe/ZSM-5 for Catalytic Methane Oxidation: From Synthesis to Catalysis. *ACS Catalysis* **2013,** *3* (4), 689-699.

82.   Pérez-Ramírez, J.; Groen, J. C.; Brückner, A.; Kumar, M. S.; Bentrup, U.; Debbagh, M. N.; Villaescusa, L. A., Evolution of isomorphously substituted iron zeolites during activation: comparison of Fe-beta and Fe-ZSM-5. *Journal of Catalysis* **2005,** *232* (2), 318-334.

83.   Hensen, E. J. M.; Zhu, Q.; Janssen, R. A. J.; Magusin, P. C. M. M.; Kooyman, P. J.; van Santen, R. A., Selective oxidation of benzene to phenol with nitrous oxide over MFI zeolites: 1. On the role of iron and aluminum. *Journal of Catalysis* **2005,** *233* (1), 123-135.

84.   Forde, M. M.; Armstrong, R. D.; McVicker, R.; Wells, P. P.; Dimitratos, N.; He, Q.; Lu, L.; Jenkins, R. L.; Hammond, C.; Lopez-Sanchez, J. A.; Kiely, C. J.; Hutchings, G. J., Light alkane oxidation using catalysts prepared by chemical vapour impregnation: tuning alcohol selectivity through catalyst pre-treatment. *Chemical Science* **2014,** *5* (9), 3603-3616.

85.   Kumar, M. S.; Schwidder, M.; Grünert, W.; Brückner, A., On the nature of different iron sites and their catalytic role in Fe-ZSM-5 DeNOx catalysts: new insights by a combined EPR and UV/VIS spectroscopic approach. *Journal of Catalysis* **2004,** *227* (2), 384-397.

86.   Pérez Vélez, R.; Ellmers, I.; Huang, H.; Bentrup, U.; Schünemann, V.; Grünert, W.; Brückner, A., Identifying active sites for fast NH3-SCR of NO/NO2 mixtures over Fe-ZSM-5 by operando EPR and UV–vis spectroscopy. *Journal of Catalysis* **2014,** *316* (0), 103-111.

87.   Mihaylov, M.; Ivanova, E.; Chakarova, K.; Novachka, P.; Hadjiivanov, K., Reduced iron sites in Fe-BEA and Fe-ZSM-5 zeolites: FTIR study of CO adsorption and (CO)-C-12-O-16-(CO)-C-13-O-18 co-adsorption. *Applied Catalysis a-General* **2011,** *391* (1-2), 3-10.

88.   Sobczak, I.; Pawlowski, H.; Chmielewski, J.; Ziolek, M., Gold and gold-iron modified zeolites-Towards the adsorptive deodourisation. *Journal of Hazardous Materials* **2010,** *179* (1-3), 444-452.

89.   Janas, J.; Gurgul, J.; Socha, R. P.; Dzwigaj, S., Effect of Cu content on the catalytic activity of CuSiBEA zeolite in the SCR of NO by ethanol: Nature of the copper species. *Applied Catalysis B-Environmental* **2009,** *91* (1-2), 217-224.

90.   Giordanino, F.; Vennestrom, P. N. R.; Lundegaard, L. F.; Stappen, F. N.; Mossin, S.; Beato, P.; Bordiga, S.; Lamberti, C., Characterization of Cu-exchanged SSZ-13: a comparative FTIR, UV-Vis, and EPR study with Cu-ZSM-5 and Cu-[small beta] with similar Si/Al and Cu/Al ratios. *Dalton Transactions* **2013,** *42* (35), 12741-12761.

91.   Fu, W. Q.; Liu, T. T.; Fang, Z. X.; Ma, Y. L.; Zheng, X.; Wang, W. C.; Ni, X. J.; Hu, M. L.; Tang, T. D., High activity and stability in the cross-coupling of aryl halides with disulfides over Cu-doped hierarchically porous zeolite ZSM-5. *Chemical Communications* **2015,** *51* (27), 5890-5893.

92.   Qin, G.; Zheng, L.; Xie, Y.; Wu, C., On the framework hydroxyl groups of H-ZSM-5 zeolites. *Journal of Catalysis* **1985,** *95* (2), 609-612.

93.   Petunchi, J. O.; Hall, W. K., On the role of nitrogen dioxide in the mechanism of the selective reduction of NOx over Cu-ZSM-5 zeolite. *Applied Catalysis B: Environmental* **1993,** *2* (2–3), L17-L26.

94.   Uppili, S.; Thomas, K. J.; Crompton, E. M.; Ramamurthy, V., Probing Zeolites with Organic Molecules: Supercages of X and Y Zeolites Are Superpolar†. *Langmuir* **2000,** *16* (1), 265-274.

95.   Benzene in Zeolite ZSM-5 Studied by Diffuse Reflectance Infrared Spectroscopy. *Applied Spectroscopy* **1990,** *44* (6), 1070-1073.

96.   Bortnovsky, O.; Sobalík, Z.; Wichterlová, B.; Bastl, Z., Structure of Al–Lewis Site in Beta Zeolite Active in the Meerwein–Ponndorf–Verley Reduction of Ketone to Alcohol. *Journal of Catalysis* **2002,** *210* (1), 171-182.

97.   *Collection of Simulated XRD Powder Patterns for Zeolites.*

98.   Perdana, I.; Creaser, D.; Öhrman, O.; Hedlund, J., A comparison of NOx adsorption on Na, H and BaZSM-5 films. *Applied Catalysis B: Environmental* **2007,** *72* (1–2), 82-91.

99.   Hwang, I. C.; Xin, M.; Woo, S. I., UHV-TPD study of NO adsorption/reaction over CuZSM-5. *Applied Surface Science* **1997,** *121–122* (0), 310-313.

100.   Regina Oliveira de Souza, T.; Modesto de Oliveira Brito, S.; Martins Carvalho Andrade, H., Zeolite catalysts for the water gas shift reaction. *Applied Catalysis A: General* **1999,** *178*, 7-15.

101.   Long, R. Q.; Yang, R. T., Fe-ZSM-5 for Selective Catalytic Reduction of NO with NH3: A Comparative Study of Different Preparation Techniques. *Catalysis Letters* **2001,** *74* (3-4), 201-205.

102.   El-Malki, E.-M.; van Santen, R. A.; Sachtler, W. M. H., Introduction of Zn, Ga, and Fe into HZSM-5 Cavities by Sublimation: Identification of Acid Sites. *The Journal of Physical Chemistry B* **1999,** *103* (22), 4611-4622.

103.   Forde, M. M.; Kesavan, L.; bin Saiman, M. I.; He, Q.; Dimitratos, N.; Lopez-Sanchez, J. A.; Jenkins, R. L.; Taylor, S. H.; Kiely, C. J.; Hutchings, G. J., High Activity Redox Catalysts Synthesized by Chemical Vapor Impregnation. *ACS Nano* **2014,** *8* (1), 957-969.

104.   Armstrong, R. D.; Freakley, S. J.; Forde, M. M.; Peneau, V.; Jenkins, R. L.; Taylor, S. H.; Moulijn, J. A.; Morgan, D. J.; Hutchings, G. J., Low temperature catalytic partial oxidation of ethane to oxygenates by Fe– and Cu–ZSM-5 in a continuous flow reactor. *Journal of Catalysis* **2015,** *330*, 84-92.

105.   Forde, M. M.; Armstrong, R. D.; Hammond, C.; He, Q.; Jenkins, R. L.; Kondrat, S. A.; Dimitratos, N.; Lopez-Sanchez, J. A.; Taylor, S. H.; Willock, D.; Kiely, C. J.; Hutchings, G. J., Partial Oxidation of Ethane to Oxygenates Using Fe- and Cu-Containing ZSM-5. *Journal of the American Chemical Society* **2013,** *135* (30), 11087-11099.

106.   Conner, W. C.; Falconer, J. L., Spillover in Heterogeneous Catalysis. *Chemical Reviews* **1995,** *95* (3), 759-788.

107.   Influence of oxidation on the stability of Pt-Co bimetallic particles entrapped in Na Y zeolite. *Catalysis by Microporous Materials Studies in Surface Science and Catalysis* **1995,** *94*, 171.

108.   Zhang, R.; Li, Y.; Zhen, T., Ammonia selective catalytic reduction of NO over Fe/Cu-SSZ-13. *RSC Advances* **2014,** *4* (94), 52130-52139.

109.   Brandenberger, S.; Kröcher, O.; Tissler, A.; Althoff, R., Effect of Structural and Preparation Parameters on the Activity and Hydrothermal Stability of Metal-Exchanged ZSM-5 in the Selective Catalytic Reduction of NO by NH3. *Industrial & Engineering Chemistry Research* **2011,** *50* (8), 4308-4319.

110.   Sultana, A.; Sasaki, M.; Suzuki, K.; Hamada, H., Tuning the NOx conversion of Cu-Fe/ZSM-5 catalyst in NH3-SCR. *Catalysis Communications* **2013,** *41*, 21-25.

111.   Kieger, S.; Delahay, G.; Coq, B.; Neveu, B., Selective Catalytic Reduction of Nitric Oxide by Ammonia over Cu-FAU Catalysts in Oxygen-Rich Atmosphere. *Journal of Catalysis* **1999,** *183* (2), 267-280.

112.   Amiridis, M. D.; Puglisi, F.; Dumesic, J. A.; Millman, W. S.; Topsoe, N. Y., Kinetic and Infrared Spectroscopic Studies of Fe-Y Zeolites for the Selective Catalytic Reduction of Nitric Oxide by Ammonia. *Journal of Catalysis* **1993,** *142* (2), 572-584.

113.   Rivallan, M.; Berlier, G.; Ricchiardi, G.; Zecchina, A.; Nechita, M.-T.; Olsbye, U., Characterisation and catalytic activity in de-NOx reactions of Fe-ZSM-5 zeolites prepared via ferric oxalate precursor. *Applied Catalysis B: Environmental* **2008,** *84* (1–2), 204-213.

114.   Long, R. Q.; Yang, R. T., Catalytic Performance of Fe–ZSM-5 Catalysts for Selective Catalytic Reduction of Nitric Oxide by Ammonia. *Journal of Catalysis* **1999,** *188* (2), 332-339.

115.   Pieterse, J. A. Z.; Booneveld, S.; van den Brink, R. W., Evaluation of Fe-zeolite catalysts prepared by different methods for the decomposition of N2O. *Applied Catalysis B: Environmental* **2004,** *51* (4), 215-228.

Optimising Cu^{II}/ZSM-5 (30) for NO_x storage   **6**

6.1 Introduction

Chapter 5 covers the initial screening of metal-exchanged zeolites for NO_x storage and a study of the effect of the zeolite framework and Brønsted acidity, as well as the nature of the exchanged metal. Among the zeolite-based catalysts studied, several present high NO_x storage performances. Those of particular interest are metal exchanged zeolites that exhibit greater NO_x desorption at high temperatures above 200 °C.

A common approach for enhancing catalyst properties is to optimise a single variable while the other variables remain fixed. The experimental results obtained thus, do not reveal the interaction between the variables involved. The optimal values of the variable are difficult to determine from these experiments simply because of the large number of experiments required. Accordingly, use of the statistical design of experiments (DOE) is effective to speed up catalysts optimisation.

There are many factors affecting NO_x storage capacity for metal exchanged zeolites. Focussing on the ion exchange preparation method, this study adopts the DOE method to enhance the adsorption/desorption properties of the $Cu^{II}/ZSM-5$ (30) catalyst system. In this chapter, experimental design is used to generate a set of data to evaluate the influence of ion exchange experimental variables on NO_x storage. As described in section 6.3, completion of the study requires an associated statistical analysis, using the response values obtained to find interactions among different experimental variables. The optimum variable values are then determined statistically, in order to maximise the catalyst's NO_x storage performance.

6.2 Application of statistical design of experiments (DOE) to optimise

NO$_x$ storage on Cu^{II}/ZSM-5 (30)

As introduced previously, the statistical design of experiments (DOE) provides the data to quantify the influence of experimental variables and associated interactions, with a relative small number of experiments. If there are many experimental variables, it is important to separate the important from the negligible ones. Only after identifying the main contributors and their interactions, can a detailed optimisation be performed.

Hence, Cu^{II}/ZSM-5 (30) catalysts were prepared by wet ion exchange (WIE) and chemical vapour impregnation (CVI) as part of a two level design, constructed using the Design-Expert® 9 statistical design and analysis software. These zeolite catalysts were evaluated for NO$_x$ storage under different reaction conditions and characterised by different techniques to correlate physicochemical properties with adsorption/desorption properties.

The storage capacity, in the absence of O$_2$, was evaluated as explained in Chapter 5, Section 5.2, through performing isothermal NO$_x$ adsorption with 0.1 % NO balance in He, followed by a TPD with He. The adsorption-desorption profiles obtained are comparable with those shown in Figure 5.2 and 5.3. Those catalysts that exhibit high performance where also tested for NO$_x$ storage in the presence of O$_2$. The adsorption-desorption profiles obtained, in this case, are comparable with those shown in Figures 5.4 and 5.5. The NO$_x$ storage capacities are summarised in bar plot figures which illustrate quantified values for the total amount of NO$_x$ (NO and NO$_2$) adsorbed and desorbed.

6.2.1 Wet ion exchange

When using WIE, the experimental method and degree of exchange are known to influence the stability and activity of metal exchanged zeolites for deNO$_x$ reactions.

Over-exchanged Cu/ZSM-5 catalysts, where the amount of Cu^{II} ion exceeds the 1:2 ratio assumed by the ion exchange reaction shown in equation 6.1, are highly active for deNO$_x$.

$$Cu^{2+} \; + \; 2\,[H^+{\cdot}AlO^{2-}] \;\; \leftrightarrow \;\; 2\,H^+ \; + \; Cu^{2+}{\cdot}2AlO^{2-} \hspace{2cm} \text{Equation 6.1}$$
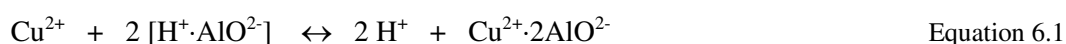
High metal loading is achieved by repeated ion exchange- up to three to four cycles [1] [2]. However, it has been reported that the degree of metal exchange via WIE is also controlled by the solution contact time, temperature and pH [3] [4] [5] [6]. In addition, the washing procedure used, after contact between the zeolite support and the metal precursor solution, also affects the degree of metal exchange. Iwamoto *et al.* [1] [7] prepared active catalysts by a single ion exchange of Cu^{II} in basic ammonia hydroxide (NH$_4$OH). By raising the pH of the copper precursor solution, [CuOH]$^+$, [Cu$_2$OH]$^{3+}$, [Cu$_2$(OH)$_2$]$^{2+}$ and [Cu$_3$(OH)$_2$]$^{4+}$ exchangeable species are formed, allowing high exchange with aluminium sites [8] [9]. Hence, the pH of the suspension of the copper salt and the zeolite during WIE is a key factor in achieving highly active catalysts.

Table 6.1. Experimental variables and level assignments in a two level factorial design to optimise the Cu^{II}/ZSM-5 (30) catalytic system prepared by WIE

Variable	Low level (-)	High level (+)
Copper precursor concentration	0.025 M	0.05 M
Solution temperature	25 °C	90 °C
Solution contact time	6 h	24 h
Solution pH	5.5	7.0
Washing volume	50 mL	100 mL

The experimental parameters of the WIE preparation procedure that affect NO$_x$ storage on Cu^{II}/ZSM-5 (30) most significantly, were screened based on a fractional two-level factorial design 2_V^{5-1}. Copper (II) acetate was used as the metal precursor. Five variables (copper precursor concentration, solution temperature, solution contact time, solution pH and washing volume) were studied in 16 experiments. Calcination conditions were held constant, at 550 °C for 3 h in static air. As shown in Table 6.1, the concentration of each variable was set at two levels, high and low, denoted by (+) and (-) signs respectively.

Cu^{II}/ZSM-5 (30) catalysts were prepared by WIE based on the DOE matrix presented in Table 6.2.

Table 6.2. Mix proportions of the experimental design for studied variables to optimise the

Cu^{II}/ZSM-5 (30) catalytic system prepared by WIE

No.	Cu^{II} precursor concentration	Solution temperature	Solution contact time	Solution pH	Washing volume
[1]	+	+	-	-	+
[2]	+	-	-	-	-
[3]	-	-	-	-	+
[4]	-	+	+	-	+
[5]	+	-	+	-	+
[6]	+	+	+	-	-
[7]	-	-	+	-	-
[8]	-	+	-	-	-
[9]	-	+	+	+	-
[10]	+	-	+	+	-
[11]	-	-	+	+	+
[12]	+	+	-	+	-
[13]	+	-	-	+	+
[14]	+	+	+	+	+
[15]	-	-	-	+	-
[16]	-	+	-	+	+

Figure 6.1 shows the NO storage capacity obtained for Cu^{II}/ZSM-5 (30) _{WIE DOE} catalysts. Bar graphs include the total amount of NO adsorbed at 30 °C and NO desorbed during the TPD up to 300 C °. The amount of NO reversibly adsorbed and hence desorbed at 30 °C is excluded from calculations.
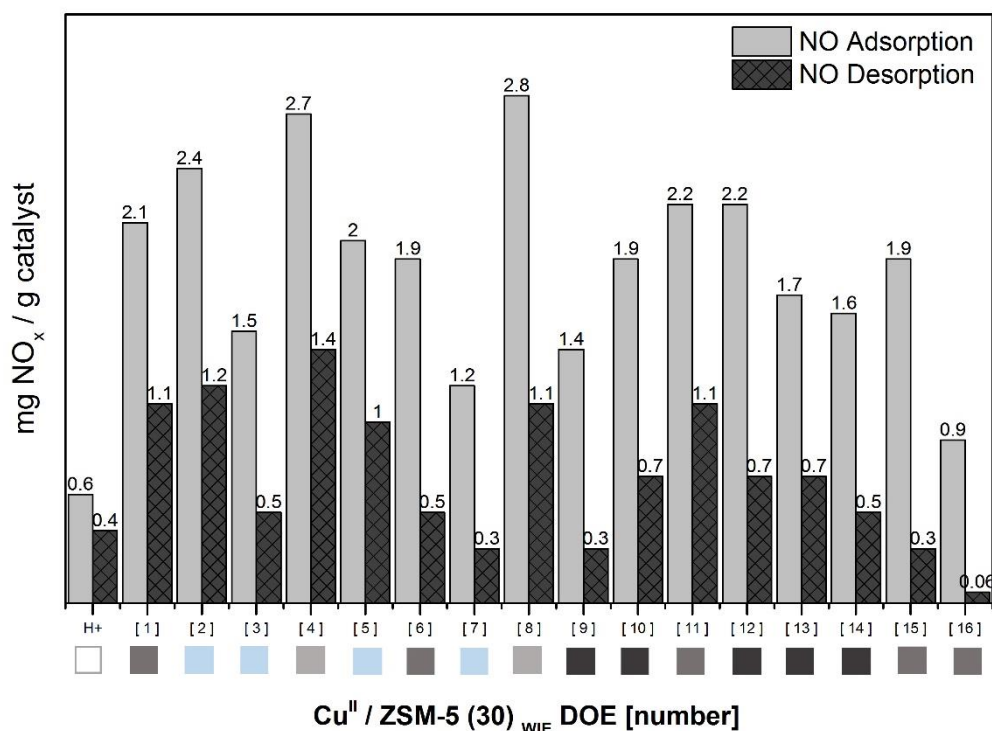
Figure 6.1. NO_x storage capacities of Cu^{II}/ZSM-5 (30) _{WIE DOE [No.]} catalysts

NO adsorption at 30 °C and TPD with He up to 300 °C

Reaction conditions: Flow reactor, GHSV = 35,000 h^{-1}, 0.1 % NO in He / He

Catalysts prepared by WIE DOE and calcined at 550 °C for 3 h in static air

The results reveal that variation of the different experimental variables affects the NO storage capacity of Cu^{II}/ZSM-5 (30) _{WIE DOE} catalysts extensively. Not only the total amount of NO adsorbed and desorbed but also the extent of reversible NO adsorption is affected by WIE experimental conditions. Additionally, the resulting colour of the Cu^{II}/ZSM-5 (30) _{WIE} catalyst is also dependant on the experimental parameters. As

presented in the x-axis of Figure 6.1, wet ion exchange of Cu^{II} onto the white support, H^{+}-ZSM-5 (30), results in a gradient of colours including light blue, light grey, grey and dark grey. The reason for colour variation is the chemical environment, as these colours are associated with different speciation of copper. While Cu(OH)$_2$ is light blue, CuO is black and Cu$_2$O is red.

Cu^{II}/ZSM-5 (30) $_{WIE\ DOE\ 4}$ and Cu^{II}/ZSM-5 (30) $_{WIE\ DOE\ 8}$ catalysts exhibit the greatest NO adsorption at 2.7 mg NO/g, 4.5 times higher than that of the unmodified ZSM-5 (30). A significant amount of the total NO adsorbed corresponds to reversible adsorption, 48 and 61% for Cu^{II}/ZSM-5 (30) $_{WIE\ DOE\ 4}$ and Cu^{II}/ZSM-5 (30) $_{WIE\ DOE\ 8}$ respectively. Based on the results it can be concluded that Cu^{II}/ZSM-5 (30) $_{WIE\ DOE\ 4}$ presents the highest storage capacity, with 2.7 and 1.4 mg NO/g adsorbed and desorbed. On the other hand, Cu^{II}/ZSM-5 (30) $_{WIE\ DOE\ 16}$ presents the lowest storage capacity, with only 0.9 and 0.1 mg NO/g adsorbed and desorbed. While the highest amount of NO adsorbed (Cu^{II}/ZSM-5 (30) $_{WIE\ DOE\ 4}$, 2.7 mg NO/g) is 3 times greater than the lowest amount of NO adsorbed (Cu^{II}/ZSM-5 (30) $_{WIE\ DOE\ 16}$, 0.9 mg NO/g) the highest amount of NO desorbed is 14 times greater than the lowest amount of NO desorbed.

It should be noted that Cu^{II}/ZSM-5 (30) $_{WIE\ DOE\ 5}$ represents the catalyst prepared using experimental conditions defined as "standard," used to prepare those WIE catalysts presented in Chapter 5 Figure 5.11 before the statistical approach was applied. Concordantly, based on NO adsorption, NO storage is enhanced by 35 % for the most active WIE catalyst Cu^{II}/ZSM-5 (30) $_{WIE\ DOE\ 4}$ when compared with the standard catalyst, Cu^{II}/ZSM-5 (30)$_{WIE\ DOE\ 5}$.

Results indicate that there is not a direct relationship between the Cu^{II} precursor concentration and NO$_x$ storage performance. Hence, using a 0.05 M aqueous solution of

copper (II) acetate is not preferable to a 0.025 M solution. While, the copper precursor solution temperature is found to have the greatest effect on the NO_x storage capacity, its beneficial effect is also related with the Cu^{II} precursor concentration and solution contact time. At a pH of 5.5, an increase in the solution temperature up to 90 °C is clearly advantageous when using a 0.025 M solution of copper (II) acetate, independent of the solution contact time. Moreover, when using a more concentrated copper (II) acetate aqueous solution (0.05 M), a high temperature (90 °C) is only favourable at short solution contact times (6 hours). No significant differences are observed for Cu^{II}/ZSM-5 (30) $_{WIE}$ catalysts prepared using different washing volumes. Contrarily to expectation, raising the pH of the Cu^{II} precursor solution by adding NH_4OH does not give rise to more active catalysts for NO_x storage. In fact, using a more basic solution generally has a detrimental effect on the NO adsorption/desorption properties of the Cu^{II}/ZSM-5 (30) $_{WIE}$ catalysts. In addition, as the solution temperature increases, the negative effect of increasing the solution pH is more significant and the amount of NO adsorbed and desorbed drops considerably (Cu^{II}/ZSM-5 (30)$_{WIE\ DOE\ 9}$ and Cu^{II}/ZSM-5 (30)$_{WIE\ DOE\ 16}$).

To obtain the results presented in Figure 6.1, only NO was quantified and the TPD was performed up to 300 °C rather than 500 °C. This should not affect the results because when NO is adsorbed in the absence of O_2, desorption occurs mainly as NO at 30 °C and 100 °C. However, as shown in Figure 6.2, the NO_x storage capacities of selected Cu^{II}/ZSM-5 (30) $_{WIE\ DOE}$ catalysts were also obtained, quantifying the amount of NO and NO_2 adsorbed at 30 °C and desorbed during He TPD up to 500 °C. Although the amount of NO adsorbed/desorbed in Figure 6.3 and 6.4 is similar for the most active WIE catalyst (Cu^{II}/ZSM-5 (30) $_{WIE\ DOE\ 4}$) and standard catalysts (Cu^{II}/ZSM-5 (30) $_{WIE\ DOE\ 5}$), major differences (up to 1 mg NO/g) are found for reversible NO adsorption over the other catalysts. Besides, an important amount of the total NO_x is desorbed as NO_2, 42 % and 28 %

for Cu^{II}/ZSM-5 (30) $_{WIE\ DOE\ 4}$ and Cu^{II}/ZSM-5 (30) $_{WIE\ DOE\ 8}$ respectively. Despite variations, Cu^{II}/ZSM-5 (30) $_{WIE\ DOE\ 4}$ desorbs more than double the amount of NO$_x$ when compared with the standard catalyst presented in Chapter 5 (Cu^{II}/ZSM-5 (30) $_{WIE\ DOE\ 5}$).
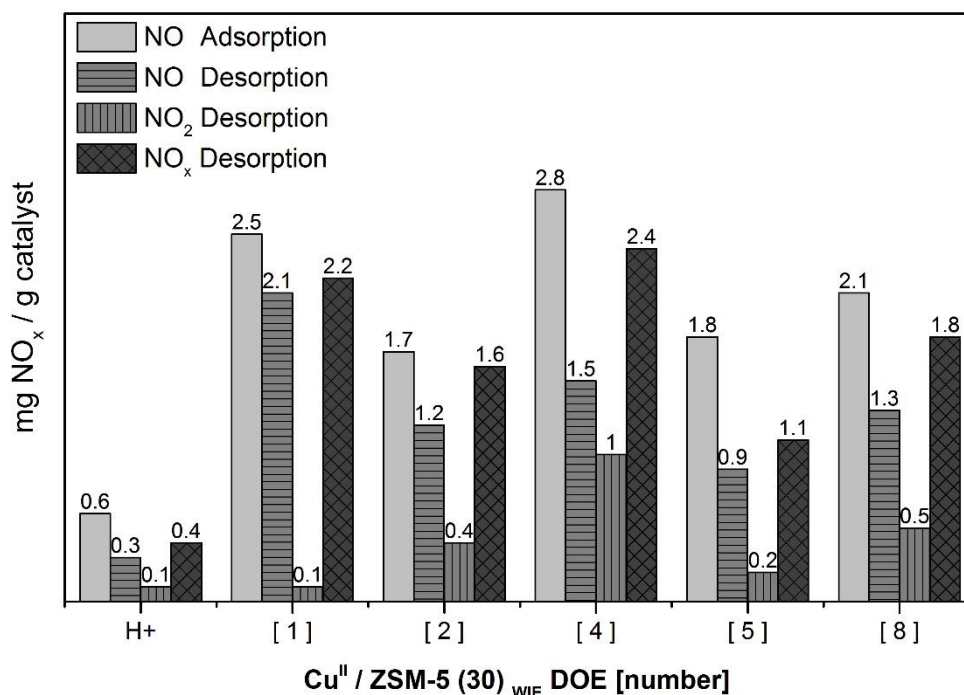

Figure 6.2. NO$_x$ storage capacities of Cu^{II}/ZSM-5 (30) $_{WIE\ DOE\ [No.]}$ catalysts

NO adsorption at 30 °C and TPD with He up to 500 °C

Reaction conditions: Flow reactor, GHSV = 35,000 h^{-1}, 0.1 % NO in He / He

Catalysts prepared by WIE DOE and calcined at 550 °C for 3 h in static air

Reusability of the most active WIE catalyst, Cu^{II}/ZSM-5 (30) $_{WIE\ DOE\ 4}$, was investigated by performing three consecutive NO adsorption-desorption experiments over the same catalyst bed. Results in Figure 6.3 show no catalyst deactivation upon reuse and variations in the amount of NO adsorbed and desorbed are within the experimental error (0.3 mg NO$_x$ /g $_{catalyst}$).

As explained in Chapter 5, O$_2$ is necessary to obtain high temperature desorption because NO$_2$ is more strongly adsorbed than NO. Thus, the storage capacity of selected Cu^{II}/ZSM-5 (30) $_{WIE\ DOE}$ catalysts was also evaluated in the presence of O$_2$.
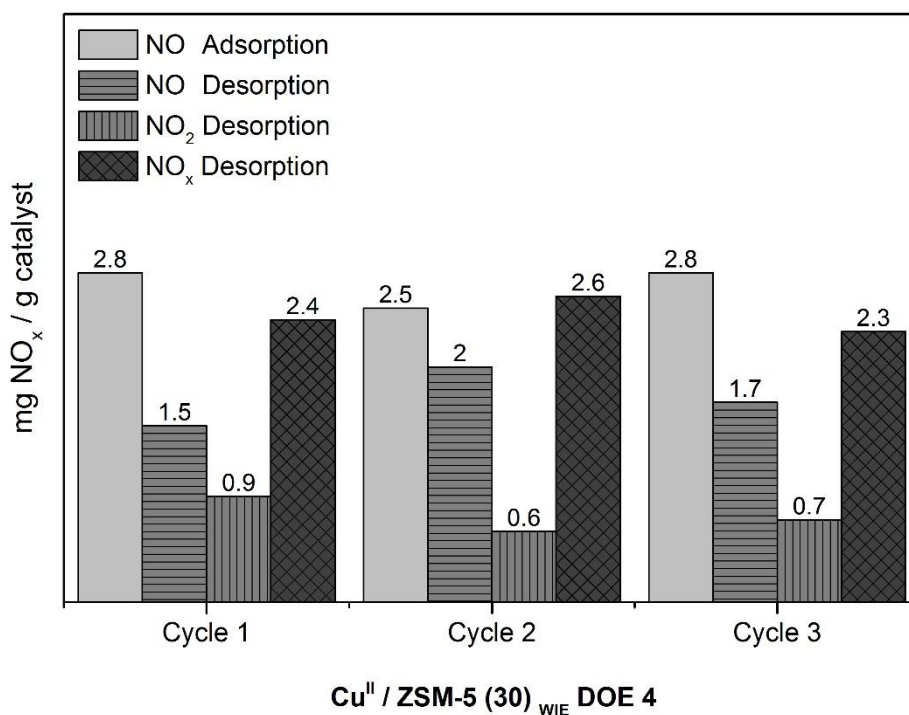
Figure 6.3. Reusability of Cu^{II}/ZSM-5 (30) $_{WIE\ DOE\ 4}$ for NO$_x$ storage

NO adsorption at 30 °C and TPD with He up to 500 °C

Reaction conditions: Flow reactor, GHSV = 35,000 h^{-1}, 0.1 % NO in He / He

Catalysts prepared by WIE DOE and calcined at 550 °C for 3 h in static air

Figure 6.4 shows the amount of NO$_x$ desorbed after NO adsorption in the presence of O$_2$ over; unmodified H$^+$-ZSM-5 (30), the most active WIE catalyst, Cu^{II}/ZSM-5 (30) $_{WIE\ DOE\ 4}$, the catalyst prepared using standard experimental conditions, Cu^{II}/ZSM-5 (30) $_{WIE\ DOE\ 5}$ and the Cu^{II}/ZSM-5 (30) $_{WIE\ DOE\ 1}$ catalyst.

Cu^{II}/ZSM-5 (30) $_{WIE\ DOE\ 4}$, also exhibits the highest NO$_x$ desorption, 8.5 mg NO$_x$/g. This is almost double that of the standard catalyst and is 2.5 times that of unmodified H$^+$-ZSM-5 (30).
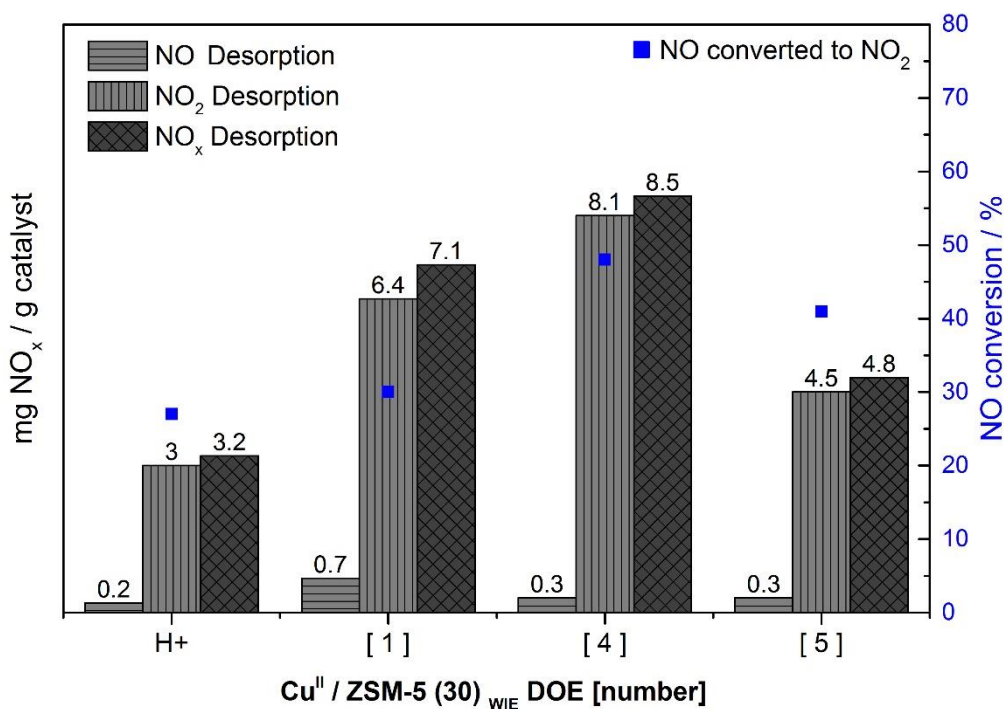

Figure 6.4. NO$_x$ storage capacity of Cu^{II}/ZSM-5 (30) $_{WIE\ DOE}$ catalysts

NO$_x$ adsorption at 30 °C (NO:O$_2$ = 1:75) and TPD with He up to 500 °C

Reaction conditions: Flow reactor, GHSV = 35,000 h^{-1}, 0.1 % NO + 7.5 % O$_2$ in He / He

Catalysts prepared by WIE DOE and calcined at 550 °C for 3 h in static air

The distribution of NO$_x$ species desorbed at different temperatures is shown in Figure 6.5. The amount of NO$_x$ desorbed at high temperature (T > 200 °C) for Cu^{II}/ZSM-5 (30) $_{WIE\ DOE}$ $_4$ is double that of the Cu^{II}/ZSM-5 (30) $_{WIE}$ catalyst prepared using standard experimental conditions, DOE [5]. Thus, Cu^{II}/ZSM-5 (30) $_{WIE\ DOE\ 4}$ shows not only the highest activity for NO adsorption in the absence of O$_2$, but also a superior degree of NO$_x$ desorption above 200 °C after NO$_x$ adsorption in the presence of O$_2$. High concentration of physisorbed NO$_2$,

desorbed at 30 °C, and thermally stable nitrate species, desorbed at high temperature, are
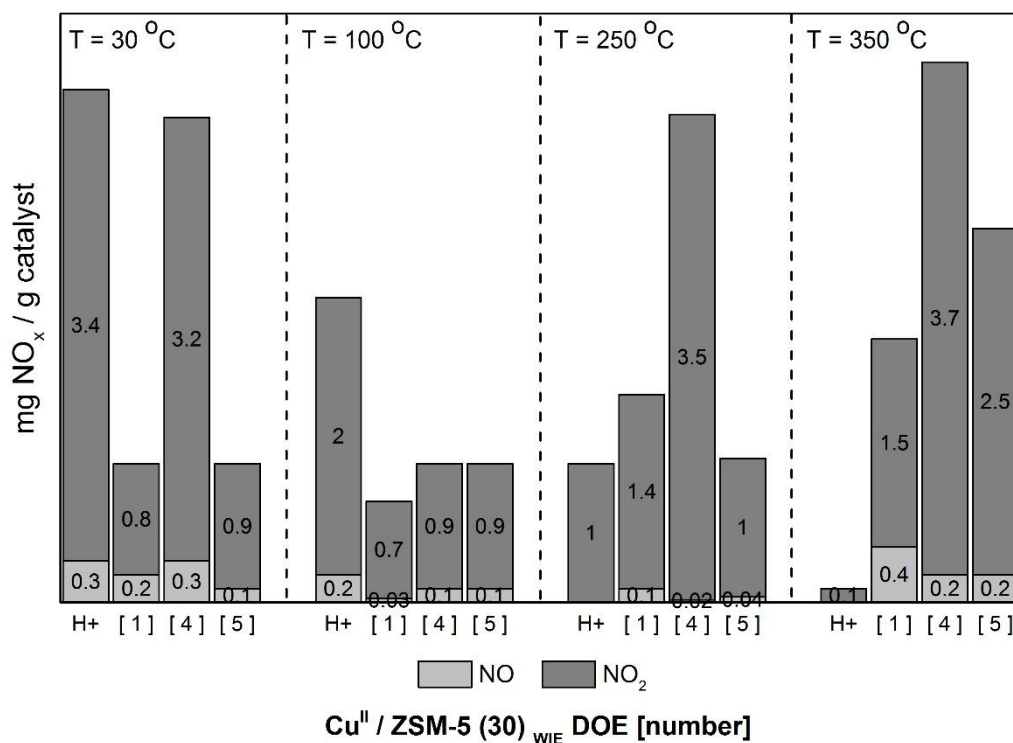
formed on Cu^{II}/ZSM-5 (30) WIE DOE 4.

Figure 6.5. Total amount of NO_x desorbed during the TPD carried out after NO_x adsorption (0.1 %

NO, 7.5 % O_2, He) on Cu^{II}/ZSM-5 (30) WIE DOE catalysts at each desorption temperature

In order to correlate the physicochemical properties of the Cu^{II}/ZSM-5 (30) WIE catalysts

with their NO_x storage performance, characterisation of the most active WIE catalyst,

Cu^{II}/ZSM-5 (30) WIE DOE 4, was performed and results were compared with that of

unmodified H^+ZSM-5 (30) and the standard catalyst, Cu^{II}/ZSM-5 (30) WIE DOE 5.

As shown in Table 6.3, incorporation of Cu_xO_y species on H^+ZSM-5 (30) decreases the

total BET surface area. The decrease in surface area is greater in the case of Cu^{II}/ZSM-5

(30) WIE DOE 4, 25 % vs. the 4 % decrease obtained for the standard Cu^{II}/ZSM-5(30)WIE DOE 5

catalyst prepared before the statistical approach was applied. The total pore volume of

H$^+$-ZSM-5 (30) also decreases after Cu exchange. In this case, the decrease in total pore volume is more significant for the standard catalyst.

Table 6.3. Physicochemical properties of Cu^{II}/ZSM-5 (30) $_{WIE}$ catalysts

	Surface area $_{BET}$ [a]	Pore volume [a]	Acidity [b]			H$_2$ Consumption[c]
			Total	250 °C	450 °C	
	m^2/g	mL/g	μmol NH$_3$/g			μmol H$_2$/g
H$^+$-ZSM-5 (30)	412	0.383	1299	260	350	181
Cu^{II}/ZSM-5 (30) $_{WIE}$	394	0.282	1439	707	100	192
Cu^{II}/ZSM-5 (30) $_{WIE\ DOE\ 4}$	311	0.331	1993	784	249	898

[a] Surface area and pore volume measured by N$_2$ physisorption, [b] acidity measured by NH$_3$-TPD and [c] hydrogen consumption obtained from the H$_2$-TPR profiles

The pore volume distribution is described in Table 6.4. Loss of micro-, meso- and macro-porous volume indicates that incorporation of copper oxide particles leads to blockage of the zeolite channels and pores. The microporous and mesoporous volumes are reduced by 23 % and 19 % for the Cu^{II}/ZSM-5 (30) $_{WIE}$ catalyst prepared using standard conditions (Cu^{II}/ZSM-5 (30) $_{WIE\ DOE\ 5}$); and by 24 % and 11% for the most active WIE catalyst (Cu^{II}/ZSM-5 (30) $_{WIE\ DOE\ 4}$).

Table 6.4. Pore volume distribution of Cu^{II}/ZSM-5 (30) $_{WIE}$ catalysts

	Pore volume/mL·g^{-1}			
	Total	Microporous (< 2 nm)	Mesoporous (2 nm – 50 nm)	Macroporous (> 50 nm)
H$^+$-ZSM-5 (30)	0.383	0.142	0.209	0.033
Cu^{II}/ZSM-5 (30) $_{WIE}$	0.282	0.110	0.169	0.003
Cu^{II}/ZSM-5 (30) $_{WIE\ DOE\ 4}$	0.331	0.108	0.186	0.037

Changes in the acidity of the zeolite catalysts were probed by NH$_3$-TPD and profiles are shown in Figure 6.6. As explained in Chapter 5, the NH$_3$ desorption peak at 250 °C is attributed to weak Brønsted and Lewis sites and that at 450 °C is assigned to strong Brønsted acid sites. Results obtained from quantification of the concentration of acid sites are listed in Table 6.3. The loading of Cu onto H$^+$-ZSM-5 (30) reduces the strong Brønsted acid site density. In addition, the peak appearing at 325 °C suggests that Cu exchange generates new, medium strength acid sites. As reported before, this is attributed to desorption of NH$_3$ from Cu(NH$_3$)$_2$$^{2+}$ complexes [10] and is more pronounced for the most active WIE catalyst, Cu^{II}/ZSM-5 (30) $_{WIE\ DOE\ 4}$. It should be noted that the optimised catalyst presents a characteristic sharp desorption peak at 425 °C, indicating the presence of a high population of strong acid sites.
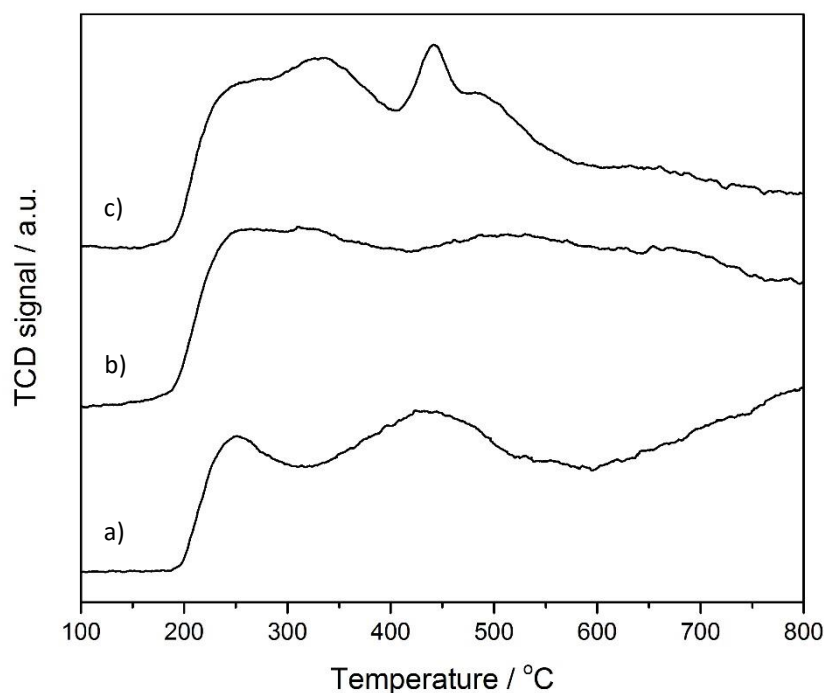

Figure 6.6. NH$_3$-TPD profiles of Cu^{II}/ZSM-5 (30) $_{WIE}$ catalysts:

a) H$^+$-ZSM-5 (30)   b) Cu^{II}/ZSM-5 (30) $_{WIE}$ c) Cu^{II}/ZSM-5 (30) $_{WIE\ DOE\ 4}$

These results are in agreement with those presented in previous publications [11]. Zeolites exchanged with divalent cations show a clear decrease in Brønsted acidity and an increase in Lewis acidity.

Due to the influence of the metal species' redox properties on storage performance, reducibility was investigated via H_2-TPR. H_2 uptake profiles of selected Cu^{II}/ZSM-5 (30) $_{WIE}$ catalysts are presented in Figure 6.7.
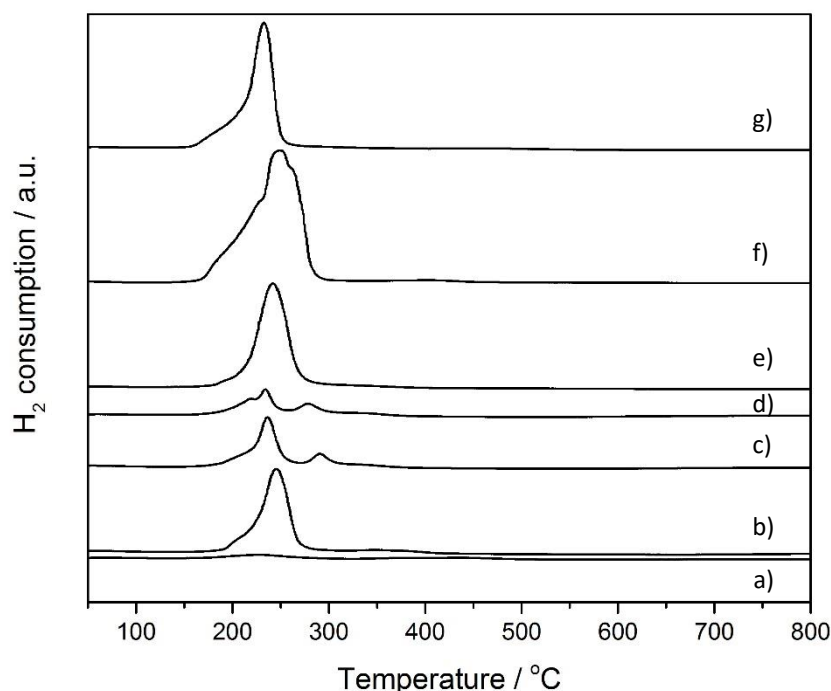
Figure 6.7. H_2-TPR profiles of Cu^{II}/ZSM-5 (30) $_{WIE}$ catalysts:

a) Cu^{II}/ZSM-5 (30) $_{WIE}$ b) Cu^{II}/ZSM-5 (30) $_{WIE\ DOE\ 1}$ c) Cu^{II}/ZSM-5 (30) $_{WIE\ DOE\ 4}$

d) Cu^{II}/ZSM-5 (30) $_{WIE\ DOE\ 8}$ e) Cu^{II}/ZSM-5 (30) $_{WIE\ DOE\ 11}$ f) Cu^{II}/ZSM-5 (30) $_{WIE\ DOE\ 14}$

g) Cu^{II}/ZSM-5 (30) $_{WIE\ DOE\ 16}$

As previously shown in Figure 5.7, Cu^{II}/ZSM-5 (30) $_{WIE}$ presents two reduction events. The first reduction peak at 225 °C is attributed to reduction of Cu^{2+} to Cu$^+$ located at cation

exchange sites and reduction of supported CuO species. The second reduction broad peak

centred at 400 °C corresponds to reduction of Cu$^+$ to Cu^0. Although the TPR profile of the

same Cu^{II}/ZSM-5 (30) $_{WIE}$ catalyst, presented in Figure 6.9 a), shows the same reduction

events, it appears as almost a flat line. This is due to relatively low H$_2$ uptake when

compared with the other catalysts in the same figure. As presented in Table 6.3, while

Cu^{II}/ZSM-5 (30) $_{WIE}$ consumes 192 µmol of H$_2$ per g catalyst, Cu^{II}/ZSM-5 (30) $_{WIE\ DOE\ 4}$

consumes 898 µmol of H$_2$ per g catalyst. The superior H$_2$ uptake exhibited for those

Cu^{II}/ZSM-5 (30) $_{WIE}$ catalysts prepared following the statistical approach, indicate higher

concentrations of reducible Cu$_x$O$_y$ species and hence, higher Cu loadings. However,

elemental analysis is required to determine the actual metal loading and degree of exchange.

The H$_2$-TPR profiles of those catalysts with superior storage performance are shown in

Figure 6.7 c), Cu^{II}/ZSM-5 (30) $_{WIE\ DOE\ 4}$ and Figure 6.9 d), Cu^{II}/ZSM-5 (30) $_{WIE\ DOE\ 8}$. They

present a similar reduction profile comprising of a first reduction peak at 240 °C with a

shoulder at 220 °C and a second reduction peak at 300 °C with a shoulder at 350 °C. The

small peak at 220 °C is assigned to CuO species, the peak at 240 °C corresponds to cationic

oligomers such as [Cu-O-Cu]$^{2+}$ and [Cu$^+$-Cu$^+$] at cation exchange sites [12] and the reduction

at 350 °C is consistent with reduction of bulk CuO. Reducibility of Cu^{II}/ZSM-5 (30) $_{WIE}$

catalysts prepared at higher pH is illustrated in Figure 6.7 e), f) and g), these H$_2$-TPR

profiles are characteristic of over-exchanged Cu/ZSM-5 catalysts with two types of zeolite

–Cu interactions. Schreier and co-workers [9] suggested that metal cations interact with

zeolites by two mechanisms: i) ion exchange at the Al exchange sites and ii) electrostatic

adsorption at silanol groups. Whilst the first is the dominant mechanism at low to mid pH,

the second dominates at high pH. The latter is more clearly manifested in zeolites with low

aluminium content such as ZSM-5, where electrostatic adsorption at high pH gives rise to

over-exchanged of metal cations.

Based on these results, it can be concluded that the distribution and speciation of Cu sites on ZSM-5 (30) is affected by the experimental conditions used during WIE. Hence, the Cu^{2+}/Cu^{+} ratio and bonding strength of the metal ions to the framework affect the reducibility of Cu$_x$O$_y$ species and consequently the NO$_x$ storage capacity. Hadjiivanov *et al.* [13] showed that NO is selectively adsorbed at Cu^{2+} cations because, whereas NO forms a strong bond with Cu^{2+}, the bond with Cu^{+} is weak.

To study the oxidation state of the surface Cu species, XPS was performed. The XPS spectra of the Cu^{II}/ZSM-5 (30) $_{WIE}$ catalysts prepared using standard conditions, Cu^{II}/ZSM-5 (30) $_{WIE\ DOE\ 5}$, and optimised the most active WIE catalyst, Cu^{II}/ZSM-5 (30) $_{WIE\ DOE\ 4}$, are presented in Figure 6.8.
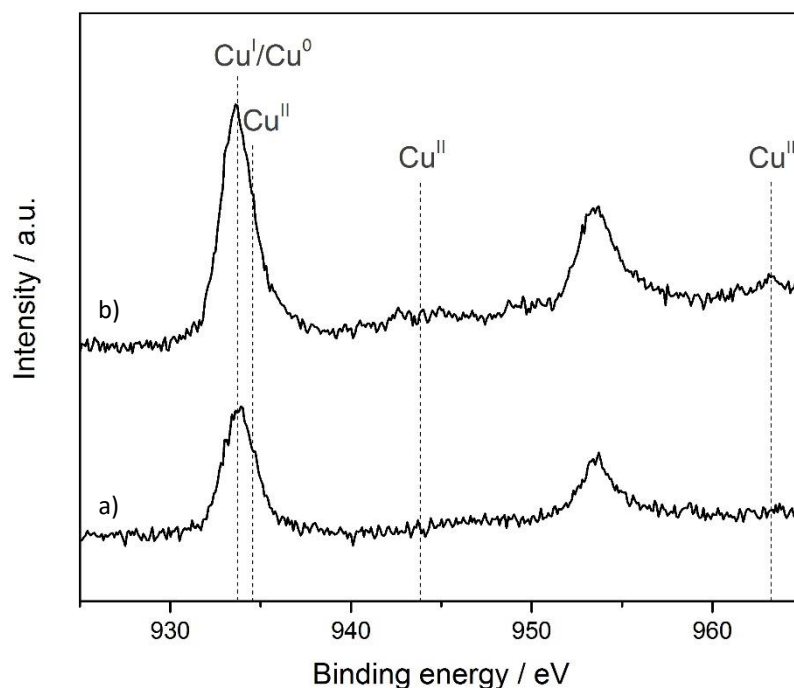

Figure 6.8. XPS spectra in the Cu 2p binding energy region of

a) Cu^{II}/ZSM-5 (30) $_{WIE}$ b) Cu^{II}/ZSM-5 (30) $_{WIE\ DOE\ 4}$

The spectra show two prominent peaks at 933.5 and 953.5 eV which are assigned to Cu 2p$_{3/2}$ and Cu 2p$_{1/2}$ respectively [14] [15]. These peaks are attributed to reduced Cu species (Cu$^+$/Cu^0). A minor Cu^{2+} contribution is also observed as a weak shoulder at 934.5 eV and 954.5 eV, comparable with the values of bulk CuO (934 and 954 eV) [16]. As proposed in previous publications [17] [18] [19] [20], the presence of shake-up features at *ca.* 10 eV above the Cu 2p$_{3/2}$ and Cu 2p$_{1/2}$ signals is evidence of an open 3d^9 shell corresponding to Cu^{2+}. Hence, those peaks shown in Figure 6.8 b) at *ca.* 943 and 953 eV confirm the presence of surface CuO species on Cu^{II}/ZSM-5 (30) $_{\text{WIE DOE 4}}$.

Surface compositions calculated by quantitative analysis of the XPS spectra are shown in Table 6.5. An increase in the surface concentration of aluminium following incorporation of copper, suggests migration of framework Al^{3+} to extra framework sites. The Cu/Al ratio is equal to 0.07 for Cu^{II}/ZSM-5 (30) $_{\text{WIE}}$ and 0.12 for Cu^{II}/ZSM-5 (30) $_{\text{WIE DOE 4}}$. Thus, although a less concentrated copper salt solution was used during WIE, a higher concentration of surface copper species, 2.76 wt.%, is achieved under the conditions used to prepare the most active WIE catalyst, Cu^{II}/ZSM-5 (30) $_{\text{WIE DOE 4}}$.

Table 6.5. Quantitative analysis of the Cu^{II}/ZSM-5 (30) $_{\text{WIE}}$ catalysts obtained from XPS spectra

Catalyst	Si		Al		O		Cu	
	At %	Wt. %	At %	Wt. %	At %	Wt. %	At %	Wt. %
H$^+$-ZSM-5 (30)	27.7	39.8	1.4	1.9	71.1	58.2	-	-
Cu^{II}/ZSM-5 (30) $_{\text{WIE}}$	29.4	40.7	5.0	6.7	65.3	51.5	0.36	1.11
Cu^{II}/ZSM-5 (30) $_{\text{WIE DOE 4}}$	28.5	38.9	7.3	9.5	63.5	49.3	0.89	2.76

Representative TEM images for the Cu^{II}/ZSM-5 (30) $_{\text{WIE DOE 4}}$ catalyst are shown in Figure 6.9. Not only small nanoparticles (1.5 – 3 nm) but also large CuO clusters (20-500 nm) are found. Quantitative analysis obtained from TEM, coupled with EDX,

confirms the presence of heterogeneously distributed copper. This accounts for between 4

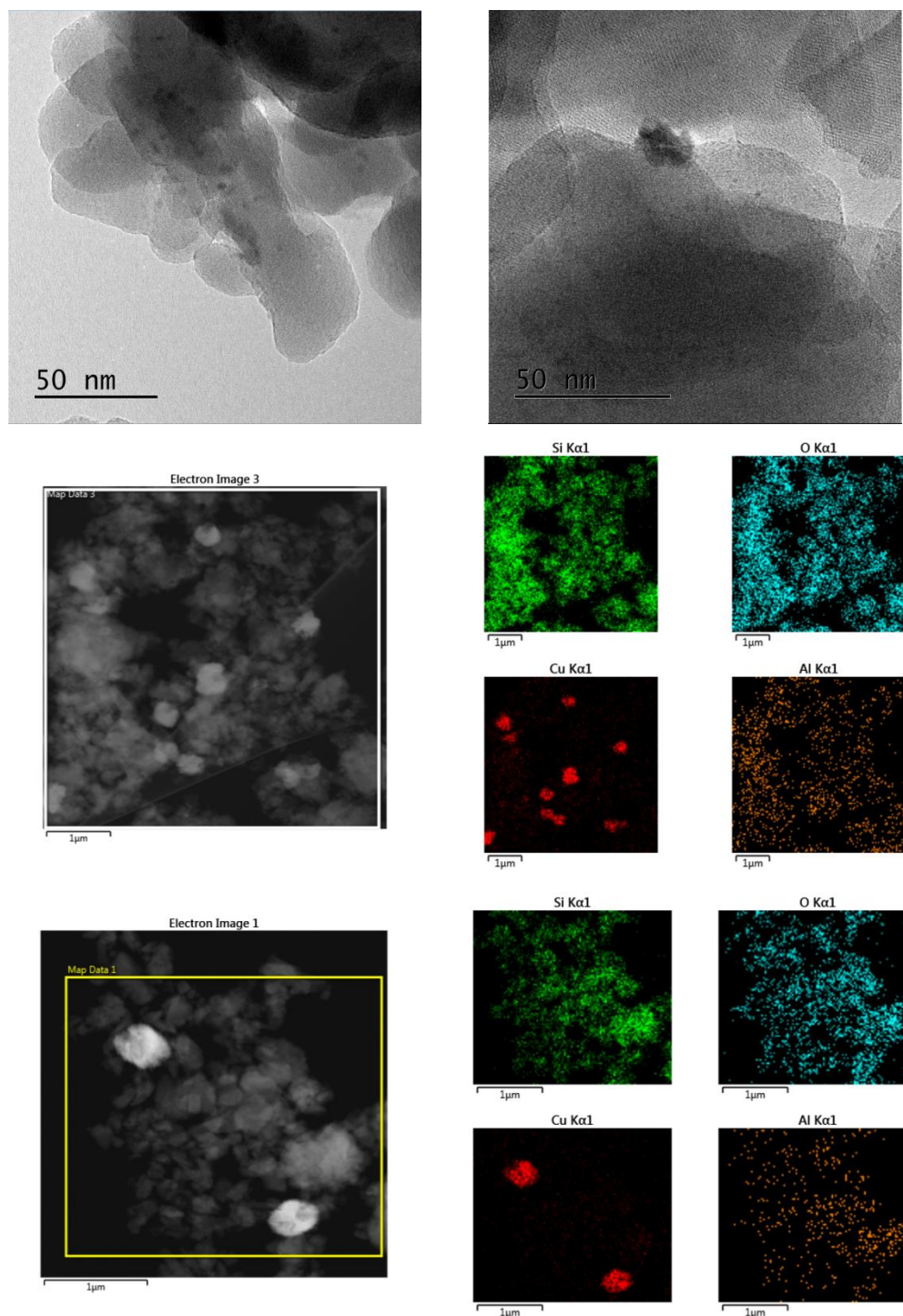and 10 wt. % of the total composition, depending on the region analysed.

Figure 6.9. Selected HRTEM and STEM images for Cu^{II}/ZSM-5 (30) WIE DOE 4

6.2.1 Chemical vapour impregnation

Selecting the correct temperature is crucial when preparing metal exchanged zeolites by CVI. Thus, the temperature should be enough to allow sublimation but not decomposition of the acetylacetonate precursor. Thermogravimetric analysis of the copper (II) acetylacetonate precursor, presented in Figure 6.10, shows that decomposition starts at *ca.* 200 °C.
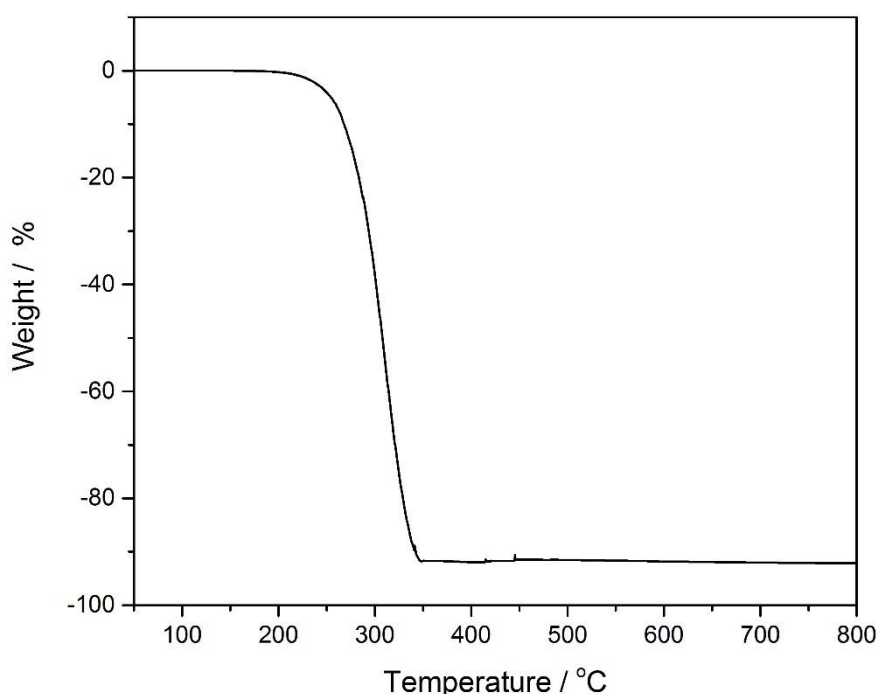
Figure 6.10. TG curve of the copper (II) acetylacetonate precursor in air

The key experimental variables for the CVI preparation technique and their effect on NO$_x$ storage over Cu^{II}/ZSM-5 (30) were screened based on a fractional two-level factorial design 2^3. Copper (II) acetylacetonate was used as the metal precursor. Three variables (copper precursor concentration, impregnation temperature and time) were studied in 8 experiments. Calcination conditions were held constant (550 °C for 3 h in static air). As shown in Table

6.6, each variable was set at two levels, high and low, denoted by (+) and (-) signs respectively.

Table 6.6. Experimental ranges of all five variables in a two-level factorial design to optimise the

Cu^{II}/ZSM-5 (30) catalytic system prepared by CVI

Variable	Low level (-)	High level (+)
Theoretical copper loading	1 wt. %	2.5 wt. %
Impregnation temperature	140 °C	150 °C
Impregnation time	1 h	2 h

Cu^{II}/ZSM-5 (30) catalysts were prepared by CVI based on the DOE matrix presented in Table 6.7.

Table 6.7. Mix proportions of the experimental design for studied variables to optimise the

Cu^{II}/ZSM-5 (30) catalytic system prepared by CVI

No.	Theoretical Cu loading	Impregnation temperature	Impregnation time
[1]	+	-	+
[2]	-	-	-
[3]	+	-	-
[4]	-	+	-
[5]	-	-	+
[6]	+	+	+
[7]	+	+	-
[8]	-	+	+

The NO$_x$ storage capacities of the Cu^{II}/ZSM-5 (30) CVI DOE catalysts were evaluated in the absence of O$_2$. Figure 6.11 shows the amount of NO adsorbed at 30 °C and the amount of NO desorbed during the TPD up to 500 C °C. The amount of NO desorbed at 30 °C, corresponding to reversible adsorption, is excluded from calculations.
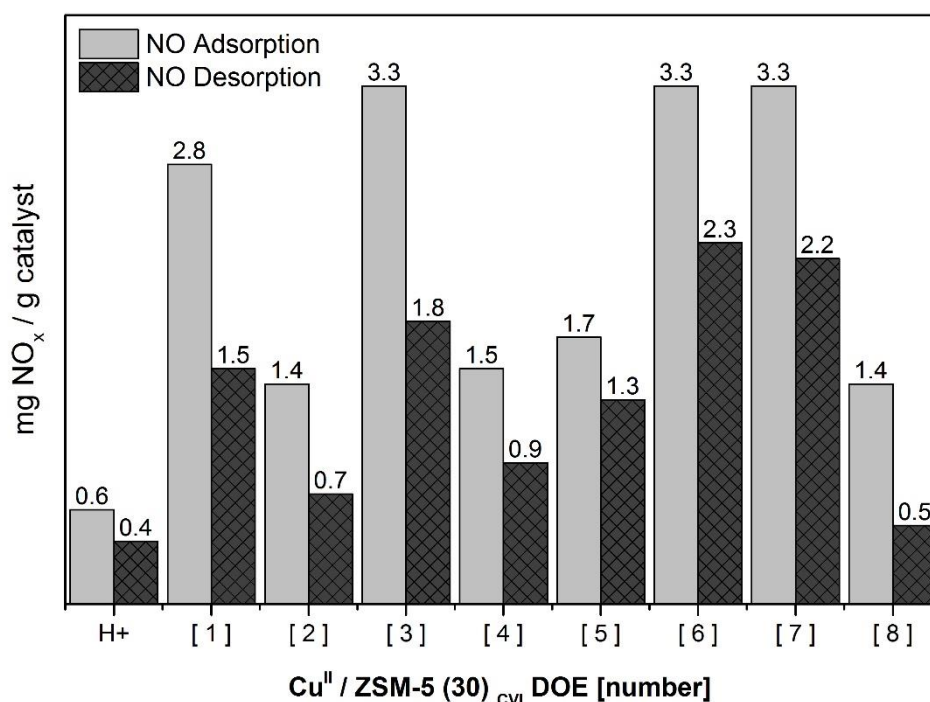
Figure 6.11. NO$_x$ storage capacities of Cu^{II}/ZSM-5 (30) CVI DOE [No.] catalysts

NO adsorption at 30 °C and TPD with He up to 500 °C

Reaction conditions: Flow reactor, GHSV = 35,000 h^{-1}, 0.1 % NO in He / He

Catalysts prepared by CVI DOE and calcined at 550 °C for 3 h in static air

Concordant with results obtained for catalysts prepared by WIE, variation of the different experimental variables affects NO storage capacity when Cu^{II}/ZSM-5 (30) catalysts are prepared by CVI. Not only the total amount of NO adsorbed and desorbed but also the extent of the reversible NO adsorption is affected by CVI experimental conditions. Both, Cu^{II}/ZSM-5 (30) CVI DOE 6 and Cu^{II}/ZSM-5 (30) CVI DOE 7, present the greatest storage performance, with 3.3 and 2.3 mg NO/g adsorbed and desorbed respectively. 30 % of the total amount of NO adsorbed corresponds to reversible adsorption. In this case, Cu^{II}/ZSM-5 (30) CVI DOE 8 represents the catalyst prepared under experimental conditions defined as "standard," used to prepare those catalysts presented in Chapter 5 Figure 5.27,

before the statistical approach was applied. The most active CVI catalyst, Cu^{II}/ZSM-5 (30) CVI DOE 6, shows double the NO adsorption capacity when compared with the standard catalyst, Cu^{II}/ZSM-5 (30) CVI DOE 8.

Results show that for Cu^{II}/ZSM-5 (30) systems prepared by CVI, the 2.5 wt.% catalysts exhibit higher NO adsorption and desorption capacities than 1 wt. % catalysts. Figure 6.12 shows the NO$_x$ storage capacity of the same catalysts expressed as mg of NO$_x$ adsorbed/desorbed per gram of metal loaded. The theoretical metal loading is calculated based on the amount of metal precursor used. When considering the theoretical metal loading, Cu^{II}/ZSM-5 (30) CVI DOE 5 exhibits a higher storage capacity, with NO desorption 2.5 times higher than that obtained for the standard catalyst.
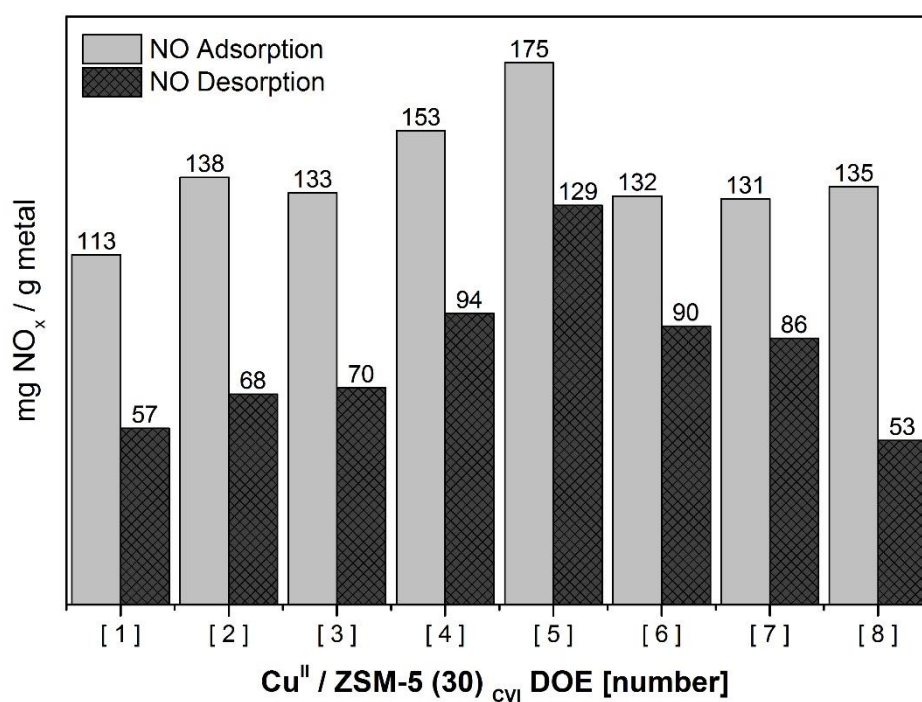

Figure 6.12. NO$_x$ storage capacities of Cu^{II}/ZSM-5 (30) CVI DOE [No.] catalysts expressed as mg NO$_x$/g metal loaded

The impregnation temperature is found to have the greatest effect on the NO$_x$ storage capacity. In addition, the optimum temperature is found to be dependent on the Cu^{II} precursor concentration. Hence, while 150 °C is the optimum sublimation temperature to enhance NO$_x$ storage over 2.5 wt.% Cu^{II}/ZSM-5 (30) $_{CVI}$ catalysts, 1 wt.% Cu^{II}/ZSM-5 (30) $_{CVI}$ catalysts perform better when prepared at 140 °C. Impregnation time is not significant, with equivalent NO$_x$ storage for catalysts where copeprCu is sublimed at the same temperature for 1 or 2 hours.
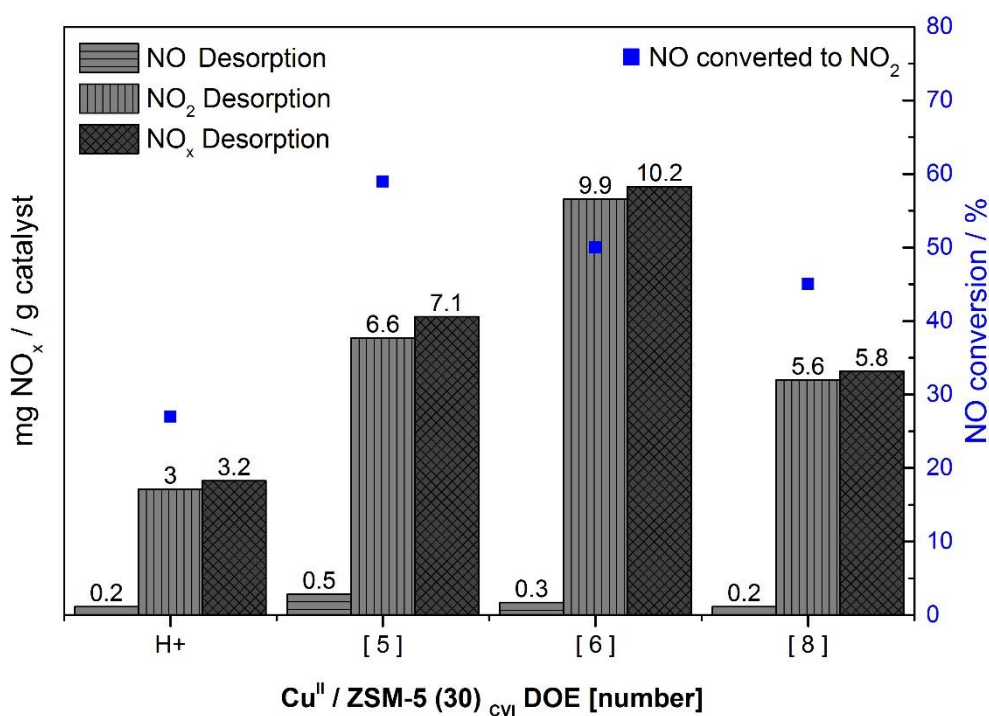
Figure 6.13. NO$_x$ storage capacity of Cu^{II}/ZSM-5 (30) $_{CVI\ DOE}$ catalysts

NO$_x$ adsorption at 30 °C (NO:O$_2$ = 1:75) and TPD with He up to 500 °C

Reaction conditions: Flow reactor, GHSV = 35,000 h^{-1}, 0.1 % NO + 7.5 % O$_2$ in He / He

Catalysts prepared by CVI DOE and calcined at 550 °C for 3 h in static air

The NO$_x$ storage capacity of selected Cu^{II}/ZSM-5 (30) $_{CVI\ DOE}$ catalysts was also evaluated in the presence of O$_2$. Figure 6.13 displays the amount of NO$_x$ desorbed after NO adsorption

in the presence of O$_2$ over unmodified H$^+$- ZSM-5 (30), the catalyst prepared using standard experimental conditions, Cu^{II}/ZSM-5 (30) CVI DOE 8, the most active 1 wt. % Cu catalyst, Cu^{II}/ZSM-5 (30) WIE DOE 5 and the most active 2.5 wt. % Cu catalyst, Cu^{II}/ZSM-5 (30) CVI DOE 6.

Cu^{II}/ZSM-5 (30) CVI DOE 6 exhibits the highest NO$_x$ desorption, 10.2 mg NO$_x$/g, almost double that of the standard catalyst and 3 times la that of unmodified H$^+$-ZSM-5 (30). Optimisation of the CVI sublimation temperature for 1 wt. % Cu catalysts results in a 22 % increase of the amount of NO$_x$ desorbed.
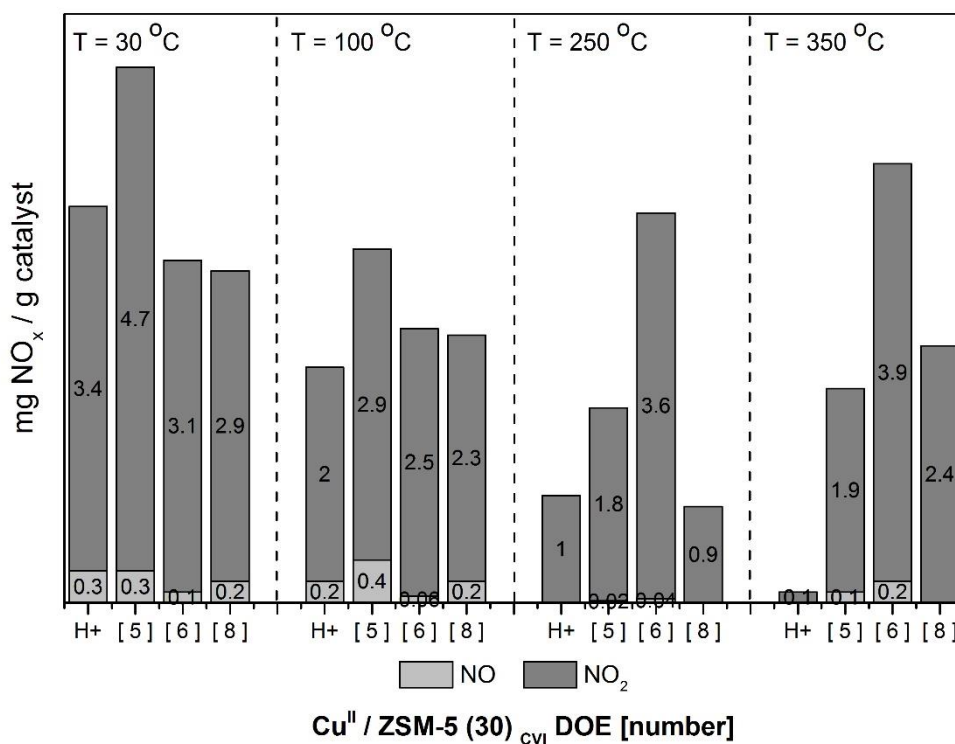

Figure 6.14. Total amount of NO$_x$ desorbed during the TPD carried out after NO$_x$ adsorption (0.1 % NO, 7.5 % O$_2$, He) on Cu^{II}/ZSM-5 (30) CVI DOE catalysts at each desorption temperature

The distribution of NO$_x$ species desorbed at different temperatures is shown in Figure 6.14. The amount of NO$_x$ desorbed at high temperature (T > 200 °C) is 7.7 mg NO$_x$/g for

Cu^{II}/ZSM-5 (30) CVI DOE 6, double than that of the most active 1 wt. % Cu catalyst, Cu^{II}/ZSM-5 (30) CVI DOE 5. While Cu^{II}/ZSM-5 (30) CVI DOE 5 presents a high concentration of physisorbed and weakly chemisorbed NO$_2$, a large amount of thermally stable nitrate species are formed on Cu^{II}/ZSM-5 (30) CVI DOE 6.

Table 6.8. Physicochemical properties of Cu^{II}/ZSM-5 (30) CVI catalysts

	Surface area BET [a]	Pore volume [a]	Acidity [b]			H$_2$ Consumption[c]
			Total	250 °C	450 °C	
	m^2/g	mL/g	μmol NH$_3$/g			μmol H$_2$/g
H$^+$-ZSM-5 (30)	412	0.383	1299	260	350	181
Cu^{II}/ZSM-5 (30) CVI	337	0.319	1290	512	67	152
Cu^{II}/ZSM-5 (30) CVI DOE 6	353	0.281	1081	674	139	316

[a] Surface area and pore volume measured by N$_2$ physisorption, [b] acidity measured by NH$_3$-TPD and [c] hydrogen consumption obtained from the H$_2$-TPR profiles

Characterisation of Cu^{II}/ZSM-5 (30) CVI DOE 6, the catalyst which exhibits the greatest NO$_x$ storage capacity in the absence and presence of O$_2$, was performed. In order to determine the cause of its superior performance, results were compared with that of the unmodified zeolite support and the standard catalyst, Cu^{II}/ZSM-5 (30) CVI.

Table 6.9. Pore volume distribution of Cu^{II}/ZSM-5 (30) CVI catalysts

	Pore volume/mL·g^{-1}			
	Total	Microporous (< 2 nm)	Mesoporous (2 nm – 50 nm)	Macroporous (> 50 nm)
H$^+$-ZSM-5 (30)	0.383	0.142	0.209	0.033
Cu^{II}/ZSM-5 (30) CVI	0.319	0.115	0.178	0.026
Cu^{II}/ZSM-5 (30) CVI DOE 6	0.281	0.125	0.144	0.012

As shown in Table 6.3, incorporation of Cu$_x$O$_y$ species onto H$^+$-ZSM-5 (30) diminishes the total surface area by 18 % for Cu^{II}/ZSM-5 (30) $_{CVI}$ and 14 % for Cu^{II}/ZSM-5 (30) $_{CVI\,DOE\,6}$. The total pore volume of H$^+$-ZSM-5 (30) is also reduced after Cu exchange, decreasing by 26 % for the most active CVI catalyst Cu^{II}/ZSM-5 (30) $_{CVI\,DOE\,6}$.

The pore volume distribution is quantified in Table 6.9. Loss of micro-, meso- and macro-porous volume indicates that incorporation of copper oxide particles leads to blockage of the zeolite channels and pores. Cu^{II}/ZSM-5 (30) $_{CVI\,DOE\,6}$ shows a large decrease in micropore volume (64 %).
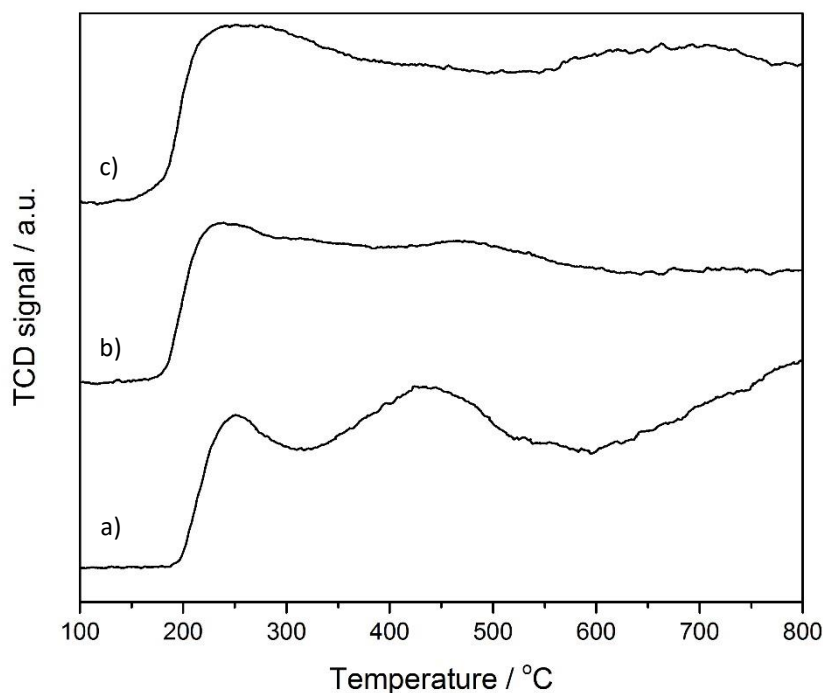

Figure 6.15. NH$_3$-TPD profiles of Cu^{II}/ZSM-5 (30) $_{CVI}$ catalysts:

a) H$^+$-ZSM-5 (30)   b) Cu^{II}/ZSM-5 (30) $_{CVI}$ c) Cu^{II}/ZSM-5 (30) $_{CVI\,DOE\,6}$

NH$_3$-TPD results shown in Figure 6.15 present the characteristic profile of metal exchanged zeolites, with a low temperature desorption peak attributed to weak Brønsted and Lewis sites and a high temperature desorption peak assigned to strong Brønsted acid sites. Results obtained from quantification of the concentration of acid sites are listed in Table 6.8. Loading of Cu onto H$^+$-ZSM-5 (30) lowers the strong Brønsted acid site density. In addition, new strong acid sites are generated on Cu^{II}/ZSM-5 (30) $_{CVI\ DOE\ 6}$, as indicated by the small amount of NH$_3$ desorbed at *ca*. 650 °C.
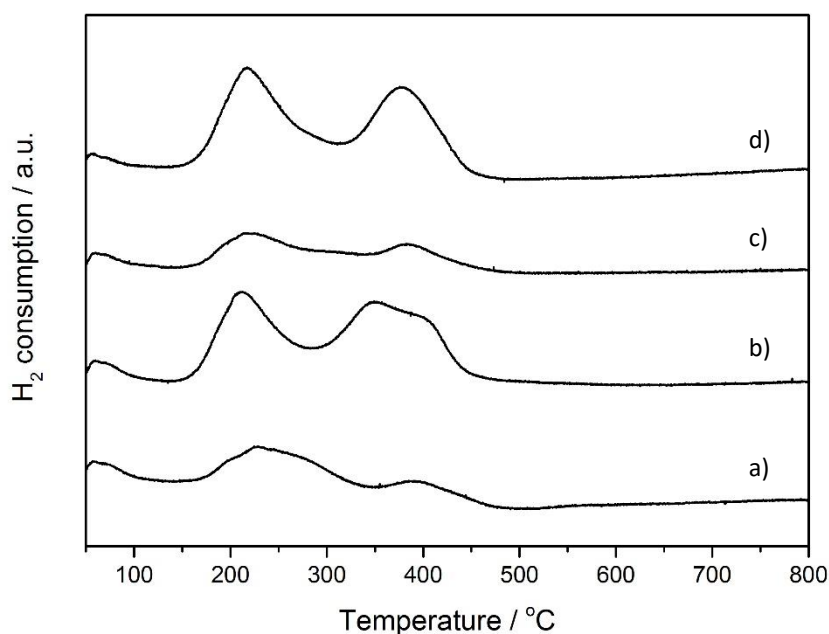
Figure 6.16. H$_2$-TPR profiles of Cu^{II}/ZSM-5 (30) $_{CVI}$ catalysts:

a) Cu^{II}/ZSM-5 (30) $_{CVI}$ b) Cu^{II}/ZSM-5 (30) $_{CVI\ DOE\ 1}$ c) Cu^{II}/ZSM-5 (30) $_{CVI\ DOE\ 5}$

d) Cu^{II}/ZSM-5 (30) $_{CVI\ DOE\ 6}$

H$_2$-TPR profiles shown in Figure 6.16 confirm that the reducibility of Cu species is not affected by the experimental conditions used during CVI. Cu^{II}/ZSM-5 (30) $_{CVI}$ catalysts show similar Cu^{2+}/Cu$^+$ ratios and comparable reduction temperatures. As presented in Table 6.8, while Cu^{II}/ZSM-5 (30) $_{CVI}$ consumes 152 µmol of H$_2$ per g of catalyst,

Cu^{II}/ZSM-5 (30) $_{CVI\,DOE\,6}$ consumes 316 µmol of H$_2$ per g of catalyst. Hence, catalysts with higher theoretical Cu loading (2.5 wt. %), exhibit a larger uptake of H$_2$, attributed to an increase in the concentration of reducible Cu$_x$O$_y$ species.

XPS spectra of the Cu^{II}/ZSM-5 (30) catalysts prepared by CVI are shown in Figure 6.17. As for the spectra of catalysts prepared by WIE, presented in Figure 6.10, the Cu 2p$_{3/2}$ peak appearing at 933.5 eV is attributed to reduced Cu$^+$/Cu^0 species with a minor contribution of Cu^{2+} species. In this case, no shake-up features associated with surface CuO species were observed.

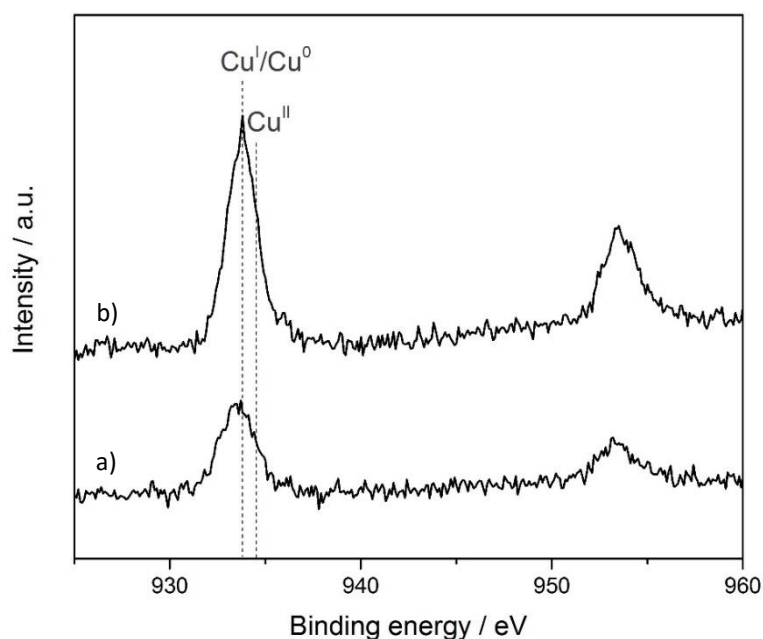**Figure 6.17.** XPS spectra in the Cu 2p binding energy region of

a) Cu^{II}/ZSM-5 (30) $_{CVI}$ b) Cu^{II}/ZSM-5 (30) $_{CVI\,DOE\,6}$

Quantitative analysis obtained from XPS spectra is presented in Table 6.10. Despite different theoretical metal loadings, 1 wt. % Cu^{II}/ZSM-5 (30) $_{CVI}$ and 2.5 wt. % Cu^{II}/ZSM-5 (30) $_{CVI\,DOE\,6}$ show a similar concentration of surface Cu species.

Table 6.10. Quantitative analysis of the Cu^{II}/ZSM-5 (30) $_{CVI}$ catalysts obtained from XPS spectra

Catalyst	Si		Al		O		Cu	
	At %	Wt. %	At %	Wt. %	At %	Wt. %	At %	Wt. %
H$^+$-ZSM-5 (30)	27.7	39.8	1.4	1.9	71.1	58.2	-	-
Cu^{II}/ZSM-5 (30) $_{CVI}$	30.2	41.8	3.8	5.1	65.6	51.7	0.47	1.49
Cu^{II}/ZSM-5 (30) $_{CVI\ DOE\ 6}$	30.1	41.6	4.7	6.2	64.8	51.0	0.39	1.23

Representative TEM images and the particle size distribution for Cu^{II}/ZSM-5 (30) $_{CVI\ DOE\ 6}$ are shown in Figure 6.18. Highly dispersed spherical copper particles with a mean particle size of 2.3 ± 0.7 nm are observed.
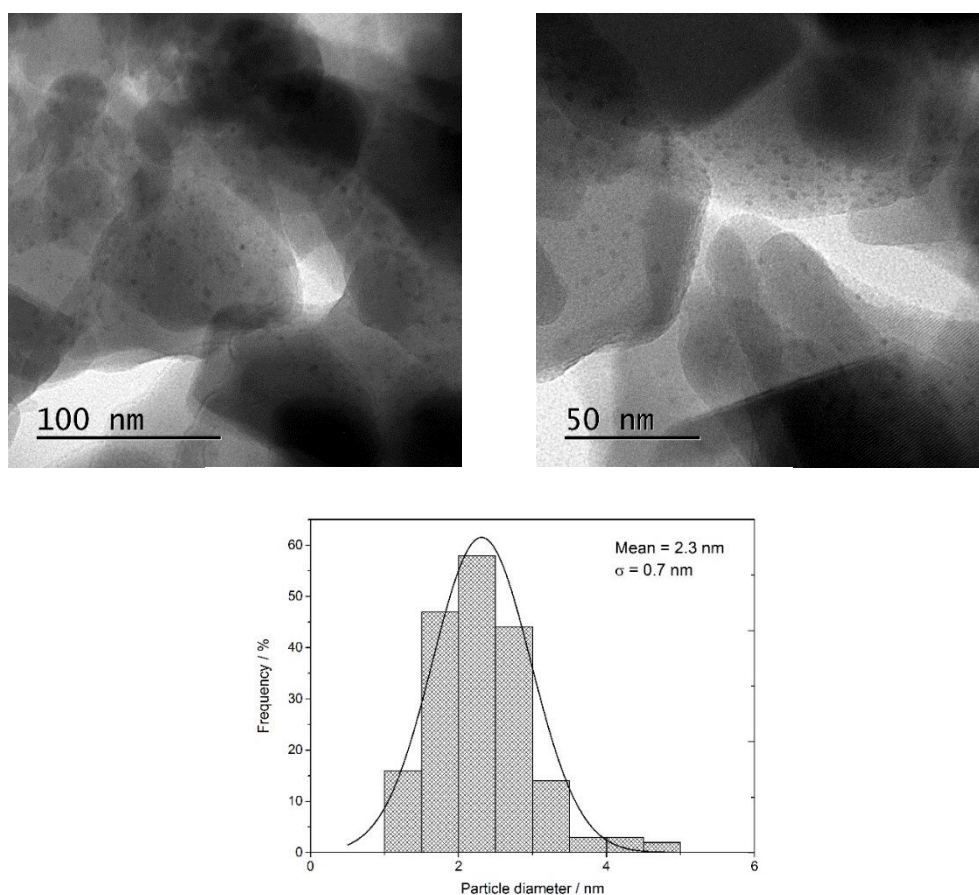

Figure 6.18. Selected HRTEM and STEM images and platinum particle size distribution for Cu^{II}/ZSM-5 (30) $_{CVI\ DOE\ 6}$

6.3 Statistical analysis of NO_x storage on Cu^{II}/ZSM-5 (30)

Results presented in this chapter show the application of the DOE method in order to investigate the effect of catalyst preparation variables on the NO_x storage capacity of Cu^{II}/ZSM-5 (30) catalysts. As mentioned previously, completion of the study requires an associated statistical analysis.

Statistical analysis will be performed using the same Design-Expert® 9 software. The set of data discussed in this chapter generates response values that should be added to the DOE matrix in the software. For NO_x storage experiments in the absence of O_2, two different response factors should be considered: the amount of NO adsorbed and amount of NO desorbed. After completion of NO_x storage experiments in the presence of O_2, the same statistical analysis could be applied using the total amount of NO_x desorbed as the response factor. In this case, using the amount of NO_x desorbed at high temperature (T > 200 °C) as the response factor will provide information which is more relevant for application of the storage catalysts under real conditions. For each response, the minimum change the design should assign as being statistically significant and the estimated standard deviation must be entered as Delta ("Signal") and Sigma ("Noise") respectively. The ratio will be calculated as Delta/Sigma. Power should exceed 80 % to ensure seeing the desired difference. Standard deviation has been estimated to be 0.1 mg NO_x/g catalyst by repeating the same storage experiment up to 3 times over selected catalysts.

After the response data has been entered, the software will apply statistical analysis to establish:

- Quantification of the influence of each experimental variable on the response.

- Identification of important individual factors dominating the NO_x storage capacity.

- Interaction between the different experimental variables studied. Determination of dependent and independent variables and of linear or nonlinear relationships between variables.

- Determination of the regression equation that calculates NO$_x$ storage capacity as a function of the experimental variables studied.

- Representation of a three-dimensional response surface, where the highest point reveals the optimal experimental variable values to maximise the NO$_x$ storage capacity.

- Experimental validation of the statistical model.

An optimum Cu^{II}/ZSM-5 (30) catalyst for NO$_x$ storage will then be prepared using the optimal predicted values for the WIE and CVI experimental variables studied. In order to confirm the effectiveness of the statistical model developed, the NO$_x$ storage capacity obtained experimentally should be comparable within the predicted optimum response value.

6.4 NO_x storage under real working conditions

After application of the statistical approach to optimise Cu^{II}/ZSM-5 (30) prepared by WIE and CVI, several catalysts demonstrate promising performance for NO_x storage. Among them, Cu^{II}/ZSM-5 (30) _WIE DOE 4_ and Cu^{II}/ZSM-5 (30) _CVI DOE 6_ exhibit the highest NO_x storage capacity, with a large amount of NO_x desorbed at high temperature. Hence, they have been selected as potential candidates for application under real working conditions.

The performance of selected Cu^{II}/ZSM-5 (30) catalysts under conditions similar to the composition of diesel exhaust effluent was evaluated. A detailed description of the experimental procedure is given in Chapter 3.3.2.1. In summary, quantitative analysis was carried out by continuously monitoring the effluent gas composition using a FTIR.
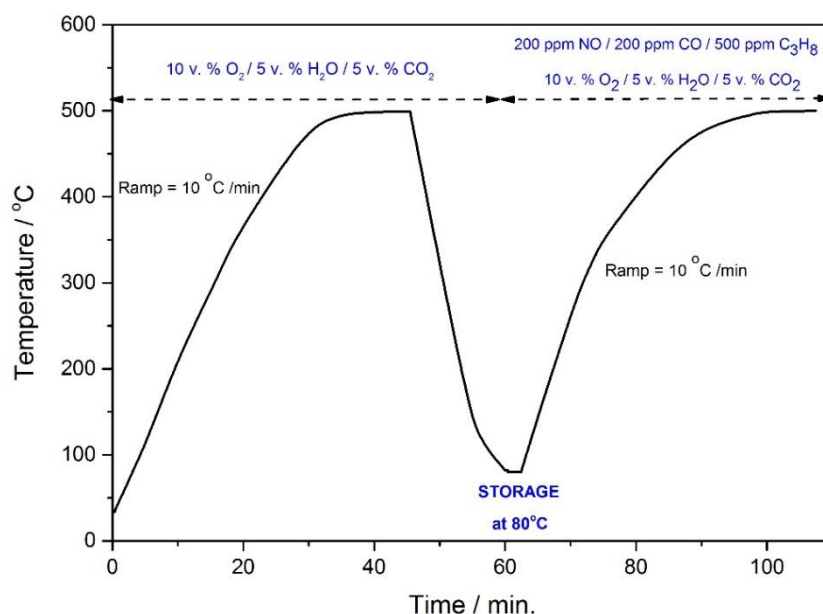

Figure 6.25. Typical temperature profile for reaction under real conditions

Pretreatment up to 500 °C with 10 v. % O_2 + 5 v. % H_2O + 5 v. % CO_2 balanced in N_2

Storage at 80 °C and TPD up to 500 °C with 10 v. % O_2 + 5 v. % H_2O + 5 v. % CO_2 +

200 ppm NO + 200 ppm CO + 500 ppm C_3H_8 balanced in N_2

Figure 6.25 shows the temperature profile and reaction conditions for evaluation of the catalytic activity under realistic conditions.

- - - Temperature in °C (dashed line)   **(---)** H$_2$O v. %   **(---)** CO$_2$ v. %   **(---)** CO ppm

(---) N$_2$O ppm   **(---)** NO ppm   **(---)** NO$_2$ ppm   **(---)** C$_3$H$_8$ ppm

Figure 6.26. Effluent concentration profile over the Cu^{II}/ZSM-5 (30) $_{WIE\ DOE\ 4}$ catalyst

Reaction conditions: Flow reactor, GHSV = 30,000 h^{-1}

Pretreatment up to 500 °C with 10 v. % O$_2$ + 5 v. % H$_2$O + 5 v. % CO$_2$ balanced in N$_2$

Storage at 80 °C and TPD up to 500 °C with 10 v. % O$_2$ + 5 v. % H$_2$O + 5 v. % CO$_2$ +

200 ppm NO + 200 ppm CO + 500 ppm C$_3$H$_8$ balanced in N$_2$

Figures 6.26 and 6.27 show the evolution of the different compounds over Cu^{II}/ZSM-5 (30) catalysts during on-line testing under real conditions. Similar profiles are obtained for the two catalysts evaluated.   The H$_2$O concentration profile shows several adsorption and

desorption peaks. H$_2$O is firstly adsorbed at room temperature and is rapidly desorbed as the temperature starts to increase during the pretreatment. A second H$_2$O adsorption event is observed during cool down at *ca.* 50 min. and is desorbed again as the temperature increases during the TPD. The CO$_2$ concentration remains constant during the experiment. During the storage period at 80 °C (60 – 62 min.), the amount of NO and NO$_2$ adsorbed is negligible and only adsorption of C$_3$H$_8$ occurs. C$_3$H$_8$ is then desorbed during the TPD at 200 °C, at which temperature H$_2$O also desorbs. The CO concentration drops considerably (from 150 ppm to 50 ppm) as the temperature increases, reaching a minimum concentration of 50 ppm at 450 °C. The concentration of C$_3$H$_8$ and NO starts to decrease when the temperature reaches 350 °C. At 500 °C, the concentration of C$_3$H$_8$ is 58 % lower than the feed concentration (from 600 to 250 ppm) and that of NO decreases by33 % (from 300 to 200 ppm).

Consumption of C$_3$H$_8$ via oxidation reactions is not considered because the concentration of H$_2$O and CO$_2$ is not increased and other partial oxidation products, such as C$_3$H$_6$, are not detected. This results suggests that under these conditions, NO is reduced to N$_2$ by C$_3$H$_8$ at temperatures above 350 °C. Thus, NO reduction is favoured over hydrocarbon combustion. Although NO reduction by propane over Cu/ZSM-5 has been reported in previous publications [21][22][23], in order to confirm C$_3$H$_8$-SCR, NO$_x$ conversion should be determined from N$_2$ formation. Hence, the effluent gas concentration must be monitored using a different technique, such as GC-TCD.

Evolution of NO$_2$ over both catalysts is shown in Figure 6.28. A small desorption peak at 325 °C and 350 °C is observed for Cu^{II}/ZSM-5 (30) WIE DOE 4 and Cu^{II}/ZSM-5 (30) CVI DOE 6 respectively. The contribution of NO$_x$ storage is minimal as only 0.1 mg NO$_x$/g catalyst is

desorbed.

--- Temperature in °C (dashed line)   (---) H_2O v. %   (---) CO_2 v. %   (---) CO ppm

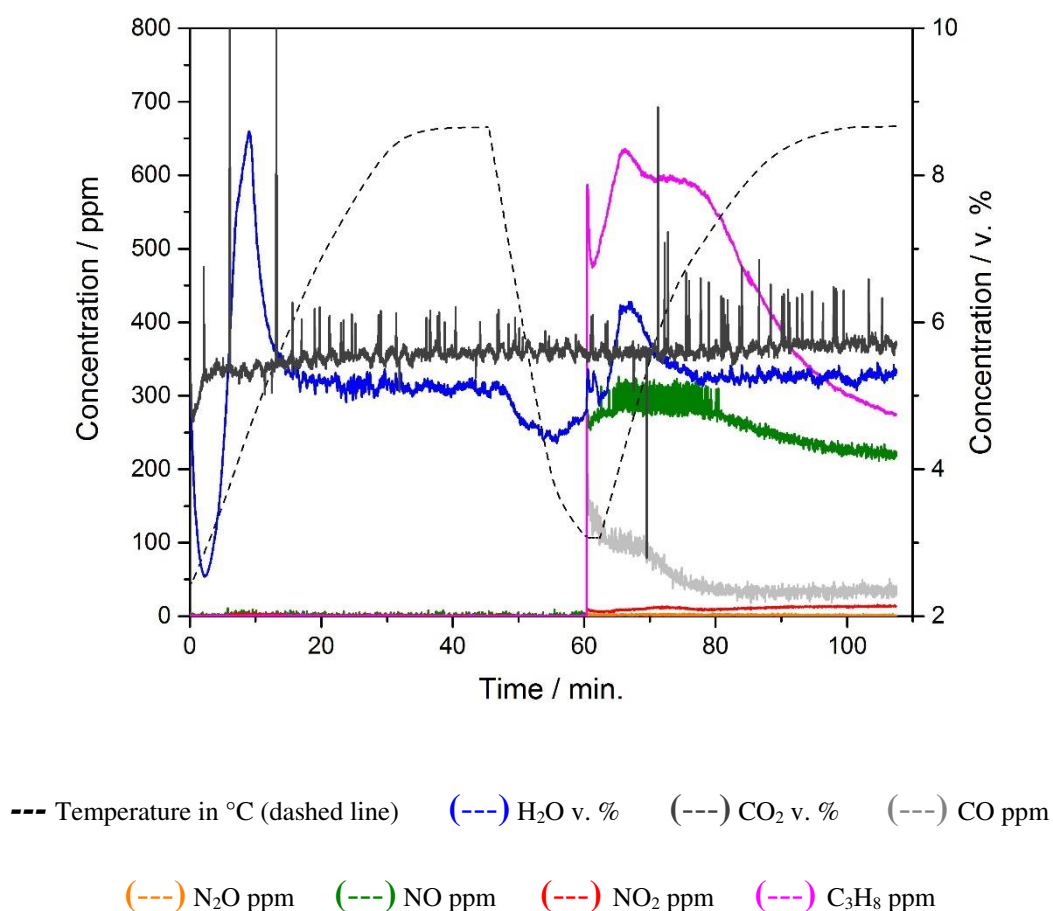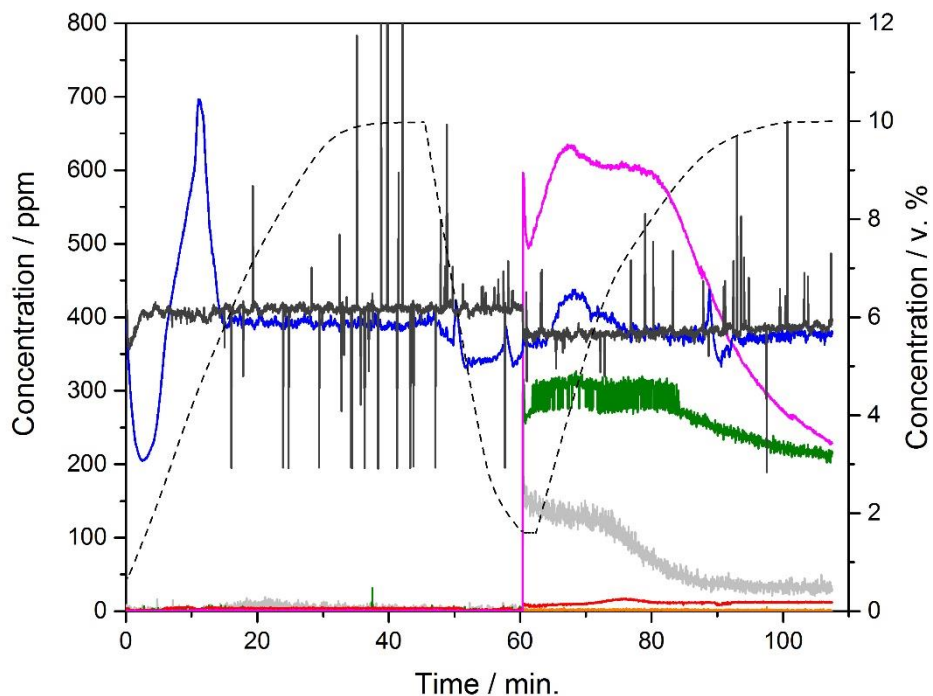(---) N_2O ppm   (---) NO ppm   (---) NO_2 ppm   (---) C_3H_8 ppm

Figure 6.27. Effluent concentration profile over the Cu^II/ZSM-5 (30) CVI DOE 6 catalyst

Reaction conditions: Flow reactor, GHSV = 30,000 h^-1

Pretreatment up to 500 °C with 10 v. % O_2 + 5 v. % H_2O + 5 v. % CO_2 balanced in N_2

Storage at 80 °C and TPD up to 500 °C with 10 v. % O_2 + 5 v. % H_2O + 5 v. % CO_2 +

200 ppm NO + 200 ppm CO + 500 ppm C_3H_8 balanced in N_2

It is widely known that the presence of H_2O decreases the NO_x adsorption capacity and causes deactivation of the catalysts because H_2O competes for the selective adsorption sites and can even blocks the pores [24]. When water vapour is added, surface reactions convert

the Cu adsorption sites into Cu(OH)$_2$, resulting in a decrease in the storage capacity Cu/ZSM-5 (30) catalysts. The presence of NO in the feed gas can also have a negative effect on the NO$_x$ storage capacity. The interaction of NO with the stored nitrates shifts the equilibrium back to NO$_2$ and desorption of nitrates occurs at lower temperatures (150 °C instead of 300-400 °C).

In this study, the main storage contribution over the Cu/ZSM-5 (30) catalysts is the adsorption of C$_3$H$_8$ at 80 °C. High hydrocarbon adsorption capacity over metal exchanged zeolites has been reported before, where a large desorption of C$_3$H$_6$ during TPD experiments was attributed to intrinsic adsorption on the zeolite support. It is believed that the HC molecules stored in the zeolite support are unlikely to be involved in the NO reduction mechanism [25].
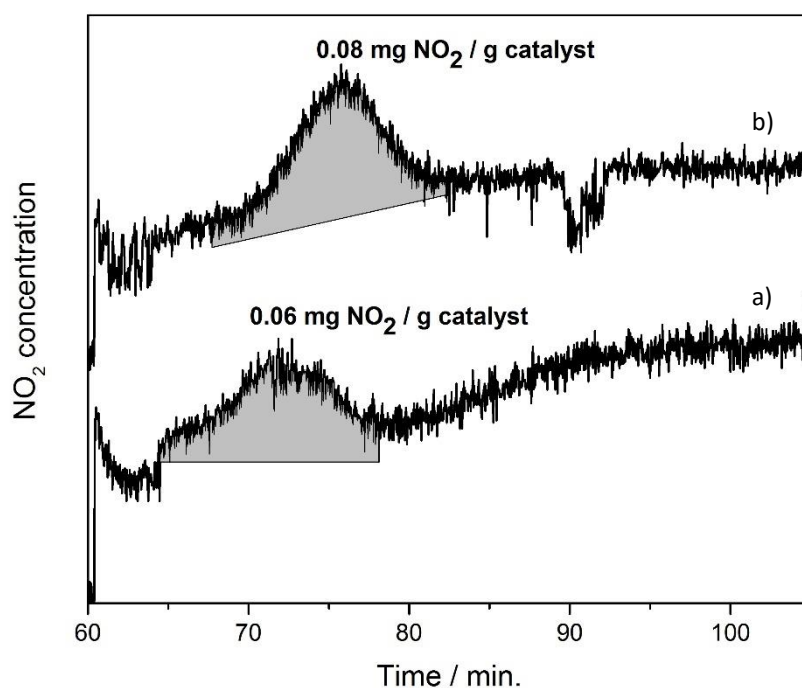

Figure 6.28. Evolution of NO$_2$ during storage and TPD under real conditions

a) Cu^{II}/ZSM-5 (30) $_{WIE\ DOE\ 4}$ b) Cu^{II}/ZSM-5 (30) $_{CVI\ DOE\ 6}$

6.5 Conclusions

This study adopts the statistical design of experiments (DOE) method to investigate the experimental variables which affect the NO$_x$ storage capacity of Cu^{II}/ZSM-5 (30) prepared by WIE and CVI.

Temperature is found to have the greatest effect on the NO$_x$ storage capacity. In addition, its influence is dependent on the copper precursor concentration. Increasing the solution temperature for WIE correlates with an increase in NO$_x$ storage where a low copper precursor concentration is used. An increase in the CVI impregnation temperature also correlates with an increase in NO$_x$ storage, however only at a high loading of Cu.

The data set generated and the relative influence of the experimental variables studied is required for subsequent optimisation via statistical analysis.

The optimal values of the studied experimental variables that maximise NO$_x$ storage over Cu^{II}/ZSM-5 (30) prepared by WIE are: 0.025 M (Cu precursor concentration), 90 °C (solution temperature) and 5.5 (solution pH). The solution contact time is not significant. The most active WIE catalyst, Cu^{II}/ZSM-5 (30) $_{WIE\ DOE\ 4}$, exhibits a NO$_x$ storage capacity which is higher than that of the catalyst prepared using standard conditions. The amount of NO$_x$ desorbed is 1.4 and 8.5 mg NO$_x$/g after NO adsorption in the absence and presence of O$_2$ respectively. Additionally, reusability studies show no deactivation of the catalyst over consecutive adsorption-desorption experiments.

The values of the experimental variables studied which affect optimal NO$_x$ storage over Cu^{II}/ZSM-5 (30) prepared by CVI are: 2.5 wt. % (theoretical Cu loading) and 150 °C (impregnation temperature). The impregnation time is not significant. The most active CVI

catalyst, Cu^{II}/ZSM-5 (30) $_{CVI\ DOE\ 6}$, exhibits a superior NO$_x$ storage capacity to that of the catalyst prepared using standard conditions. The amount of NO$_x$ desorbed is 2.3 and 10.2 mg NO$_x$/g after NO adsorption in the absence and presence of O$_2$ respectively.

While the total amount of NO$_x$ desorbed is greater for the most active catalyst prepared by CVI than that prepared by WIE, the amount of NO$_x$ desorbed at high temperature (T > 200 °C) is comparable for both catalysts, approximately 7.5 mg NO$_x$/g.

In order to find correlations between the physicochemical properties and the NO$_x$ storage capacity of the most active catalysts, Cu^{II}/ZSM-5 (30) $_{WIE\ DOE\ 4}$ and Cu^{II}/ZSM-5 (30) $_{CVI\ DOE\ 6}$, characterisation using different analytical techniques was performed.

Experimental conditions used during WIE affect the distribution and speciation of the Cu sites on the ZSM-5 (30) support as shown by H$_2$-TPR, NH$_3$-TPD and XPS. On the other hand, characterisation of the standard and most active CVI catalysts show no apparent difference in Cu speciation, despite the difference in theoretical Cu loading.

Whilst initial characterisation studies have been performed, further investigation is required for better understanding of the nature of these catalysts.

Catalytic activity of the most active Cu^{II}/ZSM-5 (30) catalysts under conditions similar to the effluent in a real working diesel exhaust was evaluated. Evolution of the different compounds suggests that the contribution of NO$_x$ storage is minimal and that C$_3$H$_8$-SCR could be taken place, reducing the amount of NO considerably.

6.6 References

1.   Iwamoto, M.; Yahiro, H.; Mine, Y.; Kagawa, S., Excessively Copper Ion-exchanged ZSM-5 Zeolites as Highly Active Catalysts for Direct Decomposition of Nitrogen Monoxide. *Chemistry Letters* **1989,** *18* (2), 213-216.

2.   Ganemi, B.; Björnbom, E.; Demirel, B.; Paul, J., Zeolite Cu–ZSM-5: material characteristics and NO decomposition. *Microporous and Mesoporous Materials* **2000,** *38* (2–3), 287-300.

3.   Öhman, L. O.; Ganemi, B.; Björnbom, E.; Rahkamaa, K.; Keiski, R. L.; Paul, J., Catalyst preparation through ion-exchange of zeolite Cu-, Ni-, Pd-, CuNi- and CuPd-ZSM-5. *Materials Chemistry and Physics* **2002,** *73* (2–3), 263-267.

4.   Soria, J.; Martı́nez-Arias, A.; Martı́nez-Chaparro, A.; Conesa, J. C.; Schay, Z., Influence of the Preparation Method, Outgassing Treatment, and Adsorption of NO and/or O2 on the Cu2+ Species in Cu-ZSM-5: An EPR Study. *Journal of Catalysis* **2000,** *190* (2), 352-363.

5.   Gervasini, A.; Picciau, C.; Auroux, A., Characterization of copper-exchanged ZSM-5 and ETS-10 catalysts with low and high degrees of exchange. *Microporous and Mesoporous Materials* **2000,** *35–36*, 457-469.

6.   Iwamoto, M.; Yahiro, H.; Tanda, K.; Mizuno, N.; Mine, Y.; Kagawa, S., Removal of nitrogen monoxide through a novel catalytic process. 1. Decomposition on excessively copper-ion-exchanged ZSM-5 zeolites. *The Journal of Physical Chemistry* **1991,** *95* (9), 3727-3730.

7.   Iwamoto, M.; Yahiro, H.; Torikai, Y.; Yoshioka, T.; Mizuno, N., Novel Preparation Method of Highly Copper Ion-exchanged ZSM-5 Zeolites and Their Catalytic Activities for NO Decomposition. *Chemistry Letters* **1990,** *19* (11), 1967-1970.

8.   Yahiro, H.; Iwamoto, M., Copper ion-exchanged zeolite catalysts in deNOx reaction. *Applied Catalysis A: General* **2001,** *222* (1–2), 163-181.

9.   Schreier, M.; Teren, S.; Belcher, L.; Regalbuto, J. R.; Miller, J. T., The nature of 'overexchanged' copper and platinum on zeolites. *Nanotechnology* **2005,** *16* (7), S582-91.

10.   Putluru, S. S. R.; Riisager, A.; Fehrmann, R., Alkali resistant Cu/zeolite deNOx catalysts for flue gas cleaning in biomass fired applications. *Appl. Catal., B* **2011,** *101* (3-4), 183-188.

11.   Cruz-Cabeza, A. J.; Esquivel, D.; Jiménez-Sanchidrián, C.; Romero-Salguero, F. J., Metal-Exchanged β Zeolites as Catalysts for the Conversion of Acetone to Hydrocarbons. *Materials* **2012,** *5* (1), 121.

12.   Regina Oliveira de Souza, T.; Modesto de Oliveira Brito, S.; Martins Carvalho Andrade, H., Zeolite catalysts for the water gas shift reaction. *Applied Catalysis A: General* **1999,** *178*, 7-15.

13.   Hadjiivanov, K.; Dimitrov, L., IR spectroscopy study of CO and NOx adsorption on a Cu/Zr-HMS catalyst. *Microporous and Mesoporous Materials* **1999,** *27* (1), 49-56.

14.   Fu, W. Q.; Liu, T. T.; Fang, Z. X.; Ma, Y. L.; Zheng, X.; Wang, W. C.; Ni, X. J.; Hu, M. L.; Tang, T. D., High activity and stability in the cross-coupling of aryl halides with disulfides over Cu-doped hierarchically porous zeolite ZSM-5. *Chemical Communications* **2015,** *51* (27), 5890-5893.

15.   Ye, Q.; Yan, L.; Wang, H.; Cheng, S.; Wang, D.; Kang, T.; Dai, H., Enhanced catalytic performance of rare earth-doped Cu/H-Sep for the selective catalytic reduction of NO with C3H6. *Applied Catalysis A: General* **2012,** *431–432* (0), 42-48.

16.   McIntyre, N. S.; Cook, M. G., X-ray photoelectron studies on some oxides and hydroxides of cobalt, nickel, and copper. *Analytical Chemistry* **1975,** *47* (13), 2208-2213.

17.   Zahmakıran, M.; Durap, F.; Özkar, S., Zeolite confined copper(0) nanoclusters as cost-effective and reusable catalyst in hydrogen generation from the hydrolysis of ammonia-borane. *International Journal of Hydrogen Energy* **2010,** *35* (1), 187-197.

18.   Zahmakiran, M.; Oezkar, S., Preparation and characterization of zeolite framework stabilized cuprous oxide nanoparticles. *Materials Letters* **2009,** *63* (12), 1033-1036.

19.   Schay, Z.; Guczi, L.; Koppany, Z.; Nagy, I.; Beck, A.; Samuel, V.; Dongare, M. K.; Sabde, D. P.; Hegde, S. G.; Ramaswamy, A. V., Decomposition of NO over Cu-AITS-1 zeolites. *Catalysis Today* **1999,** *54* (4), 569-574.

20.   Janas, J.; Gurgul, J.; Socha, R. P.; Dzwigaj, S., Effect of Cu content on the catalytic activity of CuSiBEA zeolite in the SCR of NO by ethanol: Nature of the copper species. *Applied Catalysis B-Environmental* **2009,** *91* (1-2), 217-224.

21.   Li, L.; Guan, N., HC-SCR reaction pathways on ion exchanged ZSM-5 catalysts. *Microporous and Mesoporous Materials* **2009,** *117* (1–2), 450-457.

22.   Li, L.; Zhang, F.; Guan, N.; Richter, M.; Fricke, R., Selective catalytic reduction of NO by propane in excess oxygen over IrCu-ZSM-5 catalyst. *Catalysis Communications* **2007,** *8* (3), 583-588.

23.   Adelman, B. J.; Beutel, T.; Lei, G. D.; Sachtler, W. M. H., Mechanistic Cause of Hydrocarbon Specificity over Cu/ZSM-5 and Co/ZSM-5 Catalysts in the Selective Catalytic Reduction of NOx. *Journal of Catalysis* **1996,** *158* (1), 327-335.

24.   Chang, X.; Lu, G.; Guo, Y.; Wang, Y.; Guo, Y., A high effective adsorbent of NOx: Preparation, characterization and performance of Ca-beta zeolites. *Microporous and Mesoporous Materials* **2013,** *165* (0), 113-120.

25.   Cortes, J. M. G.; Gomez, M. J. I.; de Lecea, C. S. M., The selective reduction of NOx with propene on Pt-beta catalyst: A transient study. *Applied Catalysis B-Environmental* **2007,** *74* (3-4), 313-323.

Conclusions & Future Work   *7*

7.1 Conclusions

The title and objective of this thesis arises from a novel approach, the diesel oxidation NO_x adsorption catalyst (DONAC), where NO_x is to be stored by a diesel oxidation catalyst (DOC).

Diesel oxidation catalysts are the most used technology for abatement of carbon monoxide, gas phase hydrocarbons and the soluble organic fraction (SOF) of diesel particulate matter. Much of the DOC's development has focussed on decreasing the light-off temperature in order to improve oxidation activity, principally during cold starts. On the other hand, NO_x storage-reduction (NSR) catalysts ($Pt/BaO/Al_2O_3$) are one of the most practical technologies for NO_x emission control technologies applied in lean-burn gasoline and diesel vehicles [1]. Despite very interesting results being obtained with each class of catalyst, further studies are needed to find a catalytic system sufficiently active, selective and stable.

Among DOCs, the most efficient catalysts belong to two categories: supported noble metal (Pt and Pd) catalysts [2 3 4 5 6 7 8 9] and transition metal oxide catalysts, such as Cr, Fe, Co and Mn oxides [10 11 12 13]. The noble metal-based catalysts are more active but rather unstable and expensive. Platinum-based diesel oxidation catalysts are still the most used technology. Although Al_2O_3 has been extensively used as a support, the use of other metal oxide supports has yielded more active HC oxidation catalysts [8 14 15 16 17 18]. It is then interesting to investigate the effect of the support, to obtain more economically viable supported platinum catalysts with a high sulphur tolerance.

Yazawa, Kobayashi and co-workers have published several studies which investigate the support effect in the low temperature catalytic combustion of propane over palladium [2] and platinum catalysts [4] [5] [6] by using a series of metal oxide and mixed metal oxide supports. However, a degree of uncertainty persists in determining whether the reaction is structure sensitive and in the true nature of the active site. One of the aims of this thesis is to rationalise the effect of a series of mixed TiO_2 and Al_2O_3 based supports on propane combustion in an oxidising atmosphere over platinum catalysts. The novelty of this work is that it uses a systematic study to explore the effect of multiple variables. This work addresses not only the effect of the support, platinum loading, preparation method, calcination conditions and platinum precursor, but also the effect of the titania phase composition (anatase or anatase-rutile) and an investigation of the oxidation of NO to NO_2. The latter have not previously been reported to the same level.

The most active supported platinum catalyst was found to be 1 wt. % Pt/TiO_2-SiO_2 (16 % mol Si, A-R). This catalyst exhibits a T_{50} of 270 °C for propane oxidation and T_{50} of 350 °C for NO oxidation. Because different metal loadings and experimental conditions were used, it is difficult to compare results in absolute numbers with previous publications. However, the same trends were found. Hence, in general, increasing the SiO_2 content of the TiO_2 and Al_2O_3 mixed supports gives rise to Pt catalysts which are more active for propane and NO oxidation. Variations in the oxidation properties of the supported platinum catalysts studied are mainly related to the nature of the support material rather than other variables such as preparation method, metal precursor or calcination conditions.

In order to determine the effect of the support on the structural and electronic properties of the Pt catalysts and correlate these with oxidation performance, full characterisation was performed. The oxidation state of platinum varies with the support material. In general, the presence of metallic platinum becomes more favourable with increasing SiO_2 content of

the support. There is a linear relationship between the oxidation state of platinum and catalytic activity for NO oxidation, with conversion clearly higher with an increasing presence of Pt^0. However, for the total oxidation of propane this relationship is not as unequivocal. For the anatase-rutile TiO_2 based supports, propane oxidation activity is enhanced by increasing the concentration of metallic platinum. On the other hand, anatase TiO_2 based catalysts present superior activity for propane oxidation despite platinum being present predominantly as PtO.

An interesting finding is that platinum catalysts prepared using anatase-based supports, TiO_2-(SiO_2) (A), present high performance for the total oxidation of propane but not for the oxidation of NO. These supports not only possess a high surface area but a "cloud shape" morphology with highly dispersed small TiO_2 crystallites. Morphology and phase composition play an active role in the redox properties of the support and its interaction with supported metal particles. Thus, metal-support interactions are of great importance to understand the observed differences in catalytic activity. Results suggest that the extraordinary activity of 1 wt. % Pt/TiO_2 (A) is due to highly reactive oxygen species within the titania support, which promote the total oxidation of propane but not the oxidation of NO to NO_2.

The activity of the supported platinum catalysts was found to depend strongly on oxidation state, with platinum in metallic state being most active. However, it is not only the platinum oxidation state, but the combination of several factors including metal dispersion, BET surface area, morphology and phase composition of the support that explains the variations in catalytic activity.

NSR catalysts are usually formed of precious metals, NO_x storage components and support metal oxides. NSR catalysts work in a periodic mode, switching between lean and rich

conditions. DONAC provides an alternative for NO_x abatement and requires an adsorption catalyst that stores NO_x at low temperature (T < 250 °C) and releases it at high temperatures. While BaO is the most commonly studied NO_x trapping component, metal exchanged zeolites have been widely used not only for NH_3- and HC-SCR but also as NO_x storage components. A study of the NO_x storage capacity of metal (Cu, Fe and Pt) -exchanged zeolites with different compositions ($SiO_2/Al_2O_3 = 5.1 - 50$) and structures (Y, ZSM-5 and BETA) prepared by two different exchange methods (WIE and CVI) has been addressed in this thesis.

While investigations of NO_x adsorption-desorption on metal exchanged zeolites have been reported in a number of publications, the effect of the silicon/aluminium ratio, internal channels and inclusion of base and precious metals has not previously been investigated in the level of detail presented here. In addition, the NO_x storage capacity of catalysts prepared by the CVI method, developed by Forde *et al.*[19], has not been reported before. This study also adopts the DOE method to enhance the adsorption/desorption properties of a Cu^{II}/ZSM-5 (30) catalytic system prepared by WIE and CVI. Application of statistical design of experiments is a novel approach that allows the identification of important individual variables and interactions among them in order to optimise catalytic activity with a relatively low number of experiments.

NO_x storage capacities were investigated in the absence and presence of O_2. However, NO is more weakly adsorbed on zeolites than NO_2 and thus, oxidation of NO to NO_2 is necessary to improve NO_x desorption at high temperature (T > 200 °C). Desorption at high temperatures is attributed to formation of more thermally stable nitrates. For application under real conditions, results for NO_x storage in the presence of O_2 are more telling.

When comparing different metal exchanged zeolites, it is important to consider not only the total amount of NO_x adsorbed and desorbed but also the degree of NO oxidation and distribution of NO_x species desorbed at different temperatures. The zeolite framework and acidity are found to play a crucial role in the NO_x storage capacity of metal exchanged zeolites. The DOE method was applied to investigate the way in which experimental variables affect the NO_x storage capacity of Cu^{II}/ZSM-5 (30). Whilst the data set generated provided information about the relative influence of the experimental variables studied, statistical analysis is required for subsequent optimisation. Temperature is found to have the greatest effect on the NO_x storage capacity. In addition, its influence is dependent on the copper precursor concentration.

Among the zeolite based catalysts studied, potential candidates for application under real working conditions are those that exhibit greater NO_x desorption at high temperatures above 200 °C. Due to the intrinsic adsorption capacity of the parent zeolite, H^+-ZSM-5 (23), Cu^{II}/ZSM-5 (23) catalysts prepared by WIE and CVI exhibit high NO_x storage capacities with a large amount of NO_x being desorbed at high temperatures, 6 mg NO_x/g catalyst (200 µmol NO_x/g catalyst) for Cu^{II}/ZSM-5 (23) $_{WIE}$ and 10.9 mg NO_x/g catalyst (363 µmol NO_x/g catalyst) for Cu^{II}/ZSM-5 (23) $_{CVI}$. The statistical approach allowed for a significant enhancement in the storage capacity of Cu^{II}/ZSM-5 (30) and, in particular, the amount of NO_x desorbed at high temperature. NO_x desorption at temperature above 200 °C is found to be 8.5 mg NO_x/g catalyst (283 µmol NO_x/g catalyst) for Cu^{II}/ZSM-5 (30) $_{WIE\ DOE\ 4}$ and10.2 mg NO_x/g catalyst (340 µmol NO_x/g catalyst) for Cu^{II}/ZSM-5 (30) $_{CVI\ DOE\ 6}$.

Once again, due to differences in the experimental reaction conditions used, it is difficult to compare the NO_x storage capacity obtained for the catalysts presented in this thesis with

those of similar catalysts presented in previous publications. However, the most active catalysts seem to exhibit higher performance than previously studied analogues [20] [21].

The catalytic activity of the most active Cu^{II}/ZSM-5 (30) catalysts under conditions similar to the effluent of a real working diesel engine was evaluated. Results suggest that the contribution of NO_x storage is minimal and that C_3H_8-SCR takes place, decreasing the amount of NO_x storage considerably.

In order to correlate the physicochemical properties of the metal exchanged zeolites with their NO_x storage performance, characterisation studies were performed. Results confirmed differences in the distribution and speciation of the metal sites on the zeolite support. H_2-TPR was found to provide key information in understanding the NO_x storage capacity. The initial redox state, Cu^{2+}/Cu^+ and Fe^{2+}/Fe^{3+} ratio, and bonding strength of the metal ions to the framework affect the reducibility of metal species and consequently the storage capacity.

In summary, studies carried out during the course of this thesis have led to a significant enhancement in the performance of supported platinum catalysts, for the catalytic oxidation of propane and NO, and of metal exchanged zeolites for NO_x storage. Whilst future work is required to fully understand these catalytic systems, the detailed investigations presented here provide key information to address actual needs in diesel exhaust emissions abatement.

7.2 Recommended Future Work

7.2.1 Oxidation properties of supported platinum catalysts

Completion of this work will require further characterisation studies to fully understand the catalytic systems studied. Stability tests under realistic conditions should then be carried out for those promising catalysts found.

Among the further characterisation needed, the following analytical techniques have been suggested:

ICP-MS

Quantification of the total metal loading and composition of the catalyst is crucial for determination of the active phase nature and to more accurately compare the activity of different catalysts.

CO_2-TPD and IR spectra of adsorbed pyridine.

Acidity trends obtained in this thesis for the TiO_2 (A-R) supports are inconsistent with those obtained in previous studies [22] [23] [24] [25], which showed that the Brønsted acidity of TiO_2 based supports increases with an increasing SiO_2 content. In addition, the NH_3-TPD experiments performed do not provide information about the nature of Lewis and Brønsted acid sites. Hence, further studies would be beneficial in understanding the surface acidity and basicity of the supports and catalysts in greater detail.

Propane, NO and O_2 uptake studies.

As reported previously [26] [27] [28], measuring the density of adsorbed molecules, including propane, NO and O_2, over the supported platinum catalysts will provide useful information

in understanding the effect of the support on the oxidation properties and deactivation of catalysts.

In situ Raman and IR spectroscopy

Shifts in the XPS binding energy of supported platinum catalysts exposed to different conditions have been associated with SMSI. It is widely recognised that metal-support interactions are of great importance in understanding differences in catalytic activity. Thus, probing metal-support interactions under oxidising and reducing conditions by *in situ* techniques would be of great interest [29].

TPR-TPO redox cycles, oxygen storage and oxygen mobility studies

Initial H_2-TPR experiments suggest that the oxidation properties of supported platinum catalysts depend extensively upon the inherent reducibility of the support. The extraordinary activity of 1 wt. % Pt/TiO_2 (A) is attributed to highly reactive oxygen species within the titania support, which promote the total oxidation of propane. In order to confirm this theory and understand the redox properties of the supports, repeated TPR/O cycles, oxygen storage and oxygen mobility experiments are required.

HRTEM-TEAM

Analysis of TEM images is a powerful tool for determination of the structural properties of catalysts and the structure sensitive nature of a reaction. To assess the real effect of dispersion on catalytic activity, the oxidation activities of platinum catalysts which differ in metal dispersion and particle size, but are supported on the same metal oxide, should be evaluated.

In addition, SMSI is, in many cases, related to structural modification via encapsulation. A limitation of this technique is the resolution of the instrument used. Metal particles are

sometimes overlooked as their size is below the detection limit of the instrument. Hence, use of a transmission electron microscope with higher resolution or other instrument such as an electron aberration-corrected electron microscope, will allow for more complete analysis of these catalysts.

With the development of the catalysts, understanding the reaction mechanism involved in the different oxidation reaction studies is a key issue.

Determination of kinetics for propane and NO oxidation reactions

Changing the reaction mixture composition, this is the C_3H_8:O_2 or NO:O_2 ratio, is known to affect catalyst performance [2]. Determination of the reaction orders with respect to the reactants and products, the activation energy and Arrhenius plots [30] allows elucidation of the rate determining step and might suggest possible mechanisms.

Assessment of the supports' oxidation activity

Although many studies have confirmed that metal oxide supports present negligible intrinsic oxidation activity, with the noble metal known to be the active phase, propane and NO oxidation should be performed over the bare supports to determine the inherent oxidation properties of the support.

Whilst more active supported platinum catalysts have been developed through this study, for application in real DOCs further extensive studies under conditions similar to the composition of diesel exhaust effluent are required.

Calculation of turnover frequencies

ICP-MS analysis and completion of stability tests over all catalysts is needed to calculate their TOFs at steady state.

Transient temperature cycles

Transient temperature cycles simulate changes in engine load. It has been demonstrated that when tested for propane oxidation under a transient temperature cycles Pt catalysts exhibit hysteresis behaviour. Similar tests for NO oxidation should be performed to determine variations in catalytic activity at constant exhaust composition and confirm the inverse hysteresis which was previously reported [31].

Reaction mixture composition

It is known that the oxidation reaction is hindered when using a more complex reaction mixture [32] [33] [34] [35]. Studying the inhibitory effect of CO_2, H_2O and SO_2 would allow for estimation of how the catalysts would perform under real working conditions.

Based on the results presented in this thesis, further work should be addressed to optimise and design supported metal catalysts for DOC technologies.

Other supports

Further investigations to assess the effect of other metal oxide and mixed metal oxide supports on the oxidation activity of supported platinum catalysts are needed in order to identify catalysts with high oxidation activity. Previous studies have shown that CeO_2, ZrO_2 and CeO_2-ZrO_2 supports present potential for application in hydrocarbon oxidation [36].

Different noble metals

Investigation of potential support effects on the oxidation properties of other noble metals, such as Pd, Ru or Rh, will allow identification of candidate DOCs. A study of synergism in bimetallic catalyst systems is also of interest when designing catalysts.

Additives

The low temperature propane oxidation activity, thermal stability and poisoning resistance of supported noble metal catalysts under an oxidising atmosphere has been reported to be enhanced with the electronegativity of additives [3] [4] [7] [8] [9] [15]. Hence, the effect of addition of elements including Nb, V and W, on the oxidation activity of the catalysts studied should be investigated.

7.2.2 Optimising NO_x storage in metal exchanged zeolites

Although several candidates which show promising NO_x storage performance and a large amount of high temperature NO_x desorption have been found, reproducibility and durability studies are needed to reach robust conclusions.

Whilst initial characterisation studies have been performed, these should be extended, with full analysis of the structure, morphology, porosity, acidity, composition, degree of metal exchange, redox properties and distribution of metal species as well as identification of the adsorbed N-complexes. The following analytical techniques have been suggested:

ICP-MS

Quantification of the total metal loading and composition of the catalyst is crucial in determining the degree of metal exchange and speciation.

CO_2-TPD and IR spectra of adsorbed pyridine

Further studies would be beneficial in understanding in more detail the nature of acid and base sites, both Lewis and Brønsted. While pyridine is adsorbed as pyridinium ion on a Brønsted site, is coordinatively bonded to Lewis sites. These adsorption species present

different vibrational frequencies. Lewis acid sites are associated with the bands appearing at 1450 and 1600 cm^{-1} and Brønsted acid sites with those at 1520 ad 1620 cm^{-1} [37].

XRD

Although unlikely because only extra framework exchange is expected, XRD investigations should be performed to determine possible changes in the crystallinity and unit cell dimensions of the zeolites after metal exchange.

As described in Chapter 6, completion of the optimisation by DOE requires statistical analysis of the data generated. Statistical analysis provides quantification of the influence of each experimental variable and of the interactions between different variables. Experimental validation should address the effectiveness of DOE in maximising the NO_x storage performance by preparing and assessing a catalyst under the optimal experimental conditions predicted by the statistical model.

With the development of the catalysts, understanding the mechanism involved in the formation of nitrates is a key issue. *In situ* DRIFTS studies should be used to determine the NO_x storage mechanism, identify reaction intermediates and assess the thermal stability of adsorbed surface species. Often, multiple M_xO_y species are formed on the surface of zeolites and determining the contribution of each type of site is difficult. Transient analysis techniques would help to elucidate the nature of the active phase and identify spectators.

Results presented in this thesis have already demonstrated changes in performance when a catalyst that shows a high NO_x storage capacity under model conditions, is tested under conditions similar to those in the diesel engine. Insufficient activity, narrow operating windows and sensitivity to H_2O and sulphur poisoning hinder their practical application for

NO_x storage. Hence, further investigations are required to determine how a catalyst will perform under real working conditions.

Adsorption temperature

Investigation of the effect of varying the adsorption temperature on NO_x storage would be interesting, as it affects the degree of NO oxidation and, consequently, the thermal stability of the adsorbed species formed.

Reaction mixture composition

It is known that the presence of other molecules decreases the NO_x adsorption capacity and causes deactivation of catalysts through competition for the selective adsorption sites and pore blockage [21] [38] [39] [40]. Studying the inhibitory effect of CO_2, CO, H_2O and SO_2 allows for estimation of how the catalysts would perform under real working conditions.

In order to continue with optimisation of the NO_x storage capacity, different zeolite frameworks and exchanged metals should be studied to design novel metal exchanged catalysts. Due to their abundance, low cost and high NO_x storage capacity, natural zeolites are of interest [38].

A conclusion to the study will consist of applying findings to the design of a selective hybrid catalyst with high poisoning resistance. The combination of a catalyst with high oxidation activity and an adsorbent with the capacity to store NO_x at high temperatures would be of great interest.

7.3 References

1.   Liu, G.; Gao, P.-X., A review of NOx storage/reduction catalysts: mechanism, materials and degradation studies. *Catalysis Science & Technology* **2011,** *1* (4), 552-568.

2.   Yazawa, Y.; Yoshida, H.; Takagi, N.; Komai, S.-i.; Satsuma, A.; Hattori, T., Acid Strength of Support Materials as a Factor Controlling Oxidation State of Palladium Catalyst for Propane Combustion. *Journal of Catalysis* **1999,** *187* (1), 15-23.

3.   Wu, X.; Zhang, L.; Weng, D.; Liu, S.; Si, Z.; Fan, J., Total oxidation of propane on Pt/WOx/Al2O3 catalysts by formation of metastable Ptdelta+ species interacted with WOx clusters. *J Hazard Mater* **2012,** *225-226*, 146-54.

4.   Kobayashi, M.; Morita, A.; Ikeda, M., The support effect in oxidizing atmosphere on propane combustion over platinum supported on TiO2, TiO2–SiO2 and TiO2–SiO2–WO3. *Applied Catalysis B: Environmental* **2007,** *71* (1–2), 94-100.

5.   Yazawa, Y.; Takagi, N.; Yoshida, H.; Komai, S.-i.; Satsuma, A.; Tanaka, T.; Yoshida, S.; Hattori, T., The support effect on propane combustion over platinum catalyst: control of the oxidation-resistance of platinum by the acid strength of support materials. *Applied Catalysis A: General* **2002,** *233* (1–2), 103-112.

6.   Yazawa, Y.; Yoshida, H.; Hattori, T., The support effect on platinum catalyst under oxidizing atmosphere: improvement in the oxidation-resistance of platinum by the electrophilic property of support materials. *Applied Catalysis A: General* **2002,** *237* (1–2), 139-148.

7.   Garcia, T.; Weng, W.; Solsona, B.; Carter, E.; Carley, A. F.; Kiely, C. J.; Taylor, S. H., The significance of the order of impregnation on the activity of vanadia promoted palladium-alumina catalysts for propane total oxidation. *Catalysis Science & Technology* **2011,** *1* (8), 1367-1375.

8.   Taylor, M. N.; Zhou, W.; Garcia, T.; Solsona, B.; Carley, A. F.; Kiely, C. J.; Taylor, S. H., Synergy between tungsten and palladium supported on titania for the catalytic total oxidation of propane. *Journal of Catalysis* **2012,** *285* (1), 103-114.

9.   Yazawa, Y.; Yoshida, H.; Komai, S.-i.; Hattori, T., The additive effect on propane combustion over platinum catalyst: control of the oxidation-resistance of platinum by the electronegativity of additives. *Applied Catalysis A: General* **2002,** *233* (1–2), 113-124.

10.   Puértolas, B.; Smith, A.; Vázquez, I.; Dejoz, A.; Moragues, A.; Garcia, T.; Solsona, B., The different catalytic behaviour in the propane total oxidation of cobalt and manganese oxides prepared by a wet combustion procedure. *Chemical Engineering Journal* **2013,** *229* (0), 547-558.

11.   Heynderickx, P. M.; Thybaut, J. W.; Poelman, H.; Poelman, D.; Marin, G. B., The total oxidation of propane over supported Cu and Ce oxides: A comparison of single and binary metal oxides. *Journal of Catalysis* **2010,** *272* (1), 109-120.

12.   Morales, M. R.; Barbero, B. P.; Cadús, L. E., Total oxidation of ethanol and propane over Mn-Cu mixed oxide catalysts. *Applied Catalysis B: Environmental* **2006,** *67* (3–4), 229-236.

13.   Yuranov, I.; Dunand, N.; Kiwi-Minsker, L.; Renken, A., Metal grids with high-porous surface as structured catalysts: preparation, characterization and activity in propane total oxidation. *Applied Catalysis B: Environmental* **2002,** *36* (3), 183-191.

14.   Okal, J.; Zawadzki, M.; Krajczyk, L., Light alkane oxidation over Ru supported on ZnAl2O4, CeO2 and Al2O3. *Catalysis Today* **2011,** *176* (1), 173-176.

15.	Taylor, M.; Ndifor, E. N.; Garcia, T.; Solsona, B.; Carley, A. F.; Taylor, S. H., Deep oxidation of propane using palladium–titania catalysts modified by niobium. *Applied Catalysis A: General* **2008,** *350* (1), 63-70.

16.	Garcia, T.; Solsona, B.; Murphy, D. M.; Antcliff, K. L.; Taylor, S. H., Deep oxidation of light alkanes over titania-supported palladium/vanadium catalysts. *Journal of Catalysis* **2005,** *229* (1), 1-11.

17.	Passos, F.; Oliveira, E.; Mattos, L.; Noronha, F., Effect of the support on the mechanism of partial oxidation of methane on platinum catalysts. *Catalysis Letters* **2006,** *110* (1-2), 161-167.

18.	Hoyle, N. D.; Kumarasamy, P.; Self, V. A.; Sermon, P. A.; Vong, M. S. W., Catalysis of H2, CO and alkane oxidation–combustion over Pt/Silica catalysts: evidence of coupling and promotion. *Catalysis Today* **1999,** *47* (1–4), 45-49.

19.	Forde, M. M.; Kesavan, L.; bin Saiman, M. I.; He, Q.; Dimitratos, N.; Lopez-Sanchez, J. A.; Jenkins, R. L.; Taylor, S. H.; Kiely, C. J.; Hutchings, G. J., High Activity Redox Catalysts Synthesized by Chemical Vapor Impregnation. *ACS Nano* **2014,** *8* (1), 957-969.

20.	Despres, J.; Koebel, M.; Kröcher, O.; Elsener, M.; Wokaun, A., Adsorption and desorption of NO and NO2 on Cu-ZSM-5. *Microporous and Mesoporous Materials* **2003,** *58* (2), 175-183.

21.	Landi, G.; Lisi, L.; Pirone, R.; Russo, G.; Tortorelli, M., Effect of water on NO adsorption over Cu-ZSM-5 based catalysts. *Catalysis Today* **2012,** *191* (1), 138-141.

22.	Structure, Surface Properties and Photocatalytic Activity of TiO2 and TiO2/SiO2 Catalysts Prepared at Different pH Values. *Acta Phys. -Chim. Sin.* **2011,** *27* (6), 1487-1492.

23.	Guan, K., Relationship between photocatalytic activity, hydrophilicity and self-cleaning effect of TiO2/SiO2 films. *Surface and Coatings Technology* **2005,** *191* (2–3), 155-160.

24.	Liu, T.-C.; Cheng, T.-I., Effects of SiO2 on the catalytic properties of TiO2 for the incineration of chloroform. *Catalysis Today* **1995,** *26* (1), 71-77.

25.	Properties of TiO2-SiO2 Mixed Oxides and Photocatalytic Oxidation of Heptane and Sulfur Dioxide.

26.	Performance of doped Pt/TiO, (W6+) catalysts for combustion of volatile organic compounds (VOCs). *Applied Catalysis B: Environmental* **1998,** *15*, 75-92.

27.	Mulla, S. S.; Chen, N.; Cumaranatunge, L.; Blau, G. E.; Zemlyanov, D. Y.; Delgass, W. N.; Epling, W. S.; Ribeiro, F. H., Reaction of NO and O2 to NO2 on Pt: Kinetics and catalyst deactivation. *Journal of Catalysis* **2006,** *241* (2), 389-399.

28.	Avila, M. S.; Vignatti, C. I.; Apesteguía, C. R.; Garetto, T. F., Effect of support on the deep oxidation of propane and propylene on Pt-based catalysts. *Chemical Engineering Journal* **2014,** *241* (0), 52-59.

29.	Lin, W.; Herzing, A. A.; Kiely, C. J.; Wachs, I. E., Probing Metal–Support Interactions under Oxidizing and Reducing Conditions: In Situ Raman and Infrared Spectroscopic and Scanning Transmission Electron Microscopic–X-ray Energy-Dispersive Spectroscopic Investigation of Supported Platinum Catalysts. *The Journal of Physical Chemistry C* **2008,** *112* (15), 5942-5951.

30.	Matam, S. K.; Kondratenko, E. V.; Aguirre, M. H.; Hug, P.; Rentsch, D.; Winkler, A.; Weidenkaff, A.; Ferri, D., The impact of aging environment on the evolution of Al2O3 supported Pt nanoparticles and their NO oxidation activity. *Applied Catalysis B: Environmental* **2013,** *129*, 214-224.

31.   Hauff, K.; Tuttlies, U.; Eigenberger, G.; Nieken, U., Platinum oxide formation and reduction during NO oxidation on a diesel oxidation catalyst – Experimental results. *Applied Catalysis B: Environmental* **2012**, *123–124*, 107-116.
32.   Catalytic control of diesel engine particulate emission: Studies on model reactions over a EuroPt-1 (Pt/SiO$_2$) catalyst

Applied Catalysis B: Environmental **1993,** *2*, 183-197.
33.   Burch, R.; Urbano, F. J.; Loader, P. K., Methane combustion over palladium catalysts: The effect of carbon dioxide and water on activity. *Applied Catalysis A: General* **1995,** *123* (1), 173-184.
34.   Sekizawa, K.; Widjaja, H.; Maeda, S.; Ozawa, Y.; Eguchi, K., Low temperature oxidation of methane over Pd/SnO2 catalyst. *Applied Catalysis A: General* **2000,** *200* (1–2), 211-217.
35.   Kułażyński, M.; van Ommen, J. G.; Trawczyński, J.; Walendziewski, J., Catalytic combustion of trichloroethylene over TiO2-SiO2 supported catalysts. *Applied Catalysis B: Environmental* **2002,** *36* (3), 239-247.
36.   Wang, B.; Wu, X.; Ran, R.; Si, Z.; Weng, D., IR characterization of propane oxidation on Pt/CeO2–ZrO2: The reaction mechanism and the role of Pt. *Journal of Molecular Catalysis A: Chemical* **2012,** *356* (0), 100-105.
37.   Auerbach, S. M.; Currado, K. A.; Dutta, P. K., *HANDBOOK OF ZEOLITES SCIENCE AND TECHNOLOGY*. Marcel Dekker Inc: New York, 2003.
38.   Wang, H.; Yu, Q.; Xiao, L.; Liu, T.; Yu, W.; Jiang, X.; Zhang, X.; Zheng, X., Superior Storage Performance for NO in Modified Natural Mordenite. *Chinese Journal of Chemistry* **2012,** *30* (7), 1511-1516.
39.   Pan, H.; Guo, Y.; Bi, H. T., NOx adsorption and reduction with C3H6 over Fe/zeolite catalysts: Effect of catalyst support. *Chemical Engineering Journal* **2015,** *280*, 66-73.
40.   Sultana, A.; Habermacher, D. D.; Kirschhock, C. E. A.; Martens, J. A., Adsorptive separation of NOx in presence of SOx from gas mixtures simulating lean burn engine exhaust by pressure swing process on Na–Y zeolite. *Applied Catalysis B: Environmental* **2004,** *48* (1), 65-76.

APPENDIX A

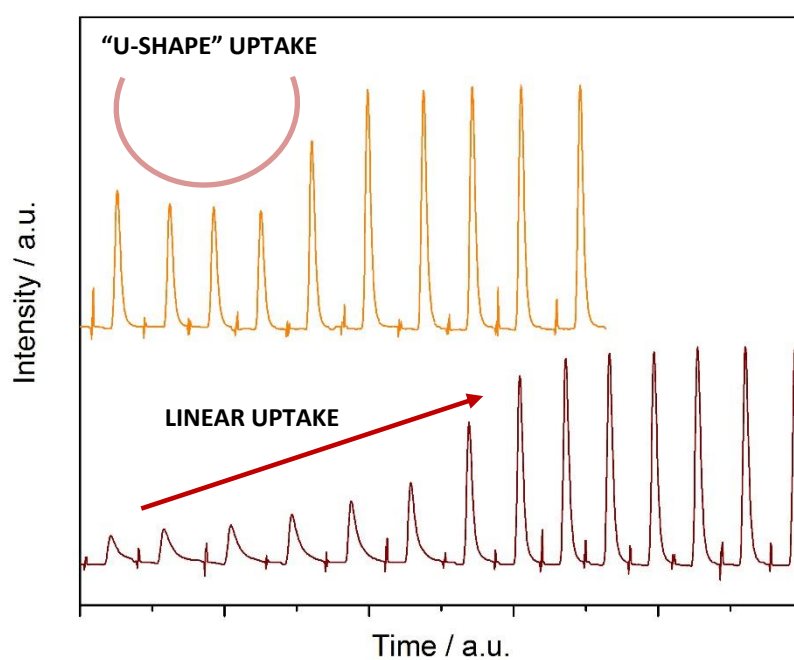Analysis by XPS and TEM-EDX confirms the presence of tungsten, W, on the TiO_2-SiO_2 (10 % mol Si, A) support.
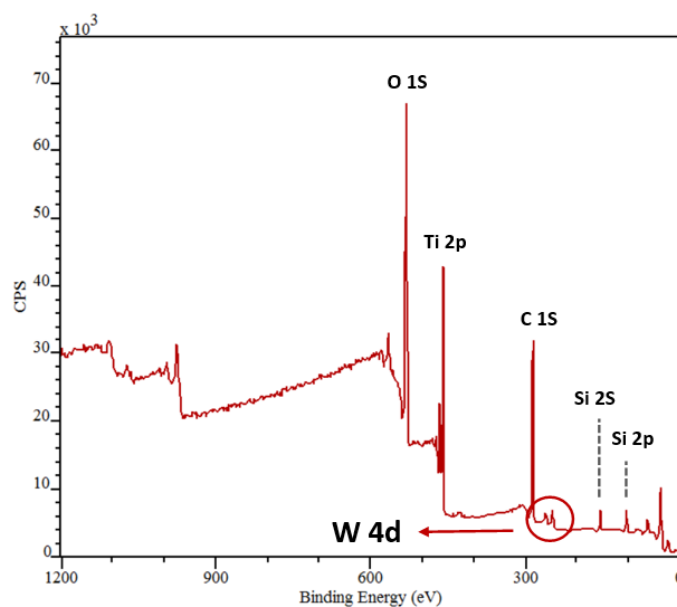
XPS wide spectrum of the TiO_2-SiO_2 (10 % mol Si, A) support
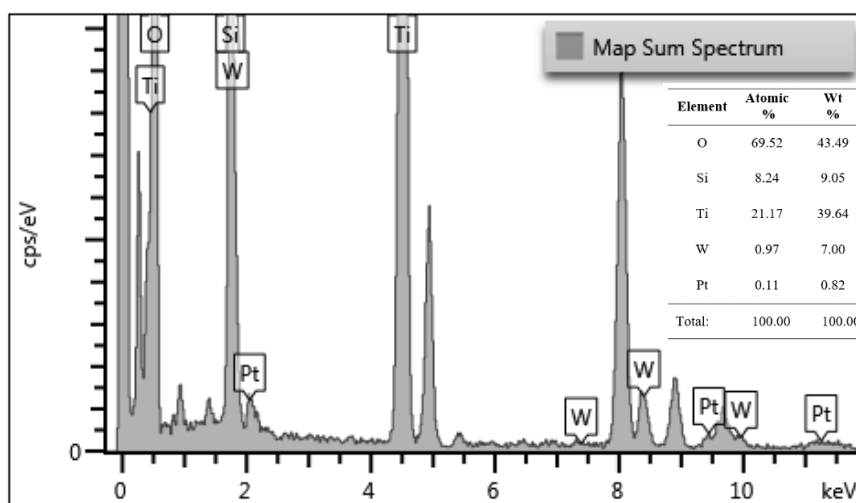
EDX spectrum of the TiO_2-SiO_2 (10 % mol Si, A) support

APPENDIX B

Representation of the typical linear and "u-shaped" CO uptake of the supported platinum catalysts.

(---) 1 wt. % Pt/TiO_2 (A-R)   **(---)** 1 wt. % Pt/TiO_2-SiO_2 (16 % mol Si, A-R)
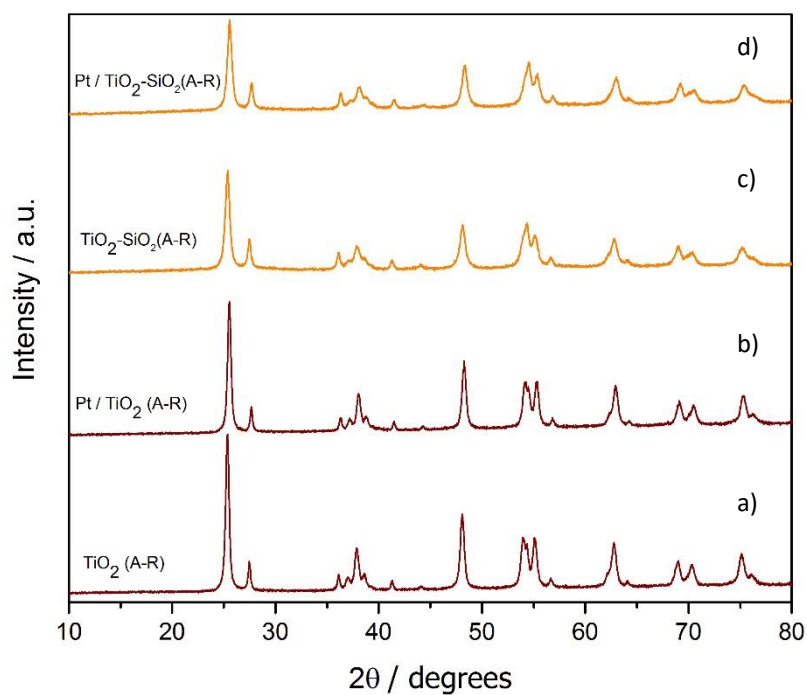
CO Chemisorption pulses obtained for 1 wt. % platinum supported catalysts

Pretreatment: 300 ^{0}C, 2 h, H_2. CO chemisorption performed at room temperature using 77 µL

pulses of CO. Sample mass used *ca*. 500 mg

Absence of diffraction lines corresponding to platinum – 2θ of 39^0 (111), 46^0 (200) and 67^0 (220) - on the XRDs of the supported platinum catalysts.

Powder X-Ray diffraction patterns of the supports and supported platinum catalysts:
a) TiO_2 (A-R)   b) 1 wt. % Pt/TiO_2 (A-R)
c) TiO_2-SiO_2 (16 mol % Si, A-R)   d) 1 wt. % Pt/TiO_2-SiO_2 (16 mol % Si, A-R)